ABSTRACT

Title of Dissertation: Quantum Computing with Josephson Junction Circuits

Huizhong Xu, Doctor of Philosophy, 2004

Dissertation directed by: Professor J. Robert Anderson
Department of Physics

This work concerns the study of Josephson junction circuits in the context of their usability for quantum computing. The zero-voltage state of a current-biased Josephson junction has a set of metastable quantum energy levels. If a junction is well isolated from its environment, it will be possible to use the two lowest states as a qubit in a quantum computer.

I first examine the meaning of isolation theoretically. Using a master equation, I analyzed the effect of dissipation on escape rates and suggested a simple method, population depletion technique, to measure the relaxation time (T_1). Using a stochastic Bloch equation to analyze the dependence of microwave resonance peak width on current noise, I found decoherence due to current noise depends on the noise spectrum. For high frequency noise with a cutoff frequency f_c much larger than $1/T_1$, I found decoherence due to noise can be described by a dephasing rate that is proportional to the noise spectral density. However, for low frequency noise such that its cutoff frequency f_c is much smaller than $1/T_1$, decoherence due to noise depends on the total rms current noise.

I then analyze and test a few qubit isolation schemes, including resistive isolation, inductor-capacitor (LC) isolation, half-wavelength resonant isolation and inductor-junction (LJ) isolation. I found the resistive isolation scheme has a severe heating problem. Macroscopic quantum tunneling and energy level quantization were observed in the LC isolated Nb/AlOx/Nb and AL/ALOx/Al junction qubits at 25 mK. Relaxation times of 4-12 ns and spectroscopic coherence times of 1-3 ns were obtained for these LC isolated qubits. I found the half-wavelength isolated junction qubit has a relaxation time of about 20 ns measured by the population-depletion techniques, but no energy levels were observed in this qubit. Experimental results suggest the LJ isolated qubit has a longer relaxation and coherence times than all my previously examined samples. Using a microwave pulse technique, a relaxation time of 50 ns was measured on this sample, the spectroscopic coherence time obtained using continuous microwave pumping is about 5-8 ns. Coherent quantum oscillations (Rabi oscillations) were also observed on this sample with a decay time of around 10 ns for a $|0> \rightarrow |1>$ level spacing of 7.6 GHz. The relaxation times are much smaller than what I would expect from my designs for all isolation schemes. Possible reasons for this inconsistency were discussed.

Using microwave spectroscopy techniques, I probed quantum phenomena in a coupled macroscopic three-qubit system that is comprised of two Nb/AlOx/Nb Josephson junctions and an LC resonator. The measured spectrum at 25 mK in the frequency range 4-15 GHz agrees well with quantum mechanical calculations, consistent with the existence of entangled states between the three degrees of freedom. These entangled states and a first-order strong coupling between two junction qubits open the possibility of using a resonator as a data bus for information storage and manipulation in a multi-qubit system. The measurements also demonstrate spectroscopy is a powerful tool and can be used to study a composite system with many qubits.

Quantum Computing with Josephson Junction Circuits

by

Huizhong Xu

Dissertation submitted to the Faculty of the Graduate School of the
University of Maryland at College Park in partial fulfillment
of the requirements for the degree of
Doctor of Philosophy
2004

Advisory Committee:

Professor J. Robert Anderson, Chairman
Professor Christopher J. Lobb, Co-advisor
Professor Frederick C. Wellstood, Co-advisor
Professor Michael A. Coplan
Professor Alex J. Dragt
Professor Richard L. Greene

DEDICATION

To my parents

ACKNOWLEDGEMENTS

I am very grateful to my advisors Dr. Bob Anderson, Dr. Chris Lobb and Dr. Fred Wellstood for their great guidance, advice and encouragement during my graduate study. Their devoted attitudes towards scientific research and discovery inspired me to continue my interest in understanding more about the natural world. The personal and professional relationship I had with them during the past three and a half years will probably remain in my memory forever.

I would like to thank the committee members, Dr. Michael Coplan, Dr. Alex Dragt and Dr. Richard Greene for their careful reading of and very helpful suggestions about my thesis.

I would like to thank the professors in the center and in the department: Dr. Nick Chant for his very helpful advice on graduate study and choosing research groups; Dr. Richard Greene for creating a vibrant research environment in the Center and for providing students with opportunities to practice their presentation skills at the Center seminar; Dr. Richard Webb for much helpful advice and lending us a sealed pump when ours failed; Dr. Michael Coplan for instructing research electronics, from which I learned many useful things that were applied to my thesis research; Dr. Bei-Lok Hu for instructing me in general relativity and giving me much helpful advice on conducting scientific research.

It would not have been possible for me to finish my research without the collaboration with other members in the Superconducting Quantum Computing Group. I would like to thank Dr. Andrew Berkely with whom I discussed interesting junction physics, built experimental apparatus, fabricated samples and performed experiments; Sudeep Dutta for many helpful discussions about junction physics and the experiment, his beautiful work in improving the experiment platform, and taking care of the experiment and continuing the measurement while I was writing my thesis; Dr. Roberto Ramos for his devoted effort in keeping the dilution refrigerator running smoothly, his support and patience in getting the small yet necessary ingredients for an experiment; Fred Strauch and Dr. Phil Johnson for many very insightful and helpful discussions and for their support in providing wonderful theoretical explanations of the data; and Hanhee Paik and Mark Gubrud for their contributions to the quantum computing project.

I am grateful to my colleagues working in the sub-basement laboratory. I am thankful to Dr. Su-young Lee and David Tobias, not only for the cookies and teas they made for the lab people, but also the laughter and joy spread around the whole lab; Dr. John Matthews and Dr. Matt Sullivan for many helpful discussions and showing me how to use LATEX; Gus Vlahacos, Soun Pil Kwon, Dr. Douglas Strachan, Su Li, Monica Lilly and Hua Xu for making the subbasement lab an interesting place to work.

I also like to thank all my colleagues in the Center for Superconductivity Research. I thank Yuanzhen Chen for the friendship and many helpful discussions; Samir Garzon for offering me a lot of help on my research; Dr. Hamza Balci for help with finding research opportunities in biophysics; and Maria Aronova, Yung-Fu Chen, Dr. Tobias Dürkop, Todd Brintlinger, Dr. Stephanie Getty, Dr. Sheng-Chiang Lee, Atif Imtiaz, Pengcheng Li, Joshua Higgins, and Dr. Mumtaz Qazilbash for their help and nice conversations.

I would like to thank Tom Loughran for keeping the ECE clean-room a clean

and nice place to do wet chemistry, and Hypres, Inc., for fabricating the niobium junction samples I measured in this thesis.

I would like to thank all the staff at the Center for Superconductivity and the Physics Department, who are among the nicest people I have every met. I want to thank Doug Bensen and Brian Straughn for their technical help and kindness, Belta Pollard, Brian Barnaby, Grace Sewlall and Cleopatra White for all their warm help and making my study at the Center an enjoyable experience.

I want to thank all the wonderful people in the Department, Jane Hessing and Lorraine DeSalvo for the kind assistance offered to me as I encountered paperwork problems, Pauline Rirskopa for giving me helpful advice and taking care of my payroll paperwork, and Jesse Anderson in always processing Z-orders promptly.

I would like to thank my girl friend, Sechun Zhang for her endless support and encouragement. Without her my graduate study would not have been as joyful and meaningful.

I would like to thank my brother, Huixing Xu for his support and giving my parents comfort while I was studying at Maryland. Finally, I thank my father Lianfang Xu and Kunmei Chen for their endless love and support, that enabled me to pursue my interests in scientific research and discovery.

TABLE OF CONTENTS

LIST OF TABLES

LIST OF FIGURES

Chapter 1

Introduction

1.1 Overview of quantum computing

To simulate the general dynamics of a system composed of N interacting two-state particles (such as spins) on a classical computer would not only require a memory size that is exponential in N, but also require diagonalizaition of an exponentially large matrix. Both requirements become impractical on even the best existing computer technologies as N approaches about 50.

In 1982, Feynman first proposed the idea of a universal quantum simulator to reproduce the behavior of any desired quantum system [1]. This primitive concept of a quantum computer was formalized by Deutsch in 1985 by introducing quantum circuits that are made of quantum bits (qubits) and universal gate sets [2]. In 1992, Deutsch and Jozsa proposed the first quantum computing algorithm that can solve a certain class of problems exponentially faster than any classical computation methods [3]. Two years later, Shor discovered the integer factorization algorithm [4], which can find the prime factors of a larger integer number exponentially faster than any known classical computation methods, and the field of quantum computation started to expand very rapidly. Shor's algorithm stimulated the physics community to begin seriously considering how to experimentally implement quantum computing.

The idea of simulating the quantum dynamics of a composite system using a quantum computer, shown by Lloyd [5] in 1996 to be implementable, could be used to enhance our understanding of composite systems and may lead to new discoveries. On the other hand, Shor's algorithm would make a quantum computer the world's fastest code breaker since most public-key cryptography methods utilize large integers whose prime factors are impractical to find using classical computers. In 1996, Grover also reported discovery of an algorithm for searching a database, which offers a quadratic speed-up compared to the existing fastest classical search method [6].

The underlying reason why a quantum computer can perform certain classes of calculations faster than a classical computer is that the state of a quantum system can exist in a superposition of all possible states. This superposition principle can be used for a type of parallel processing of information, which is impossible on a classical processor.

However, quantum parallel processing of information does not necessarily guarantee that a quantum computer is faster than a classical computer. This is because reading the final result requires making a quantum measurement of the system, and a single measurement on an n-qubit system can only provide n bits of classical information [7]. This is a tiny fraction of the total information contained in an arbitrary state of the system. Quantum computation will be advantageous if algorithms are designed to make sure the output state after many complicated calculations contains only n bits of classical information.

Closely related to the computing side of quantum information processing is data transmission in the quantum world. Quantum superdense coding [8] and quantum teleportation [9], which do not have analogs in the classical world, were developed by Bennett and his co-workers in the early 1990's. Quantum teleportation allows states to be faithfully transmitted from one location to another without possibility of being stolen by a third party to extract useful information. Superdense coding

allows classical information to be transmitted with a smaller number of resources via a quantum channel.

These potential applications have stimulated global research in quantum information science and how to build a quantum computer. The reader is referred to the book by Nielsen and Chuang [10] for an introductory overview of the theory of quantum computing.

1.2 DiVincenzo criteria

A classical computer has an architecture that involves a systematic organization of individual components such as the memory, processor, input devices and output devices. Similarly a quantum computer, if built, will also possess an architecture. At this stage, it is mainly a conjecture as to what a real quantum computer will look like. However, in order for a system to have the potential for use as a quantum computer, it has to satisfy the DiVincenzo criteria [11]:

1. a scalable physical system of well-characterized qubits;
2. the ability to initialize the state of the qubits to a simple fiducial state;
3. long (relative) decoherence times, much longer than the gate-operation time;
4. a universal set of quantum gates,
5. a qubit-specific measurement capability,
6. the ability to interconvert stationary and flying qubits and
7. the ability to faithfully transmit flying qubits between specified locations.

The first criterion contains two conditions, one is a well-characterized qubit, the other is scalability, i.e. that an arbitrary number of qubits can be connected together. A classical bit can have two possible values, 0 or 1; similarly a qubit is made of two quantum states, $|0>$ and $|1>$. Essentially any two-level system can be used a qubit, but some of them may be well characterized, some may not. A quantum computer, will require many qubits. Therefore scalability is a necessary

requirement.

The second criterion just says that computation must start from a known state, so the ability of initializing the state of the qubits is a necessary condition.

The fourth criterion is based on the idea that quantum information, which includes the quantum phase factors of the qubits, is potentially very sensitive to noise in the environment. Once the phase coherence of the system is lost, i.e. the system decoheres, logic operations on the system only lead to meaningless results. Therefore, long coherence times (the time scale over which the system maintains coherence) are required, preferably much longer than the times required for logic gates to be completed.

The fourth criterion says that logic gates are required in order to manipulate quantum information. DiVincenzo showed that the combination of single qubit gates and certain types of two-qubit gates are sufficient to accomplish any quantum computing task [12]. Lloyd extended this work and concluded that a combination of single-qubit gates and any two-qubit gate can form a universal set of quantum gates [13]. The single qubit gates can be described mathematically as $|0>\rightarrow \left(\cos\theta|0> + \sin\theta e^{-i\phi}|1>\right)$, which is equivalent to control of both degrees of freedom (θ and ϕ) on a Bloch sphere if one pictures $|0>$ as spin down and $|1>$ as spin up. There are many types of two-qubit gates. The most studied one is perhaps the Controlled-NOT (CNOT) gate, whose function is to change the state of a target qubit depending on the state of the control qubit. If the control qubit is in $|0>$, then the state of the target qubit remains unchanged. On the other hand the state of the target will be flipped if the control qubit is in $|1>$.

The fifth criterion says that one must be able to measure the state of all the qubits. All currently available algorithms require this. However, it is not impossible that this requirement may be relaxed for some certain problems as new algorithms are discovered.

The last two of the DiVincenzo criteria are necessary conditions for distributed

quantum computing. Since a quantum computer does not have to be distributed, these requirements are not in the same class as the first five criteria.

There are two other elements that are hidden in the above list that deserve some further discussion: entanglement and error correction.

Quantum entanglement

Entanglement is a peculiar feature of the quantum world, i.e. it can not be explained by the laws of classical mechanics [14, 15]. A state of a composite system is said to be entangled if it cannot be expressed as a direct product of the individual particle states (inseparable) [16]. Intuitively we can say that for an entangled state a description of each particle's state is not sufficient to describe the state of the entire system. Entanglement is the property that permits violation of Bell's inequalities [17]. Because of the non-classical nature of entanglement, it is of special interest from the point of view of the foundations of quantum mechanics.

Entanglement has also received a large amount of attention because of its importance in quantum computing. It is believed that entanglement is the main feature of quantum systems that makes exponential speedup of calculations possible [18]. Entanglement is also required in quantum teleportation [9], and is needed to implement quantum logic gates. In addition, the theory of error correction (see below), which is necessary for fault-tolerant quantum computing, is heavily based on the properties of some special kinds of entangled states.

Many questions related to entanglement still remain open, such as the best way to quantify entanglement in an inseparable mixed state and its underlying role in quantum computation.

Quantum error correction

Both classical and quantum information are sensitive to noise. In both classical and quantum computers, error correction can be used to reduce the effects of noise. Error

correction can guarantee fault-tolerant computation even using unreliable gates as long as the unreliability is below some threshold.

The simplest approach to error correction is based on the general idea of coding a logical qubit using many physical qubits. A variety of error correction methods have been proposed, including early ones by Shor [19] and Steane [20] which require an error threshold of the order of 10^{-6}. These error models assumed uncorrelated random noise across the qubits. However, recent work by Steane [21] shows that under mild assumptions the threshold can be as large as 10^{-3}. Theoretically, the error threshold cannot exceed 1/2. Therefore in principle there is still room to push the threshold up to a range that can be readily accessed by current experiments (say 0.01).

These error correction methods make use of multiple copies of information to make the information robust against corruption. For example, the minimum coding to correct for amplitude or phase errors (but not both) utilizes three physical qubits to represent a single logical qubit. When the logical qubit is initialized to $|0>$, then all three physical qubits are initialized to zero, and computation is applied to the three qubits simultaneously. This scheme can be used to correct single qubit flip errors. In this case, a superposition state of the logical qubit, $(|0> + |1>)/\sqrt{2}$ will be coded as a maximum entangled state between the three physical qubits: $(|000> + |111>)/\sqrt{2}$.

An alternative approach for error correction is to utilize the symmetry in the physical interaction underlying the noise sources. These error correction methods are often referred to as decoherence-free subspace encodings [22]. Such techniques are passive in contrast to the active correction methods discussed above and thus may ultimately be easier to implement for a large number of qubits.

1.3 Experimental realization

A variety of physical systems have been proposed for realization of qubits in a quantum computer. For a general overview of different approaches, the reader is referred to Ref. [11]. Each physical system proposed for quantum computing tends to differ in terms of the actual qubit and the interactions used for logic gates. However, in a broad context, these systems can be grouped into eight classes: nuclear magnetic resonance (NMR), ion trap, neutral atom, optics, cavity quantum electrodynamics (QED), solid state, superconducting, and unique approaches such as electrons on a film of superfluid helium.

Investigations of each class are being pursued at this time. Some are more advanced, with gates between a few qubits demonstrated, while others have not even succeeded in characterizing a single qubit. However, since the field is advancing so fast, it is not possible now to say which approach is the most promising. I can nevertheless list a few general advantages and disadvantages that are associated with each approach.

NMR quantum computing

Nuclear magnetic resonance (NMR) has been around for more than a half century [23, 24]. NMR Quantum computing [25, 26] involves using qubits that are chemically distinct nuclear spins (on specific sites on specific molecules in a solution) with long relaxation times $T_1 > 1$ s and coherence times $T_2 \sim 1$ s. While the spin state cannot be initialized at room temperature, "pseudo-pure" states can be selected in the presence of a magnetic field at room temperature. Single qubit rotations can be realized using the fact that the spins in a molecule have distinct chemical shifts and thus have slightly different resonance frequencies. The natural interaction (chemical screening, dipolar, and hyperfine) between different spins can be used to design two qubit gates.

Very-well characterized experimental systems and techniques, and relatively long coherence times are the strengths of this approach. However, there are several disadvantages associated with this approach. First, the system does not appear to be scalable, because qubits are defined through the internal Hamiltonian of a given molecule. A limit of 10 qubits is perhaps the maximum number one can achieve in liquid NMR quantum computing. Second, the gate speed is slow, typically less than 1 kHz. Finally, room-temperature versions of this approach are based on ensemble measurement (a minimum of 10^6 spins in the solution is required in order to beat the noise). Furthermore single spin detection and control has not been achieved so that one cannot avoid this ensemble approach. Analysis of such computations shows that they are essentially classical and that one cannot achieve the exponential speed up found in a real quantum computer. However, it is possible to use this approach to perform some simple calculations in very restricted cases, for example, a seven-qubit computer based on NMR has been built and used to factor the number 15 ([27].

Ion-trap quantum computing

The idea of ion trap quantum computing was first proposed by Cirac and Zoller [28] in 1995. The qubit states in this scheme are two hyperfine or Zeeman sublevels in the electronics ground state of an ion, or the ground state and the first excited state of weakly allowed optical transitions. Since direct Coulomb interaction is very weak due to the large spacing between two ions ($> 1\mu m$), coupling between two qubits is mediated through the motional states in the trap. Qubit initialization and read-out can be accomplished using standard optical techniques (pumping and light scattering) with high fidelity, and motional states in the trap can be initialized by laser cooling. The coherence times in the hyperfine levels are very long (>10 min), the decay times for the weakly allowed transitions are about 1 s. The life time of the motional states are shorter, typically between 100 μ s and 100 ms. All these times are significantly longer than the gate times (< 10 μs). Recently some significant

progress has been made using this scheme, including two-qubit gates [29, 30] and creation and control of three-qubit entangled states [31, 32].

Despite this progress, scalability of this approach remains unknown. Although, concepts such as moving-ion qubits [33, 34] and coupling to photon modes [35, 36] were proposed, experimental implementations of these ideas need to be demonstrated.

Neutral-atom quantum computing

Neutral-atom quantum computing [37, 38] is conceptually similar to ion-trap quantum computing. While ions can be trapped by electric fields, neutral atoms can be trapped by optical lattices, or magnetic fields. The internal atomic states (ground state hyperfine levels) can be used as qubit states and motional states of the trap can be used to mediate interaction between two qubits. Similar to ion-traps, qubit initialization can be accomplished by standard optical pumping techniques, and motional states in the trap can be initialized by laser cooling. Since neutral atoms are weakly coupled to the environment, coherence times as long as many minutes are expected for these qubits, although this has not been demonstrated by experiments. Single qubit states are analogous to those for ion-traps.

Although two-qubit gates are not that straightforward compared to ion-traps, there are proposals for two-qubit gates based on the optically induced conditional electric-dipole interaction between two atoms when they are brought into close proximity [39]. The speed of these gates are limited by the trap frequency, which is typically between 10 kHz and 10 MHz. Read-out of individual qubit states is not clear in this scheme, since the atoms are separated by less than a wavelength of the trapping lasers. Solutions to this problem have been proposed, such as designing optical lattices with potential wells separated by more than a wavelength [40].

Optical quantum computing

The quantum nature of light has been known for almost a century. In principle, single photon occupation of two polarization modes can be used as a qubit. Photons have intrinsically long lifetimes because the influence of the thermal environment (k_BT) is negligible compared to the photon frequency. However photons can be lost easily due to imperfect optical elements (mirrors, beam splitters, phase shifters, etc.). Coherence times as large as 1 μs have been achieved in a high-quality optical storage cavity; this is much longer than typical expected gate times of the order of ns.

Single qubit rotations are easily implemented in this system [41]. However, due to the extremely small photon-photon interaction, realization of two-qubit gates appears to be difficult. Surprisingly, the process of photon detection itself can lead to effective photon-photon nonlinearities [42]. Knill, Laflamme and Milburn [43] showed that deterministic single-photon sources and high-efficiency single-photon detectors may be used to realize scalable quantum computing with only linear optical elements. This linear optics quantum computing scheme is now the major scheme studied in optics quantum computing.

This approach has the apparent advantage of interfacing to various quantum-communication applications. Photons as flying qubits can be faithfully transmitted in free space over a long distance. However, if the photons are confined to structures with well-defined modes, such as optical fibers, photon loss over a distance of meters needs to be taken into consideration.

Qubit initialization and read-out have not been demonstrated faithfully in this scheme. Qubit initialization requires reliable, on-demand, single photon sources, which have not been demonstrated. In order to realize an individual qubit read-out, single photon detectors with high efficiency (99%) are required, but have not been demonstrated.

Cavity QED quantum computing

Cavity QED quantum computing refers to coherent interaction of a material qubit (trapped atoms, trapped ions, etc.) with a single photon mode in an optical or microwave cavity. The drive for this approach is to realize the sixth DiVincenzo criterion, coherent interconversion of quantum states between stationary qubits and flying qubits, which is a necessary condition for distributed quantum computing. The systems studied in this approach include Rydberg atoms in microwave cavities [44], neutral atoms in optical cavities [45], ion-traps interacting with optical cavities [46, 47] and more recently, superconducting qubits interacting with a resonator [48, 49, 50].

The challenges facing this scheme are more or less the same as those for the ion-trap and neutral atom approaches. For the flying qubits, single photon sources and detectors are required for initialization and readout.

In addition, this approach also requires realization of the strong coupling limit: a small, extremely low-loss cavity is required to enhance the electric field per photon such that the coherent Rabi frequency of the atom-field interaction is faster than the spontaneous decay rates of the atom and the field. Current technology is good enough to achieve the strong coupling limit, but the quality factor is not that high.

Solid state spin-based quantum computing

Solid state systems are generally complicated and it is hard to implement the kind of coherent state control a quantum computer demands. However, a large variety of quantum effects exist in solid state systems and by using the spacial precision that modern lithography can achieve, it has become increasingly possible to engineer solid state systems with a desired Hamiltonians. The first ideas of quantum computing using solid state systems were proposed by Loss and DiVincenzo [51] based on the spin of a single electron in a GaAs quantum dot, and by Kane [52] based on the

nuclear spin of a ^{31}P atom in silicon.

The underlying concept of the qubit here is essentially the same as in liquid NMR. The Zeeman levels of the spin in the presence of an external magnetic field (a few Tesla) can be used as a qubit. At millikelvin temperatures, the spins can be polarized in one direction, which fulfills initialization of the qubit state. One might expect the spin coherence time to be the same as in liquid NMR. However, spin relaxation in solids is much more complicated than in liquids and a variety of decoherence mechanisms exist. So far only ensemble measurements of spin coherence time are available. For example, T_2 is about 1 μs for electrons in GaAs, and on the order of 1 ms for ^{31}P in Si. Although these times are much longer than the expected gate times ($\sim$1 ns), the relaxation time and coherence time of a single spin are still unknown.

Likewise, while rotations are trivial for an ensemble of spins using a transverse rf magnetic field, single qubit operation still needs to be demonstrated.

In contrast to the natural internal interaction between spins in a molecule in liquid NMR, here the interaction between two spins can be engineered. For the quantum dot approach, two quantum dots of a size $\sim$50 nm can be fabricated next to each other with a separation of 200 nm. Coulomb interaction between the two electrons in the dots can be controlled via an electrical gate between the dots. For two ^{31}P donors in Si are separated by 20 nm and the state of the nuclear spin can be transferred to the spin of the donor electron via the hyperfine interaction. Interaction between the two donor electrons can then be controlled by electrical gates. However, so far there is no report of experimental demonstration of such two-qubit gates.

Perhaps the most difficult part of this approach is performing the individual qubit measurements. It essentially requires high precision single spin detection. Methods being pursued so far include: (i) convert spin information to charge information and detect the resultant charge transfer using highly sensitive electrometers [51], such as

a single electron transistor; (ii) transport current measurement (for quantum dot) [53], and (iii) magnetic resonance force microscopy [54].

Despite a lot of uncertainty in this approach, spin-based solid state quantum computing has some attractiveness, mainly due to its potential for compatibility with existing microfabrication industry, and its potential for inherent scalability, high density of qubits, and fast gate operations.

1.4 Superconducting quantum computing

Superconducting quantum computing has the advantage of inherent scalability, since superconducting circuits can be fabricated by lithography. The gate times are also relatively fast (< 10 ns) compared to ion-traps and neutral atoms. Since superconductivity is an inherently low-dissipation coherent quantum state, long coherence times in these systems are expected. In addition, superconducting systems are electronic circuits in which qubit control (gates and individual-qubit readout) can be implemented via electric or magnetic methods. Initialization of superconducting qubits is realized by cooling the system to its ground state. Typically temperatures of 20-30 mK are required if the first excited state is about 5-10 GHz above the ground state.

A variety of individual qubits based on Josephson junctions have been implemented [55], including flux qubits [56, 57, 58, 59, 60, 61], charge qubits [62, 63] and phase qubits [64].

Flux qubit

Flux qubits are based on the general principle that only an integer value of the flux quantum $\Phi_0 \equiv h/2e$ can be trapped inside a superconducting ring. Mooij and Orlando[57, 58] have developed a flux qubit that is a superconducting ring interrupted by three junctions, in which the two qubit states correspond to the two

directions of the circulating current in the ring, clockwise and counter-clockwise. A superposition of these two states [59] and coherent quantum oscillations [65] between the two states with a coherence time of 150 ns were demonstrated.

A simpler type of flux qubit, the rf SQUID, is a superconducting loop interrupted by one Josephson junction. Spectroscopic evidence for superposition of the two qubit states was also observed [60]. Since these qubits are made of superconducting loops, they are sensitive to magnetic field noise, but relatively insensitive to electric field or charge noise.

Charge qubit

One well-studied charge-qubit is the Cooper-pair box [62], which is basically a superconducting electrode (the island) connected to a superconducting reservoir by a small Josephson junction. Due to the large charging energy associated with the small capacitance of the junction, the number of charges on the island is a good quantum number and it can be controlled by applying a voltage to a gate that is capacitively coupled to the island. The qubit states correspond to n and $n+1$ pairs on the island. The level spacings between the two states can be adjusted by the gate voltage, and oscillations between the two states can be excited using microwaves. Coherent oscillations between the two qubit states were demonstrated by Nakamura *et al.* [62]. More recently, evidence for entanglement between two charge qubits was observed [66] and two-qubit gates were demonstrated [67]. The coherence times observed in these systems are about 2 ns, rather short compared to the expected value if decoherence is solely from spontaneous emission. This large decoherence was attributed by the authors [62] to the constant detection via quasiparticle tunneling through the probe junction.

A modified scheme in the charge qubit regime was demonstrated by the Saclay group [63]. The qubit is still a Cooper-pair box, but the readout is not through quasiparticle tunneling, but via the switching of a big junction (two small junctions

are used to isolate the island, while the two small junctions and the big junction form a loop). By the use of a gate voltage and a magnetic flux piercing the loop, the system can be biased at an optimal operating point where the system is insensitive to charge fluctuations to first order. The readout via the big junction can be turned on when measurement is needed to minimize decoherence during gate operations. A relaxation time of 1.8 μs and a coherence time of 500 ns were demonstrated.

Phase qubit

A third approach using Josephson junctions for quantum computing involves using the phase regime, which is the topic of this thesis. In this approach, the qubit is basically a single Josephson junction [64] that is biased at a constant current, therefore it is also referred to as a current-biased Josephson junction. The simplicity of the circuit makes it very attractive as a candidate for a qubit. Furthermore the system is relatively insensitive to magnetic flux noise and charge noise, unlike flux or charge qubits.

The dynamics of the system is analogous to an anharmonic oscillator, with unequal level spacings in the potential well. Therefore the ground state and the first excited state can be singled out as the two qubit states. These states are metastable due to the anharmonicity and they can tunnel out of the potential well to dissipative running states. The ground state and the first excited state have very different tunneling rates, and thus can be distinguished with a high fidelity.

This approach also has some weaknesses. First, the junction is now directly connected to electrical leads that supply the bias current. Therefore the electromagnetic environment to which the qubit is coupled depends on the bias leads. Care must be taken to engineer the bias lines such that energy relaxation is slow. The noise in the bias lines can also cause significant decoherence. The mechanisms of decoherence are not entirely clear, and measurements of coherence time from different groups show very inconsistent results, ranging from tens of ns [68] to 1 us [69, 70].

Therefore further understanding and more measurements of decoherence time in the phase qubit are needed.

In order to realize a quantum computer, coupling between two and more qubits is required. In this thesis, I describe a first study of a coupled system comprised of two junction qubits and a inductor-capacitor (LC) resonator. The measurements can be interpreted from many points of view: a resonator as a qubit; capacitive coupling between two junction qubits; and two stationary qubits coupled to a flying qubit in analogy to a cavity-QED type experiment.

It is noteworthy that these superconducting circuits are macroscopic, not only because they are large in size (1 μm to 1 mm), but also because all the quantum phenomena observed in these circuits can be explained by a macroscopic variable [71], the phase difference across a Josephson junction. The fact that the phase difference can describe all the quantum physics that are based on the collective motion of billions of Cooper-pairs is a clear manifestation of macroscopic quantum phenomena. Therefore it is interesting to study quantum phenomena in these macroscopic circuits not only from the point of view of quantum computing, but also from the point of view of testing fundamental principles of quantum mechanics in a macroscopic system.

1.5 Summary

In this chapter, I have briefly outlined the state of quantum computing. I also explained the basic idea underlying the exponentially fast speed of quantum computing. The strengths and weaknesses of each experimental realization of a quantum computer were summarized. The purpose of this was not to provide judgement of the different approaches, but to give a sense of the diversity of the field. Finally, I have listed the different approaches that are being pursued by the superconducting community. A general picture of the phase qubit, which is the subject of this thesis,

was presented.

The rest of the thesis is organized as follows. Chapter 2 is a detailed description of the basic physics associated with a current-biased Josephson junction. Chapter 3 discusses the physics underlying the relaxation process in the phase qubit. Modeling of the relaxation process and methods to measure the relaxation time (T_1) are presented. Chapter 4 focuses on analysis of decoherence mechanisms. In particular, a method is proposed to look at decoherence due to low frequency noise. Chapter 5 discusses various single qubit designs with potentially long relaxation and coherence times. Chapter 6 focuses on details of the experiment setup, including the dilution refrigerator, filtering and signal bandwidth, and low noise instrumentation. Chapter 7 presents measurement results on the relaxation time and decoherence time in various single qubits. Chapter 8 focuses on microwave spectroscopy of a coupled three-body system. Chapter 9 presents some preliminary results on state measurement in a coupled qubit system. Finally, Chapter 10 concludes with a summary of the key results and a few comments on some future work.

Chapter 2

Josephson Junction Physics

Among the various superconducting devices used for quantum computation, the current-biased Josephson junction is perhaps the simplest. In this chapter, I will first discuss the basic current-voltage (I-V) relations of a Josephson junction and then introduce a model for the Josephson junction. I next discuss the classical dynamics of the system, followed by a quantum mechanical description of the system, including energy levels and quantum tunneling phenomena. At the end of this chapter, I describe the experimental method I used to probe the system.

2.1 Josephson junctions

Electrons in a superconductor form Cooper pairs for temperatures below the transition temperature (T_c) of the superconductor [72]. Since these pairs are in a collective motion corresponding to the ground state of the system, their behavior can be described by a wave function, i.e.

$$\Psi(\vec{r},t) = A(\vec{r},t)e^{i\theta(\vec{r},t)} \tag{2.1}$$

Equation 2.1 describes the state of all the Cooper pairs, and the square of the norm of the wave function can be interpreted as the density of the Cooper pairs at location $\vec{r}$ and time t. Moreover, the phase of the wave function is coherent throughout the

superconductor.

If two superconductors are separated by a very thin layer of insulator, then a Josephson junction [73] is formed. (see Fig. 2.1).

When the insulator thickness is small enough, the electronic wave functions from the two sides can overlap. The consequence of this overlap is that the phases of the two wave functions are correlated and Cooper pairs can coherently tunnel from one side of the junction to the other side with a tunneling strength strongly dependent on the insulator thickness. Indeed, if γ is the difference of the two phases, the relation between the tunneling current I flowing through the junction and the voltage V across the junction is given by

$$I = I_0 \sin \gamma \tag{2.2}$$

$$V = \frac{\Phi_0}{2\pi} \frac{d\gamma}{dt} \tag{2.3}$$

where $\Phi_0 = \mathrm{h/2e} = 2.07 \times 10^{-15}$ T m^2 is the flux quantum, and I_0 is the critical current of the junction. Eqs. 2.2 and 2.3 were first derived by Josephson [73], and are commonly referred as the dc and ac Josephson relations.

The variable γ is macroscopic because the two phases are from the wave functions of a macroscopic number of Cooper pairs in the two superconductors and it completely describes the coherent tunneling of pairs through the barrier [71] (the number can be estimated as the pairs in a volume of the junction area and a coherence length).

From the Josephson relations, we know a current that is smaller than I_0 can flow through the junction without dissipation, i.e. the junction stays in a zero-voltage state. If one tries to force a current that is larger than I_0 to flow through the junction, then from the Josephson relation, γ can no longer possess a stationary solution. This leads to the junction switching to a finite-voltage state. To fully understand

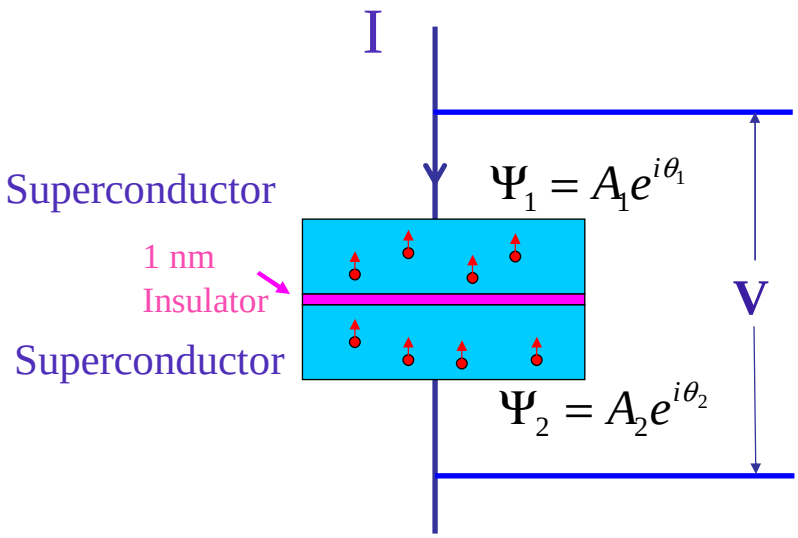

Figure 2.1: Schematic of a Josephson tunnel junction. Two superconductors are separated by a thin layer of insulator. Each circle in the two superconductors denotes a Cooper pair. The Cooper pairs on the two sides are described by wave functions $A_1 \exp(i\theta_1)$ and $A_2 \exp(i\theta_2)$, respectively. The current I and voltage V are related to $\gamma = \theta_1 - \theta_2$ through the Josephson relations.

the dynamics of this switching process, we need to consider two additional things that are inherent with a Josephson junction, the shunt resistance R and the shunt capacitance C.

2.2 RCSJ model

Since the junction is made of two overlapping superconducting plates, there will be a capacitance C between the two plates. In addition, at any finite temperature there will be electronic excitations (quasi-particles) present. For a voltage V across the junction less than the gap voltage V_g, the quasi-particles can incoherently tunnel through the barrier causing dissipation and producing an effective voltage-dependent shunt resistance R_{qp}. According to the BSC theory [72], this resistance due to quasi-particle tunneling obeys

$$R_{qp} = R_N \exp(eV_g/2k_BT) \tag{2.4}$$

where R_N is the resistance of the junction in the normal state. For $V > V_g$, there is enough energy available from the voltage source to break Cooper pairs, causing the shunt resistance R to be comparable to R_N. In some cases, a shunt resistance is deliberately added to the junction, in which case the total shunt resistance R is the parallel resistance of the quasi-particle resistance and the external one. I note that the quasi-particle resistance R_{qp} is typically very large [74] for both Al ($V_g = 0.4$ mV) and Nb ($V_g = 2.8$ mV) junctions for the temperatures used in our experiment (around 30 mK).

Figure 2.2 shows a schematic of the resistively-capacitively shunted junction (RCSJ) model. The cross represents the bare junction, whose current-voltage relations can be found from the Josephson equations.

With this model, one can write an equation for the total current I_b flowing through the circuit,

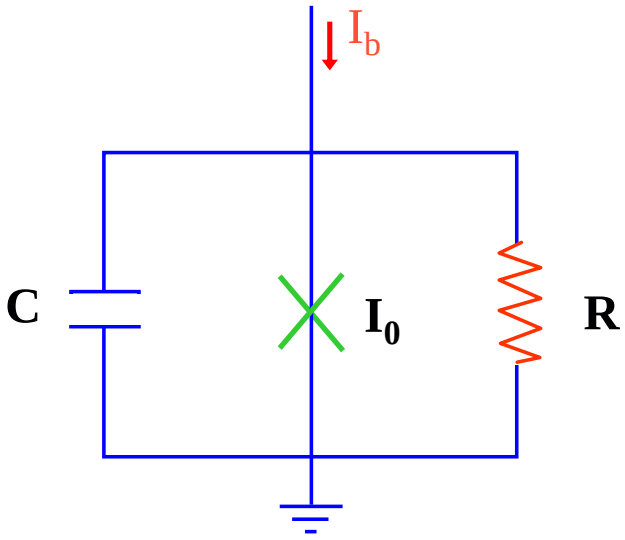

Figure 2.2: The RCSJ model of an ideal Josephson junction. The cross denotes the Josephson junction itself. The capacitor comes from the two parallel superconducting plates forming the junction. The shunt resistance R is the total parallel resistance of the quasi-particle resistance R_{qp} and an external resistance if it exists.

$$I_b = I_0 sin(\gamma) + C\frac{\Phi_0}{2\pi}\ddot{\gamma} + \frac{\Phi_0\dot{\gamma}}{2\pi R} \tag{2.5}$$

One can solve Eq. 2.5 for γ as a function of time for a given bias current I_b. The dc voltage can be taken as a time average of the time derivative of γ. One needs to keep in mind that the shunt resistance R in general is strongly voltage-dependent and highly nonlinear, which makes solving Eq. 2.5 difficult.

For junctions where the time constant RC is much larger than the inverse of the characteristic frequency ($\sim \sqrt{2\pi I_0/\Phi_0 C}$) of the system, the I-V curve is hysteretic (see Fig. 2.3). For $I_b < I_0$, there is zero voltage across the junction. However at some bias current that is smaller than the critical current, the voltage across the junction jumps discontinuously to the gap voltage V_g. For bias currents slightly above the critical current, the voltage stays at the gap voltage. As one further increases the bias current, the voltage increases linearly with the bias current, showing an ohmic behavior with a resistance of R_N (see Fig. 2.3). If the bias current is now reduced below the critical current, V remains at V_g until the current reaches the retrapping current. Thus the device characteristics are hysteretic.

This hysteretic behavior can be qualitatively understood from Eq. 2.5 and the voltage dependence of the shunt resistance R. For $I_b < I_0$, there exists a static solution $\gamma = \arcsin(I_b/I_0)$ for Eq. 2.5, therefore $V \equiv <\dot{\gamma}> = 0$ is allowed. However when $I_b > I_0$, γ must be time dependent, and it turns out $\dot{\gamma}$ will increase with time, which causes the voltage to increase. However when V increases to V_g, Cooper pairs start to break and the shunt resistance suddenly decreases to a value that is comparable to R_N, which conducts most of the bias current. When the bias current is much larger than I_0, the junction is normal and behaves just like a resistance R_N.

From this discussion it is not obvious why the junction stays at the gap voltage while the bias current is reduced. Furthermore the switching of the junction to the finite voltage state does not occur at a fixed bias current. Instead the switching is spread over a range of bias currents that are always below I_0. To answer these

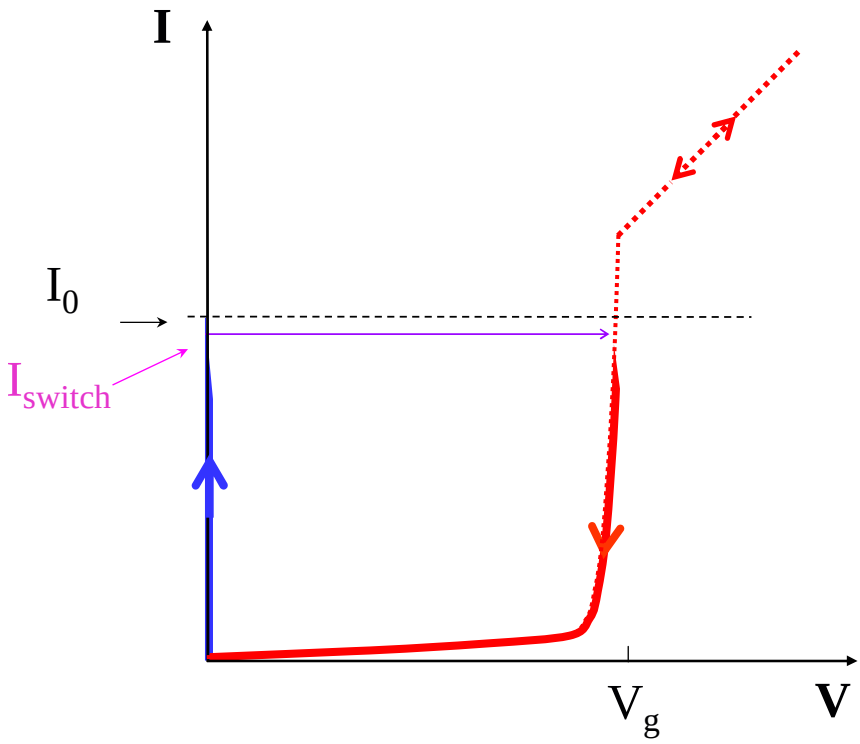

Figure 2.3: I-V curve for a lightly damped Josephson junction. The switching happens at a bias current that is slightly smaller than the critical current I_0.

questions, we need to carefully examine the junction behavior described by Eq. 2.5.

2.3 Classical dynamics of a current-biased Josephson junction

To proceed, I use the analogy between Eq. 2.5 and the motion of a particle with a effective mass $m = C(\Phi_0/2\pi)^2$ moving in a tilted washboard potential

$$U(\gamma) = -\Phi_0/2\pi(I_0 \cos\gamma + I_b\gamma) \tag{2.6}$$

subject to a damping force. Equation 2.5 can be rewritten as

$$m\ddot{\gamma} = -\frac{dU(\gamma)}{d\gamma} - \left(\frac{\Phi_0}{2\pi}\right)^2 \frac{\dot{\gamma}}{R} \tag{2.7}$$

I note that the washboard potential given by Eq. 2.6 depends on the bias current I_b. Three examples of the washboard potential for $I_b = 0.1I_0$, $I_b = 0.99I_0$, and $I_b = 1.2I_0$ are shown in Fig. 2.4 (a)-(c).

Notice the particle can be trapped inside a well for $I_b < I_0$ and this will give zero voltage across the junction [see Fig. 2.4(a)]. However, for $I_b > I_0$, the potential barrier disappears and the particle must roll down the slope so that a voltage will be observed [see Fig. 2.4(b)]. If the damping resistance R is small, once the particles starts rolling, it can continue rolling even if the tilt gets less steep, resulting in hysteretic behavior. When the bias current is so small that the kinetic energy the particle gains moving from one barrier to the next is equal to the energy dissipated, the particle slows down and the junction retraps to the zero-voltage state. It turns out that the retrapping current is related to the quality factor Q of the system by $I_r = 4I_0/\pi Q$ [72], where $Q = \sqrt{2\pi I_0/\Phi_0 C}RC$ is the quality factor.

To understand why switching happens in a range of bias currents that are smaller than the critical current, we need to include the thermal noise from the resistor,

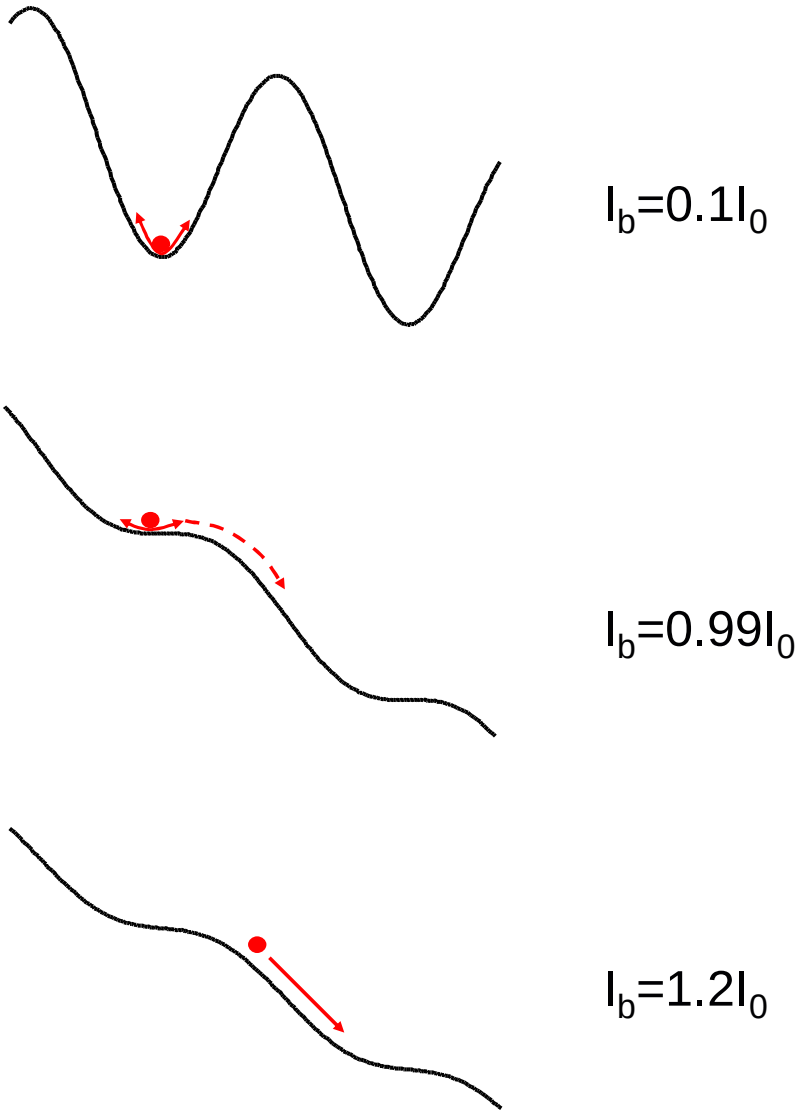

Figure 2.4: Washboard potential at various bias currents. (a) For $I_b = 0.1I_0$, the particle is trapped inside a well. (b) For $I_b = 0.99I_0$, the barrier is very small so the particle is barely trapped and can be readily thermally excited out of the well. (c) For $I_b = 1.2I_0$, the well no longer exists and the particle will roll down the potential landscape.

which adds an additional noise current to the bias current. We then change Eq. 2.7 by adding a noise force term,

$$m\ddot{\gamma} = -\frac{dU(\gamma)}{d\gamma} + F_n(t) - \left(\frac{\Phi_0}{2\pi}\right)^2 \frac{\dot{\gamma}}{R} \tag{2.8}$$

where $F_n(t) = -\Phi_0/2\pi I_n(t)$, and $I_n(t)$ is a random noise current from the resistor. The correlation function for $I_n(t)$ is given by

$$< I_n(0)I_n(t) > \cong \frac{4k_BT}{R}\delta(t) \tag{2.9}$$

where T is the temperature of the shunt resistance R.

With this noise, the particle will move at the bottom of the well with an oscillation frequency depending on the curvature of the potential. This bias-current-dependent oscillation angular frequency is called the plasma frequency and is given by

$$\omega_p = \omega_0 \left[1 - \left(\frac{I_b}{I_0}\right)^2\right]^{1/4} \tag{2.10}$$

where $\omega_0 = \sqrt{2\pi I_0/\Phi_0 C}$ is the plasma angular frequency at zero bias current.

The energy associated with small oscillations obeys a Boltzmann distribution, i.e. $P(E) = \exp(-E/k_BT)$, where $P(E)$ is the probability of the particle having energy E. If the energy is larger than the barrier height ΔU, then the particle can escape out of the well and roll down the slope, as depicted in Fig. 2.5.

We can define the escape rate Γ as the inverse of the life time of the particle in the well. For this type of thermally-activated escape, Kramers [75] derived an expression for the escape rate:

$$\Gamma_K = \frac{\omega_p}{2\pi} \exp\left(-\frac{\Delta U}{k_BT}\right) \tag{2.11}$$

Here the plasma frequency ω_p is used as an attempt frequency, and ΔU is the barrier height. One can show that ΔU depends on the bias current according to

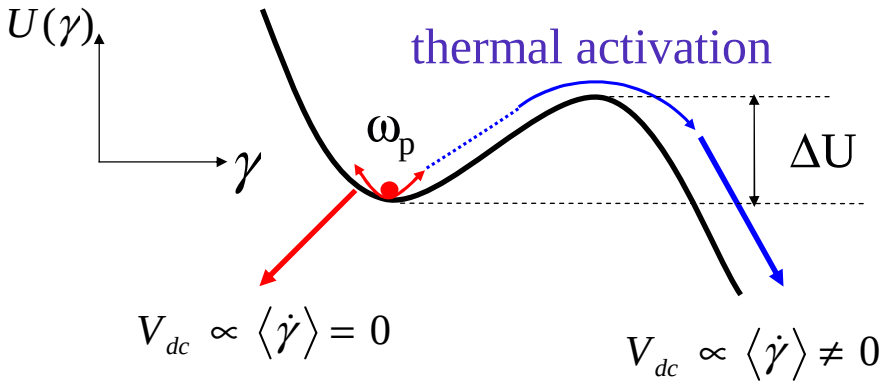

Figure 2.5: Classical picture of escape by thermal activation. The particle oscillates with a frequency of ω_p at the bottom of the well, occasionally it can acquire energy greater than the barrier height ΔU, and escape out of the well.

$$\Delta U = \frac{I_0 \Phi_0}{\pi} \left[\sqrt{1 - \left(\frac{I}{I_0}\right)^2} - \frac{I}{I_0} \arccos(I/I_0) \right] \tag{2.12}$$

Therefore as one increases the bias current, the barrier height ΔU decreases and the escape rate increases exponentially. Since for our typical experimental parameters the well is very deep for small bias currents, and gets comparable to $k_B T$ only when the bias current is close to the critical current, we can only observe escape near I_0. Furthermore, the escape is a stochastic process that does not occur at one fixed bias current, but spans a range of bias currents.

Kramers' escape rate formula is not entirely accurate. Due to the very high escape rates for particles with energies near or above ΔU, particles with high energies no longer follow a Boltzmann distribution; there is a population depletion effect for $E > \Delta U$ as shown by Büttiker, Harris and Landauer [76]. Including depletion, the modified escape rate is [76]

$$\Gamma_{BHL} = a_t \frac{\omega_p}{2\pi} \exp\left(-\frac{\Delta U}{k_B T}\right) \tag{2.13}$$

where the prefactor a_t is given by

$$a_t = \frac{4}{\left[\sqrt{1 + 5Qk_B T/9\Delta U} + 1\right]^2} \tag{2.14}$$

where $Q = \omega_p RC$ is the quality factor. One can see that a_t can be smaller than 1 for a high Q system. This is because, for a high Q system, it takes a longer time to reach equilibrium once the particles with high energies have escaped, which results in population depletion for $E > \Delta U$ and a reduced escape rate.

2.4 The quantum picture of a current-biased Josephson junction

The above discussion of escape is essentially a classical theory. However experimentalists found that escapes were observed [77, 78] even for temperatures such that $k_B T << \Delta U$. The measured escape rates cannot be explained by the classical escape rate formula Eq. 2.13. To explain these observed phenomena requires a quantum picture of the system.

Returning to the equation of motion for the system, i.e. Eq. 2.7, and neglecting the damping and noise terms for the moment, we can write the following Hamiltonian for the system,

$$H_0 = \frac{p^2}{2m} + U(\gamma) \tag{2.15}$$

where the effective mass $m = C(\Phi_0/2\pi)^2$, and the washboard potential $U(\gamma) = -\Phi_0/2\pi(I_0\cos(\gamma) + I_b\gamma)$, and $p = -i\hbar\frac{\partial}{\partial\gamma}$ is the canonical momentum operator.

Solving Schrödinger's equation will lead to quantized energy levels in the washboard potential[1] (see Fig. 2.6).

The anharmonicity of the potential well leads to interesting phenomena that will allow us to use the junction as a qubit.

For I_b near I_0, for convenience we can expand the washboard potential near the minimum potential position $\gamma_0 = \arcsin(I_b/I_0)$ to find a cubic potential,

$$U_c(q) = \frac{27}{4}\Delta U\left(\frac{q}{q_0}\right)^2\left(1 - \frac{q}{q_0}\right) \tag{2.16}$$

[1]Since the particles is trapped in one well, here we just concentrate on the energy levels in one well. The levels outside the well are important to understand tunneling, as we will see in a moment.

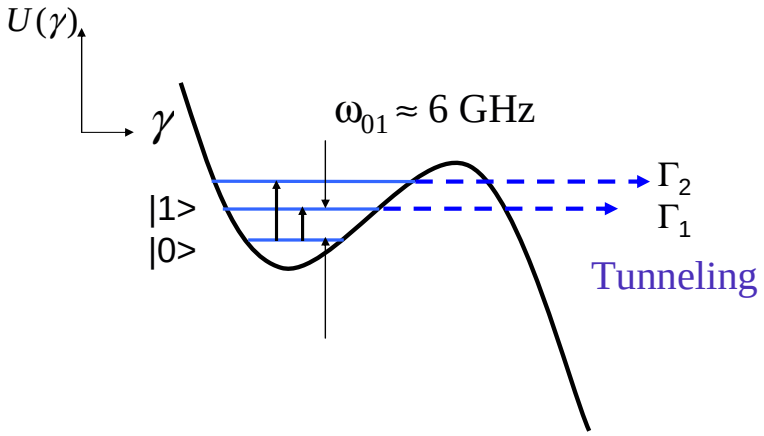

Figure 2.6: Washboard potential with three energy levels inside the well. Due to the anharmonicity of the potential, the ground state and the first excited state can be used as qubit states $|0>$ and $|1>$. These two states can be distinguished due to their distinct tunneling rates (horizontal dashed arrows). The vertical arrows denote inter-level transitions. Note the typical level spacing in our experiment is around 6 GHz or 300 mK in terms of temperature. Thus low temperatures ($\sim$30 mK) are required to see these levels.

where $q = \gamma - \gamma_0$ and

$$q_0 = \frac{1}{2\omega_p}\sqrt{\frac{54\Delta U}{m}} \tag{2.17}$$

This cubic potential will lead to unequal level spacings in the well. Let us label the level spacing between the ground state and the first excited state in terms of the corresponding transition frequency as ω_{01}, the level spacing between the first excited state and the second excited state as ω_{12}, *etc.* Employing perturbation theory, one can calculate these level spacings and obtain [79]

$$\omega_{01} \cong \omega_p \left(1 - \frac{5}{36}\alpha\right) \tag{2.18}$$

$$\omega_{12} \cong \omega_p \left(1 - \frac{5}{18}\alpha\right) \tag{2.19}$$

where $\alpha = \hbar\omega_p/\Delta U$ describes the depth of the well. We can see from the above equations that the anharmonicity is large only for I_b near I_0 where the well contains only a few levels. If we use the full washboard potential, we find[2]

$$\omega_{01} \cong \omega_p \left(1.00 - 0.16\alpha + 0.06\alpha^2 - 0.24\alpha^3\right) \tag{2.20}$$

and

$$\omega_{12} \cong \omega_p \left(0.995 - 0.316\alpha + 0.411\alpha^2 - 1.81\alpha^3\right) \tag{2.21}$$

The unequal level spacings will allow us to address levels of interest without making transitions to other levels. For quantum computation, we can thus choose the ground state and the first excited state as $|0>$ and $|1>$, and address them using excitations with appropriate frequencies.

Due to the finite barrier height, states inside the well can transition to the continuum outside the well through quantum tunneling. Therefore the states in the

[2]These formulae are found by fitting numerically calculated level spacings using the full washboard potential; they work well for $\hbar\omega_p/\Delta U < 0.40$.

well are metastable. The quantum tunneling rates can be calculated using the WKB approximation to find

$$\Gamma_i = \frac{\omega_i}{2\pi} \exp\left(-\frac{2}{\hbar}\int_{q_1}^{q_2} \sqrt{2m(U_c(q) - E_i)}\, dq\right) \tag{2.22}$$

where ω_i and E_i are the attempt frequency and energy of the particle in the i-th state, and q_1 and q_2 are the boundaries where $E_i = U_c(q_1) = U_c(q_2)$. Given the energy levels E_i, we can evaluate the integral in Eq. 2.22 (see Appendix A) and find

$$\Gamma_0 = 12.7 \left(\frac{7.2\Delta U}{\hbar\omega_p}\right)^{1/2} \frac{\omega_0}{2\pi} \exp\left(-\frac{7.2\Delta U}{\hbar\omega_p}\right) \tag{2.23}$$

$$\Gamma_1 = 393.2 \left(\frac{7.2\Delta U}{\hbar\omega_p}\right)^{3/2} \frac{\omega_1}{2\pi} \exp\left(-\frac{7.2\Delta U}{\hbar\omega_p}\right) \tag{2.24}$$

From the above equations, we can show for our experimental parameters that escape happens for I_b near I_0, where $\Delta U/\hbar\omega_p$ is about 2 to 4. Since that the escape rate for the first excited state is much higher than the ground state (about a factor of 500 higher for typical parameters), we can easily distinguish which state the system is in by measuring the tunneling rate.

The quantum tunneling rates are independent of temperature. But for high temperatures such that $k_B T \gg \hbar\omega_p$, escape will be dominated by the thermal-activation. Only when $k_B T \ll \hbar\omega_p$, will one observe quantum-tunneling-dominated escape and be able to distinguish $|0>$ and $|1>$. This condition on temperature is also the naive condition to observe quantized energy levels in the system, although it will turn out this is not quite right, as I will discuss in Chapter 3.

To probe the quantized energy levels and manipulate the states, one can apply current at the appropriate frequency (typically a few GHz in our experiment) to the system and measure the escape rate. Since $|1>$ has a much higher escape rate than $|0>$, if particles are excited from the ground state to the first excited state, an enhancement of the escape rate will be observed. This technique was first used

by Martinis, Devoret and Clarke in the mid 1980's to demonstrate the existence of energy levels in the system [80].

The above discussion does not include the effects of damping or noise. The presence of these will complicate the simple picture presented here. Damping will cause particles in excited states to relax to lower states. Noise will cause the level spacings to fluctuate and induce decoherence. In addition to these effects, more subtle effects occur. For example, Caldeira and Leggett found the quantum tunneling rate from the ground state in the presence of damping is given by [81]

$$\Gamma_0 = a_q(\frac{\omega_p}{2\pi}) \exp\left[-7.2\frac{\Delta U}{\hbar\omega_p}\left(1+\frac{0.87}{Q}+\cdots\right)\right] \tag{2.25}$$

where $a_q = \sqrt{120\pi(7.2\Delta U/\hbar\omega_p)}$. The effect of the damping is to localize the wave function inside the well and thus reduce the tunneling rate.

The detailed effects of damping and noise - dissipation and decoherence - will be discussed in Chapters 3 and 4 respectively.

2.5 Escape rate measurement

As seen above, we need to measure the escape rate of the junction to distinguish the state of the phase qubit. Since escape only occurs for bias currents near the critical current, we need to bias our junction at a current near I_0. One way to measure the escape rate is to bias the qubit at a fixed current at time $t = 0$ and measure when it escapes. One repeats this measurement for tens of thousands of times and then calculates an average lifetime and the escape rate. The procedure can be repeated to get escape rates for different bias currents. In this thesis, I use a current ramp method first developed by Fulton and Dunkleberger [82] to measure the escape rate.

In the ramp current technique, the bias current is steadily ramped from zero to a current that exceeds the critical current of the junction, and one measures when the junction escapes with respect to the start of the ramp. This measurement is

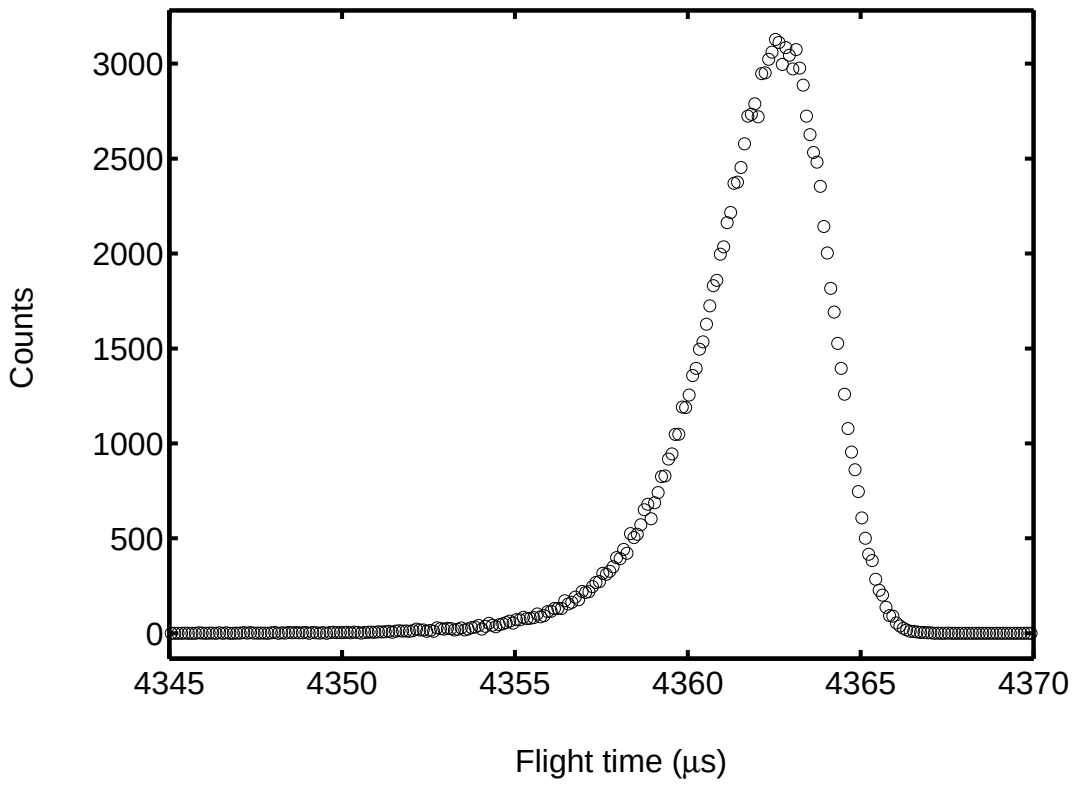

Figure 2.7: A typical junction switching histogram. The switching histogram is for Nb Josephson junction sample RESJJ-Nb with a critical current of 125.28 μA and a capacitance of 1.1 pF. The data was taken at the base temperature of the dilution refrigerator (25 mK) and with a sawtooth bias current ramped at 200 Hz. The y-axis is the number of counts in 100 ns bins and the x-axis is the time from the start of the current ramp, which was at about 0.029 A/s.

repeated for tens of thousands of times and a histogram is constructed (see Fig. 2.7). From this histogram and knowing how the bias current depends on time, I can obtain the escape rate as a function of the bias current (see Fig. 2.8).

The conversion procedure can be understood from the following rate equation,

$$dN(t) = -\Gamma(t)N(t)dt \tag{2.26}$$

where $N(t)$ denotes the particles that have survived up to time t, $\Gamma(t)$ denotes the escape rate at time t, and $dN(t)$ is the number of particles that escape during the

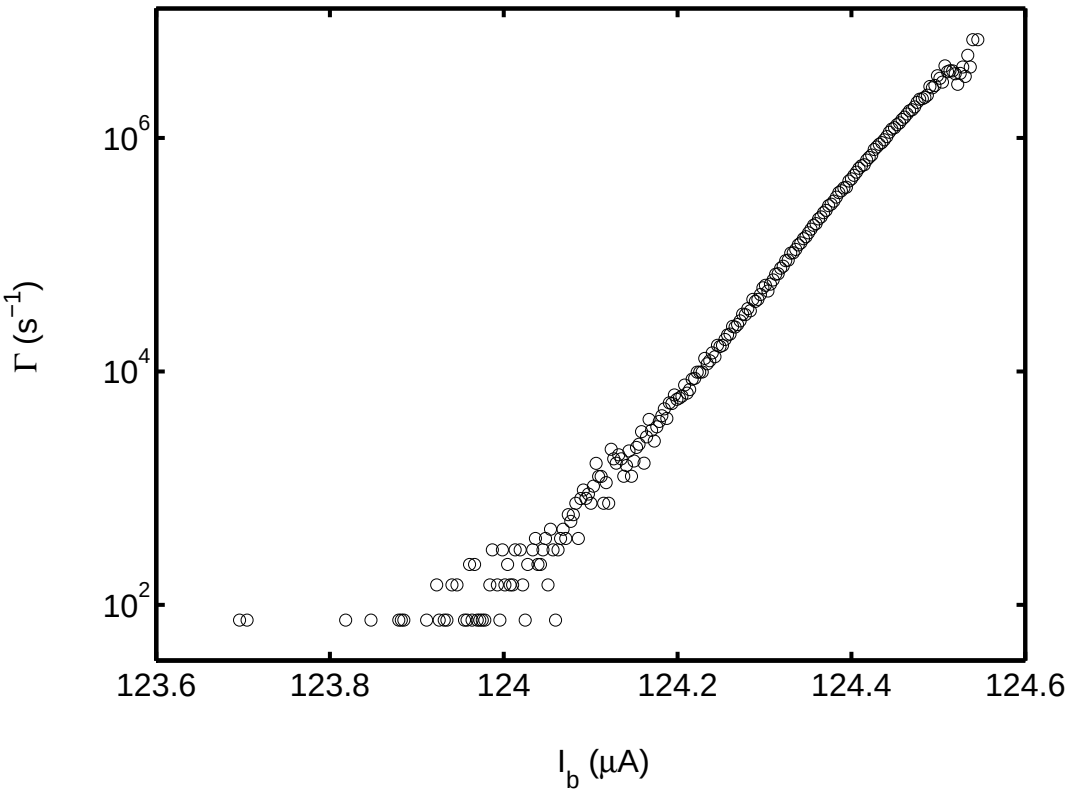

Figure 2.8: Escape rate curve found from the histogram shown in Fig. 2.7 using Eq. 2.27. Note the escape rate increases exponentially with bias current.

time interval from t to $t + dt$.

Integrating Eq. 2.26 from t_i to $t_{i+1} = t_i + \Delta t$ and assuming $\Gamma(t)$ is a constant during this interval Δt, one finds

$$\Gamma(t_i) = -\frac{1}{\Delta t} \ln \left(\frac{N(t_{i+1})}{N(t_i)} \right) \tag{2.27}$$

where $N(t_{i+1})$ and $N(t_i)$ are the number of particles that survived up to time t_{i+1} and t_i respectively. The $N(t_i)$ can be found from the histogram $h(t_i)$ using $N(t_i) = \sum_{j=i}^{\infty} h(t_j)$.

Using the time-dependent functional form of the ramp $I_b = f(t)$, one can convert time to bias current, and thus find the escape rate as a function of bias current (see Fig. 2.8).

2.6 Summary

In this chapter, I discussed the basic physics of Josephson junctions including the RCSJ model, the classical dynamics of the system and the quantum picture. The Josephson relations are the key to understanding this system, but the inclusion of the shunt resistance and capacitance are important for a complete understanding. The classical dynamics gives us understanding of the system in the high temperature limit. In terms of quantum computing, we are mainly interested in the quantum behavior. The junction can also be viewed as a tunable anharmonic oscillator. For a qubit, we can treat the junction as a two-level system, with the ground state $|0>$ and the first excited state $|1>$. The level spacing between the two states can be adjusted using the bias current, and the two states can be distinguished by their distinct tunneling rates. Manipulation of the two states can be realized by applying microwave current to the system. Finally, I have described the experimental method I used to measure the escape rate.

Chapter 3

Dissipation in a Josephson Junction Qubit

In the RCSJ model, a shunt resistance R is used to describe dissipation. From a broader point of view, R incorporates all dissipative interactions of the qubit with the environment. The damping due to this shunt will cause the qubit to relax from excited states to the ground state. In this chapter I examine how relaxation affects the non-coherent quantum dynamics of a current-biased Josephson junction. As shown below, analysis of the non-coherent dynamics of our system can reveal an important aspect of the qubit, the dissipation time T_1. The effect of relaxation on coherent dynamics and other decoherence mechanisms will be dealt with in Chapter 4.

3.1 The master equation

As discussed in Chapter 2, the Hamiltonian of the qubit can be written as

$$H_0 = \frac{p^2}{2m} - \frac{\Phi_0}{2\pi}\left[I_0\cos(\gamma) + I_b\gamma\right] \tag{3.1}$$

where the effective mass $m = C(\Phi_0/2\pi)^2$, and p is the canonical momentum operator $-i\hbar\frac{\partial}{\partial\gamma}$. For bias current $I_b < I_0$, there are quantized energy states in the well, which

can be denoted as $|i>$, where $i = 0, 1, 2, \cdots$. These states are metastable since they can transition to the continuum outside the well through quantum tunneling. Other processes that can broaden the levels are inter-level transitions induced by relaxation and thermal noise. Due to tunneling the populations in these metastable states will not follow an exact Boltzmann distribution.

For low dissipation, the non-coherent dynamics of the system can be described by a master equation [83, 84]. Larkin and Ovchinnikov [83] showed that

$$\frac{d\rho_i(t)}{dt} = \sum_{j \neq i} [W_{ji}\rho_j(t) - W_{ij}\rho_i(t)] - \Gamma_i \rho_i(t) \tag{3.2}$$

where $i = 0, 1, 2, \cdots, n$, ρ_i is the probability of finding the particle in the i-th state $|i>$, W_{ji} is the transition rate from the j-th level to i-th level due to relaxation and noise, and Γ_i is the quantum tunneling rate from the i-th level.

The measured escape rate $\Gamma(t)$ is related to $\rho_i(t)$ and Γ_i by

$$\Gamma(t) \equiv -\frac{d \ln [\rho(t)]}{dt} = \frac{1}{\rho(t)} \sum \Gamma_i \rho_i(t) \tag{3.3}$$

where $\rho(t) = \sum \rho_i(t)$ is the probability of finding the particle in the zero-voltage state. Therefore the problem of calculating the total escape rate comes down to finding $\rho_i(t)$ by solving the coupled Eq. 3.2.

3.2 Inter-level transitions

To proceed, we need to identify processes that lead to inter-level transitions. Recall that the dynamics of the junction is governed by

$$m\ddot{\gamma} = -\frac{dU(\gamma)}{d\gamma} + F_n(t) - \left(\frac{\Phi_0}{2\pi}\right)^2 \frac{\dot{\gamma}}{R} \tag{3.4}$$

where $F_n(t) = -\Phi_0/2\pi I_n(t)$, $I_n(t)$ is the noise current from the junction with a correlation function $< I_n(0)I_n(t) > \cong 4k_BT\delta(t)/R$, and T is the temperature of the shunt resistance.

Due to damping caused by the shunt R, the higher levels can relax to lower levels by losing energy to the environment, similar to spontaneous emission in atomic systems. I can denote the rate of spontaneous emission from the j-th level to the i-th level by Γ_{ji}, for $j > i$ (see Fig. 3.1). These rates are related by the detailed balance condition, as shown below. It turns out that the rates are also closely related to $1/RC$, where C is the junction capacitance.

In addition to relaxation, there are two other processes that can also induce inter-level transitions: thermal noise, which acts as a random force $F_n(t)$, and applied excitations (microwaves).

3.2.1 Noise-induced inter-level transitions

Here we consider the low damping limit, i.e. $Q = \omega_p RC \gg 1$. In this limit, the damping term and the noise term can be treated as perturbations to the canonical Hamiltonian H_0. I denote the perturbation term associated with the noise by $H_n = -\Phi_0 I_n(t)\gamma/2\pi$. I then use time-dependent first order perturbation theory to calculate W_{ij}^t, the thermal noise-current induced transition rate (transition probability per unit time) from $|i>$ to $|j>$. As shown in Appendix B, I find

$$W_{ij}^t = \frac{\Delta E}{2Re^2} \frac{|<i|\gamma|j>|^2}{\exp\left(\Delta E/k_B T\right) - 1} \tag{3.5}$$

where $\Delta E = |E_i - E_j|$ is the level spacing between the i-th and j-th level, and $<i|\gamma|j>$ is the matrix element of γ between the i-th and j-th level.

From Eq. 3.5, we see the transition rate from $|j>$ to $|i>$ is equal to that from $|i>$ to $|j>$, i.e.

$$W_{ij}^t = W_{ji}^t \tag{3.6}$$

This means thermal noise tends to equalize the populations among different levels. However, due to the spontaneous relaxation with rate Γ_{ji}, where $j > i$, the

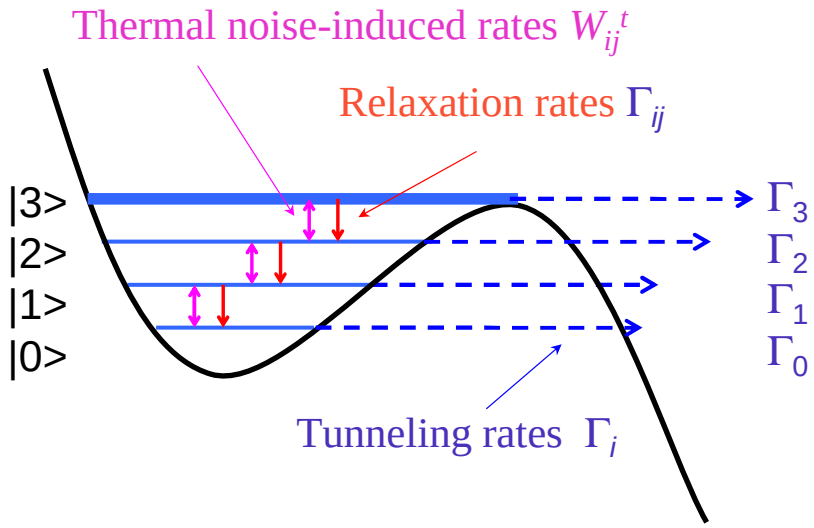

Figure 3.1: Quantum dynamics inside the washboard potential. The downward arrows indicate spontaneous relaxation processes with rates Γ_{ij}, the horizontal arrows denote quantum tunneling processes with rates Γ_i. The vertical bi-directional arrows represent transitions due to thermal noise with rates W_{ij}^t. Not shown here are inter-level transitions due to applied microwaves with rates W_{ij}^m.

net result of these two processes is a Boltzmann distribution among the levels. If we impose the detailed balance condition on the rates, we can find the spontaneous relaxation rates Γ_{ji}. For $j > i$, the detailed balance condition implies

$$W_{ij}^t \exp\left(\Delta E/k_B T\right) = W_{ji}^t + \Gamma_{ji} \tag{3.7}$$

or,

$$\Gamma_{ji} = W_{ij}^t \left[\exp\left(\Delta E/k_B T\right) - 1\right] \tag{3.8}$$

From Eq. 3.8, we can calculate the spontaneous rates if we know the noise-induce transition rates. The levels deep inside the well are very harmonic, therefore we have $|< i|\gamma|i+1>|^2 = \left|< i|\sqrt{\hbar/2m\omega}(a+a^\dagger)|i+1>\right|^2 = 2e^2(i+1)/C\Delta E$, and

$$\Gamma_{ji} = \frac{j}{RC}, \text{ for } j = i+1 \tag{3.9}$$

Therefore the spontaneous rate from $|1>$ to $|0>$ is $1/RC$, which is just what one expects from classical theory. However, the relaxation rate from a higher level increases with occupation number. In the literature, people often use the dissipation time T_1 to quantify this relaxation process, and then the relaxation rate is just $1/T_1$. As far as the qubit states $|0>$ and $|1>$ are concerned, we thus have $T_1 \approx RC$.

For levels near the barrier top that are anharmonic, the matrix elements must be calculated from their wave functions before the relaxation rates can be found. In addition, transitions can happen not only between nearest neighbor levels, but also between any two levels due to the large anharmonicity.

3.2.2 Microwave-induced inter-level transitions

In order to observe energy levels, we can apply microwaves to drive transitions from lower levels to higher levels, where the tunneling rate is much higher.

To proceed, let us denote the microwave current by $I_1 \cos(\omega_1 t)$, where I_1 and ω_1 are the microwave amplitude and angular frequency, respectively. For small

microwave power, we can use first order perturbation theory to calculate the rates due to the perturbation $H^{\mu} = -I_1\Phi_0\gamma/2\pi$ and find[1]

$$W_{ij}^m = W_{ji}^m = \frac{I_1^2}{16e^2}| < i|\gamma|j > |^2 \frac{X_{ij}}{(\omega_1 - \Delta E/\hbar)^2 + X_{ij}^2/4} \tag{3.10}$$

where X_{ij} is the uncertainty in the level spacing ΔE due to the width of the levels involved in the transition, and is given by

$$X_{ij} = \sum_{k\neq i} W_{ik}^t + \sum_{k\neq j} W_{jk}^t + \sum_{k<i} \Gamma_{ik} + \sum_{k<j} \Gamma_{jk} + \Gamma_i + \Gamma_j \tag{3.11}$$

From Eq. 3.10, we see the microwave-induced transition rate is proportional to the microwave power (proportional to I_1^2). For harmonic levels, microwaves can only induce transitions between nearest levels, i.e., from i to $j = i + 1$, we then have

$$W_{ij}^m = W_{ji}^m = \frac{P_m}{4RC\Delta E} \frac{X_{ij}}{(\omega_1 - \Delta E/\hbar)^2 + X_{ij}^2/4} \tag{3.12}$$

where $P_m = I_1^2 R/2$ is the microwave power. In particular, when the microwave frequency is in resonance with the level spacing, i.e. $\omega_1 = \Delta E/\hbar$, the temperature is low and tunneling is negligible, the microwave-induced transition rate between $|0>$ and $|1>$ is

$$W_{01} = W_{10} = \frac{1}{RC} \frac{P_m}{\Delta E/RC} \tag{3.13}$$

The term $\Delta E/RC$ can be interpreted as the power at which particles in excited states lose energy by relaxation. Therefore the microwave-induced transition rate is proportional to the ratio of the pumping power to the power lost by spontaneous relaxation.

[1]This formula can also be derived from study of the coherent dynamics of the system using the Bloch equation as discussed in Chapter 4.

3.3 Energy levels and tunneling rates

In order to solve Eq. 3.2, we need to know the energy levels, wave functions and tunneling rates.

3.3.1 Hard-wall boundary condition

Although the levels are metastable, the tunneling rates are small compared to the level spacing unless the levels are very close to the barrier top. For levels deep inside the well, we define the two points γ_1 and γ_2 as the points where the potential has adjacent local maxima (see Fig. 3.2). We then use a finite difference method to solve the time-independent Schrödinger equation and find the eigen-values and eigen-vectors of an $N \times N$ matrix, where N is the size of the coordinate grid. N was chosen such that the discrepancy between the numeric solution and that from the Bohr-Sommerfeld quantization rule is less than 0.1% (typically $N \approx 1000$). For bias current not close to I_0 this allows us to avoid errors introduced if one used a cubic approximation [84, 85].

Tunneling rates from deep levels can then be approximated by the WKB formula

$$\Gamma_i = \frac{\omega_i}{2\pi} \exp\left(-\frac{2}{\hbar}\int_{q_1}^{q_2} \sqrt{2m(U_c(q) - E_i)}\, dq\right) \tag{3.14}$$

where ω_i and E_i are the attempt frequency and energy of the particle in the i-th state, and q_1 and q_2 are the boundaries where $E_i = U_c(q_1) = U_c(q_2)$. Using the energy E_i obtained from solving the Schrödinger equation, we can evaluate the integral in Eq. 3.14 to find the tunneling rate. Since we are only interested in the low damping limit, the effect of dissipation on the tunneling rates is negligible.

For levels near the top of the barrier, the above boundary conditions for the Schrödinger equation no longer hold and Eq. 3.14 becomes invalid for finding tunneling rates. However, the energies of these levels, and tunneling rates from them, can still be found by generalizing the Bohr-Sommerfeld quantization rule, as shown

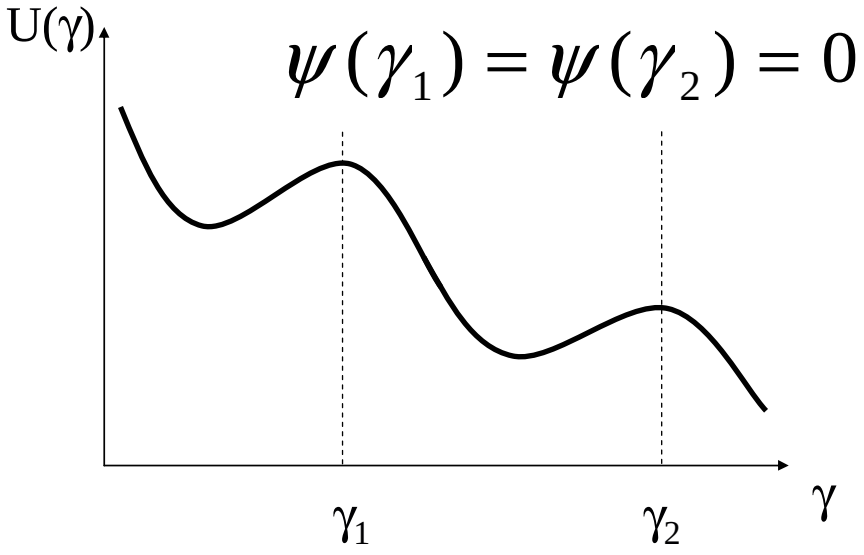

Figure 3.2: The hard-wall boundary condition. The local maxima (separated by 2π in γ) are chosen to be the boundaries. The hard-wall boundary condition, $\Psi(\gamma_1) = \Psi(\gamma_2) = 0$ can be used to solve for the eigen-states deep inside the well.

by Kopietz and Chakravarty [85].

3.3.2 Transmission boundary condition

Although one can use the methods given by Kopietz and Chakravarty [85] to find the energies and tunneling rates, this technique does not yield the wave functions for the states. In order to find the wave functions of these states and also check how good are the hard-wall boundary conditions and the WKB method for finding the energies and tunneling rates of the deep levels, I used the transmission boundary condition method [86].

The basic idea is to allow wave functions to leak out of the right-side of the well since the barrier height is not that large compared to the energies of the states, especially for states near the barrier top. With this boundary condition, one does not use the local maxima of the potential as the two boundaries. Instead one just needs to picks up two points where the change in potential is much smaller than the difference between the potential and the expected energy. Let γ_1 and γ_2 denote the left and right boundaries, we impose the following boundary conditions

$$\Psi_0 = \exp(-\lambda\,\delta\gamma)\Psi_1 \tag{3.15}$$

$$\Psi_{N+1} = \exp(ik\,\delta\gamma)\Psi_N \tag{3.16}$$

where Ψ_1 and Ψ_N are the values of the wave function at the two boundaries, and Ψ_0 and Ψ_{N+1} are the values of the wave function just one step outside the boundary, $\delta\gamma$ is the step size of the grid, k and λ are wave vectors for the right boundary and left boundary. The wavevectors are given by

$$\lambda = \sqrt{2m(U(\gamma_1) - E)}/\hbar \tag{3.17}$$

$$k = \sqrt{2m(E - U(\gamma_N))}/\hbar \tag{3.18}$$

Using Eqs. 3.15 and 3.16 and the Schrödinger equation on a finite-grid, one finds an $N \times N$ tri-diagonal matrix. The eigenvalues of the matrix correspond to the energies of the levels. Because both λ and k are energy-dependent, searching for the eigenvalues can only be done by iteration. I usually start with the energies found using the hard-wall boundary condition. After a few iterations with the transmission boundary condition, the eigenvalue picks up an imaginary part that corresponds to the tunneling rate from this state. Then the eigenvalue for the eigenstate $|i>$ can be written as

$$< i|H_0|i >= E_i - i\hbar\Gamma_i/2 \tag{3.19}$$

where E_i is the real part denoting the energy of the state, and Γ_i denotes the tunneling rate.

The eigenvalues found using this method agree with other well-established methods [87]. For the levels deep inside the well, I found the hard-wall boundary condition and the WKB method give results that are within 2% of this method. For the levels above the barrier, the convergence of the transmission boundary condition method is slow as there are really no well-defined levels but rather a density of states. However our calculations suggest that there is always one broad but relatively well-defined level just above the barrier. I therefore treat the continuum as one broad level with a large spread, the level $|n>$ in Eq. 3.2 refers to this broad level (there are n levels inside the well, labeled as $|0>$, $|1>$, $\cdots$, $|n-1>$).

3.4 Escape rate at finite temperature

Once the various rates are known, I can now try to solve Eq. 3.2. Here I limit my discussion to the case of no applied microwaves.

In general, the potential well, the energy levels and the wave functions change with time (as a result of the bias current ramp). As seen above, the dependence of inter-level transition rates and tunneling rates on the bias current is rather complicated. As a result, Eq. 3.2 cannot be solved analytically. However under the stationary condition, one can write down the expression for the total escape rate in closed form.

3.4.1 Stationary condition

If the ramp is slow enough to reach a stationary condition (as discussed below), then Eq. 3.2 can be solved in a simple way. Due to tunneling, the sum of the populations in all the levels decreases with time, but the total escape rate only depends on the relative ratio of these populations $\rho_i(t)$. Since the population does not follow a Boltzmann distribution (due to tunneling), the ratio of these populations will change as the tunneling rates change (as a result of the bias current ramp). I note that the escape rate increases exponentially with bias current, so that for a linear bias current ramp, I can write for the tunneling rates,

$$\Gamma_i(t) = \Gamma_i(0) \exp(-\alpha t) \tag{3.20}$$

where $\alpha = -\frac{d \ln \Gamma_i}{dt}$ is a quantity characterizing the ramp speed.

As the tunneling rates increase, the higher levels get more and more depopulated, which means ρ_i/ρ_0 is decreasing for $i > 0$. If the ramp is slow so that

$$\alpha \ll \frac{1}{RC} \tag{3.21}$$

then the system always has enough time to establish an equilibrium state with time-independent relative ratios of the populations. In other words, a stationary condition can be reached where $\rho_i(t)/\rho_0(t)$ is a constant. Then when the bias current changes slowly to a new value, new equilibrium states will be subsequently established.

Under this stationary condition, for any bias current, we then have

$$\frac{d}{dt}\left(\frac{\rho_i(t)}{\rho(t)}\right) = 0 \tag{3.22}$$

Using the above equation, one can then rewrite Eq. 3.2 as

$$\sum_{j\neq i}(W_{ji}\rho_j(t) - W_{ij}\rho_i(t)) + (\Gamma - \Gamma_i)\rho_i(t) = 0 \tag{3.23}$$

and $\Gamma = \sum \Gamma_i \rho_i(t)/\rho(t)$ is the total escape rate.

In general, it is still not easy to solve Eq. 3.23. However for temperatures not too high, we will have $\Gamma \ll \Gamma_i$ for $i > 0$ (which is fulfilled in almost all our experiments). Thus for $i > 0$, we can ignore Γ in Eq. 3.23 and get

$$\sum_{j\neq i}(W_{ji}\rho_j(t) - W_{ij}\rho_i(t)) - \Gamma_i\rho_i(t) = 0 \tag{3.24}$$

where $i = 1, 2, \cdots, n$. This equation can be easily solved to obtain the ratios of populations, i.e. ρ_i/ρ_0 and the total escape rate is then given by

$$\Gamma = \frac{\Gamma_0 + \sum_{i=1}^{n}\Gamma_i\rho_i/\rho_0}{1 + \sum_{i=1}^{n}\rho_i/\rho_0} \tag{3.25}$$

The above equation can then be used to calculate how the escape rate depends on bias current. Notice the above equation is applicable for any temperature provided $\rho_i/\rho_0 \ll 1$ for $i > 0$. In contrast, the Caldeira-Leggett formula Eq. 2.25 only applies for tunneling from the ground state, and the classical escape rate formula Eq. 2.13 can only be used when $k_B T \gg \hbar\omega_p$.

3.4.2 Population depletion in higher levels

For simplicity, here we just assume there are just two levels, $|0>$ and $|1>$ [2]. Using Eq. 3.24, we can find the ratio of ρ_1 to ρ_0,

[2]This analysis can be readily generalized to the case of many levels.

$$\frac{\rho_1}{\rho_0} = \frac{W_{01}}{W_{10} + \Gamma_1} \tag{3.26}$$

The total escape rate is then given by

$$\Gamma = \frac{\rho_0\Gamma_0 + \rho_1\Gamma_1}{\rho_0 + \rho_1} = \Gamma_0 \frac{W_{10} + \Gamma_1}{W_{01} + W_{10} + \Gamma_1} + \Gamma_1 \frac{W_{01}}{W_{01} + W_{10} + \Gamma_1} \tag{3.27}$$

where W_{01} and W_{10} are the inter-level transition rates, given by

$$W_{01} = \frac{1}{T_1} \frac{1}{\exp(\Delta E/k_B T) - 1} \tag{3.28}$$

$$W_{10} = \frac{1}{T_1} \frac{\exp(\Delta E/k_B T)}{\exp(\Delta E/k_B T) - 1} \tag{3.29}$$

where ΔE is the $|0>$ to $|1>$ level spacing.

From Eq. 3.27, we see that the total escape rate is a weighted sum of the tunneling rates from the ground state and the first excited state. The total escape rate calculated using Eq. 3.27 for temperatures of 25 mK and 90 mK for the parameters of sample LCJJ-Nb2 (see Chapter 7) are plotted in Fig. 3.3.

In the low-temperature limit, the relative weight for the ground state is almost 1 since $W_{01} \ll W_{10}$, but the relative weight for the first excited state depends on how Γ_1 compares to W_{10}. For small bias currents, $\Gamma_1 \ll W_{10}$, and thus the relative weight for the $|1>$ state is just the Boltzmann factor $\exp(-\Delta E/k_B T)/(\exp(-\Delta E/k_B T) + 1)$. This means the total escape rate is always larger than Γ_0 and the total escape rate curve is essentially parallel to the one for Γ_0.

However, as I_b increases, Γ_1 increases until it is comparable to and then larger than W_{10}. At this bias, the relative weight for the $|1>$ state will decrease and can be significantly smaller than the Boltzmann factor. This causes the total escape rate to increase more slowly than at small bias currents. Finally for high bias currents where $\Gamma_1 >> W_{10}$, the relative weight for the $|1>$ state goes to zero, and the total escape rate just collapses to Γ_0, as seen in Fig. 3.3. Intuitively one can understand

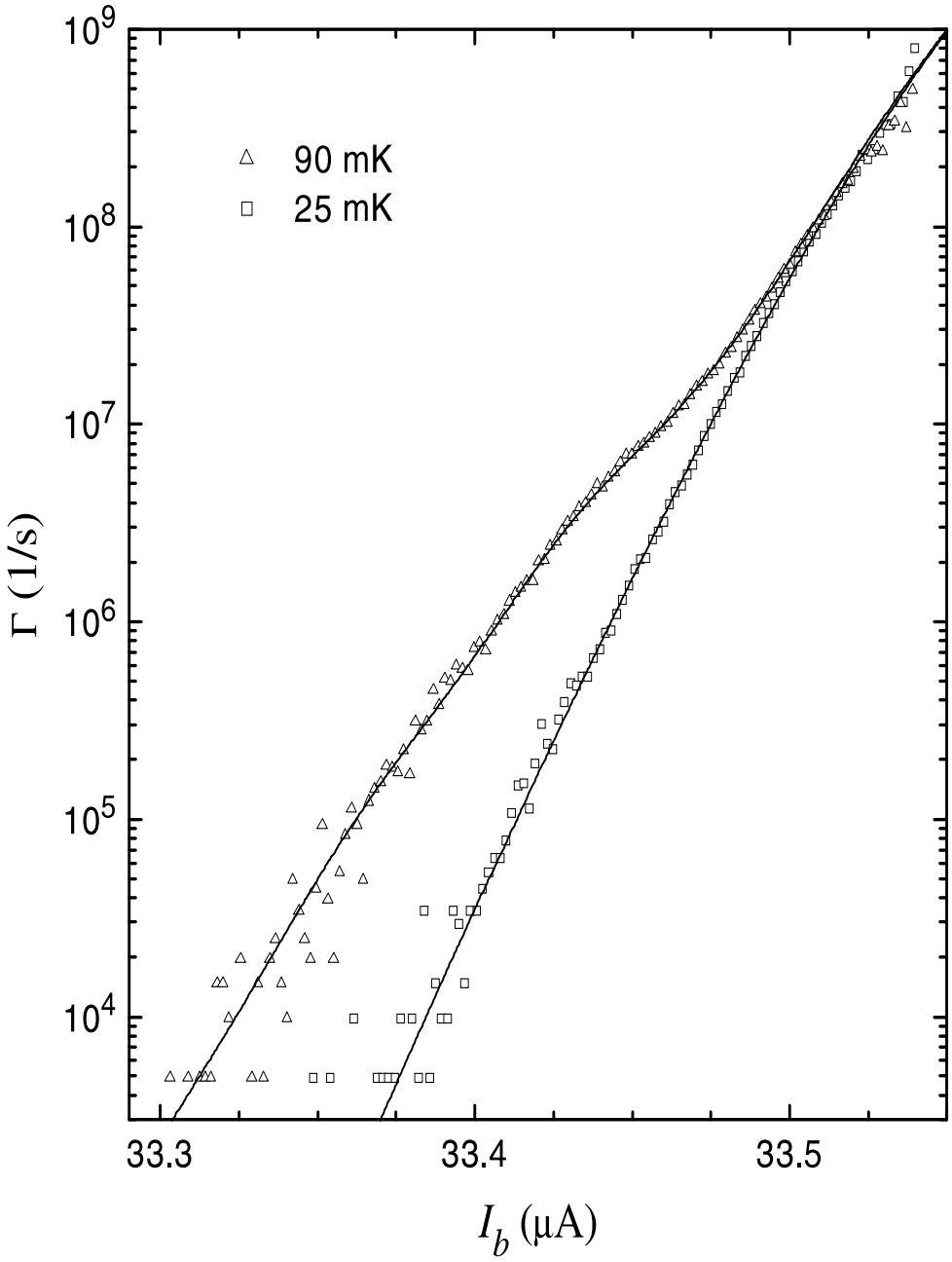

Figure 3.3: Theoretically predicted escape rates (solid lines) for the parameters of sample LCJJ-Nb2 (see Chapter 7) for a slow ramp. Squares and triangles are data taken on sample LCJJ-Nb2 at 25 mk and 90 mK, respectively. The ramp rate is dI/dt =0.7 A/s and $\alpha = 7.5 \times 10^7$/s.

this collapse as due to population depletion in the first excited state as a result of its high tunneling rate.

The place where collapse happens is marked by the condition $\Gamma_1 \approx W_{10}$, and the total escape rate at this point is

$$\Gamma = \Gamma_0 + \frac{W_{01}}{2} \approx \frac{W_{01}}{2} \tag{3.30}$$

Therefore from the total escape rate at the collapse point, we can directly read W_{01} and if $\Delta E/k_B T$ is known, we can obtain the relaxation time T_1 using Eq. 3.28.

3.4.3 Fast ramp

So far my discussion has been limited to the stationary case, where the condition $\alpha = \left|\frac{\partial \ln \Gamma}{\partial t}\right| \ll 1/T_1$ is satisfied. Interesting phenomena occur as one increases the ramp rate.

The dynamics of this system under fast ramp conditions was first studied by Silvestrini, Ovchinnikov and Cristiano [88] using the master equation 3.2. They found the escape rate curve starts to oscillate when the ramp rate gets very high and the temperature is high (∼1 K). Fig. 3.4 shows a calculation I did in this limit using Eq. 3.2. Silvestrini and his coworkers [88] argued that these oscillations were essentially manifestations of the quantized energy levels in the well. Remarkably, this kind of oscillations was observed in later experiments that were carried out with high ramp rates [89, 90] at temperatures as high as 1K.

As the bias current increases, the highest level approaches the barrier top and its tunneling rate increases rapidly. Since the ramp rate is very fast, relaxation will not be fast enough to reduce the population in this level to the stationary value. The net effect is that the contribution to escape rate from the highest level is the tunneling rate weighted by a Boltzmann factor. This results in a rapid increase of the total escape rate. However, eventually the population in this level gets depleted

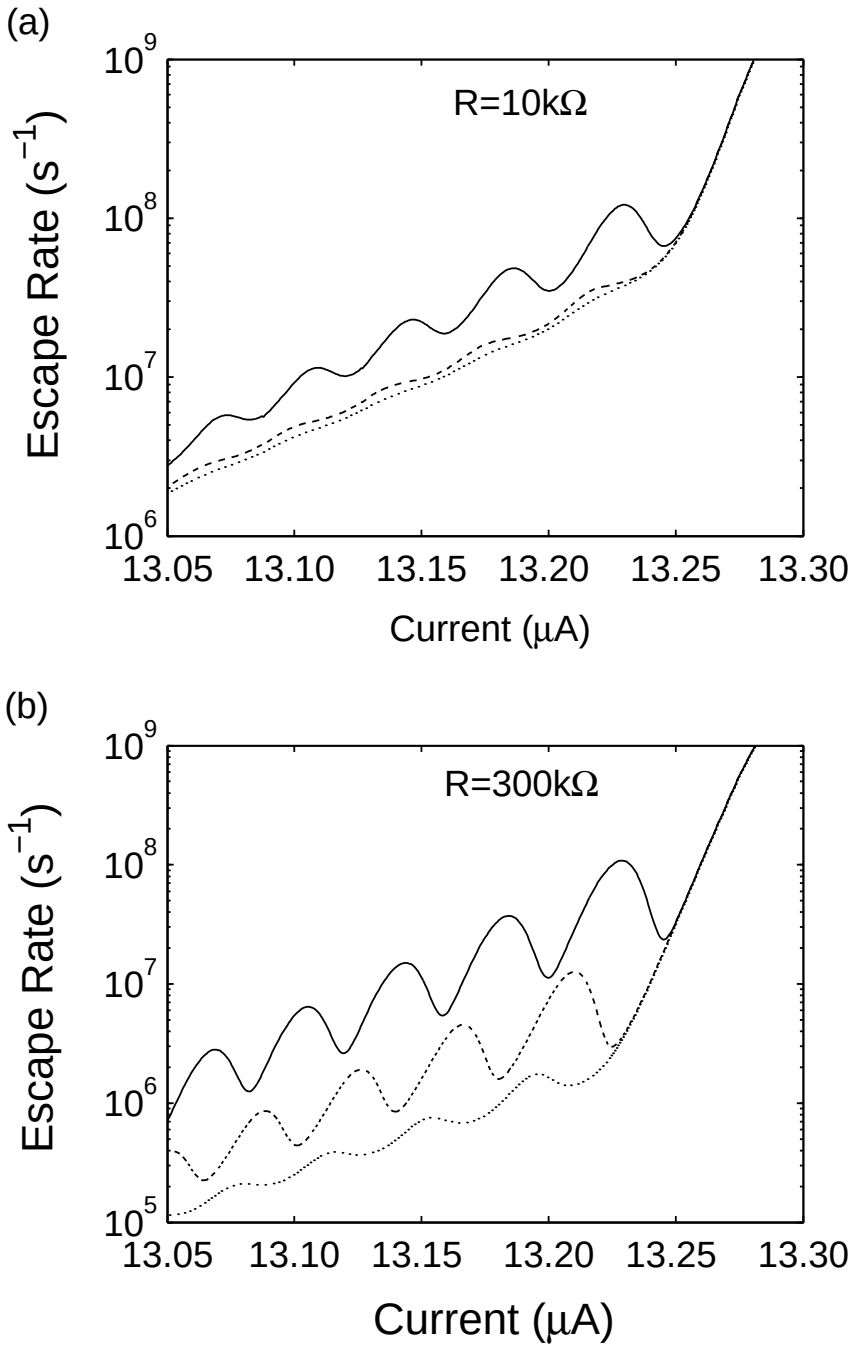

Figure 3.4: Calculated escape rates for a junction with $I_0 = 13.335$ μA and $C = 4.378$ pF at 500 mK for a fast current ramp. (a) $R = 10$ kΩ, (b) $R = 300$ kΩ. Solid lines correspond to a ramp with $dI_b/dt = 7$ A/s ($\alpha = 1.6 \times 10^8$/s), dashed lines correspond to $dI_b/dt = 0.7$ A/s ($\alpha = 1.6 \times 10^7$/s), and dotted lines correspond to $dI_b/dt = 0.07$ A/s ($\alpha = 1.6 \times 10^6$/s).

due to tunneling, so the total escape rate starts to decrease. The next cycle will begin as the next level below the barrier top approaches the barrier top. The result is an oscillation in escape rate, which can be viewed as evidence for quantized energy levels. Since this effect is related to the relaxation process, the relaxation time T_1 can be obtained from fitting the measured escape rate curve. Note that in order to see the oscillations, high temperatures are also required in order to have some finite populations in upper levels.

Both this effect and the population-depletion effect are the consequence of two competing processes, the relaxation process and the tunneling process. However, the two phenomena are distinct. The oscillations occur because the relaxation rate ($\sim 1/RC$) is smaller than the rate of change of the tunneling rates ($\alpha = d \ln \Gamma_i / dt$). But the population-depletion effect is a result of the relaxation rate being smaller than the tunneling rate. Therefore population depletion can be observed under a stationary condition with a temperature that is about half of the level spacing, while the oscillations in the escape rate curve can only be observed under fast ramp conditions and the temperature can be higher than the level spacing. Although a fast ramp current can be easily applied to the junction, calibration of the ramp function is not easy due to delays and distortion of the ramp waveform by the bias lines. From the experimental point of view it is much easier to perform population-depletion experiments under slow ramps, provided we can reach low enough temperatures.

3.5 Resonant activation

There are other ways to manifest the existence of the quantized levels in the well even at high temperatures. The key concept is to create non-stationary conditions, which can be achieved not only by a fast ramp [89], but also by resonant activation [80] or a fast change in the bias current [69].

For example, when we apply microwaves to the system, we have additional

microwave-induced inter-level transition rates as given by Eq. 3.10. Therefore the total inter-level transition rates are given by

$$W_{ij} = W_{ij}^t + \Gamma_{ij} + W_{ij}^m \tag{3.31}$$

$$W_{ji} = W_{ji}^t + W_{ji}^m \tag{3.32}$$

where we have assumed $i > j$.

Let us first assume zero temperature for the system. Then the total escape rate without microwaves applied is just Γ_0. When microwaves with a fixed frequency ω_1 are applied to the system, since the bias current will change the potential of the qubit, we then expect that at some bias current where the $|0>$ to $|1>$ level spacing ΔE is close to $\hbar\omega_1$. The population in the ground state will then be driven to the first excited state, and we expect an increase in the escape rate. This technique was first used Martinis *et al.* to demonstrate the existence of energy levels in single junctions [80].

3.5.1 T_1 measurement

If we assume that only the lowest two levels are relevant, and furthermore $W_{01}^m \ll \Gamma_{10}$, [3] one finds that the escape rate with applied microwaves is[4]

$$\Gamma_m = \frac{W_{01}^m}{\Gamma_{10} + \Gamma_1}\Gamma_1 + \Gamma_0 \tag{3.33}$$

Recall that the rate due to microwaves is given by

$$W_{01}^m = \frac{P_m}{4RC\Delta E}\frac{X_{01}}{(\omega_1 - \Delta E/\hbar)^2 + X_{01}^2/4} \tag{3.34}$$

[3] This is the low microwave power limit; most of our experiments are in this limit.

[4] In typical resonant activation experiments, the bias current is ramped slowly, so the stationary solution of the master equation can be used.

where $P_m = I_1^2 R/2$ is the microwave power, ω_1 is the microwave frequency, and $X_{01} = \Gamma_{10} + \Gamma_0 + \Gamma_1$ is the uncertainty in the level spacing ΔE due to the life times of the states. Substituting Eq. 3.34 into Eq. 3.33, and assuming $\Gamma_1 \ll \Gamma_{10}$, we find

$$\Gamma_m = \frac{P_m \Gamma_{10}/4\Delta E}{(\omega_1 - \Delta E/\hbar)^2 + \Gamma_{10}^2/4}\Gamma_1 + \Gamma_0 \tag{3.35}$$

From Eq. 3.35, we can see the escape rate with microwaves applied will display resonance peaks when the microwave frequency ω_1 matches the level spacing. We can include more levels in our calculations, which results in multiple resonance peaks as the microwave frequency matches the level spacings between $|2>$ and $|3>$, between $|1>$ and $|2>$, and between $|0>$ and $|1>$ (see Fig. 3.5). We note that the higher level transitions will be observed only if the temperature is high enough to populate the lower of the two levels involved in the transition.

It is often useful to introduce the relative difference between the escape rate with microwave (Γ_m) and the escape rate without microwave (Γ). I can define the enhancement Δ as

$$\Delta = \frac{\Gamma_m - \Gamma}{\Gamma} \tag{3.36}$$

For the above two-level analysis at $T = 0$, we have

$$\Delta = \frac{P_m \Gamma_{10}/4\Delta E}{(\omega_1 - \Delta E/\hbar)^2 + \Gamma_{10}^2/4}\frac{\Gamma_1}{\Gamma_0} \tag{3.37}$$

We see that the response of the system to an external microwave drive is a Lorentzian with a full width at half maximum (FWHM) of Γ_{10}, the relaxation rate. If this enhancement in escape rate due to microwaves is measured, one can readily extract the relaxation time T_1 from the resonance width. However, this analysis does not include the effect of current noise, which can cause additional broadening.

Higher-order resonances have corresponding wider widths, since the relaxation rate are proportional to the occupancy number of the state. Thus, the FWHM of

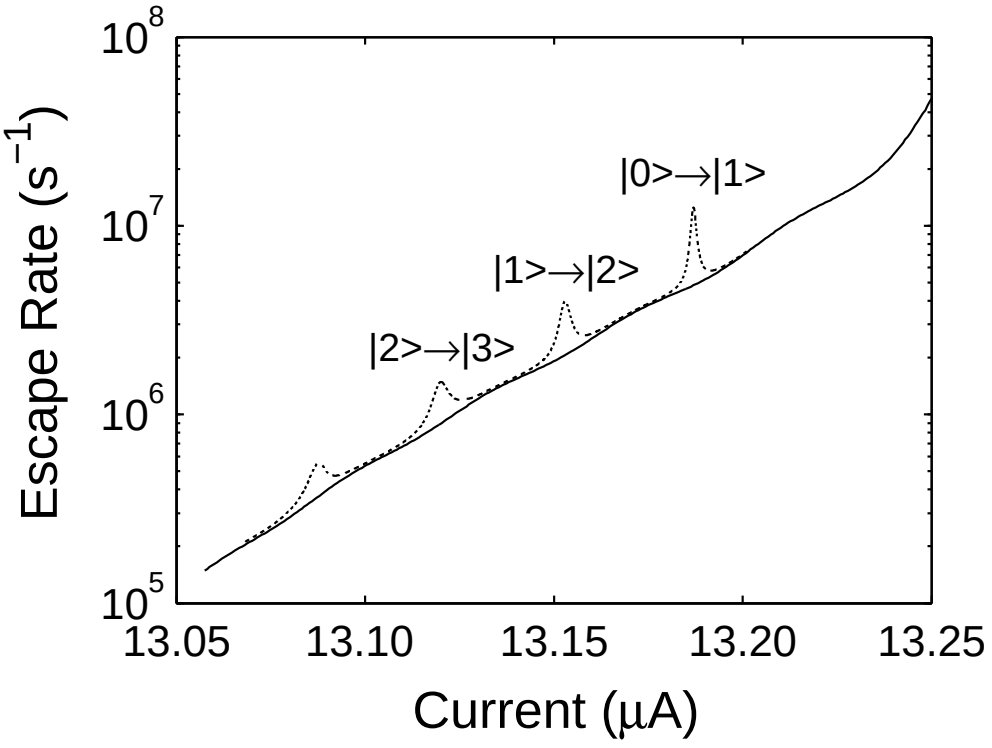

Figure 3.5: Calculated escape rates for junction with $I_0 = 13.335$ μA, $R = 10$ kΩ, and $C = 4.378$ pF at 250 mK with a slow ramp. Solid line is for no microwave, dashed line for 5.5 GHz microwaves with an amplitude of $I_1 = 0.5$ nA.

the $|i> \rightarrow |i+1>$ transition is $2i+1$ times larger than the $|0> \rightarrow |1>$ transition. By comparing the widths of different transitions, one can check this simple scaling and determine if additional smearing is present.

3.5.2 Resonance broadening at finite temperatures

At finite temperatures, the widths of transitions will be broadened compared to the widths at zero-temperatures due to noise-induced inter-level transitions.

If we calculate the enhancement at finite temperatures, we will find the resonance shape of the $|i> \rightarrow |i+1>$ transition is still Lorentzian with the FWHM to be $X_{i,i+1}$. If we ignore the broadening due to tunneling rates[5], we find

$$X_{i,i+1} = W^t_{i,i-1} + 2W^t_{i+1,i} + W^t_{i+1,i+2} + \Gamma_{i,i-1} + \Gamma_{i+1,i} \tag{3.38}$$

Using the relation between the relaxation rates and the rates due to thermal noise, we have

$$X_{i,i+1} = \frac{1}{T_1}\left[\coth\left(\frac{\Delta E}{2k_BT}\right) - 1\right] + X_{i,i+1}(T=0)\coth\left(\frac{\Delta E}{2k_BT}\right) \tag{3.39}$$

where $X_{i,i+1}(T=0) = (2i+1)/(T_1)$ is the FWHM of the resonance at zero temperature. In particular for the $|0> \rightarrow |1>$ transition, the width at a finite temperature is related to the zero-temperature width $1/T_1$ by

$$X_{01} = \frac{1}{T_1}\left[2\coth\left(\frac{\Delta E}{2k_BT}\right) - 1\right] \tag{3.40}$$

Figure 3.6 shows calculations of enhancement at finite temperatures for a Josephson junction with a critical current of 13.335 μA and capacitance of 4.378 pF at temperatures of 25 mK, 250 mK and 2.5 K. Enhancements for two shunt resistances of 300 Ω and 10 kΩ at 25 mK are shown in Fig. 3.6 (a). One can clearly see that

[5] $|i> \rightarrow |i+1>$ resonance broadening due to tunneling will be significant for transitions occurring in shallow wells where the $|i+1>$ state has a large tunneling rate.

the $|0> \rightarrow |1>$ resonance peak for 10 kΩ (solid line) is much sharper than that for 300 Ω (dashed line). There are no higher order resonance peaks due to the low population in excited levels. At 250 mK, which is near the level spacing in this junction, more resonance peaks show up for 10 kΩ and 300 kΩ [see Fig. 3.6(b)]. Only one broad classical resonance peak is predicted for 300 Ω. At 2.5 K, well-resolved resonance peaks are predicted only for 300 kΩ [see Fig. 3.6(c)], and the widths are larger than those at 250 mK. This suggests that quantized energy levels can be observed at temperatures much higher than the level spacing when the system is under microwave irradiation and the shunt resistance is high enough. This behavior is consistent with the experiments in the fast ramp regime since both fast ramp and microwave pumping create a non-stationary distribution of the populations. However, to our knowledge, no one has yet observed such microwave resonances at such high temperatures.

From Fig. 3.6, we see that the width of a resonance peak increases as temperature increases, and decreases as the shunt resistance increases. This is consistent with our analysis of the resonance width. From the dependence of the width on temperature and the shunt resistance, we find that the cutoff temperature where the effect of energy level quantization is still observable scales as the zero temperature relaxation time T_1 of the system [91]. For ongoing experiments in quantum computing, this result provides another way to test if a system has a large relaxation time by demonstration of energy level quantization at temperatures much larger than the level spacing. For Josephson junction qubits with level spacings typically on the order of 10 GHz, this implies that energy level quantization should be observable at temperatures as high as 4 K if the dissipation time of the system is more than 1μs.

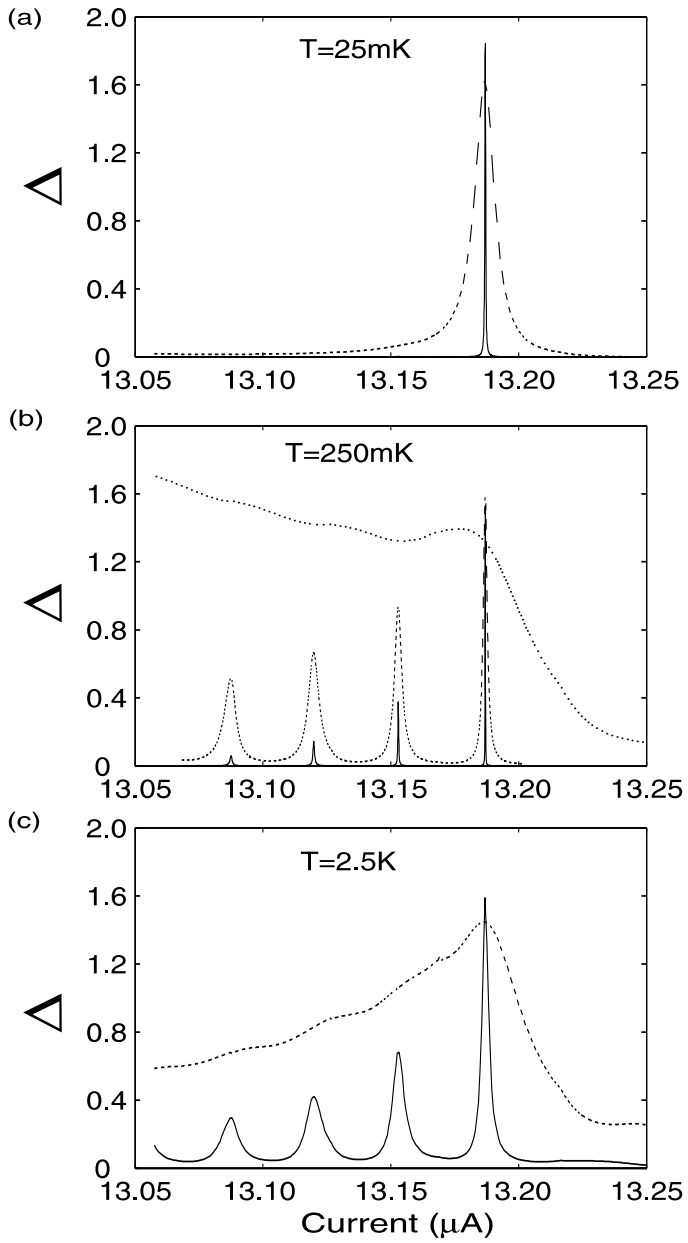

Figure 3.6: Calculated enhancement (relative difference of two escape rates with and without microwaves) for junction with $I_0 = 13.335$ μA and $C = 4.378$ pF when 5.5 GHz microwaves applied. (a) $T = 25$ mK, solid line for $R = 10$ kΩ , dashed line for $R = 300$ Ω. (b) $T = 250$ mK, solid line for $R = 300$ kΩ, dashed line for $R = 10$ kΩ, dotted line for $R = 300$ Ω. (c) $T = 2.5$ K, solid line for $R = 300$ kΩ, dashed line for $R = 10$ kΩ.

3.6 Summary

In this chapter, I described the master equation and applied it to study the non-coherent quantum dynamics of a current-biased Josephson junction qubit. I examined the mechanisms for various inter-level transitions and described briefly numerical methods to calculate these transition rates. Finally, I described three methods that can be used in principle to measure the dissipation time T_1 of our qubit: the population-depletion method with a slow ramp, the fast ramp method at high temperatures, and the resonant activation method. The prediction of the observability of energy level quantization at high temperatures for an extremely low-damped qubit provides a clear way to test whether the qubit has a long dissipation time, provided additional broadening due to current noise (as discussed in Chapter 4 is not present

.

Chapter 4

Decoherence in a Josephson Junction Qubit

Dissipation causes a qubit to relax from the excited state to the ground state by losing energy. This process is characterized by the time T_1. However, relaxation can also disturb the phase evolution when the qubit state oscillates between the ground state and an excited state in the presence of an external microwave drive. This distinct effect is called decoherence. In addition to dissipation-induced decoherence, other non-dissipative sources, such as noise, can also induce decoherence. In fact, in certain limits noise can dominate decoherence. In this chapter, I use the density matrix to study decoherence due to both dissipation and noise.

4.1 The RCSJ model revisited

In Chapter 3, I used the resistively capacitively shunted junction (RCSJ) model to describe the dynamics of a junction qubit. However, at microwave frequencies, the impedance of the bias leads may not be a pure resistance. Furthermore, the low-frequency (a few MHz to a few hundred MHz) electromagnetic environment can also have an important effect on the behavior of the qubit. To capture this structure, I use a complex admittance shunted junction model (see Fig. 4.1) to replace the

RCSJ model.

The complex admittance $Y(\omega)$ can represent an arbitrary dissipative environment, in contrast to the ohmic environment of the RCSJ model. The complex admittance can be due to the bias leads and any additional circuits that are on the bias leads. For example, a resonant inductor-capacitor (LC) network (see Fig. 4.2) used to isolate the junction can produce a resonant structure in the electromagnetic environment.

Although exact expressions for the dynamics of a current-biased Josephson junction linearly coupled to such an arbitrary dissipative environment can be written [92, 93], the calculations are complicated, making them difficult to compare with data. However, many effects due to $Y(\omega)$ can be captured by a spectral function $S_J(\omega)$ [92, 94], which for our system is just the zero-temperature noise power spectral density of the bias current

$$S_J(\omega) = 2\hbar\omega Re[Y(\omega)] \tag{4.1}$$

At finite temperature T, the power spectral density of the thermal noise in the bias current is [95, 96]

$$S_I(\omega/2\pi) = \frac{2S_J(\omega)}{\exp(\hbar\omega/k_BT) - 1} \tag{4.2}$$

Figure 4.3 shows two idealized examples of how $S_I(\omega/2\pi)$ could behave; the dashed line is for an ohmic load of 1.5kΩ at 150 mK, and the solid line for an LC isolation network at 150 mK (see Fig. 4.2, $L_i = 20$nH and $C_i = 1$nF).

For high frequency noise such that the bandwidth f_c of the noise[1] is much larger than $1/T_1$ and $1/T_2$, where T_2 is the phase coherence time of the system, then the

[1]The cutoff frequency for an LC isolation circuit is roughly $1/2\pi\sqrt{L_iC_i}$. For an ohmic environment, the cutoff frequency is set by the temperature of the load as a result of the Boltzmann factor.

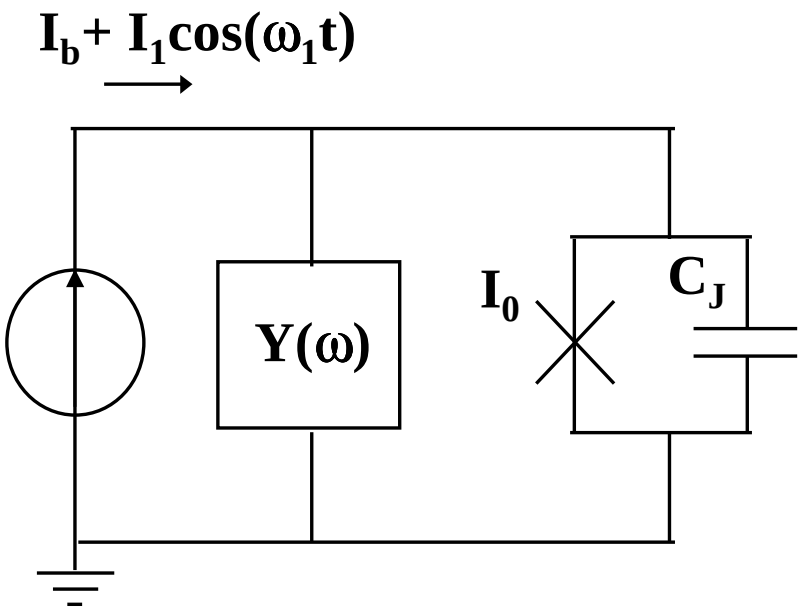

Figure 4.1: Complex impedance shunted Josephson junction model.

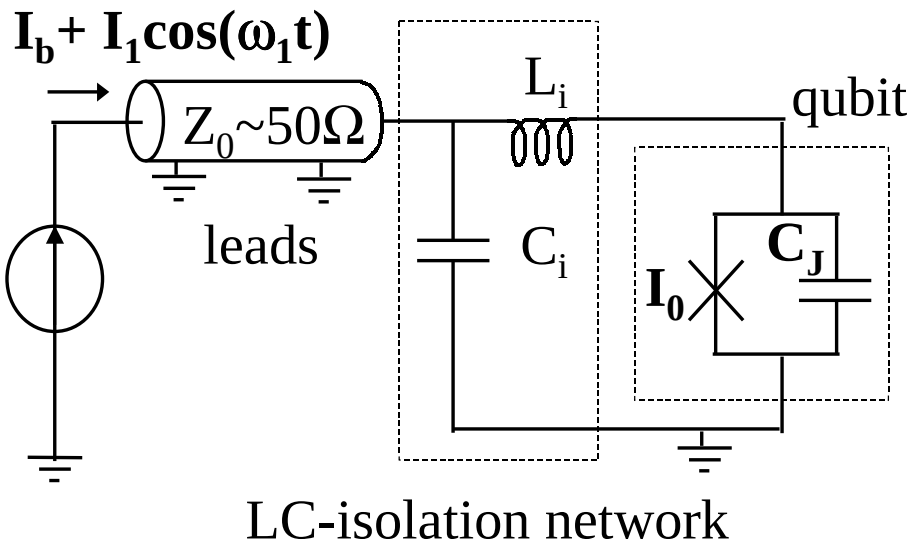

Figure 4.2: Schematic of an LC-isolated Josephson junction.

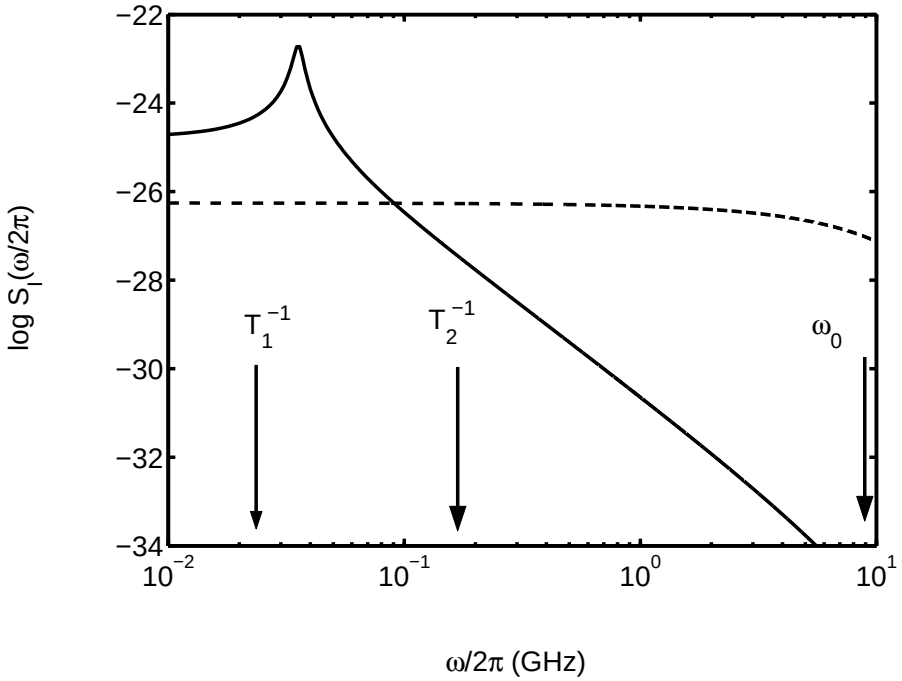

Figure 4.3: Two idealized examples of the thermal noise spectral density. The positions of the relaxation rate $1/T_1(2\pi \times 23$ MHz), the dephasing rate $1/T_2(2\pi \times 180$ MHz), and the typical oscillation frequency ($2\pi \times 9.8$ GHz) of the system are indicated by the arrows. The dashed line is for an Ohmic load of 1.5 kΩ at 150 mK indicating most of the spectrum is in the frequency range above $1/T_1$ and $1/T_2$. The solid line is for an LC isolation network at 150 mK, L_i= 20 nH and $C_i = 1$ nF assumed. The spectrum has a significant weight below $1/T_1$ and $1/T_2$.

dynamics can be described by a master equation for the reduced density matrix [24]. Using this approach, several groups have modeled decoherence in superconducting qubits [97, 98]. While these methods may be valid for high frequency noise (such as an ohmic environment), they are inadequate if there is significant noise at frequencies below $1/T_1$ (such as for an LC isolation network), and further analysis of the density matrix is required.

4.2 The harmonic oscillator bath model

To study the effect of an arbitrary dissipative environment on the coherent dynamics of the system, I use the density matrix approach.

The density operator $\hat{\rho}$ of the total system obeys:

$$i\hbar\dot{\hat{\rho}} = [\hat{H}_{tot}, \hat{\rho}] \tag{4.3}$$

where $\hat{H}_{tot}$ is the Hamiltonian of the qubit and the environment,

$$\hat{H}_{tot} = \hat{H}_0 + \hat{H}_B + \hat{H}_C \tag{4.4}$$

where $\hat{H}_B$ and $\hat{H}_C$ are the bath and coupling Hamiltonians respectively, and $\hat{H}_0$ is the Hamiltonian of the isolated junction given by,

$$\hat{H}_0 = \frac{\hat{p}^2}{2m} - \frac{\Phi_0}{2\pi}\left[I_0\cos(\hat{\gamma}) + I_b\hat{\gamma} + I_1\cos(\omega_1 t)\hat{\gamma}\right] \tag{4.5}$$

where I_1 and ω_1 are the microwave amplitude and angular frequency respectively.

4.2.1 Caldeira-Leggett model

Assuming a harmonic oscillator bath and bilinear coupling [81, 93] as first proposed by Caldeira and Leggett, then $\hat{H}_B$ and $\hat{H}_C$ can be written as [81]

$$\hat{H}_B = \sum_{i=1}^{N} \left(\frac{\hat{p}_i^2}{2m_i} + \frac{1}{2} m_i \omega_i^2 \hat{x}_i^2 \right) \tag{4.6}$$

$$\hat{H}_C = -\hat{\gamma} \sum_{i=1}^{N} c_i \hat{x}_i + \sum_{i=1}^{N} c_i \frac{c_i^2 \hat{\gamma}^2}{2 m_i \omega_i^2} \tag{4.7}$$

where $\hat{x}_i$ and $\hat{p}_i$ are the generalized coordinate and momentum operators of the i-th oscillator in the bath with mass of m_i, frequency of ω_i, and coupling coefficient c_i .

Tracing both sides of Eq. 4.3 over the bath coordinates, the equation of motion for the reduced density operator of the qubit becomes (see Appendix C):

$$\frac{\partial \hat{\rho}_S}{\partial t} = \frac{1}{i\hbar} [\hat{H}_0 + \hat{H}_n, \hat{\rho}_S] + D(\hat{\rho}_S) \tag{4.8}$$

where $\hat{H}_n = -\Phi_0 I_n(t) \hat{\gamma} / 2\pi$, $I_n(t)$ is the current noise flowing through the junction and $D(\hat{\rho}_S)$ is a memory damping term. $Y(\omega)$ is related to m_i, ω_i, and c_i. As shown in Ref. [99]:

$$Y(\omega) = \frac{2\pi^3}{\Phi_0^2} \sum_{i=1}^{N} \frac{c_i^2}{m_i \omega_i} \delta(\omega - \omega_i) \tag{4.9}$$

The power spectral density of the current noise is solely determined by $Y(\omega)$ and can now be linked to the model parameters. Due to the current noise the Hamiltonian of the qubit is stochastic.

4.2.2 The stochastic Bloch equation

In order to solve Eq. 4.8, we choose a basis for the density operator. Since the potential of the qubit can be described by a tilted washboard and the phase qubit states are localized in one of the wells, we choose the lowest three metastable states in a well as our basis[2]. However, $\hat{H}_0$ includes the microwave pumping term and this

[2]Here the basis is not the complete Hilbert space, but the computation subspace of the Hamiltonian. The logical qubit states are the two lowest metastable states, but the 3rd state is important for measurement and gate operations.

makes it inconvenient to find the states of the system. We then rewrite Eq. 4.5 as

$$\hat{H}_0 = \hat{H}_b + \hat{H}^\mu \tag{4.10}$$

where $\hat{H}_b = \frac{\hat{p}^2}{2m} - \frac{\Phi_0}{2\pi}\left[I_0\cos(\hat{\gamma}) + I_b\hat{\gamma}\right]$ denotes the 'base' Hamiltonian, and $\hat{H}^\mu = -\frac{\Phi_0}{2\pi}I_1\cos(\omega_1 t)\hat{\gamma}$ denotes the microwave pumping term. Let $|i>$ $(i = 0, 1, 2)$ denote the three metastable states associated with the 'base' Hamiltonian $\hat{H}_0$. Equation 4.8 then reads in matrix form,

$$\frac{\partial \rho_{ij}}{\partial t} = \frac{1}{i\hbar}\sum_k (H_{ik}\rho_{kj} - \rho_{ik}H^*_{jk}) + D_{ij} \tag{4.11}$$

where $\rho_{ij} =< i|\hat{\rho}_S|j >$, $H_{ij} =< i|\hat{H}_0 + \hat{H}_n|j >$, and $D_{ij} =< i|D(\hat{\rho}_S)|j >$ takes relaxation into account.

It is rather difficult to evaluate D_{ij} in this form because, in the presence of low frequency current noise, the metastable states of the system are constantly changing. Also, damping that occurs on a much faster time-scale will tend to relax the system to the resulting time-dependent states. To take into account the effects of low frequency noise, I choose to work in a time-dependent basis formed by the metastable states $|i'>$ of $\hat{H}_0 + \hat{H}_n$. I consider only the limit of weak damping such that both $1/T_1$ and $1/T_2$ are much less than the characteristic frequency of the system. In this limit, one can show [84]

$$D'_{j'j'} = \sum_{i'>j'} \Gamma_{i'j'}\rho'_{i'i'} - \sum_{k'<j'} \Gamma_{j'k'}\rho'_{j'j'} \tag{4.12}$$

and

$$D'_{i'j'} = -\frac{\Gamma_{i'j'}}{2}\rho'_{i'j'},\ i' > j' \tag{4.13}$$

Here $D'_{i'j'} =< i'|D(\hat{\rho}_S)|j' >$, $\rho'_{i'j'} =< i'|\hat{\rho}_S|j' >$, and $\Gamma_{i'j'}$ is the relaxation rate from $|i'>$ to $|j'>$ as introduced in Chapter 3. We now need to express the first part of Eq. 4.11 in the basis formed by the metastable states $|i'>$ of $\hat{H}_0 + \hat{H}_n$. To do so, we

use the unitary transformation $\rho'_{i'j'} = \sum_i \sum_j N_{i'i}\rho_{ij}N^*_{j'j}$ where $N_{i'i} =< i'|i >$ and $\rho_{ij} =< i|\hat{\rho}_S|j >$. I find the following equation of motion for the density matrix $\rho'_{i'j'}$

$$\frac{\partial \rho'_{i'j'}}{\partial t} = \frac{1}{i\hbar}\sum_{k'}\left[(H'_{i'k'} + H^N_{i'k'})\rho'_{k'j'} - \rho'_{i'k'}(H'_{j'k'} + H^N_{j'k'})^*\right] + D'_{i'j'} \tag{4.14}$$

where

$$H'_{i'j'} =< i'|\hat{H}_b + \hat{H}_n|j' > + < i'|\hat{H}^\mu|j' > \tag{4.15}$$

$$H^N_{i'j'} = i\hbar\sum_k \dot{N}_{i'k}N^*_{j'k} \tag{4.16}$$

Finally, I need to take into account tunneling from the metastable states to the finite-voltage (running) states. As discussed in Chapter 3, $< i'|\hat{H}_b + \hat{H}_n|j' >$ has the form,

$$< i'|\hat{H}_b + \hat{H}_n|j' >= \left(E'_{i'} - \frac{i\hbar}{2}\Gamma_{i'}\right)\delta_{i'j'} \tag{4.17}$$

where $E'_{i'}$ denotes the energy of the state $|i' >$ and $\Gamma_{i'}$ represents the tunneling rate from the metastable state. Substituting Eq. 4.17 into Eq. 4.14, I obtain an equation for the reduced density matrix in the time-dependent basis formed by $|i' >$ [99]:

$$\begin{aligned}\frac{\partial \rho'_{i'j'}}{\partial t} =& \frac{1}{i\hbar}\sum_{k'}\left[(H^\mu_{i'k'} + H^N_{i'k'})\rho'_{k'j'} - \rho'_{i'k'}(H^\mu_{j'k'} + H^N_{j'k'})^*\right] \\ &+ \frac{E'_{i'} - E'_{j'}}{i\hbar}\rho'_{i'j'} - \frac{\Gamma_{i'} + \Gamma_{j'}}{2}\rho'_{i'j'}\end{aligned} \tag{4.18}$$

After a two-level approximation, the equation resembles the optical Bloch equation except for the tunneling and noise terms. To preserve this distinction, we will call Eq. 4.18 the "stochastic Bloch equation".

The stochastic Bloch equation is expressed in terms of the time-dependent metastable states of a current-biased Josephson junction. It can be used to analyze junction

behavior under realistic conditions where low frequency noise, dissipation due to bias leads, and tunneling are the significant mechanisms of decoherence. Once I solve Eq. 4.18, I can compute the total escape rate Γ a function of bias current I_b

$$\Gamma = \left\langle \frac{\sum_{i'} \Gamma_{i'} \rho'_{i'i'}}{\sum_{i'} \rho'_{i'i'}} \right\rangle \tag{4.19}$$

Here $\rho'_{i'i'}$ denote the probability of finding the qubit in $|i' >$, and the bracket $\langle\rangle$ denotes a time average. Since most microwave spectroscopy experiments are done under slow ramp conditions, I can take the average over an infinite time interval.

I can calculate the density matrix ρ' for no microwave power ($I_1 = 0$) and small applied microwave power $I_1 \neq 0$, then find the escape rates under both conditions using Eq. 4.19. To compare with experimental data, we can compute the enhancement of escape rate

$$\Delta = \frac{\Gamma(I_1 \neq 0) - \Gamma(I_1 = 0)}{\Gamma(I_1 = 0)} \tag{4.20}$$

For simplicity from this point on, I drop the prime on the state indices as all the states are in the time-dependent basis.

4.3 Decoherence due to noise

For most of my work, I used spectroscopy to characterize decoherence in the system by looking at the resonance width. Although one can look at the behavior of the system in the time domain (such as Rabi oscillations) to understand decoherence, the spectroscopy method provides a simple way to quantify decoherence and it can be applied in cases where the time-domain method is too difficult to use.

4.3.1 Two-level approximation

Equation 4.18 can be solved numerically for a multi-level system. However, analysis of Eq. 4.18 using a two-level approximation already yields interesting results. For a two-level system with small current noise, the unitary matrix N can be approximated as

$$N = \begin{bmatrix} 1 & \alpha I_n(t) \\ -\alpha I_n(t) & 1 \end{bmatrix} \tag{4.21}$$

where $\alpha = \Phi_0 < 0|\hat{\gamma}|1 > /h\omega_0$, and $\omega_0 = (E_1 - E_0)/\hbar$ with $E_1 - E_0$ being the $|0>$ to $|1>$ energy level spacing for the qubit.

Using Eqs. 4.16 and 4.21, I can rewrite Eq. 4.18 for a two-level system, obtaining:

$$\frac{\partial \rho'_{00}}{\partial t} = iF(t)x'_- + \alpha \dot{I}_n x'_+ + \Gamma_{10}\rho'_{11} - \Gamma_0 \rho'_{00} \tag{4.22}$$

$$\frac{\partial \rho'_{11}}{\partial t} = -iF(t)x'_- - \alpha \dot{I}_n x'_+ - \Gamma_{10}\rho'_{11} - \Gamma_1 \rho'_{11} \tag{4.23}$$

$$\frac{\partial \rho'_{01}}{\partial t} = i\left[\omega_0 + \delta\omega(t)\right]\rho'_{01} + \left[iF(t) + \alpha \dot{I}_n\right] x'_z - X_{01}\rho'_{01} \tag{4.24}$$

$$\frac{\partial \rho'_{10}}{\partial t} = -i\left[\omega_0 + \delta\omega(t)\right]\rho'_{10} + \left[-iF(t) + \alpha \dot{I}_n\right] x'_z - X_{01}\rho'_{10} \tag{4.25}$$

where the constant Γ_{10} is the relaxation rate from $|1>$ to $|0>$, $X_{01} = (\Gamma_{10} + \Gamma_1 + \Gamma_0)/2$, $x'_\pm = \rho'_{10} \pm \rho'_{01}$, $x'_z = \rho'_{11} - \rho'_{00}$, $F(t) = \Omega\cos(\omega_1 t)$, $\Omega = \Phi_0 < 0|\hat{\gamma}|1 > I_1/h$ is the bare Rabi angular frequency, ω_1 and I_1 are the microwave angular frequency and amplitude respectively, and

$$\delta\omega(t) = \frac{1}{\hbar}\frac{\partial(E_1 - E0)}{\partial I_b} I_n(t) \tag{4.26}$$

is the $|0>$ to $|1>$ level spacing fluctuation due to current noise.

Each term in Eqs. 4.22-4.25 can be associated with a physical meaning. Terms containing $F(t)$ can be interpreted as microwave pumping, since they reflect the effect of off-diagonal elements on the evolution of the diagonal elements of the density

matrix, and vice versa. Similarly, terms containing $\alpha\dot{I}_n(t)$ cause noise induced inter-level transitions. The two terms $\Gamma_1\rho'_{11}$ and $\Gamma_0\rho'_{00}$ describe the effect of population decrease due to tunneling. Both relaxation and tunneling can lead to decoherence, which is described by the two terms containing X_{01}. Finally, due to current noise the level spacing will fluctuate. The effect of this time-dependent level spacing on free evolution is captured by terms containing $\omega_0+\delta\omega(t)$. We also note that the equations for the diagonal terms resemble the form of the master equation used in Chapter 3 to discuss the relaxation process. The difference here is that the microwave pumping and the noise-induced transitions are interconnected to the off-diagonal terms, while in the master equation the two terms can be written as a product of some rates and the diagonal terms themselves. The equations for the off-diagonal terms are critical for understanding both decoherence and coherent processes in the system.

While Eqs. 4.22-4.25 can be solved numerically, we can gain insight by obtaining analytic results under certain idealized conditions. To proceed, we consider the case where the tunneling rates Γ_1 and Γ_0 are much smaller than the energy relaxation rate Γ_{10}. In this limit $\rho'_{11}+\rho'_{00}=1$ and Eqs. 4.22-4.25 take the exact form of the optical Bloch equation [100], except for the noise terms. In order to distinguish the effects of the $\delta\omega(t)$ term from the $\alpha\dot{I}_n$ term, we examine their effects separately.

4.3.2 Transitions due to noise

To understand the $\alpha\dot{I}_n$ term, I set $\delta\omega(t)=0$. Transforming Eqs. 4.22-4.25 to the Fourier domain, one can show that the $\alpha\dot{I}_n x'_+$ term is equal to $\Gamma_+ x'_z$ (see Appendix D), where Γ_+, as we will see later, can be interpreted as a transition rate and is given by,

$$\Gamma_+ = \alpha^2 \int_0^\infty S_I(\omega/2\pi)\omega^2 \frac{\Gamma_-(\omega_0^2+\omega^2+\Gamma_-^2/4)}{(\omega_0^2-\omega^2+\Gamma_-^2/4)^2+\omega^2\Gamma_-^2}\,\frac{d\omega}{2\pi} \tag{4.27}$$

Similarly, we can show that $\alpha \dot{I}_n x'_z$ is equal to $\Gamma_+ x'_+$. We then rewrite Eqs. 4.22-4.25 as

$$\frac{\partial \rho'_{00}}{\partial t} = iF(t)x'_- + \Gamma_+ x'_z + \Gamma_{10}\rho'_{11} \tag{4.28}$$

$$\frac{\partial \rho'_{11}}{\partial t} = -iF(t)x'_- - \Gamma_+ x'_z - \Gamma_{10}\rho'_{11} \tag{4.29}$$

$$\frac{\partial \rho'_{01}}{\partial t} = i\omega_0 \rho'_{01} + iF(t)x'_z - \Gamma_+ x'_+ - X_{01}\rho'_{01} \tag{4.30}$$

$$\frac{\partial \rho'_{10}}{\partial t} = -i\omega_0 \rho'_{10} - iF(t)x'_z - \Gamma_+ x'_+ - X_{01}\rho'_{01} \tag{4.31}$$

From the above equations we see that Γ_+ is a rate for inter-level transitions. Setting $F(t) = 0$ and solving the above equation, one can find the time average of ρ'_{11} is given by

$$< \rho'_{11} >= \frac{1 + x'_z}{2} = \frac{\Gamma_+}{\Gamma_{10} + 2\Gamma_+} \tag{4.32}$$

Indeed, Γ_+ is exactly the thermal-noise-induced transition rate W^t_{10} introduced in Chapter 3. At that time we calculated W^t_{10} for an ohmic environment. From Eq. 4.27, we can now calculate this rate for an arbitrary dissipation environment with a known noise spectral density $S_I(\omega/2\pi)$. From Eq. 4.27 we see that low frequency components of $S_I(\omega/2\pi)$ do not contribute significantly to Γ_+ unless $S_I(\omega/2\pi)$ diverges faster than $1/\omega^2$. If the main contribution to Γ_+ is from noise around ω_0 such as in the ohmic damping case, then Eq. 4.27 reduces to

$$\Gamma_+ = \frac{S_I(\omega_0/2\pi)}{8e^2} | < 0|\gamma|1 > |^2 = \frac{\hbar\omega_0}{2Re^2} \frac{| < i|\gamma|j > |^2}{\exp(\hbar\omega_0/k_B T) - 1} \tag{4.33}$$

where $1/R$ is the real part of the admittance $Y(\omega)$ at ω_0 seen by the junction. Once Γ_+ is obtained, one can use the detailed balance condition to deduce the relaxation rate Γ_{10} by forcing $< \rho'_{11} >$ to obey the Boltzmann distribution. If $|0>$ and $|1>$ are nearly harmonic states, one finds $\Gamma_{10} = 1/RC$.

The effect of $\alpha\dot{I}_n$ is to induce inter-level transitions, which can also be studied using the master equation for the diagonal elements as shown in Chapter 3.

4.3.3 Decoherence due to low frequency noise

To understand the effect of the $\delta\omega(t)$ term, one has to consider the dynamics of the complete density matrix including the off-diagonal elements.

To proceed, I set $\alpha\dot{I}_n = 0$. Using the rotating wave approximation [100], I find that Eqs. 4.28-4.31 yield an equation (Eq. E-1 in Appendix E) for the Fourier transform of $(e^{-i\omega_1 t}\rho'_{01} - e^{i\omega_1 t}\rho'_{10})/2i$. Solving Eq. E-1, I obtain (see Appendix E)

$$< \rho'_{11} >= \frac{\Omega^2/2}{\Omega^2 + (1+A)\Gamma_{10}^2/2 + (2-B)\varepsilon^2} \tag{4.34}$$

where $\varepsilon = \omega_0 - \omega_1$ is the detuning, $S_d(\omega/2\pi) = \left[\frac{1}{\hbar}\frac{\partial(E_1-E_0)}{\partial I_b}\right]^2 S_I(\omega/2\pi)$ is the spectral density of $\delta\omega(t)$, and

$$A = \int_0^\infty \frac{S_d(\omega/2\pi)}{\omega^2 + \Gamma_{10}^2/4}\,\frac{d\omega}{2\pi} \tag{4.35}$$

$$B = \int_0^\infty \mathrm{Re}[G(\omega)]\,\frac{d\omega}{2\pi} \tag{4.36}$$

where

$$\begin{aligned} G(\omega) =& F(\omega)\left[2 + \frac{1}{1/2 + i\omega/\Gamma_{10}}\right] \\ & - \frac{F(\omega)\int_0^\infty S_d \mathrm{Re}[F(\omega)]\,\frac{d\omega}{2\pi}}{1/2 + \int_0^\infty S_d \mathrm{Re}[F(\omega)/2 + 1/(1/2 + i\omega/\Gamma_{10})]\,\frac{d\omega}{2\pi}} \end{aligned} \tag{4.37}$$

and

$$F(\omega) = \frac{\frac{1}{\Gamma_{10}/2} + \frac{1}{i\omega+\Gamma_{10}/2}}{i\omega + \Gamma_{10}/2 + \frac{\Omega^2}{i\omega+\Gamma_{10}} + \frac{\varepsilon^2}{i\omega+\Gamma_{10}/2}} \tag{4.38}$$

From the form of Eq. 4.34 we conclude that the $\delta\omega(t)$ term results in resonance broadening.

Setting $\Omega = 0$, we find $\rho'_{11}|_{I_1=0} = 0$, and the escape rate enhancement under microwaves will be

$$\begin{aligned}\Delta &= \frac{<\rho'_{11}\Gamma_1 + \rho'_{00}\Gamma_0>|_{I_1\neq 0} - <\rho'_{11}\Gamma_1 + \rho'_{00}\Gamma_0>|_{I_1=0}}{<\rho'_{11}\Gamma_1 + \rho'_{00}\Gamma_0>|_{I_1=0}} \\ &\approx \frac{\Gamma_1 - \Gamma_0}{\Gamma_0} <\rho'_{11}> \end{aligned} \tag{4.39}$$

The approximation holds for small current noise, where we can ignore the time dependence of Γ_1 and Γ_0 and replace $<\rho'_{ii}\Gamma_i>$ by $<\rho'_{ii}>\Gamma_i$. Equation 4.39 shows that the escape rate enhancement is determined by $<\rho'_{11}>$ since, for a reasonably sharp resonance, the ratio of Γ_1 to Γ_0 will be nearly constant in the neighborhood of the resonance.

We now define the spectroscopic coherence time T_2^* to be the inverse of the half-width at half maximum of the resonance. Since, from Eqs. 4.35-4.38, B generally depends on the detuning ε in a complicated way, it is difficult to find a general analytic expression for T_2^*. However, if $S_d(\omega/2\pi)$ has a constant value S_0 below some cutoff frequency $f_c \gg \Gamma_{10}/2\pi$, we find

$$A = \frac{S_0}{2\Gamma_{10}} \tag{4.40}$$

$$B = \frac{S_0/\Gamma_{10}}{1 + S_0/2\Gamma_{10}} \tag{4.41}$$

and

$$\frac{1}{T_2^*} = \frac{\Gamma_{10}}{2}\sqrt{\frac{1+A}{1-B/2}} = \frac{\Gamma_{10}}{2} + \frac{S_0}{4} \tag{4.42}$$

From Eq. 4.42 we see that the decoherence rate is just that due to dissipation ($\Gamma_{10}/2$) plus an additional $S_0/4$ due to current noise. This result reproduces those found

using the Bloch-Redfield approximation [97, 98] or by simply considering the mean squared phase noise [101]. Therefore, in this case the spectroscopic coherence time T_2^* is exactly the same as the phase coherence time T_2.

In the opposite limit $f_c \ll \Gamma_{10}/2\pi$, we find

$$A = \frac{4S_0 f_c}{\Gamma_{10}^2} \tag{4.43}$$

$$B = \frac{16S_0 f_c}{2S_0 f_c + \Gamma_{10}^2/2 + 2\varepsilon^2} \tag{4.44}$$

and thus

$$\frac{1}{T_2^*} = \left[\frac{1}{2}S_0 f_c + \frac{\sqrt{80(S_0 f_c)^2 + 8S_0 f_c \Gamma_{10}^2 + \Gamma_{10}^4}}{4}\right]^{1/2} \tag{4.45}$$

Equation 4.45 implies that the resonance broadens due to both dissipation and the rms current noise. For $S_0 f_c \gg \Gamma_{10}^2$, Eq. 4.45 reduces to:

$$\frac{1}{T_2^*} = 1.65\sqrt{S_0 f_c} = 1.65\left|\frac{1}{\hbar}\frac{\partial(E_1 - E_0)}{\partial I_b}\right|\sigma_I \tag{4.46}$$

where $\sigma_I = \sqrt{S_I f_c}$ is the total rms current noise.

The dependence of resonance width on the rms current noise is not surprising. In the case of slow fluctuations, for each repeated measurement of the system, there will be a nearly constant but different noise current, which will cause the transition to occur at a slightly different bias current each time. We also note that it is inappropriate in this limit to use the mean squared phase noise to characterize the coherence, since phase correlation has been completely destroyed on a time scale that is much smaller than $1/f_c$ due to a short T_1. Therefore Eq. 4.45 cannot be interpreted as a dephasing rate $1/T_2$; instead, it should be considered as a spectroscopic coherence time T_2^* that characterizes decoherence due to dissipation and noise. Since this spectroscopic coherence time includes the effect of the entire noise spectrum, this sets a lower bound for the coherence time (T_2) of the system. In

principle T_2 could be greater than T_2^* if a different measurement technique is used, such as a spin-echo.

If the noise spectrum is such that neither of the two limits discussed above is valid, then there is generally no simple analytic expression for the resonance width. Nevertheless, Eq. 4.34 can still be evaluated numerically to get the resonance shape.

From the above analytical results obtained under the two-level approximation, we see noise can induce inter-level transitions as well as decoherence. While the inter-level transition effect can be described by a transition rate, decoherence induced by noise depends on the noise spectral density. For high frequency noise, this effect can be captured by a dephasing rate, while for low frequency noise the total rms current noise contributes to resonance broadening and one cannot use a dephasing rate to describe the broadening.

For a real system, higher levels can be populated and there can be significant decoherence due to quantum tunneling [102]. For this general case we must include all the relevant levels and take tunneling into account. This can be done by performing a numerical simulation of Eq. 4.18 and computing the escape rate and enhancement according to Eqs. 4.19 and 4.20. The simulation results and comparison with experimental data will be discussed in Chapter 7.

4.4 Time-domain analysis of the Bloch equation

So far, I have discussed the long-time behavior of the density matrix in the context of spectroscopy. Here I want to study the short-time behavior of the density matrix where coherence is preserved.

4.4.1 Temporal behavior

As discussed above, decoherence due to high frequency noise can be described by a dephasing rate, and the spectroscopic coherence time T_2^* is equal to the phase

coherence time T_2. In the case of high frequency noise, we can rewrite Eqs. 4.28-4.31 as

$$\frac{\partial \rho'_{00}}{\partial t} = i\Omega \cos(\omega_1 t)(\rho'_{10} - \rho'_{01}) + \rho'_{11}/T_1 \tag{4.47}$$

$$\frac{\partial \rho'_{11}}{\partial t} = -i\Omega \cos(\omega_1 t)(\rho'_{10} - \rho'_{01}) - \rho'_{11}/T_1 \tag{4.48}$$

$$\frac{\partial \rho'_{01}}{\partial t} = i\omega_0 \rho'_{01} + i\Omega \cos(\omega_1 t)(\rho'_{11} - \rho'_{00}) - \rho'_{01}/T_2 \tag{4.49}$$

$$\frac{\partial \rho'_{10}}{\partial t} = -i\omega_0 \rho'_{01} - i\Omega \cos(\omega_1 t)(\rho'_{11} - \rho'_{00}) - \rho'_{10}/T_2 \tag{4.50}$$

where $\Omega = \Phi_0 < 0|\hat{\gamma}|1 > I_1/h$ is the bare Rabi frequency. In obtaining the above equations, I have made two assumptions. First I have assumed the temperature is low enough that the thermal rate Γ_+ is negligible compared to the relaxation rate $1/T_1$. Second I have assumed tunneling rates are also small compared to $1/T_1$.[3] Notice I have replaced Γ_{10} by $1/T_1$, and include the decoherence effect due to noise via $1/T_2$, where T_2 is the same as the spectroscopic coherence time T_2^* as given by Eq. 4.42.

Equations 4.47-4.50 imply that the dynamics of the system in this limit is identical to that of a two-level system in atomic physics that can be described by the optical Bloch equation [100]. The five relevant parameters in this description are: the level spacing ω_0, the microwave frequency ω_1, the bare Rabi frequency Ω, the relaxation time T_1 and the coherence time T_2.

Analogy to the Bloch equation

In order to solve Eqs. 4.47-4.48, I make an analogy between the optical Bloch equation and the original Bloch equation. When the microwave drive frequency ω_1 is

[3]It is straightforward to include decoherence due to tunneling by adding $(\Gamma_0 + \Gamma_1)/2$ to $1/T_2$, and adding $-\Gamma_0 \rho'_{00}$ and $-\Gamma_1 \rho'_{11}$ to the equations for ρ'_{00} and ρ'_{11} to account for the population changes.

close to the level spacing ω_0, the system will be forced to rotate in the same direction as the applied microwave drive, while the counter rotation component is negligible. Therefore we can use the rotating wave approximation [100] to simplify Eqs. 4.47-4.50. These equations can be rewritten as,

$$\dot{u} = \varepsilon v - u/T_2 \tag{4.51}$$

$$\dot{v} = -\varepsilon u + \Omega w - v/T_2 \tag{4.52}$$

$$\dot{w} = -\Omega v - (w - w_0)/T_1 \tag{4.53}$$

where $\varepsilon = \omega_0 - \omega_1$ is the detuning, $w_0 = -1/2$, and u, v and w are related to the density matrix by

$$u = \frac{e^{-i\omega_1 t}\rho'_{01} + e^{i\omega_1 t}\rho'_{10}}{2} \tag{4.54}$$

$$v = \frac{e^{-i\omega_1 t}\rho'_{01} - e^{i\omega_1 t}\rho'_{10}}{2i} \tag{4.55}$$

$$w = \frac{\rho'_{11} - \rho'_{00}}{2} \tag{4.56}$$

Equations 4.51-4.53 are exactly the original Bloch equations for the motion of a magnetic moment moving in a combination of a static magnetic field in the z-direction and a transverse rotating field subject to relaxations in all three directions (see Fig. 4.4).

For comparison, the equation of motion for a magnetic moment $\vec{m}$ in the laboratory frame is

$$\frac{d\vec{m}}{dt} = \gamma_0 \vec{m} \times \vec{B} - \hat{R} \cdot (\vec{m} - \vec{m}_0) \tag{4.57}$$

where γ_0 is the gyromagnetic ratio, $\vec{m}_0$ is the equilibrium value for $\vec{m}$, and $\vec{B}$ is the total field given by $\vec{B} = B_1 \cos(\omega_1 t)\hat{i} - B_1 \sin(\omega_1 t)\hat{j} + B_0 \hat{k}$, and $\hat{R}$ is the relaxation tensor with $R_{11} = R_{22} = 1/T_2$, $R_{33} = 1/T_1$ and zero for all other elements.

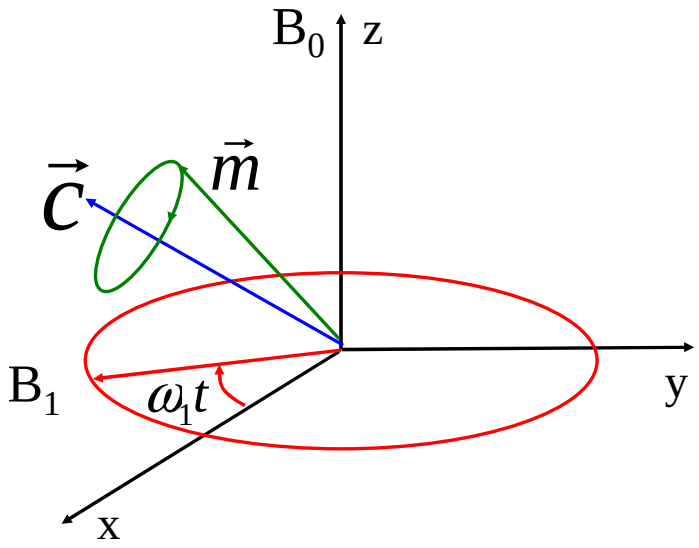

Figure 4.4: A pictorial description of the Bloch equation. In the laboratory frame, the moment rotates around the direction of the total magnetic field, which is constantly changing. However in the rotating frame, the moment rotates around a fixed axis $\vec{c}$. When $\omega_0 = \omega_1$, i.e. on resonance, $\vec{c}$ is the x-axis in the rotating frame. In the absence of relaxation, the magnitude of the moment will remain unchanged, hence the motion of the moment will be constrained on a sphere i.e. the Bloch sphere.

By introducing a frame that is rotating with the transverse magnetic field, one can show that in this frame the magnetic moment $\vec{m}'$ rotates around a fixed axis $\vec{c} = \Omega\hat{i} + (\omega_0 - \omega_1)\hat{k}$, where $\Omega = \gamma_0 B_1$ and $\omega_0 = \gamma_0 B_0$. Therefore the variables u, v and w introduced above are analogous to the x, y and z components of the magnetic moment in the rotating frame. In this picture, the dissipation time T_1 and coherence time T_2 correspond to the longitudinal and transverse relaxation times of a magnetic moment.

Steady state solution

By letting $\dot{u} = \dot{v} = \dot{w} = 0$, we can find the steady solution of Eqs. 4.51-4.53

$$\rho_{11}'^{eq} = w_{eq} - w_0 = \frac{\Omega^2 T_1 T_2/2}{1 + T_2^2(\omega_0 - \omega_1)^2 + \Omega^2 T_1 T_2} \tag{4.58}$$

This is the long-time behavior of the density matrix, and one sees the system is in a mixed state. This is exactly what spectroscopy probes. If we plot $\rho_{11}'^{eq}$ as a function of ω_0 with ω_1 held constant, we can deduce the coherence time from the resonance shape. From the above equation, the half width at half maximum (HWHM) of the resonance is

$$\text{HWHM} = \frac{1}{T_2}\sqrt{1 + \Omega^2 T_1 T_2} \tag{4.59}$$

For small microwave power such that $\Omega^2 T_1 T_2 \ll 1$, we have the half width at half maximum is the inverse of T_2. I note that when the power increases the resonance will broaden accordingly.

The amplitude of the resonance increases with applied microwave power but saturates at 1/2 for powers such that $\Omega^2 T_1 T_2 \gg 1$.

No relaxation

If the relaxation and decoherence processes are very slow, then on a short time scale I can ignore the terms involving $1/T_1$ and $1/T_2$. Assuming that the microwave power is switched on at $t = 0$ and $\rho'_{11}(0) = 0$ and $\rho'_{00}(0) = 1$, I can then solve the Bloch equation exactly to find

$$\rho'_{11}(t) = \frac{\Omega^2}{2\Omega'^2}\left[1 - \cos(\Omega' t)\right] \tag{4.60}$$

where $\Omega' = \sqrt{\Omega^2 + (\omega_0 - \omega_1)^2}$ is the Rabi oscillation angular frequency. From Eq. 4.60, we see ρ'_{11} oscillates between 0 and Ω^2/Ω'^2 with a frequency Ω'. The minimum Rabi frequency is determined by the microwave power. Detuning causes an increase in the Rabi frequency, with a corresponding decrease in the oscillation amplitude. In order to see a reasonable oscillation amplitude, $\omega_1 \approx \omega_0$ is required.

On resonance

For a real system, T_1 and T_2 are finite. Most interesting experiments are also at near-resonance, i.e. $\omega_1 \approx \omega_0$. An exact solution in this case can be obtained:

$$\rho'_{11}(t) = \rho'^{eq}_{11} - \rho'^{eq}_{11} e^{-t/T'}\left[\cos(\Omega' t) + \frac{\sin(\Omega' t)}{T'\Omega'}\right] \tag{4.61}$$

where $\rho'^{eq}_{11} = \frac{\Omega^2 T_1 T_2/2}{1+\Omega^2 T_1 T_2}$ is the equilibrium value, T' is related to T_1 and T_2 by

$$\frac{1}{T'} = \frac{1}{2T_1} + \frac{1}{2T_2} \tag{4.62}$$

and Ω' is the oscillation frequency, given by

$$\Omega' = \sqrt{\Omega^2 - (1/2T_1 - 1/2T_2)^2} \tag{4.63}$$

In the high power limit such that $\Omega T_1 >> 1$ and $\Omega T_2 >> 1$, we have $\Omega' = \Omega$, $\rho'^{eq}_{11} = 1/2$, and

$$\rho'_{11}(t) = \frac{1}{2} - \frac{1}{2}e^{-t/T'}\cos(\Omega t) \tag{4.64}$$

The behavior of this function is a decaying oscillatory curve, the oscillation period is the inverse of Ω, and the decay constant is determined by T'.

Figure 4.5 shows a few examples of the time dependence of ρ'_{11} for various microwave powers. For small powers, since $\Omega' < 1/T'$, ρ'_{11} does not have enough time to complete a cycle before it approaches the equilibrium value. In the high power limit, it behaves like an oscillatory function and furthermore the oscillation frequency increases as the power increases.

From the decaying behavior, I can get the time constant T', which depends on both T_1 and T_2. If T_1 can be determined by an independent method such as the population depletion technique, one can then obtain T_2 from T'. This T_2 should be exactly the same as the T_2^* determined from the half width at half maximum of the spectroscopy resonance in the case of high frequency noise. Of course, if low frequency noise is present then we expect $T_2^* < T_2$.

4.4.2 Power dependence

Besides looking at the long-time behavior and the short-time behavior, one can also choose to look at the behavior of the system on an intermediate time scale. This can be done by applying continuous microwave power or a long pulse while the level spacing is being ramped, as shown in Fig. 4.6.

In this case one can look at the behavior near the point where the frequency of the system matches the microwave frequency. For a sufficiently fast ramp, the system does not have time to settle to its equilibrium state at the resonance point. Clearly the behavior of ρ'_{11} will depend on how fast the ramp is compared to T_1 and T_2. Figure 4.7 shows the calculated behavior of ρ'_{11} for a system with $T_1 = T_2 = 100$ ns and a ramp speed such that ω_0 is changing at $-2\pi \cdot 0.6$ GHZ/μs under various

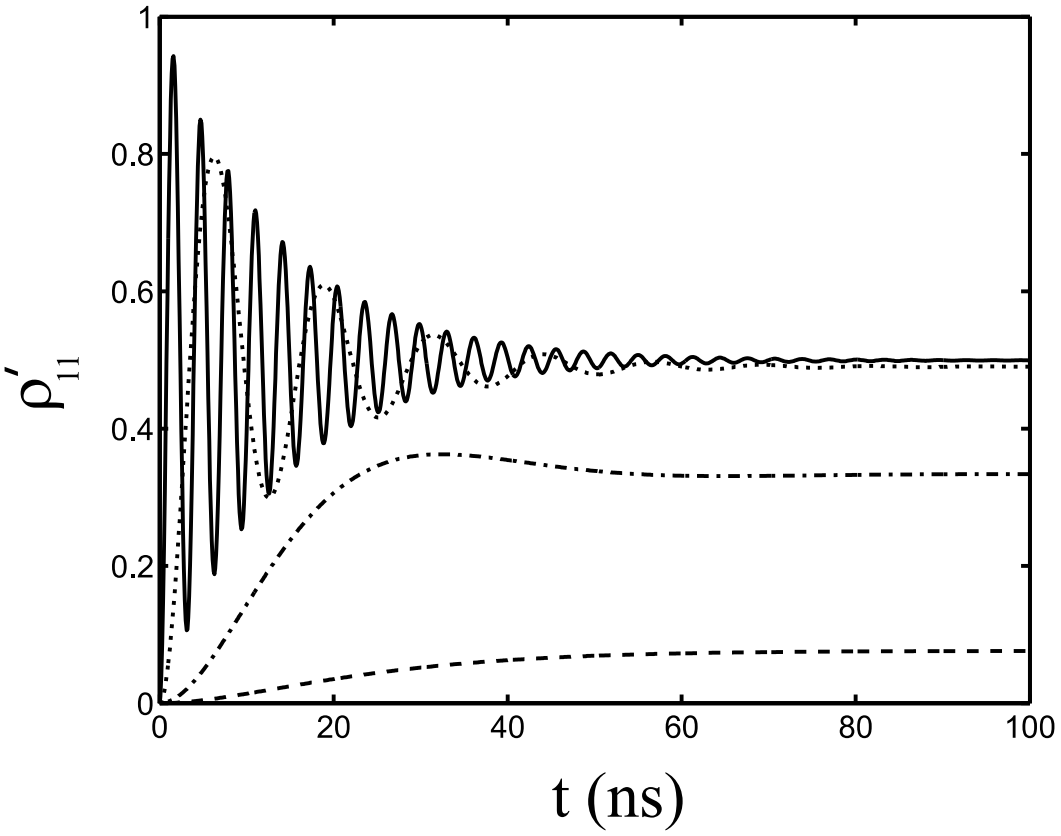

Figure 4.5: Theoretically predicted Rabi Oscillations for $T_1 = 10$ ns, $T_2 = 20$ ns and $\omega_0/2\pi = \omega_1/2\pi = 5.4$ GHz. Solid line for $\Omega = 2\times10^9$/s, dotted line for $\Omega = 5\times10^8$/s, dash-dotted line for $\Omega = 1 \times 10^8$/s, and dashed line for $\Omega = 3 \times 10^7$/s. Notice oscillations show up for high microwave powers only and the oscillation frequency increases with the power. The decay time T' in this case is about 13 ns.

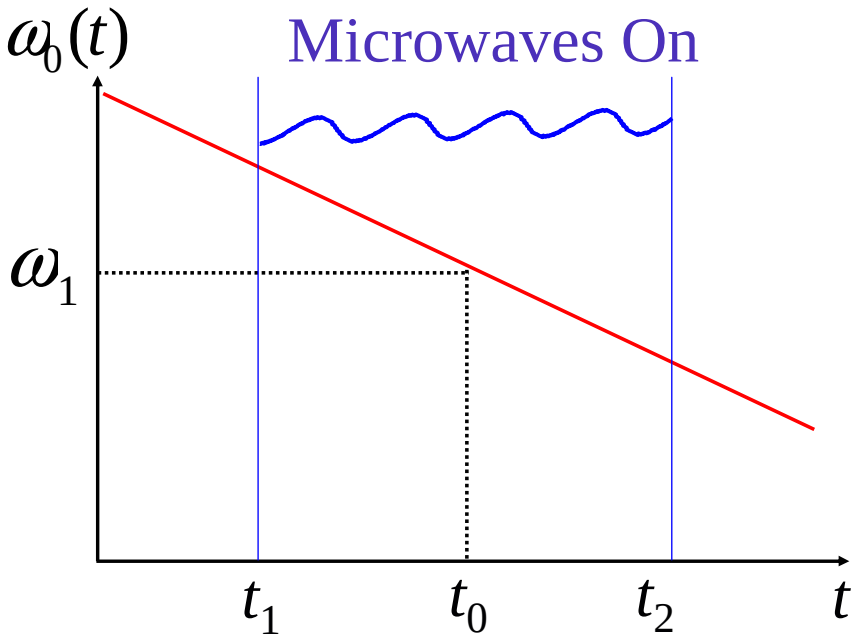

Figure 4.6: Schematic of Rabi oscillation experiment in the continuous sweep mode where the level spacing ω_0 is being ramped and the microwave frequency is kept at ω_1. Microwaves are turned on between t_1 and t_2, and at t_0 the system is in resonance with the drive. By adjusting the slope of the ramp, in principle this type of measurement can be used to reveal T_1 and T_2.

microwave powers.

The point marked by $t = 0$ is where the system is in resonance with the microwaves. One can see for small powers, ρ'_{11} starts to increase around $t = 0$ and oscillates near this resonance point before decaying with even faster and smaller oscillations. However, for larger powers, ρ'_{11} starts to increase before $t = 0$ and by the time the system is in resonance with microwaves, coherence has already been lost so no oscillation is observed.

It is also interesting to note that the maximum value of ρ'_{11} first increases with power, then starts to decrease for high powers. The maximum value of ρ'_{11} is plotted in Fig. 4.8 for $T_1 = 100$ ns and various T_2. Indeed for large T_2, ρ'_{11max} first increases with power, then decreases and eventually for high powers it settles to the equilibrium value 1/2. However for small T_2, the overshoot is not there. Simulations for $T_1 = 10$ ns do not show any overshoot behavior either. Therefore observation of this overshoot behavior can provide us information about T_1 and T_2.

4.4.3 The times probed by different methods

Table 4.1 summarizes the different times and methods to measure them.

From Table 4.1, we see that the times probed by the three methods are different when the system has low frequency noise. In the case of high frequency noise, there are just two independent quantities T_1 and T_2, and the three independent measurements can provide a consistency check. If no noise is present, decoherence will come solely from dissipation, and there is only one independent parameter, T_1.

4.5 Summary

In this chapter, I have derived a stochastic Bloch equation, which includes both dissipation and noise, to study decoherence in the Josephson junction qubit. The spectroscopic coherence time T_2^* provides a simple way to understand how dissi-

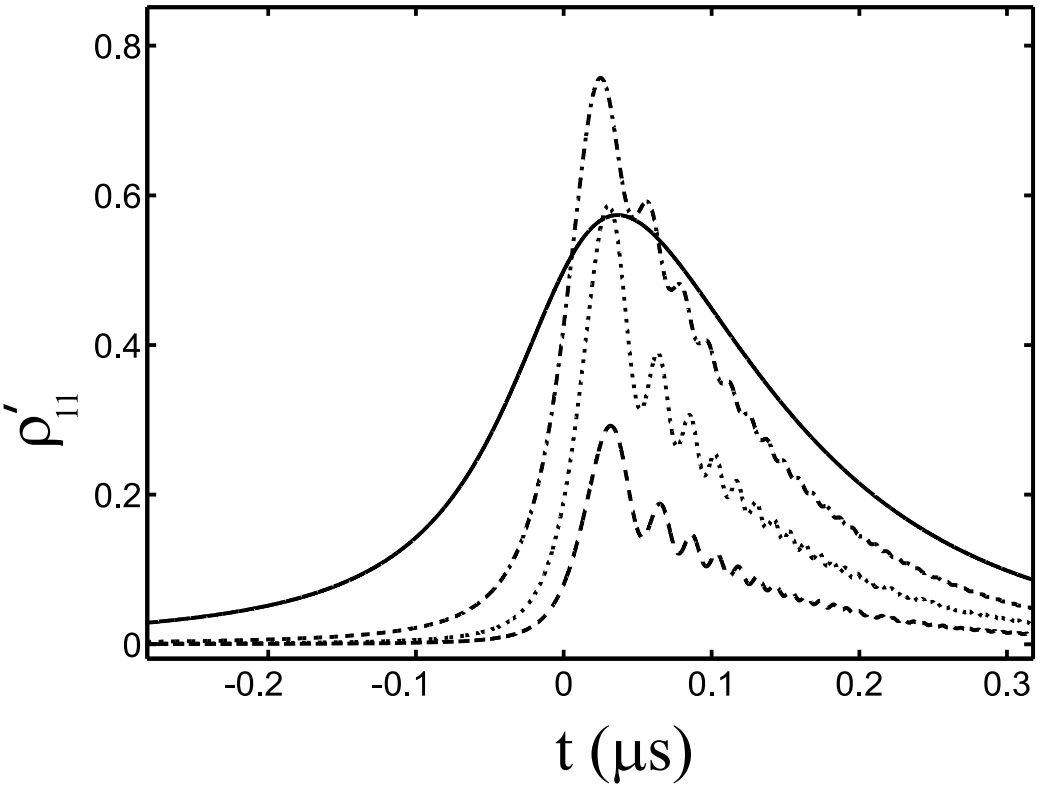

Figure 4.7: Calculated ρ'_{11} in the sweep mode for $\omega_1/2\pi = 5.4$ GHz, $T_1 = T_2 = 100$ ns and a ramp rate of $-2\pi \cdot 0.6$ GHZ/μs. Solid line for $\Omega = 3 \times 10^8$/s, dash-dotted line for $\Omega = 1 \times 10^8$/s, dotted line for $\Omega = 5 \times 10^7$/s, and dashed line for $\Omega = 3 \times 10^7$/s. Note the maximum value of ρ'_{11} first increases with power, then starts to decrease for high powers.

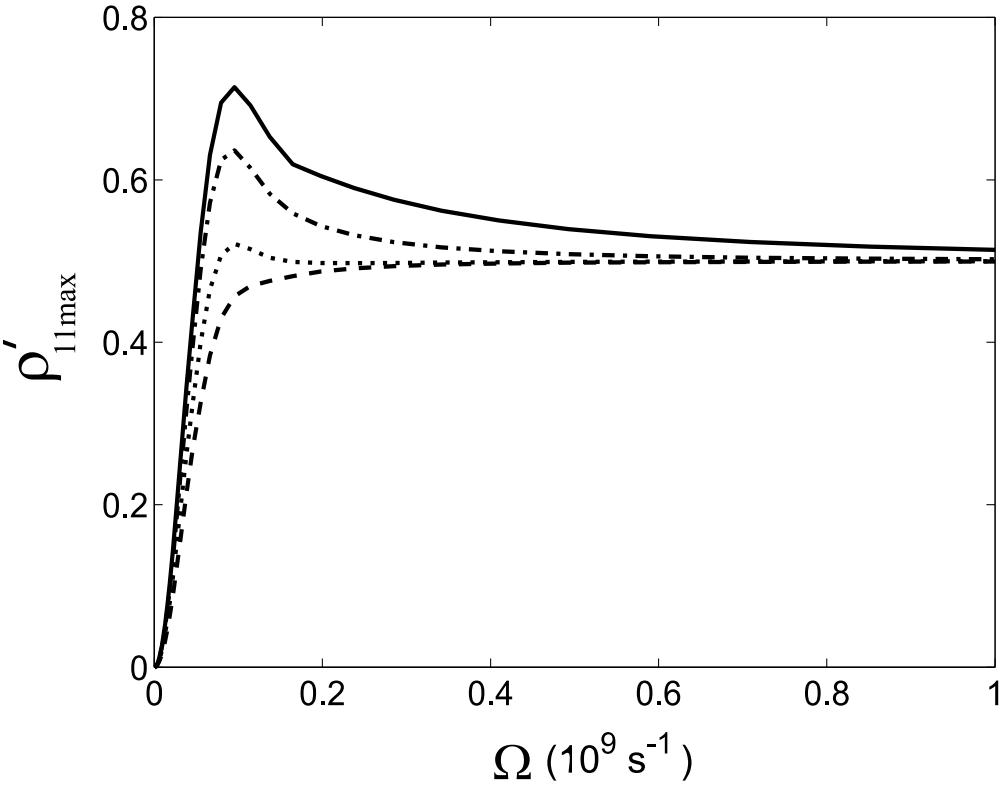

Figure 4.8: Calculated power dependence of the maximum ρ'_{11} in the continuous sweep mode for $\omega_1/2\pi = 5.4$ GHz, a ramp rate of $-2\pi \cdot 0.6$ GHZ/μs, $T_1 = 100$ ns and various T_2. Solid line for $T_2 = 100$ ns, dash-dotted line for $T_2 = 50$ ns, dotted line for $T_2 = 20$ ns, and dashed line for $T_2 = 10$ ns. The overshoot behavior is visible for large T_2, but completely disappears for $T_2 < 10$ ns. Note for large powers, ρ'_{11max} approaches 1/2.

Table 4.1: Times probed by different methods

Methods	Measured Quantity	Low frequency noise	High frequency noise	No noise
Level depletion	T_1	T_1	T_1	T_1
Spectroscopy	T_2^*	T_2^*	T_2	$2T_1$
Rabi oscillation	T'	-[a]	$1/(1/2T_1 + 1/2T_2)$	$4T_1/3$

[a]In the case of low frequency noise, it is not clear under what conditions the exponential decay can be observed.

pation and noise affect decoherence. For high frequency noise, the spectroscopic coherence time T_2^* reduces to the phase coherence time T_2, in agreement with previous work. However, for low frequency noise, T_2^* depends on both the rms current noise and T_1, and decoherence cannot be described by a dephasing rate. For high frequency noise, I have also used the optical Bloch equation to study the short-time behavior of the density matrix where coherence is maintained. Finally a comparison between the times obtained from the different methods was made.

Chapter 5

Designs of Qubits and Qubit Isolation

In order to achieve a long dissipation time T_1 and coherence time T_2, we need to engineer the electromagnetic environment for the Josephson junction. From Chapters 3 and 4, we know that the dissipation time T_1 is roughly the RC time constant, where R is the inverse of the real part of the admittance seen by the junction at the plasma frequency and C is the junction capacitance. Low frequency noise (i.e. the part of the spectrum below the frequency $1/2\pi T_1$) can cause decoherence, while high frequency noise is averaged out and its effect on decoherence is negligible. Therefore increasing R and reducing low frequency noise are the main concerns for our qubit design.

5.1 Resistively isolated Josephson junction

The first idea we tried was to use a large resistor to isolate a current-biased Josephson junction [64].

5.1.1 Basic idea

If we place large resistors R in series with the Josephson junction, as shown in Fig. 5.1, then these large resistors are in series with any lead resistance and also block current noise. The resistor becomes the shunt resistance for the junction at the

plasma frequency[1]. I note that the circuit in Fig. 5.1 is equivalent to the RCSJ model.

Due to the large resistance R, if we measure the voltage at the current supply (two-wire measurement), then the junction switching voltage will be in series with a large background signal from the bias current. Also the signal will be slow due to RC roll-offs. Therefore we used a second pair of leads that are also resistively isolated for voltage measurement (see Fig. 5.1)[2]. To increase the signal speed, we used a cold amplifier that consisted of a transformer and a dc SQUID to detect the switching voltage of the junction.

5.1.2 Experimental realization

To build the above circuit, we needed to fabricate a large resistor. The resistor needed to be very close to the junction so that at microwave frequencies it was not capacitively shunted by long leads. Since this large resistor would also carry a bias current for the junction, we also had to worry about Joule heating. Heating at low temperatures is problematic and electron "cooling fins" are needed to take the heat out.

Figure 5.2 shows a schematic of the resistors and their heat sinks used in our experiment. A photo of the patterns fabricated using photo-lithography are shown in Fig. 5.3. The resistor is made of 650 segments of 150 Ω NiCr resistors. Each segment is 14 μm long, 5 μm wide and 15 nm thick. The cooling fins are also made of NiCr but with a thickness of 0.6 μm, and are 1 mm long and 18 μm wide. The junction is fabricated in the middle.

The mechanisms behind thermal sinking of the thin-film NiCr resistors are explained in detail in Ref. [64]. Essentially the difficulty in effective cooling of the

[1]The rest of the bias lines acts like a 50 Ω impedance at such high frequencies.

[2]The actual shunt resistance for the junction is then the parallel of the resistance in the current leads and that in the voltage leads.

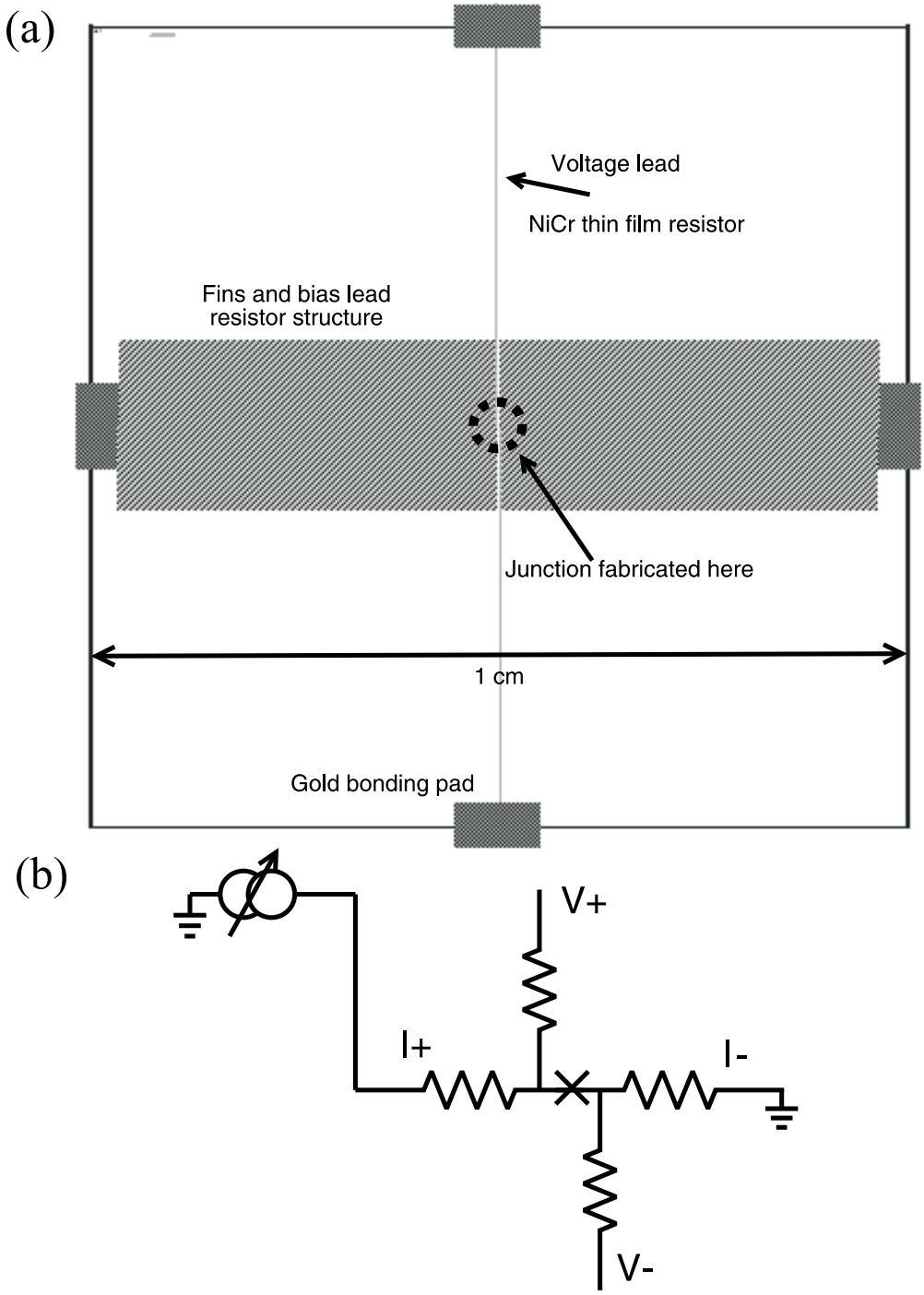

Figure 5.1: Schematic of a resistively isolated Josephson junction. (a) Chip layout. (b)Circuit schematic.

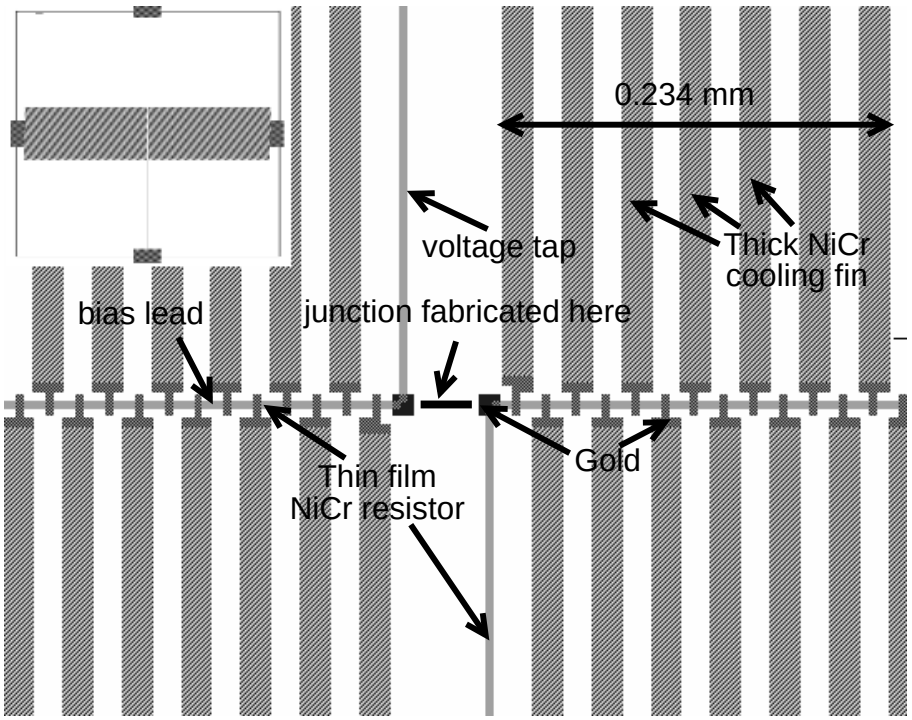

Figure 5.2: Design of a NiCr resistor and its heat sink.

electrons in a resistor at millikelvin temperatures is due to the fifth-power law that governs how electrons radiate heat via emissions of phonons [103, 104, 105, 106]. The result is that the electron temperature can be much higher than the phonon temperature when power is applied. However one can use a large volume of normal metal to reduce this thermal bottleneck between electrons and phonons. In the above design the large volume of the cooling fins bring the electron temperatures to around 50 mK if the phonons are at a temperature of 20 mK.

However the electrons in the thin-film NiCr resistor can be much hotter than the temperature of the electrons in the heat sink. This is because the electron-phonon thermalization process is slow in the resistor due to its tiny volume[3]. The only

[3]Because the electron temperature is around 100 mK, the phonons emitted by these hot electrons have a wavelength that is much larger than the thickness of the film (150 Å), therefore they cannot be confined in the film by reflection at the interface [105]. Thus the phonon temperatures in the film are the same as the substrate.

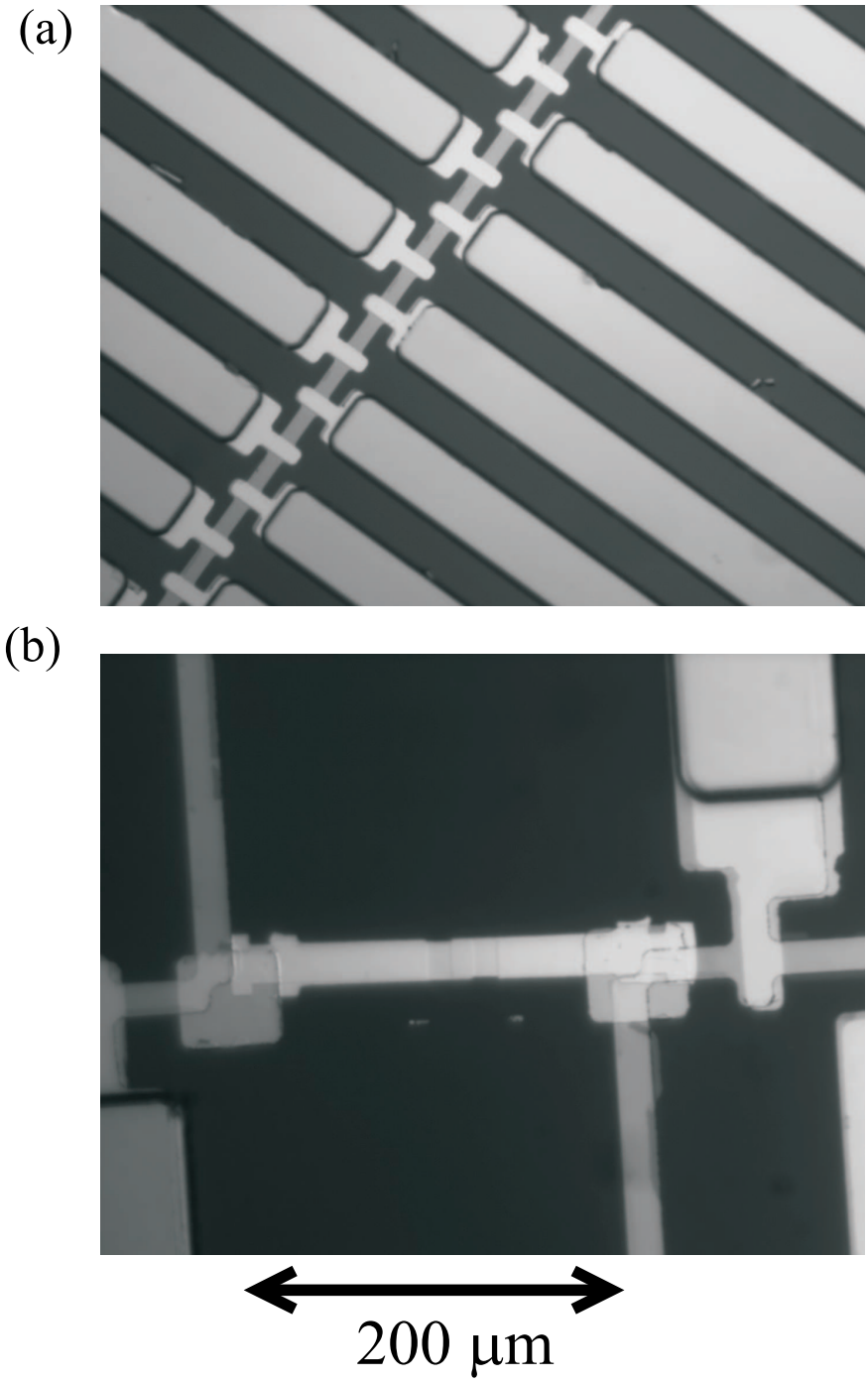

Figure 5.3: Photo of NiCr resistor and its heat sink. (a) NiCr cooling fins. (b) 20 μm $\times$ 5 μm Al/AlOx/Al junction.

effective thermalization process is electron diffusion. This depends on the electronic specific heat, electron scattering length and Fermi velocity. To proceed, we assume that in each segment of the resistor, the electron temperature at the two boundaries will be same as the electron temperature in the cooling fins, then one can calculate the temperature distribution along the segment. Analysis of this situation suggests that [64] the maximum electron temperature is given by

$$T_e^{max} \approx \left[T_b^2 + T_p^2\right]^{1/2} \tag{5.1}$$

where T_b is the electron temperature at the two boundaries, and $T_p = eIR_s/k_B$ is the temperature increase due to Joule heating, where R_s is the resistance of each segment. I note that T_p is essentially the potential energy drop for a single electron across the segment. This result is not surprising since it is just expressing conservation of energy for each individual electron. For $I = 1$ μA, we estimate $T_e^{max} \approx T_p = 140$ mK, which is much hotter than the base temperature of our refrigerator (20 mK).

Cold amplifier

To detect the switching voltage, we connected the V_+ and V_- leads to a transformer which was coupled to a dc SQUID. The primary of the transformer was made of copper, and the secondary of the transformer was made of a single turn of niobium foil that was connected to the input coil of a hysteretic dc SQUID. A signal of $\Phi_0/800$ would allow us to do single shot measurements of junction switching. Therefore a gain of larger than 3 in the transformer was required to boost the original signal (4 nA=400 μV/100 kΩ) to 12 nA given that the mutual inductance between the input coil and the dc SQUID loop is around 200 pH [107]. Unfortunately the transformer was not designed to allow efficient detection of the junction switching during our trial. However we could still use the two current leads to measure the voltage. To remove the large background signal due to the 100 kΩ isolation resistance, a

bridge circuit was used to cancel out the background signal. However, due to the capacitance in the leads ($\sim$ 1 nF), the rise time of the signal was about 200 μs, which limited our timing resolution to 20 μs[4]. This low resolution was acceptable as long as we used a slow ramp so that resonance width in time was much larger than the time resolution.

5.1.3 Advantages and disadvantages

The restively isolated Josephson junction qubit is attractive in principle due to its relative simplicity and broad-band isolation. The relaxation time T_1, according to the above design can be as large as 40 ns for a junction capacitance of 0.4 pF[5]. Because the isolation is broadband, decoherence due to noise is determined by the noise spectral density, which is very small for a 100 kΩ resistance.

The major disadvantage is the heating of the resistor. This causes the junction temperature to be close to the level spacing and makes it difficult to see quantum effects in the system. One cannot increase the junction capacitance without increasing the critical current of the junction. But large critical currents make the heating even worse. Therefore even with an isolation resistance of 100 kΩ, it is difficult to achieve much more than 40 ns for T_1.

In retrospect we also realized that the large area of the cooling fins will also give rise to a capacitance between each cooling fin and the copper plane where the chip is mounted. For a typical substrate thickness of 100 μm (sapphire substrate), this capacitance is about 16 fF. Analysis of the circuit with this capacitance included shows the isolation resistance is less than 500 Ω at 5 GHz. This suggests that the design will not work.

---

[4]The Blue amplifier designed by Cawthorne [108], which has a voltage noise of 100 nv/$\sqrt{\text{Hz}}$ and a bandwidth of 100 kHz, was used to amplify the voltage signal.

[5]This is for a 3 μm $\times$ 3 μm junction, although one can use a larger size, then the critical current will also increase, which leads to more heating.

We built a resistively isolated junction sample labeled as RJJ-Al in the rest of the thesis. Measurements on this sample are presented in Chapter 7.

5.2 LC isolated Josephson junction

5.2.1 Basic idea

Resistive isolation of the qubit from the environment is simple in principle, but suffers from excessive heating and difficulties in achieving isolation at high frequencies. One way to avoid this problem is to use nondissipative elements such as inductors and capacitors to block the noise from getting to the qubit.

The objective of isolation is to prevent noise (generated by dissipative elements) from reaching the junction. As far as relaxation is concerned, the blocking should occur around the plasma frequency of the junction. A large resistance will do the job, but it causes heating. To replace the resistor, one can use an inductance, since the impedance of a inductor increases with frequency. For example, the impedance of a 10 nH inductance is about 300 Ω at 5 GHz. Due to freezing of magnetic moments in ferrites at millikelvin temperatures, one cannot use large inductors that are made of ferrite cores. The maximum lumped inductance one can obtain is about 10 nH at 5 GHz given the vacuum permeability is 1 nH/mm.

In order to achieve further blocking of the noise, one can use an inductor-capacitor (LC) isolation network (see Fig. 5.4a). In this scheme, the resonance frequency of the LC circuit is well below the plasma frequency of the junction. Because of current division, external noise currents coming down the bias leads at high frequencies will be mainly shunted by the capacitance C_i. Therefore the junction is relatively isolated from the leads. Using the complex admittance shunted junction model (see Fig. 5.4b), we can convert the LC network to a complex admittance. We have

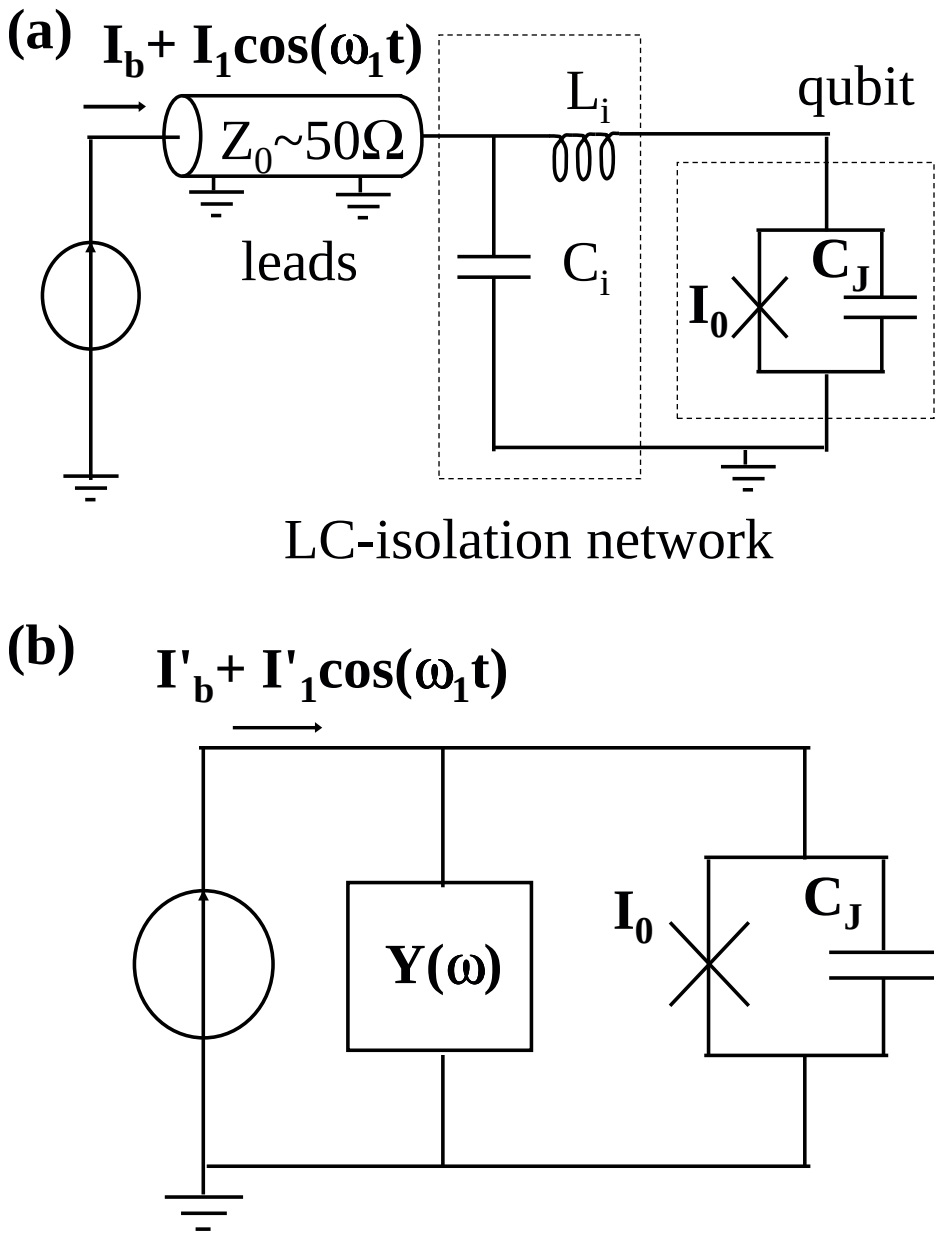

Figure 5.4: Circuit schematic of an LC isolated Josephson junction. (a) Circuit schematic. (b) Equivalent circuit. I'_b and I'_1 represent current sources in the equivalent circuit.

$$Y(\omega) = \frac{1}{jL_i\omega + \frac{R_L}{jR_LC_i\omega+1}} \tag{5.2}$$

where $R_L \approx 50\ \Omega$ (above 10 MHz) is the lead impedance from the top of the cryostat to the LC isolation network. Since relaxation is determined by the inverse of the real part of the admittance, one finds

$$R_{eff}(\omega) = \frac{1}{\mathrm{Re}[Y(\omega)]} = \frac{L_i^2\omega^2}{R_L} + R_L\left(1 - L_iC_i\omega^2\right)^2 \tag{5.3}$$

If L_iC_i is chosen such that $L_iC_i\omega_p^2 \gg 1$ and $(R_LC_i\omega_p)^2 \gg 1$, then the shunting resistance at the plasma frequency is given by

$$R_{eff}(\omega_p) \approx R_LL_i^2C_i^2\omega_p^4 \tag{5.4}$$

The above expression agrees with our intuitive understanding that the noise is blocked because of current division by the LC network, i.e. the lead resistance is stepped up by the LC transformer. Therefore in order to have a large shunt resistance, large L_i and C_i are preferred. In other words, the resonance frequency of the LC circuit should be made much smaller than the plasma frequency of the junction. For example, for $L_i = 10$ nH, $C_i = 10$ pF, $\omega_p = 5$ GHz and $R_L = 50\ \Omega$, one finds $R_{eff}(\omega_p) \approx 500$ kΩ, which leads to a relaxation time of 2 μs for a typical junction capacitance of 4 pF.

I note that the imaginary part of $Y(\omega)$ can be described by a shunt inductance $L_{eff}(\omega)$,

$$L_{eff}(\omega_p) = \frac{L_i^2\omega^2 + R_L^2(1 - L_iC_i\omega^2)^2}{\omega^2L - R_L^2C_i\omega^2(1 - L_iC_i\omega^2)} \tag{5.5}$$

At the plasma frequency this effective inductance is equal to $L_i \approx 10$ nH. Thus the effect of the complex part of $Y(\omega)$ is negligible compared to the junction inductance, which is in parallel and typically smaller than 1 nH.

I also note that in Eq. 5.3, if we let $C_i = 0$, then we have

$$R_{eff}(\omega) = R_L \left(\frac{L_i^2 \omega^2}{R_L^2} + 1 \right) \tag{5.6}$$

This RL network will also boost the shunt resistance when $L_i\omega >> R_L$, in which case, the large impedance due to the inductance provides reduction of the noise level.

In reality at high frequencies, the capacitance C_i always has some stray inductance L_s. Then C_i in the above equations should be replaced by $C_i/(1 - L_s C_i \omega^2)$. If L_s is so large that $L_s C_i \omega^2 >> 1$, then the effective shunt resistance at the plasma frequency will be given by

$$R_{eff}(\omega) = \frac{L_i^2 \omega^2}{R_L} + R_L \left(\frac{L_i}{L_s} \right)^2 \tag{5.7}$$

The second term in the above equation essentially represents the effect of an inductance divider.

5.2.2 Experimental realization

The experimental realization of the LC-isolated Josephson junction is relatively straightforward. The key thing is that the LC circuit should be adjacent to the junction so that the junction sees the LC circuit at microwave frequencies without any parasitic elements. We have tested this design on both Al and Nb junctions.

Surface mounted LC isolation circuit

We made Al junctions by double-angle evaporation (see below). Due to complications in making on-chip inductors[6] and capacitors, we choose to use surface-mounted

[6]Spiral geometry is required in order to make a 10 nH inductor with a short total electrical length, which requires via structures. Such multi-layer elements require an insulation layer (typically SiO_2), which complicates fabrication.

inductors (10 nH) [109] and capacitors (10 pF) [110] as shown in Fig. 5.5. The core of the inductor is alumina and the wires are wound from copper. The inductor contacts are made of lead/tin solder alloy with a slightly magnetic nickel buffer layer (although non-magnetic materials are preferred). The self resonance frequency of the inductor is above 8 GHz, so that in the frequency range 5 - 7 GHz, it can be treated as a inductor. The capacitor is made of multi-layer porcelain with copper barriers and non-magnetic solder contact pads [110]. The dielectric loss and temperature dependence of the capacitance should be negligible at 25 mK. The self resonance frequency of the capacitor is around 3 GHz, above which it becomes inductive. If we include a parasitic series inductance of 0.3 nH, we can use Eq. 5.7 to find that the effective resistance is around 57 k Ω at 5 GHz. This should give us a relaxation time of T_1 =230 ns. The series resistances in the inductor and the capacitor (both made from Cu) should be much lower than 0.1 Ω, and their effect on the effective R should be negligible.

After the junctions were fabricated, the L and C components were mounted on the gold contacts of the Al junction as shown in Fig. 5.5 using silver-filled epoxy [111]. The whole chip (with junctions already made) was cured at 80°C in air for 1.5 hours.

On-chip LC isolation circuit

We also used on-chip LC isolated Nb junctions to test this isolation scheme. The samples were fabricated by Hypres, Inc. [112] according to a CAD drawing we supplied. Two samples were tried, one with an on-chip inductance of 10 nH, the other with an 8 nH inductance. The circuit layout is shown in Fig. 5.6(a)-(b), where the square spirals are the inductor and the big squares in the middle are capacitors. The latter sample contains two identical LC isolated junctions that are 0.7 mm apart and connected by a loop containing two coupling capacitors. A photo of the LC isolated single-Nb-junction sample is shown in Fig. 5.6(c). A photo of the LC

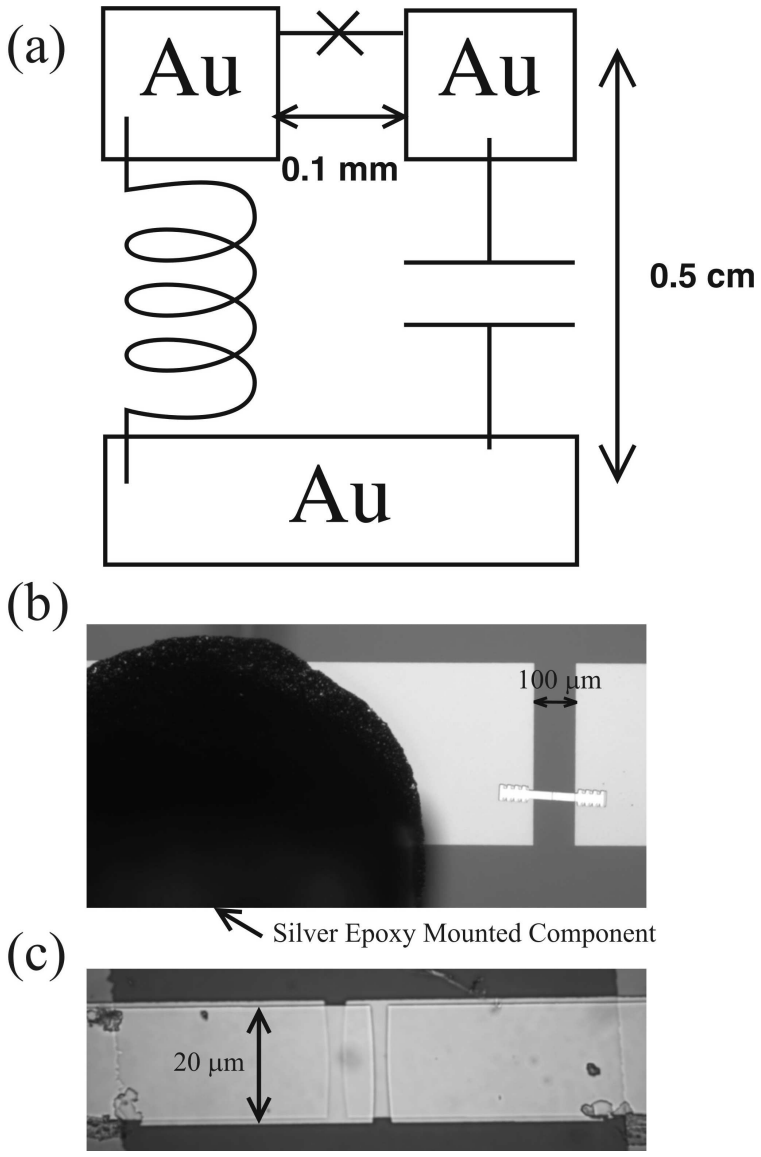

Figure 5.5: Sample LCJJ-Al. (a) A schematic of the LCJJ-Al sample. (b) A photo of the LCJJ-Al sample. (c) Close-up view of the Al/AlOx/Al junction overlap area.

isolated coupled-Nb-junction sample is shown in Fig. 5.7.

In order to be able to treat the inductance as a lumped element, we want the total electrical length of the inductor to be much less than a quarter wavelength at the junction plasma frequency. At 5 GHz, we estimate $\lambda/4 \approx 5$ mm in silicon as a result of its high dielectric constant ($\epsilon = 12$).

The inductor is made of a planar square spiral with an inner diameter d_{in}, outer diameter d_{out} and n turns. Using the formula in Ref. [113], the inductance is given by

$$L \approx 2.34\mu_0 \frac{n^2 d_{avg}}{1 + 2.75\rho} \tag{5.8}$$

where $d_{avg} = (d_{out} - d_{in})/2$ and $\rho = (d_{out} - d_{in})/(d_{out} + d_{in})$ is the filling factor. For the single-Nb-junction sample, the design has an inner diameter of 65 μm, an outer diameter of 120 μm, and 8 turns, which leads to an expected inductance of 10 nH. The total length of the inductance is 3 mm which is below $\lambda/4$ at 5 GHz. For sample LCJJ-Nb2, the outer diameter is 112 μm and there are 7 turns; thus the total inductance is 8 nH and the total length is 2.5 mm.

The stray capacitance across the inductor also needs to be considered. In the above design, the main stray capacitance is merely due to the overlap of the via lead with the coils on the bottom layer (see Fig. 5.6b). A rough estimate of this overlap (16 μm $\times$ 10 μm with a separation of 200 nm of SiO_2) leads to a stray capacitance of 30 fF. If I assume this capacitance is shunting the total inductance, the self resonance frequency is above 5 GHz. The actual self resonance frequency could be even higher due to the distributed nature of the stray capacitance.

One might also want to include a series resistance in the inductor to take into account eddy current losses in the copper ground plane on which the chip is mounted. A rough estimate using the transformer concept gives a series resistance of 1 $\mu\Omega$ [79] which is completely negligible in terms of its effect on R_{eff}.

The capacitor for both samples is formed by two 450 μm $\times$ 450 μm parallel

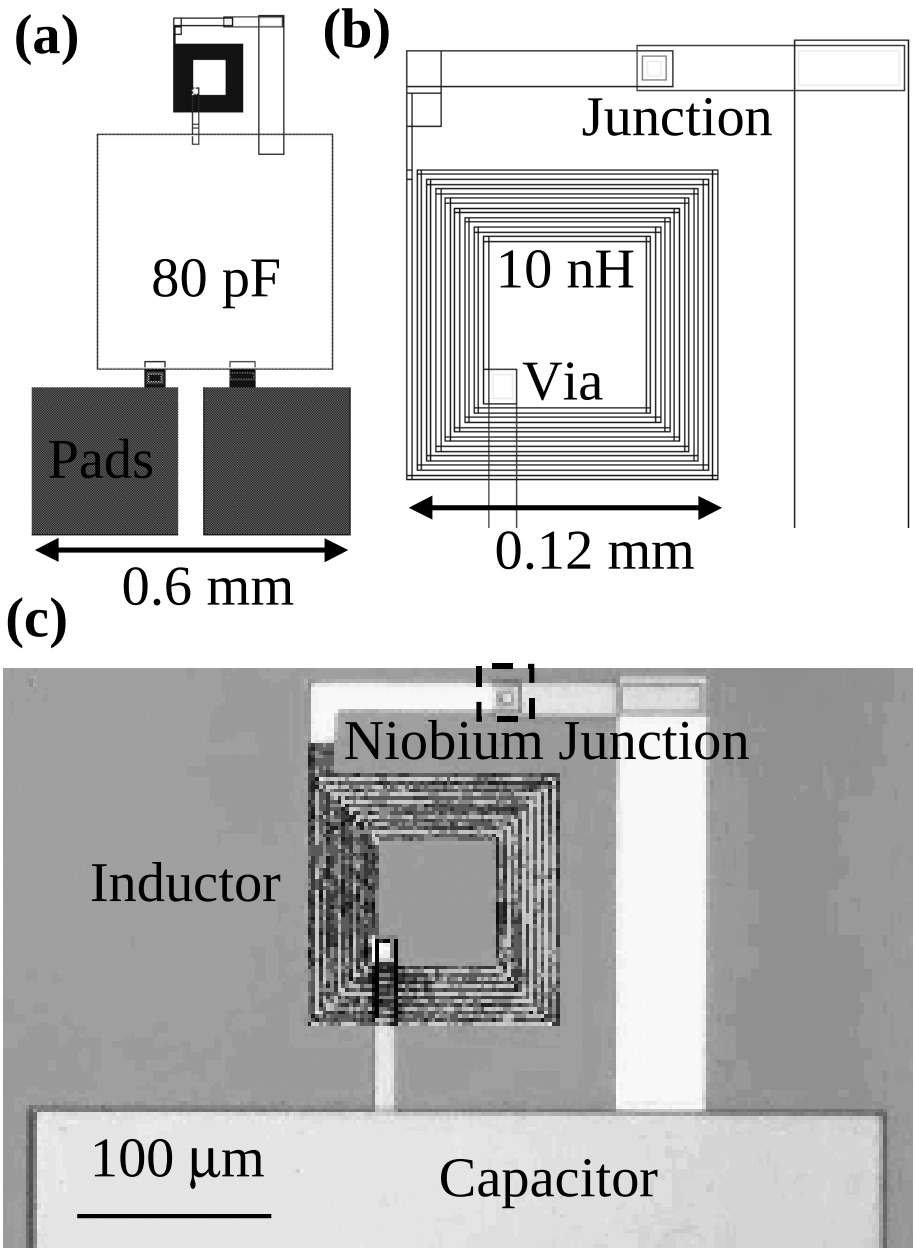

Figure 5.6: Sample LCJJ-Nb1. (a) Circuit design. (b) Close-up view of the spiral inductor design. (c) Photo of the sample.

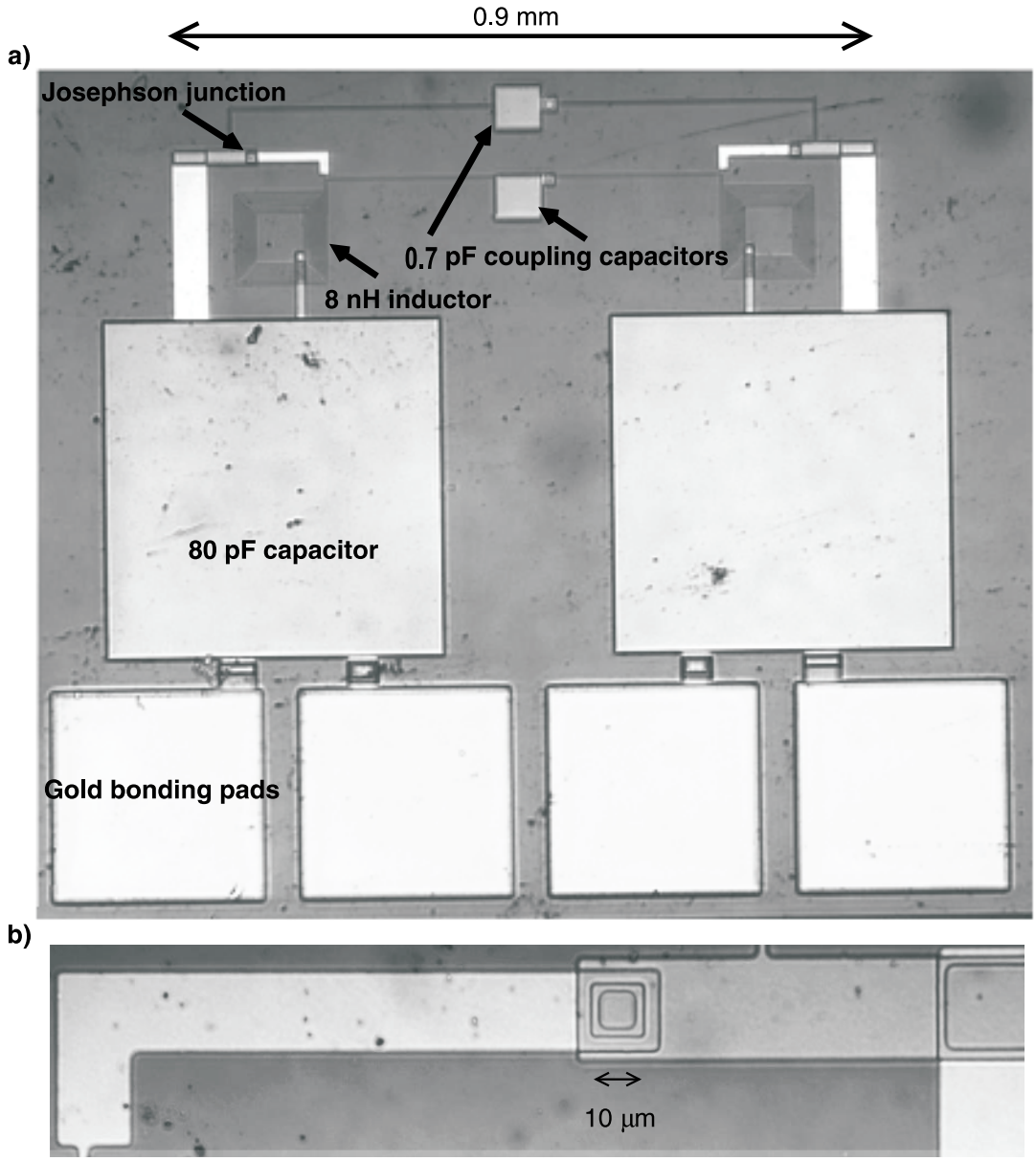

Figure 5.7: Photo of sample LCJJ-Nb2. (a) Overall view. (b) Detail of Nb/AlOx/Nb junction.

plates separated by a 100 nm-thick layer of SiO_2. This leads to a capacitance of 80 pF. The series inductance of this capacitor is negligible as the plate thickness is 100 nm which is much less than the plate size.

Using Eq. 5.4, I estimate $R_{eff} \approx 30$ MΩ for the single-Nb-junction sample and $R_{eff} \approx 20$ MΩ for the double-Nb-junction sample. In both cases, the expected relaxation time should be larger than 80 μ s.

5.2.3 Advantages and disadvantages

The LC isolation scheme is simple and may lead to a large T_1 without heating the junction. However in retrospect, we found that the circuit has a problem associated with current noise in the system.

Due to the resonance of the LC circuit, the effective resistance in Eq. 5.3 displays a resonance dip at $\omega = 1/\sqrt{L_i C_i}$. Therefore the noise spectral density which is given by

$$S_I(\omega/2\pi) = \frac{4\hbar\omega \mathrm{Re}[Y(\omega)]}{\exp(\hbar\omega/k_B T) - 1} \approx \frac{4k_B T}{R_{eff}(\omega)} \tag{5.9}$$

will peak at $\omega = 1/\sqrt{L_i C_i}$. The approximation holds for temperatures such that $\hbar\omega/k_B T << 1$. If one integrates this noise spectral density from zero to infinity to obtain the square of the total rms current noise, one finds

$$\sigma_I^2 = \int_0^\infty S_I(\omega/2\pi)\,\frac{d\omega}{2\pi} = \frac{k_B T}{L_i} \tag{5.10}$$

The total rms current noise is thus given by $\sqrt{k_B T/L_i}$. For a temperature of 50 mK and $L_i = 10$ nH, the total rms noise seen by the junction is roughly 8.3 nA, which is large enough to effectively reduce the coherence time to a few ns under typical experimental conditions.

However, according to my discussion in Chapter 4, the system should not be sensitive to high frequency noise that is above $1/2\pi T_1$. According to the above

estimate, T_1 is of the order of μs; therefore only the noise below 1 MHz would induce decoherence in the system. Since the noise due to the LC resonance is centered around $1/2\pi\sqrt{L_iC_i} \approx 180$ MHz, which is much greater than $1/2\pi T_1 \sim 1MHz$, we should not have decoherence problem. However, experimental results show that the relaxation time is rather short ($\sim$ 4 ns). Therefore decoherence due to the LC resonance was a major problem. The source of the short dissipation time was not clear.

The surface-mounted LC isolated Al junction sample is labeled as LCJJ-Al in the rest of the thesis. The LC isolated single Nb junction sample is labeled as LCJJ-Nb1, and the LC isolated coupled Nb junction sample is labeled as LCJJ-Nb2. Results on these samples are presented in Chapter 7.

5.3 Resonantly isolated Josephson junction

Since high frequency noise has less effect on decoherence, it is best to move the resonance frequency of the LC circuit up such that $1/\sqrt{L_iC_i} >> 1/T_1$. Increasing the LC resonance frequency also helps to reduce the noise level due to the Boltzmann factor. However from Eq. 5.3, we know when $1/\sqrt{L_iC_i}$ gets comparable to ω_p, the effective resistance will decrease dramatically due to the fourth-power dependence on $\omega_p\sqrt{L_iC_i}$. Therefore there is a balance between increasing R_{eff} and reducing decoherence due to low frequency noise.

One limit is to set the LC resonance frequency the same as the junction frequency, and replace the lumped LC circuit by a resonant transmission line.

5.3.1 Basic idea

We have mainly been looking at the problem of reducing dissipation and decoherence from the point of view of preventing external noise from getting to the junction. Equivalently we can also thinking about this problem as preventing the junction

from losing energy to its environment. To prevent the ac voltage across the junction from radiating power, we can put the junction at one end of a cavity that is formed by a half-wavelength (at the plasma frequency) transmission line while leaving the other end open. Current bias leads can be attached to the middle point of the transmission line (see Fig. 5.8).

The idea is that since the two ends of the transmission line are voltage antinodes, the middle point will be a voltage node. Therefore the dissipation over the current bias lines can be minimized.

One can also use the transmission line model to analyze this circuit. At the plasma frequency, the impedance at the middle is

$$Z_m(\omega_p) = \frac{Z_0^2 R_L}{Z_0^2 + jZ_l R_L} \tag{5.11}$$

where Z_0 is the characteristic impedance of the transmission line, R_L is the impedance of the current bias line, and jZ_l denotes the impedance at the open end of the cavity, needed to account for stray capacitance. The admittance seen by the junction is thus

$$Y(\omega_p) = \frac{Z_m(\omega_p)}{Z_0^2} = \frac{R_L}{Z_0^2 + jZ_l R_L} \tag{5.12}$$

and R_{eff} is given by

$$R_{eff}(\omega_p) = \frac{Z_0^2}{R_L} + R_L \left(\frac{Z_l}{Z_0}\right)^2 \tag{5.13}$$

Thus we see that in order to have a large R_{eff}, a small Z_0 and a large Z_l is preferred. For a stray capacitance of 10 fF at the open end, and $Z_0 \approx 50\ \Omega$, we estimate $R_{eff} = 50$ kΩ at 10 GHz, leading to $T_1 = 200$ ns for $C = 4$ pF.

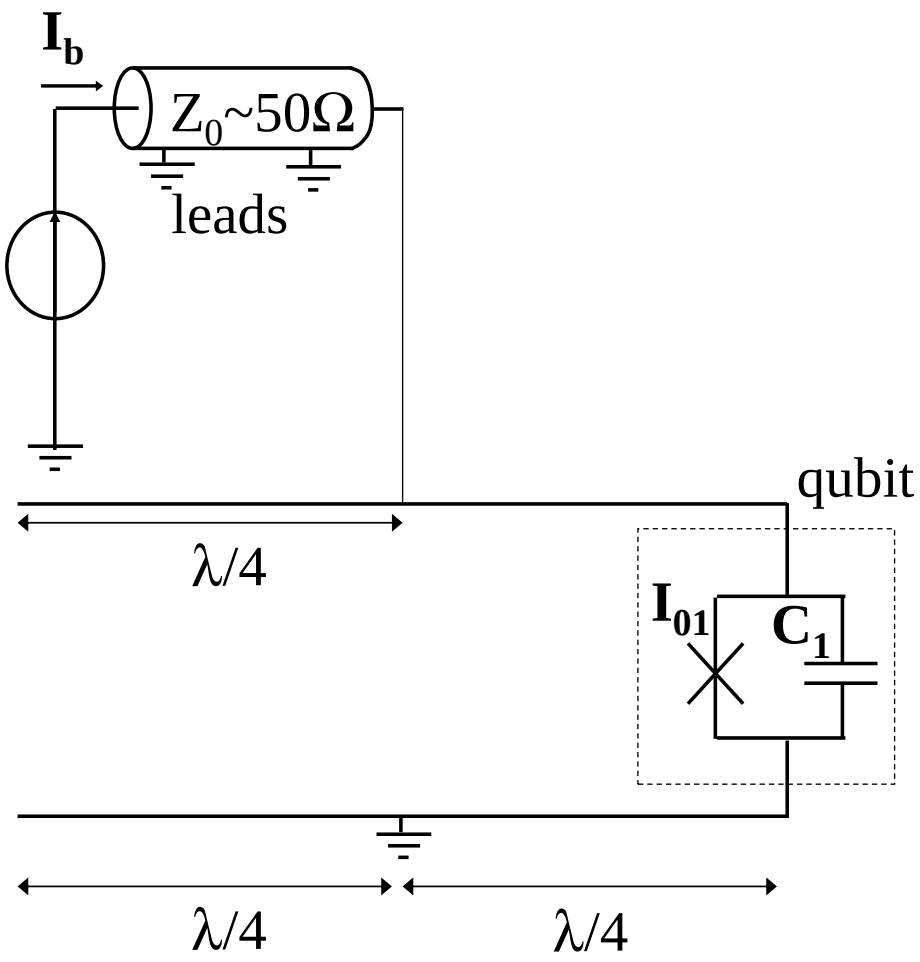

Figure 5.8: Circuit schematic of a resonantly isolated junction. Note current bias leads are attached in the middle of the transmission line.

5.3.2 Experimental realization

Figure 5.9 shows the design drawing and a photo of the sample made by Hypres, Inc. The transmission line is formed by two parallel plates that are 60 μm wide and are separated by 200 nm. The transmission line has a total length of 4.75 mm, and contact pads are attached in the middle. Using the dielectric constant of the silicon, we estimate this geometry will provide a half-wavelength resonator at a frequency of 10 GHz.

5.3.3 Advantages and disadvantages

Since this design is using a half-wavelength transmission line, there should be no resonances below the plasma frequency, and some low frequency noise should be avoided.

The most undesirable property of this design is it only functions around one particular frequency; that is, when the total length is equal to the half wavelength. This scheme might be useful if the parameters for both the junction and the resonator are designed carefully. Also, this design does not block low-frequency noise that is present in the leads.

This resonantly isolated Nb junction sample is labeled as RESJJ-Nb in the rest of the thesis. Results on this chip are presented in Chapter 7.

5.4 LJ isolated Josephson junction

All of the above LC isolation schemes do not isolate the junction from low frequency noise, which causes decoherence. Resonant isolation only works at a single frequency. In order to achieve broadband isolation, a impedance transforming scheme was first proposed and implemented by Martinis and his coworkers [68]. The basic idea of the impedance transforming scheme is similar to the inductance divider I discussed

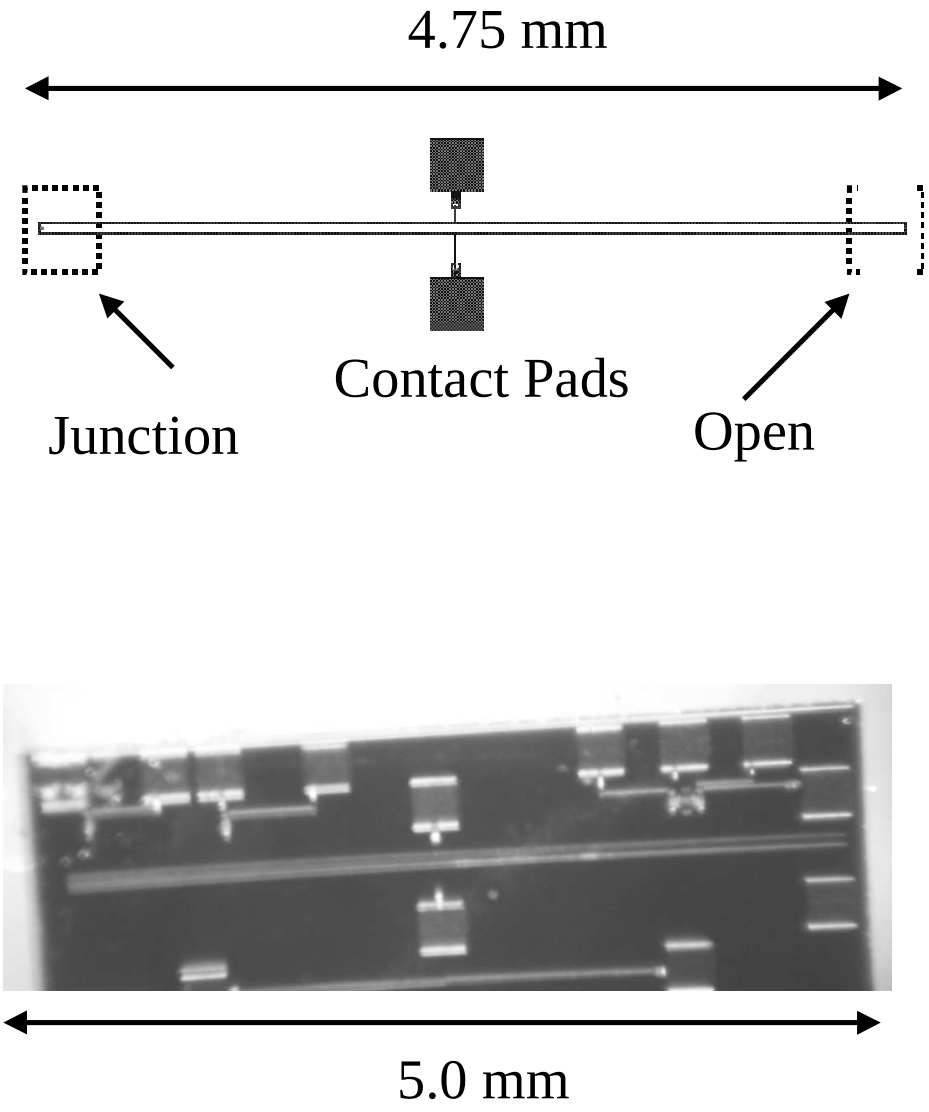

Figure 5.9: The design drawing and a photo of the RESJJ-Nb sample where the transmission line is formed by two parallel plates that are 60 μm wide and are separated by 200 nm. One end is the qubit junction, the other end is left open.

above.

If one replaces the isolation capacitor C_i with an inductor L_{i2}, then we have

$$R_{eff}(\omega) = \frac{L_i^2 \omega^2}{R_L} + R_L \left(\frac{L_i}{L_{i2}} \right)^2 \tag{5.14}$$

where L_i is the inductor in series with the junction and R_L is the impedance of the bias line. In order for this scheme to work, L_i must be much greater than L_{i2}.

However, placing an inductor across the junction will make it difficult to detect the junction switching. When the junction switches, the gap voltage will be divided between the big inductor L_i and the small inductor L_{i2}, so the signal will be very small. This problem can be solved by placing another Josephson junction in the small inductor arm of the circuit.

5.4.1 Basic idea

Figure 5.10 shows a schematic of the inductor-junction (LJ) isolated qubit scheme.

Note that the qubit junction (big cross in Fig. 5.10) is protected by the inductor and isolation junction (small cross in Fig. 5.10) network from noise in the bias line. For the inductive divider to work, the isolation junction must be kept in its zero-voltage state. The isolation junction displays an effective minimum inductance (due to the Josephson relations) that can be written as

$$L_{j2} = \frac{\Phi_0}{2\pi I_{02}} \tag{5.15}$$

where I_{02} is the critical current of the isolation junction. Including the stray inductance L_{s2} in series with the isolation junction, we find the total shunt inductance L_{i2}

$$L_{i2} = L_{j2} + L_{s2} \tag{5.16}$$

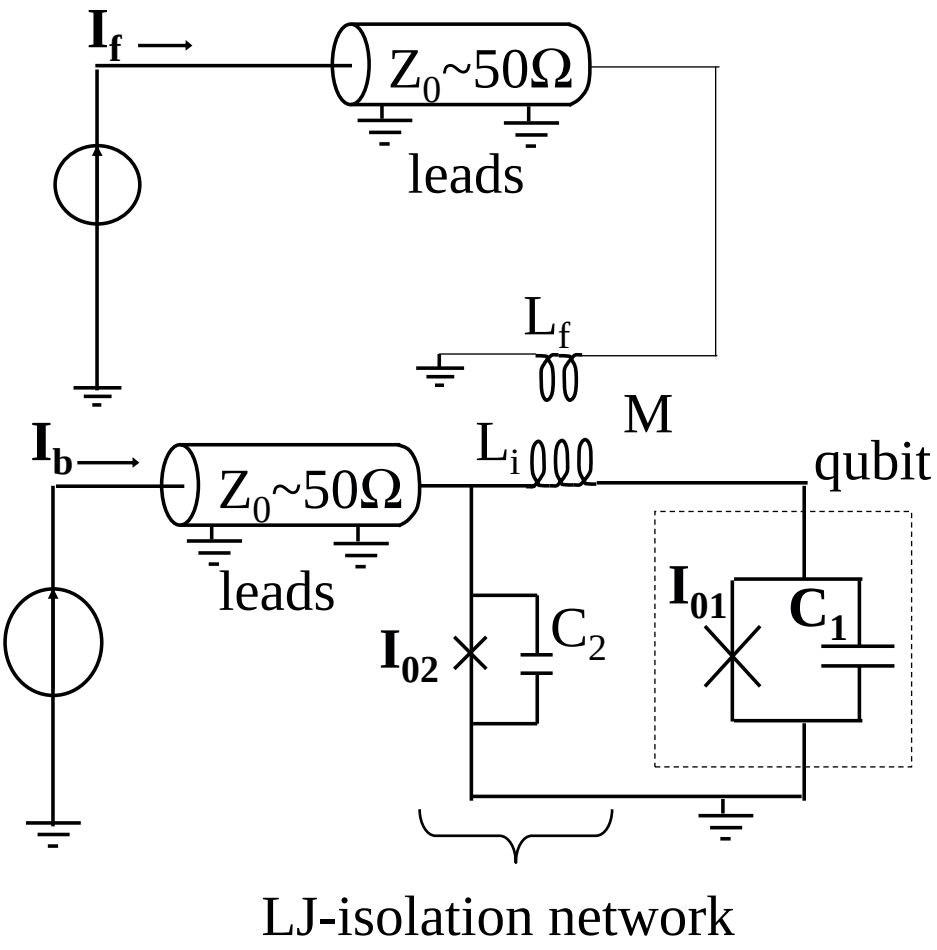

Figure 5.10: Circuit schematic of an LJ isolated junction.

Inductance divider

The current from the bias leads will be divided according to the inductance ratio L_i/L_{i2}. Let I_b be the total current supplied in the bias line. The currents flowing through the qubit junction (I_{b1}) and the isolation junction (I_{b2}) are

$$I_{b1} = \frac{I_b L_{i2}}{L_i + L_{i2}} \tag{5.17}$$

$$I_{b2} = \frac{I_b L_i}{L_i + L_{i2}} \tag{5.18}$$

By choosing $L_i \gg L_{i2}$ the majority of the current will flow through the isolation junction. This is not exactly what we want; in this case the isolation junction switches first and then triggers the qubit junction to switch.

In order to be able to bias the qubit junction while keeping the isolation junction in its zero-voltage state, a flux bias line is placed near the large inductor (see Fig. 5.10). Through the mutual inductance between the flux bias line and the large inductor, a circulating current in the junction loop can be induced. One can choose the polarity and the magnitude of this circulating current such that it tends to cancel the current flowing in the isolation junction. Let I_f be the current in the flux line, and M be the mutual inductance between the flux line and the big inductor L_i. Then the total bias current flowing through the qubit junction (I_{t1}) and the isolation junction (I_{t2}) are

$$I_{t1} \approx \frac{I_b L_{i2}}{L_i + L_{i2}} + \frac{I_f M}{L_i + L_{i2}} \tag{5.19}$$

$$I_{t2} \approx \frac{I_b L_i}{L_i + L_{i2}} - \frac{I_f M}{L_i + L_{i2}} \tag{5.20}$$

These are approximate since they neglect the non-linear behavior of the junctions. From Eq. 5.20, we see that if $I_f = I_b L_i/M$, then the total current flowing through the isolation junction will be zero and the junction will stay in its zero voltage

state. Meanwhile, the total current in the qubit junction will equal the bias current supplied by the current bias leads, i.e.

$$I_{t1} = I_b \tag{5.21}$$

In this scheme, provided L_i is large, the dynamics of the qubit junction resembles a single junction, while the isolation junction acts as a noise filter and also an amplifier to detect the switching of the qubit junction. This is because once the qubit junction switches, the voltage it outputs will force the isolation junction also to switch, producing an easily detectable signal.

Hamiltonian analysis

Although the above discussion was from the point of view of an inductive divider that treated the isolation junction as an inductor, one can do a full analysis. Let γ_1 and γ_2 denote the phase differences across the qubit junction and the isolation junction, then the dynamics of the system can be described by the Hamiltonian,

$$H = \frac{p_1^2}{2m_1} + \frac{p_2^2}{2m_2} + U(\gamma_1, \gamma_2) \tag{5.22}$$

where p_1 and p_2 are the canonical momenta corresponding to γ_1 and γ_2, and $m_1 = C_1(\Phi_0/2\pi)^2$ and $m_2 = C_2(\Phi_0/2\pi)^2$ are the effective masses of the two degrees of freedom. $U(\gamma_1, \gamma_2)$ is a two-dimensional potential and given by

$$U(\gamma_1, \gamma_2) = -\frac{\Phi_0}{2\pi}\left(I_{01}\cos\gamma_1 + I_{02}\cos\gamma_2 + I_b\gamma_2\right) + \frac{\left((\gamma_1 - \gamma_2)\Phi_0/2\pi - MI_f\right)^2}{2L_i} \tag{5.23}$$

This is just the Hamiltonian of an asymmetrical dc SQUID. Setting $\partial U(\gamma_1, \gamma_2)/\partial\gamma_1 = \partial U(\gamma_1, \gamma_2)/\partial\gamma_2 = 0$, we have the following equations

$$I_b = I_{01}\sin(\gamma_1) + I_{02}\sin(\gamma_2) \tag{5.24}$$

$$\gamma_1 - \gamma_2 = -2\pi \frac{L_i I_{01} \sin(\gamma_1) - M I_f}{\Phi_0} \tag{5.25}$$

In order to force the isolation junction into the zero-voltage state, we choose $\gamma_2 = 0$ and obtain the optimal bias condition,

$$I_b = I_{01} \sin(\gamma_1) \tag{5.26}$$

and

$$I_f = \frac{1}{M} \left(L_i I_b + \frac{\gamma_1 \Phi_0}{2\pi} \right) \tag{5.27}$$

Under the condition $L_i I_b \gg \Phi_0$, Eq. 5.27 reduces to the same result as the simple inductive divider.

Relaxation time

For this circuit, the dissipation coming from the current bias leads has already been described above, i.e.

$$R^b_{eff} = \frac{L_i^2 \omega^2}{R_L} + R_L \left(\frac{L_i}{L_{i2}} \right)^2 \tag{5.28}$$

However, the flux bias line can also contribute dissipation. We can find the effective resistance R^f_{eff} by transforming the dissipative element in the flux bias line to the junction loop. The impedance seen by the qubit junction is

$$Z(\omega) = j\omega L_i + \frac{M^2 \omega^2}{R_L + j\omega L_f} \tag{5.29}$$

where R_L is the impedance of the flux line at high frequencies, and L_f is the self inductance of the flux loop. Converting $Z(\omega)$ to an effective resistance, we have

$$R^f_{eff} = R_L \left(\frac{L_i}{M} \right)^2 + \frac{(M^2 - L_i L_f)^2 \omega^2}{M^2 R} \approx R_L \left(\frac{L_i}{M} \right)^2 \tag{5.30}$$

where the approximation holds for $M^2 \approx L_i L_f$, which is the strong coupling limit.

The total effective resistance is a parallel combination of the above two resistances. For parameters $L_i = 3$ nH, $L_{i2} = 60$ pH, and $M = 30$ pH, I find $R^b_{eff} = 125$ kΩ, $R^f_{eff} = 500$ kΩ and $R_{eff} = 100$ kΩ, which corresponds to a relaxation time of 400 ns for a 4 pF junction.

Decoherence due to noise

The inductance divider also reduces decoherence from low-frequency current noise. This can be verified by examining Eq. 5.19, which describes the current flowing through the qubit junction. The rms noise in I_{t1}, the total bias current for the qubit junction, is

$$\sigma^2_{I_{t1}} = \sigma^2_{I_b} \left(\frac{L_{i2}}{L_i + L_{i2}} \right)^2 + \sigma^2_{I_f} \left(\frac{M}{L_i + L_{i2}} \right)^2 \tag{5.31}$$

Therefore the current noise in the current bias line and the flux bias line has been reduced by factors of $\frac{L_{i2}}{L_i+L_{i2}}$ and $\frac{M}{L_i+L_{i2}}$, respectively.

5.4.2 Experimental realization

Our LJ isolated junction sample was fabricated by Hypres, Inc. The Nb/AlOx/Nb qubit junction size is 10 μm × 10 μm, while the isolation junction is 7 μm × 7 μm, and the nominal critical currents of the junctions are 100 μA and 50 μA respectively. Fig. 5.11 shows the design of the sample while Fig. 5.12 shows a photo.

The large inductor L_i is a planar square spiral with an inner diameter of 42 μm, an outer diameter of 84 μm and 6 turns. Using Eq. 5.8 for the inductance of a square spiral, I estimate $L_i \approx$3.3 nH.

The experiment is performed at $I_{02} = 10$ μA, and from the geometry of the sample (see Fig. 5.12), one can tell the stray inductance in series with the isolation junction is about 30 pH; thus I estimate L_{i2} to be 60 pH.

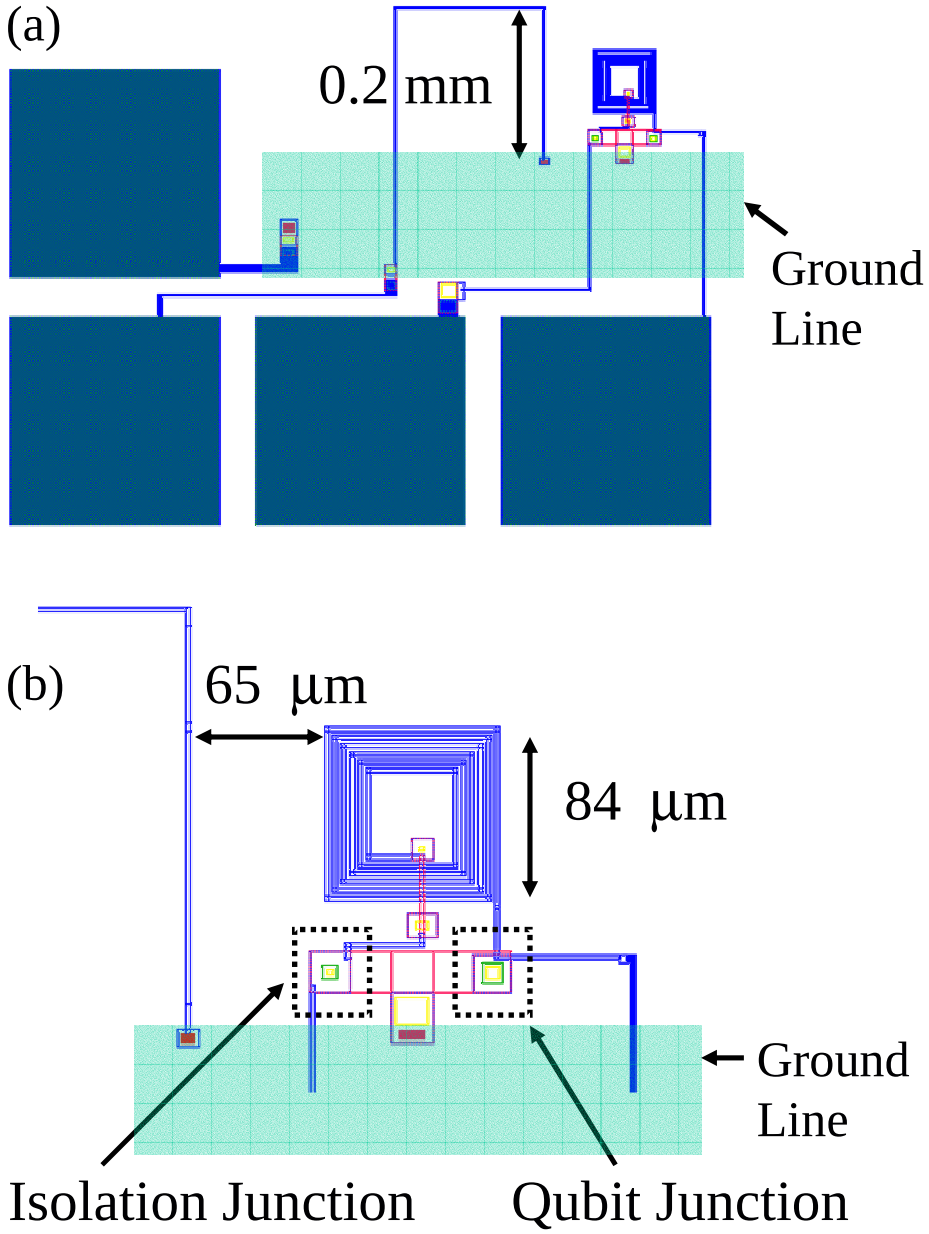

Figure 5.11: Lithography design of the LJJJ-Nb sample. (a) Chip Layout. (b) Detail of the LJ isolation network.

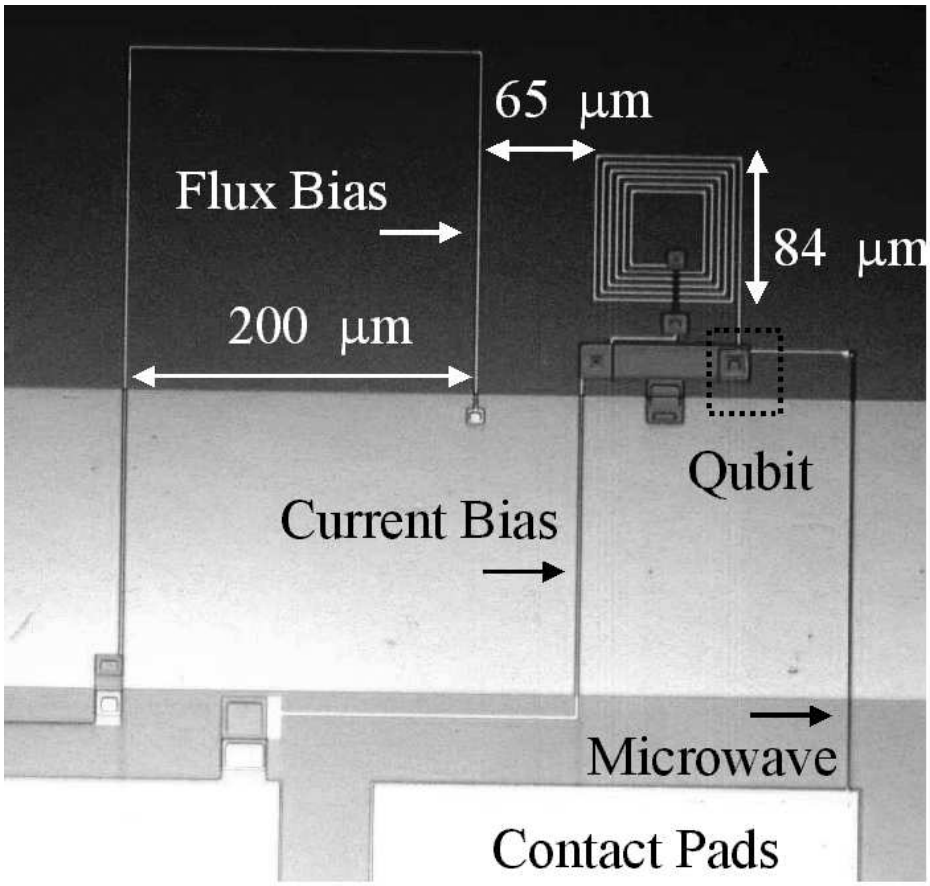

Figure 5.12: Photo of sample LJJJ-Nb.

The flux loop is made of three sides[7], each side is 200 μm long, and the separation between the flux loop and the large inductor is 65 μm (see Fig. 5.12). From this I estimate the mutual inductance between the flux loop and L_i is $M \approx 30$ pH.

Most of the circuits except for the large inductor and the flux loop, sit above a Nb ground plane to minimize stray magnetic coupling.

5.4.3 Advantages and disadvantages

The LJ isolated junction qubit is very appealing in terms of broadband filtering to reduce decoherence due to low frequency noise. But these attractive features come at the cost of complexity. Moreover, in order for the inductance divider to work, one requires $L_i \gg L_{j2}$ which means $L_i I_{02} \gg \Phi_0$. Therefore the circuit, if viewed as a dc SQUID, has a potentially high degree of magnetic hysteresis [72]. This can be verified by examining the two-dimensional potential given in Eq. 5.23. The potential displays many local minima. Unlike the single junction case, these minima are not identical. Therefore starting from different local minima[8] in which the system is initially trapped, the subsequent dynamics of the system can be dramatically different when the bias current is ramped. Analysis of the junction switching data will thus be more complicated than a true single junction qubit.

This LJ isolated single Nb junction sample is labeled as LJJJ-Nb in the rest of the thesis. Results on the sample are presented in Chapter 7.

5.5 Sample fabrication

Al junctions (RJJ-Al and LCJJ-Al) were fabricated in house using photo-lithography and E-beam lithography, while Nb junctions (LCJJ-Nb1,LCJJ-Nb2,RESJJ-Nb and LJJJ-Nb) were fabricated by Hypres, Inc. [112] using photo-lithography.

[7]The fourth side is the ground plane.

[8]The different minima correspond to different flux trapped in the loop.

For the home-made samples, photo-lithography was used to define large-size patterns (> 5 μm), such as the NiCr resistors and NiCr heat sinks for the RJJ-Al sample and gold contact pads. E-beam lithography was used to define the junction pattern with a feature size of 2 μm.

5.5.1 Photo-lithography for contact pads

The main process used in our fabrication process is liftoff. Liftoff consists of three steps:

(a) Photoresist pattern. A 1.5-2 μm layer of Shipley 1813 photoresist was spun onto a blank wafer[9]. After UV exposure in a contact aligner, the chip was soaked in chlorobenzene for 90 seconds to harden the top part of the resist[10] and subsequently baked at 90°C for 90 seconds. The pattern was then developed in CD-30 developer for approximately 30 seconds[11]. After developing, we checked the undercut on the photoresist pattern using an optical microscope.

(b) Metal deposition. Depending on the type of metal and the film thickness, there are many choices for this deposition step. For gold contact pads, we used thermal evaporation. To facilitate sticking of gold to the substrate, a wetting layer of 1 nm Cr is used. Typically a layer of 20 nm gold was subsequently evaporated at a speed of 0.5-1 nm/s.

(c) Liftoff. The chip is soaked in acetone for liftoff of the metals on unwanted areas. The liftoff usually takes about 1-2 hours[12]. If necessary, a photoresist stripper

[9]We used a sapphire substrate for RJJ-Al and an oxidized (2.5 μm SiO_2) silicon wafer for LCJJ-Al.

[10]This will facilitate creation of undercuts when the photoresist is developed, and help create a clean edge on the film pattern.

[11]A rough rule is to wait for dissolving of the resist and then develop for another equal length of time.

[12]If the process does not complete in this time, it usually means something is wrong, for example

such as μstrip is used to remove any residue that might be stuck at the corners of the patterns. The sample is then cleaned with acetone, methanol, isopropanol and DI water for the next lithography step.

For sample LCJJ-Al, the liftoff process was used for defining the gold contact pads.

For sample RJJ-Al, the above liftoff process was repeated three times to form a thick NiCr layer (for the heat sink), a thin NiCr layer (for the isolation resistor) and a gold layer (for contact pads and also on top of thick NiCr)[13]. The thick NiCr layer (0.5-0.8 μm) was deposited by dc sputtering at 500 W for 2.5 minutes in less than 5 mTorr of argon, as thermal evaporation of thick NiCr left highly stressed films that can easily peel off[14]. Both the thin NiCr layer and the gold layer were deposited by thermal evaporation in a cryo-pumped deposition chamber.

To prevent contact problems between the thick NiCr layer and the thin NiCr layer, we ion-milled the thick NiCr film before depositing the thin NiCr film. An alternative to this all-liftoff process is an all-etching process, with three layers of deposition (thin NiCr, gold and then thick NiCr), done in the same chamber without breaking vacuum, followed by three steps of etching [79].

5.5.2 E-beam lithography for junctions

In our home-made Al samples, junctions were defined using E-beam lithography. Although one can also use photo-lithography to create junctions, it is inconvenient since a different mask must be made every time the pattern changes.

(a) The first step is to make an e-beam resist pattern using three layers of

not enough undercut.

[13]In Fig. 5.3, the fabrication order is different, with thin NiCr first, gold layer second, and then the thick NiCr layer.

[14]The argon pressure is crucial in producing stress-free films, films sputtered in a 5 mTorr of Ar do not seem to have noticeable stress and can pass the scotch-tape test.

MMA8.5MAA EL11 [15]and one layer of PMMA C6. Each layer of MMA8.5MAA EL11 was spun at 1500 rpm for 45 seconds onto a well-cleaned[16] wafer that already has gold contact pads. After spinning, the wafer is placed in an oven at 120°C for 20-30 minutes. This results in a thickness of 1 μm for each layer. After the layers of MMA8.5MAA EL11 are done, a layer of PMMA C6 was spun in the same way as the MMA8.5MAA El11 layer.

The whole wafer was then diced into individual chips for E-beam writing. The writing of the bridge pattern (see Fig. 5.13) was done using a JOEL 5400 SEM. The typical geometry of the junction bridge is 20 μm long and 2 μm wide. Stable and stress-free mounting of the chip on the writing stage is important to produce stress-free patterns. The chip was then developed in a solution of MIBK:IPA(1:3) for 70 seconds followed by 20 seconds in IPA and another 5 seconds of IPA rinse. After developing, an optical inspection of the bridge must be done to ensure a clear bridge structure is obtained without cracks and shorts.

(b) The second step is double angle evaporation of Al. With the bridge pattern created, one can use double angle deposition to create junctions [114]. The chip was loaded into a vacuum chamber that is cryopumped to the low 10^{-6} Torr range. In order to obtain good contact between Au and Al, the exposed Au pads were first argon ion-milled at 300 V at a pressure of 10^{-4} Torr for about 10 seconds. We estimate the milling rate for gold under this condition is a few Å/s.

Next, a 30 nm layer of Al was deposited at an incident angle of θ (the incident angle is defined as the angle between the beam and the normal to the chip)[17]. The

[15]For small area junctions, two layers of MMA8.5MAA EL11 were used as for the RJJ-Al sample.

[16]If the gold contacts are freshly made, wet cleaning with photoresist stripper is probably enough, but one can also do plasma etching of the sample (with a few hundred mTorr of O_2 at 150 W).

[17]The number quoted here is the thickness in the case of perpendicular deposition; therefore more deposition (to be multiplied by $1/\cos\theta$) is required in order to achieve 30 nm of Al in the case of deposition with an incident angle θ.

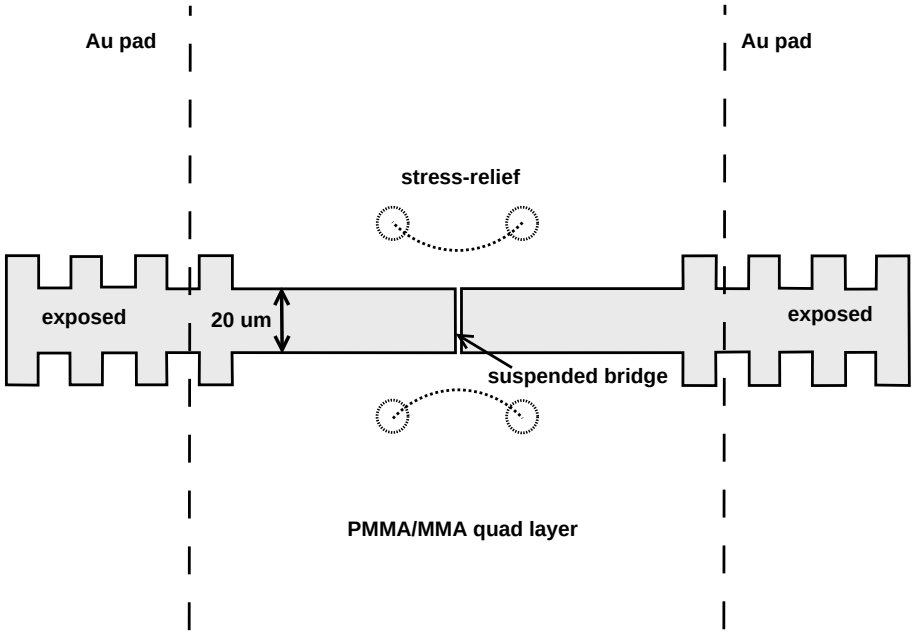

Figure 5.13: Al/AlOx/Al Josephson Junction E-beam lithography pattern. The stress relief patterns near the bridge were sometimes necessary and were intentionally underexposed. The bridge shown here is 20 μm long and 2 μm wide. The actual junction size also depends on the metal deposition step. The notch pattern is used to avoid larger junction effects.

deposition was done at a typical speed of 0.5-1 nm/s after pre-evaporation of at least 10 nm. Lower deposition speed tends to create Al films that display a yellowish color. After evaporation of the first Al layer, oxygen was introduced into the chamber and the pressure ramped to 18 Torr within a minute. The Al film was oxidized for 10 minutes. Following this oxidation, another 30 nm of Al was deposited at an incident angle of $-\theta$. This oxidation condition reproducibly generate junctions with a critical current density of about 13 A/cm^2 and a junction specific capacitance of about 40 fF/μm^2.

The result of this double angle deposition is a junction with the length being the bridge length l, and the width being $2h\tan(\theta) - w$, where h is the thickness of the MMA layer and w is the width of the bridge. For the RJJ-Al sample, we used a bridge length of 3 μm and a bridge width of 2 μm, and a deposition angle of 45°, resulting in a junction size of 3 μm $\times$ 2 μm. For the LCJJ-Al sample, we have a bridge length of 20 μm and a bridge width of 2 μm, and a deposition angle of 60°, resulting in a junction size of 20 μm $\times$ 5 μm.

(c) The third step is liftoff. This step is the same as that for photo-lithography. One caution is the sample should not sit in acetone for too long as the junction oxide barrier may degrade [115]. After liftoff, the sample was cleaned with acetone, methanol and isopropanol (DI water cleaning should be avoided) and placed in a vacuum chamber immediately, if possible.

5.5.3 Contact resistance between gold and aluminum

Some of the samples we made had large contact resistance, presumably between the Au contact pads and the Al leads of the junction.

Our main suspicion about the cause was failure of the Al film at the gold edge due to the sharp edges on the gold contact pads. For gold pads that were created with large undercuts in photo-lithography, we did not measure noticeable contact

resistances.

In depositing metals, we also adopted the rule of having a thicker Al layer (upper layer) than the gold layer (lower layer), in which case good contacts could be made between Au and Al even in the presence of a sharp edge on the gold pad.

We also used ion-milling of the exposed gold pads before deposition to prevent contamination-related bad contacts.

Using a four probe measurement at room temperature, one can measure the normal state resistance of the junction (sensing current should not exceed the expected critical current of the junction), and the critical current of the junction can be estimated from the junction size and a critical current density based on the oxidation condition. The product of the normal resistance and the critical current should be equal to $\pi V_g/4$ according to Ambegaokar and Baratoff [116]. For Al junctions, this number is about 300 μV. If the measured number is significantly more than this, contact resistance probably exists. With the above modifications, samples without noticeable contact resistances were successfully fabricated.

5.5.4 Hypres samples

All the Nb junction samples (LCJJ-Nb1,LCJJ-Nb2,RESJJ-Nb and LJJJ-Nb) were made by Hypres, Inc. Their Nb junction trilayer process can produce a minimum feature size of about 2 μm, more than sufficient for our needs. I-V measurements of these junctions were generally satisfactory, without any noticeable contact resistance. The junction critical current density was fixed at roughly $100\mu A/cm^2$.[18] In most of our experiments, a magnetic field that is parallel to the plane of the junction overlap area (typically below 50 Gauss) is used to suppress junction critical currents to a value which is more appropriate for our needs. The junction specific

[18]They have recently introduced a 30 $\mu A/cm^2$ process, which is more suitable for quantum computing, and also have a 1000 A/m^2 process for digital applications.

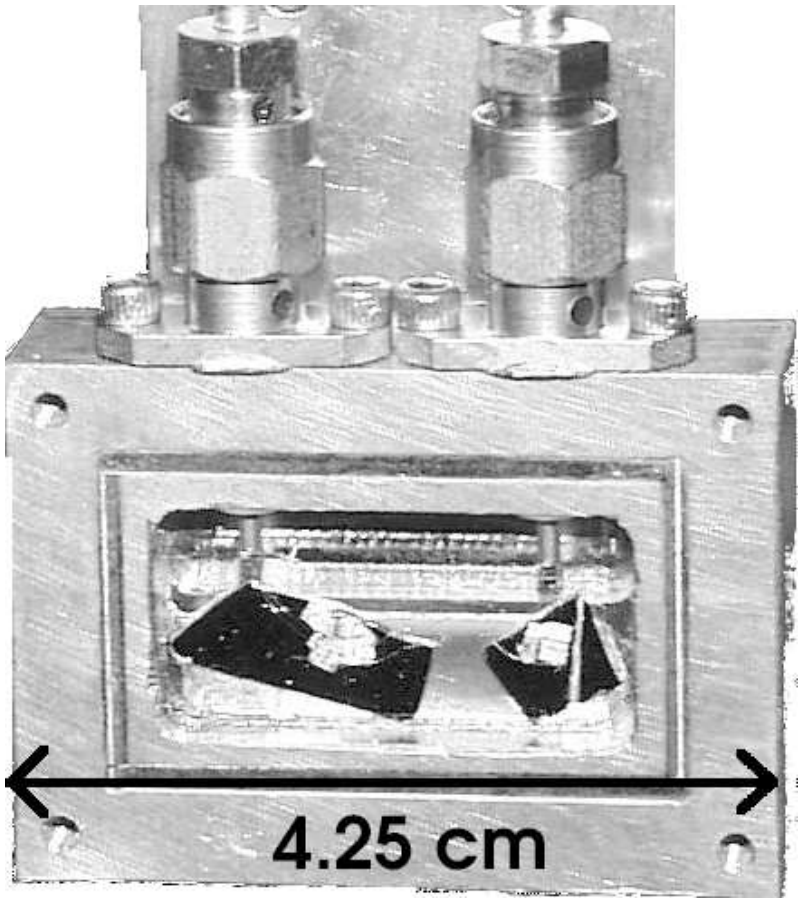

Figure 5.14: The Cu sample box used for all samples except LJJJ-Nb.

capacitance is around 40 fF/μm^2, similar to that for our Al junctions.

5.5.5 Sample mounting

Two sample boxes were used to mount the samples. For RJJ-Al, LCJJ-Al, LCJJ-Nb1 and LCJJ-Nb2, a Cu box was used (see Fig. 5.14), while for RESJJ-Nb and LJJJ-Nb, an Al box was used (see Fig. 5.15). The Al box was superconducting at $T < 1K$ and was used for magnetic shielding.

For mounting, the back of a chip is coated with a small amount of silver paint to ensure good thermal contact; then the chip is gently pressed onto the Cu surface. GE varnish is then applied to the four corners to provide mechanical anchoring. The four sides of the chip were then covered with silver paint to provide good thermal

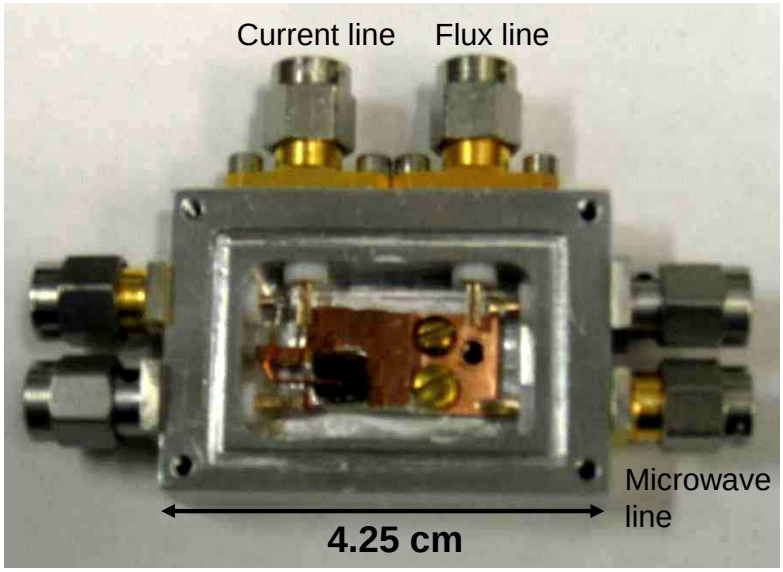

Figure 5.15: The Al sample box used for sample LJJJ-Nb.

contact.

After the chip is mounted, we wirebond the contact pads. For samples other than LJJJ-Nb, two wirebonds were made, one contact pad was wirebonded (with Al 1% Si wire) to the inner pin of an SMA jack mounted on the wall of the box, and the other contact pad was wirebonded directly to the inner surface of the box serving as the return line for the bias current. For LJJJ-Nb, four wirebonds were made, one for the current bias line, one for the flux bias line, a third one for the microwave line, and the last one to connect the ground plane to the inner surface of the Al box. This last line serves as the return line for the bias current and the flux current.

5.6 Summary

In this Chapter, I discussed four different qubit designs: (a) resistively isolated Josephson junction, (b) LC isolated Josephson junction, (c) resonantly isolated Josephson junction, and (d) LJ isolated Josephson junction. Some of the advantages and disadvantages of these four designs were briefly discussed. Resistive isolation is simple in principle but hard to implement due to heating. LC isolation in principle can produce an extremely large relaxation time but suffers from low frequency noise. Resonant isolation in principle reduces relaxation and decoherence significantly but it only works at the resonant frequency. LJ isolation provides broadband filtering but involves two degrees of freedom and is much more complicated than the other isolation schemes. Six samples (RJJ-Al, LCJJ-Al, LCJJ-Nb1, LCJJ-Nb2, RESJJ-Nb and LJJJ-Nb) based on these four designs were built.

Chapter 6

Experimental Setup

In this chapter, I discuss the experimental setup including the dilution refrigerator, the wiring inside the refrigerator, the measurement procedure and the instrumentation.

6.1 The dilution refrigerator

The low temperatures needed for our experiment are provided by an Oxford Instruments Model 200 dilution refrigerator. It has an original base temperature of 8.45 mK. With the wiring added the fridge can reach temperatures of around 20 mK and has a cooling power of 200 μW at 100 mK.

The refrigerator is attached to an insert that is fixed to an isolation table that is supported by a frame made of four stainless-steel legs on top of a sand-filled frame (see Fig. 6.1). To work on the refrigerator and mount samples, the helium bath dewar and μ-metal shield can be dropped through the floor to a lower level of the building. The refrigerator insert, dewar and μ-metal shield are mounted in a screened room that was made by Universal Shielding Corporation. The attenuation of the screened room is around 70 dB at 100 MHz. The control panel for the gas handling system sits outside the screened room on the same floor as the screened room. All the pumps except a diffusion pump for evacuating the inner can are on

the lower level. Fig. 6.1 shows a schematic of the arrangement of the refrigerator, the control panel and the pumps.

Because there is no electrical isolation between the metal pumping tubes and the screened room wall, the wall and the fridge are grounded by the pumps through the pumping tubes. IN addition, there are power supply boxes attached to the screened room wall, which create another ground. Since the two grounds are far away from each other, there will be a fluctuating voltage difference and hence a current will flow over the wall. It would have been preferred to ground the screened room and the fridge by an earth ground using a thick copper rod, and isolate all pumping tubes from the wall. When the experiment is running, all instruments should be battery-powered (or run on isolation transformers) to avoid extra grounds and ground loops.

Besides the diffusion pump for the inner vacuum can, another three pumps (sealed pump, 1 K pot pump and roots pump) are used for the refrigerator. Table 6.1 lists the pumps that have been used and their main specifications.

6.1.1 The magnet

We used a superconducting magnet to generate a field in the z-direction (vertical, in the plane of the junction overlap area) in order to suppress the critical current of the junctions.

The magnet was custom-built by Cryomagnetics, Inc., using twisted multifilamentary NbTi (T_c = 9.8 K, H_c =12 T at 4.2 K) wires in a copper matrix. The field to current ratio is 111.3 gauss/A, and the maximum rated current is 4.49 A. Given that the critical field of Aluminum is around 100 gauss, a current of less than 1 A is required.

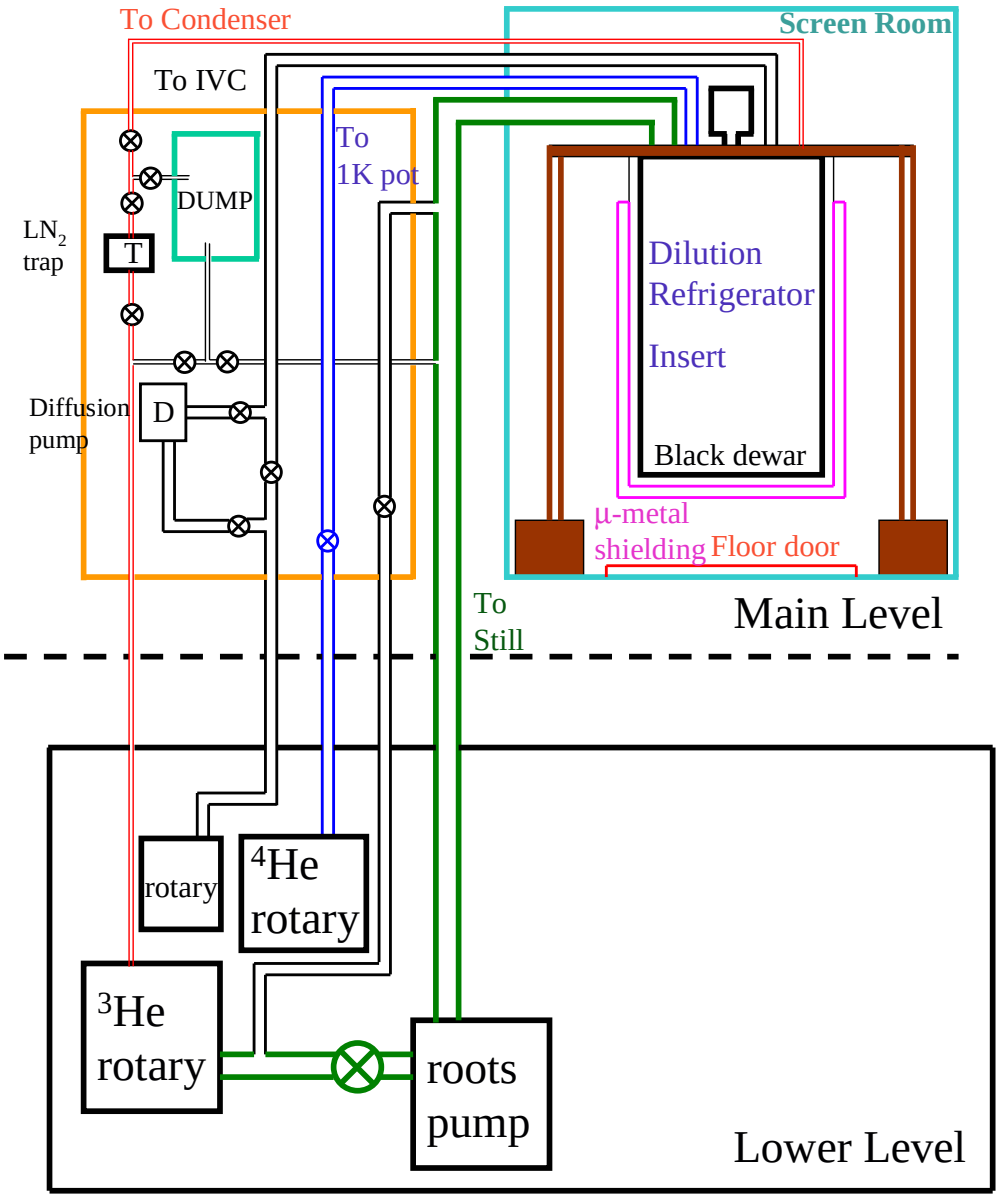

Figure 6.1: Oxford Instruments Model 200 dilution refrigerator and pumps. Note the fridge is inside a screened room and all the pumps are on the lower level.

Table 6.1: List of Pumps used for the Oxford Model 200 refrigerator

Pump model	Usage	Flow rate (m^3/h)	Ultimate pressure (10^{-3}mbar)	Inlet pressure (mbar)
LH RUVAC WSU501	Roots pump	505	-	80[a]
LH TRIVAC S16B	Roughing pump	16	< 25	-
LH TRIVAC S40B	1K pot pump	40	< 25[b]	-
LH TRIVAC S65B[c]	Sealed pump	65	< 25	-
ALCATEL 2063	1K pot pump	60	< 3	-
ALCATEL 2063H[d]	Sealed pump	60	< 3	60

[a]This is the maximum difference pressure between inlet and outlet.

[b]We tested the pump and found the ultimate pressure is about 35 mTorr.

[c]This pump is built for Oxford with modifications on the regular model of S65B.

[d] The pump is water cooled for optimal performance and extended usage.

6.1.2 Thermometry and heaters

The temperatures at various places in the fridge are monitored by several types of thermometers. An Allen-Bradley carbon resistor thermometer is mounted on the top surface of the vacuum can flange. This is useful for monitoring a temperature range of 4 K to 300 K. Two carbon resistors are mounted on the 1 K pot and the still. The resistance values vary somewhat from run to run, but even so, the performance is adequate to monitor the relative temperature changes on the pot and the still while cooling down the refrigerator. A germanium thermometer, which is good from 300 K to 100 mK and very repeatable from run to run, is mounted on the mixing chamber to monitor its temperature during the cool-down process. A calibrated ruthenium oxide thermometer from Scientific Instruments is used to read the temperature of the mixing chamber below 100 mK. The resistances of these thermometers are measured by an AVS-47 resistance bridge made by RV-Elektroniikka Oy PICOWATT.

There are several heaters on the fridge for controlling the operation of the dilution refrigerator. A heater on the still with a maximum power of 50 mW can be used to increase the mix flow rate, and a heater on the mixing chamber (0.2 μW to 20 mW) can be used to control the temperature of the mixing chamber. The powers for these two heaters are provided by an Oxford 2603 Power Supply. We also used the TS-530 Temperature Controller from PICOWATT to precisely control the mixing chamber temperature by the use of a feedback circuit between the bridge readout and the output from the temperature controller.

There is a separate heater on the pot that can provide a maximum power of 2 W. There are two additional high power heaters that we used to heat the charcoal bags on the mixing chamber and at the bottom of the vacuum can (the charcoal bags were used to absorb helium that accumulated from a cold leak). The two heaters provide maximum powers of 0.5 W and 4 W respectively and are very useful during the warm-up process. Figure 6.2 shows the interior of the Oxford Model 200 dilution

refrigerator.

6.2 The dilution refrigerator wiring

As discussed in Chapter 2, I need to measure the switching of a Josephson junction to its voltage state while the bias current is slowly swept. In some of our experiments the same lead is used for current biasing and voltage monitoring, while in other cases I used separate lines for the current and voltage. Also, I need to apply microwaves to the system to carry out spectroscopy measurements. Therefore broadband lines suitable for transmitting microwave frequency signals are also needed.

The measurements I want to perform are very sensitive to the electromagnetic environment that the junction sees. Although the sample holder is thermally anchored and shielded, the leads that connect the junction to the room temperature instruments can still introduce a large amount of noise and heat to the sample. Therefore broad-band filtering from low frequency to the junction characteristic frequency is required to keep the sample cold and reduce noise seen by the junction. Fig. 6.3 shows a schematic of the wiring and filtering inside the fridge. Figures 6.4 and 6.5 show the actual wiring and filtering inside the fridge.

In my experiment, each current bias line is constructed as follows. There is a 40-inch long Manganin wire from the top of the cryostat to a 4 K connection box. This is followed by another 40-inch long Thermocoax cable [117] from the 4 K box to the mixing chamber. This is followed by a home-made rf filter and a home-made copper-powder microwave filter, which is connected to the sample box.

The idea of using Thermocoax as a microwave filter was apparently first proposed by Zorin [118]. The type 1 NcAc Thermocoax cable we used has a stainless steel (type 304L) jacket with an outer diameter of 0.5 mm and an inner diameter of 0.35 mm. The central wire is made of NiCr (80/20) alloy with an outer diameter of 0.17 mm. The dielectric material between the conductors is highly compacted MgO

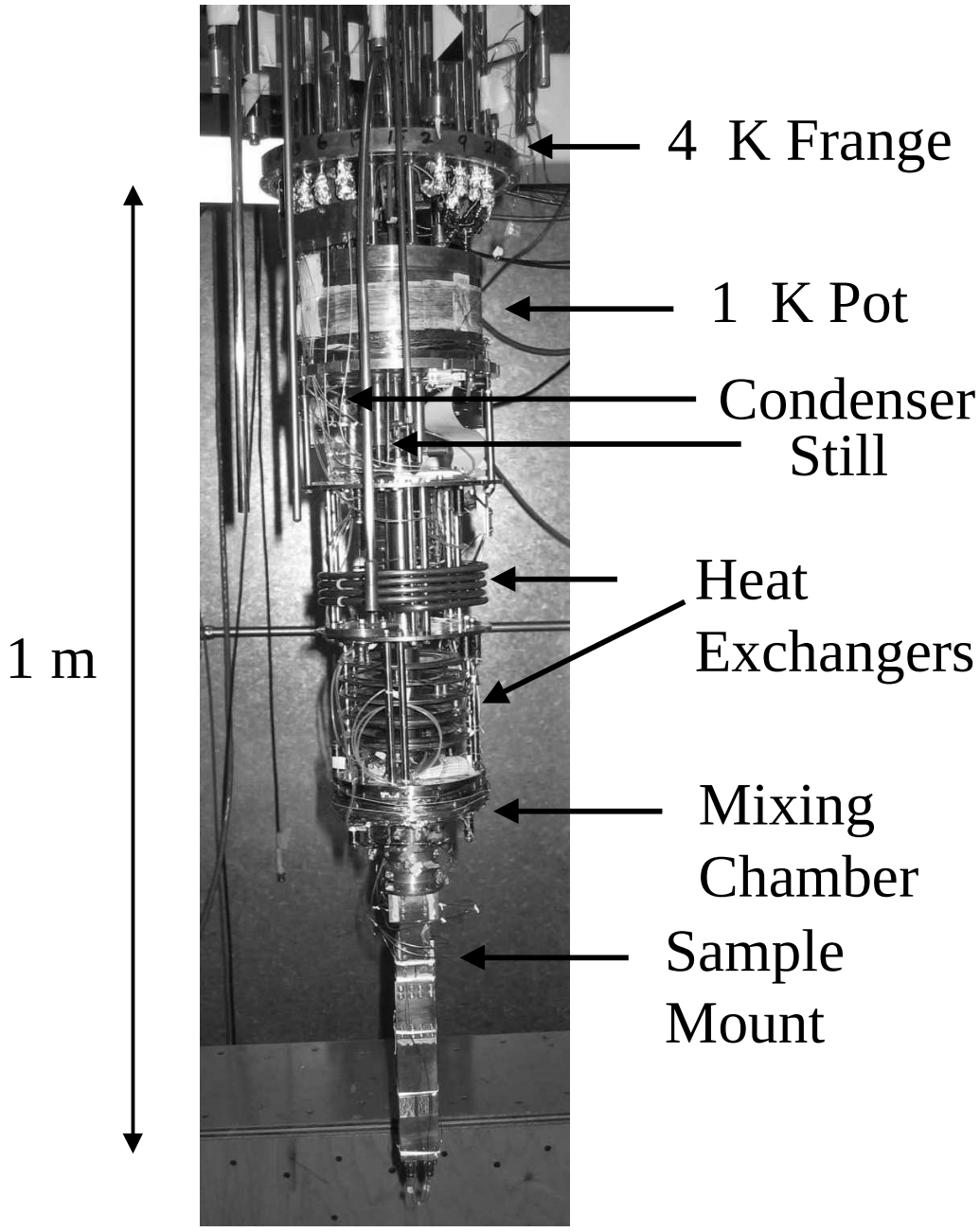

Figure 6.2: The interior of the Oxford Model 200 dilution refrigerator.

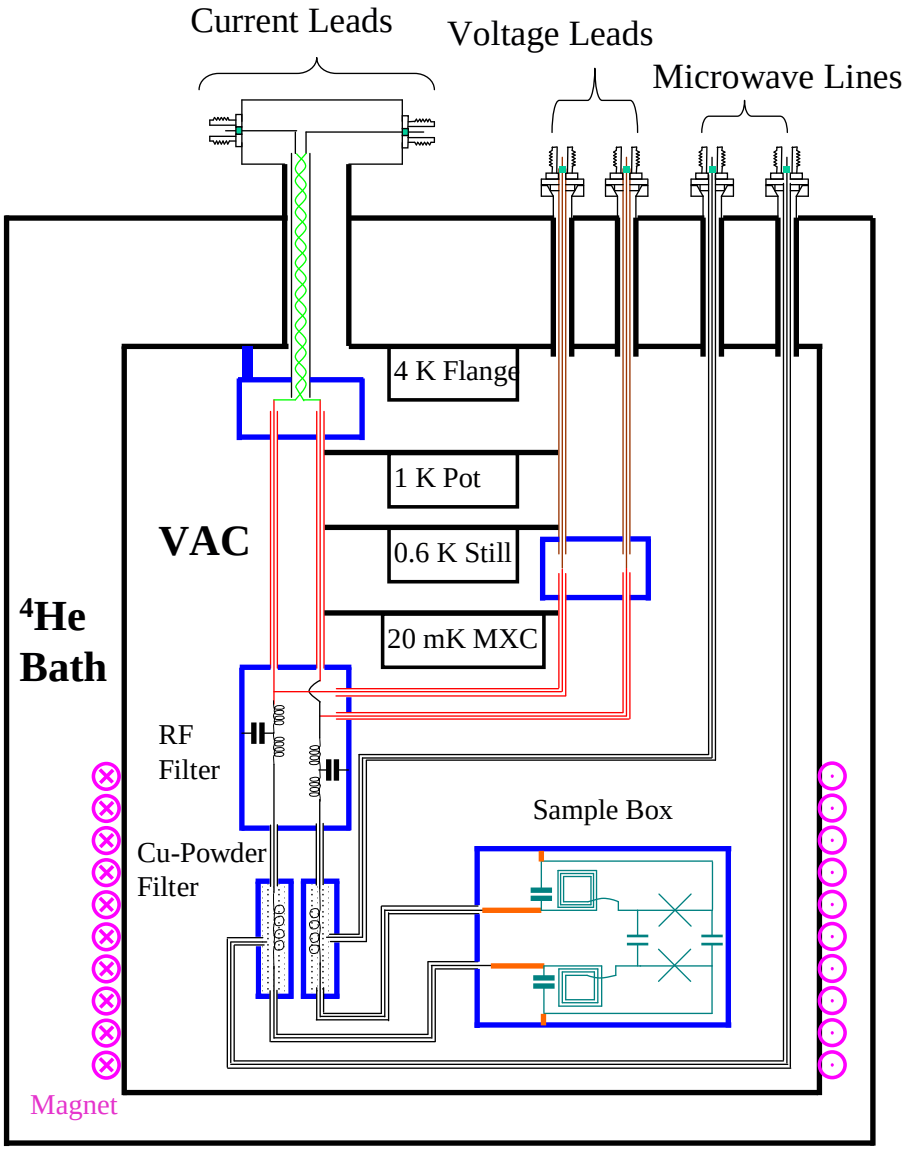

Figure 6.3: Schematic of the wiring inside the fridge. Note the green wires, red cables, brown cables and black cables represent the manganin wires, the Thermocoax cable, the LakeShore cable and the microwave cables respectively.

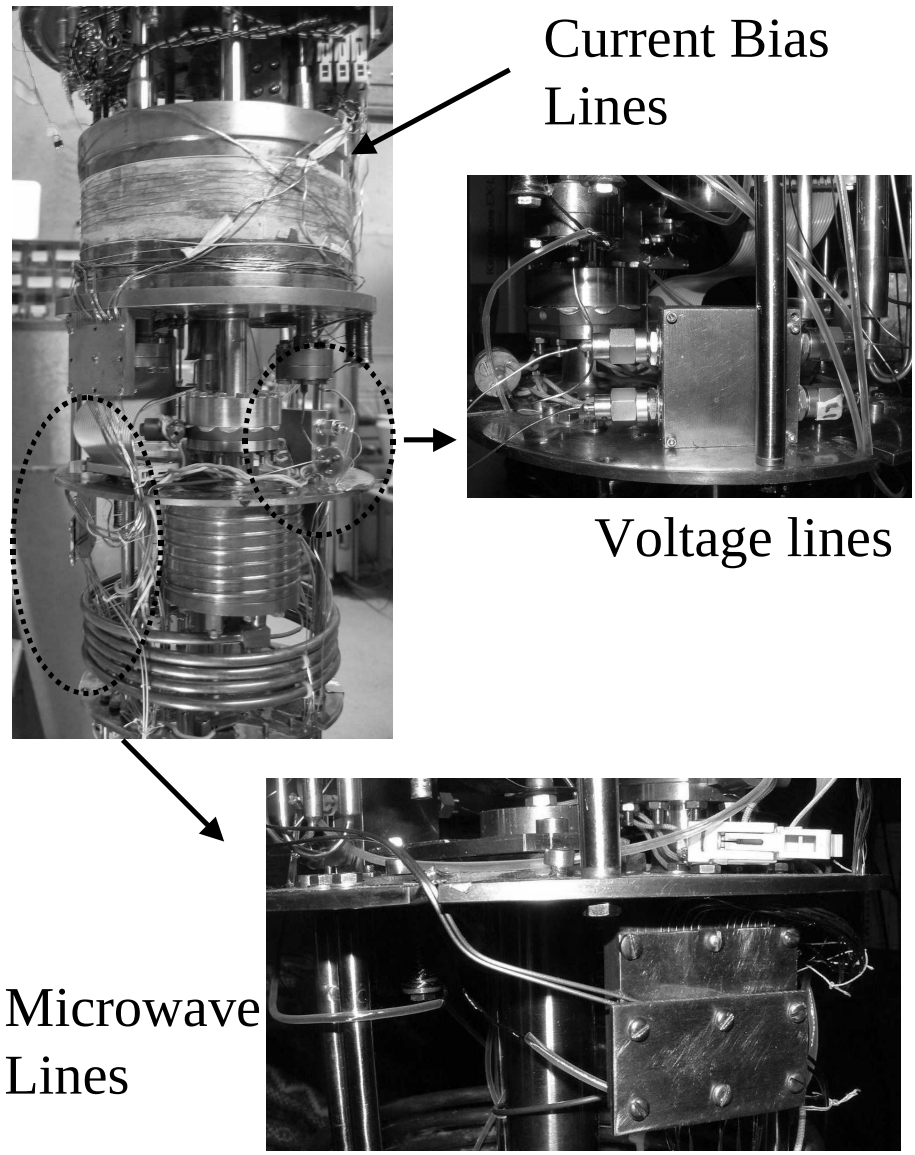

Figure 6.4: The wiring inside the dilution refrigerator vacuum can (top part). Thermocoax cables as bias lines, UT-34-SS-SS from Micro-Coax as microwave lines, and CC-SR-10 from LakeShore as voltage lines.

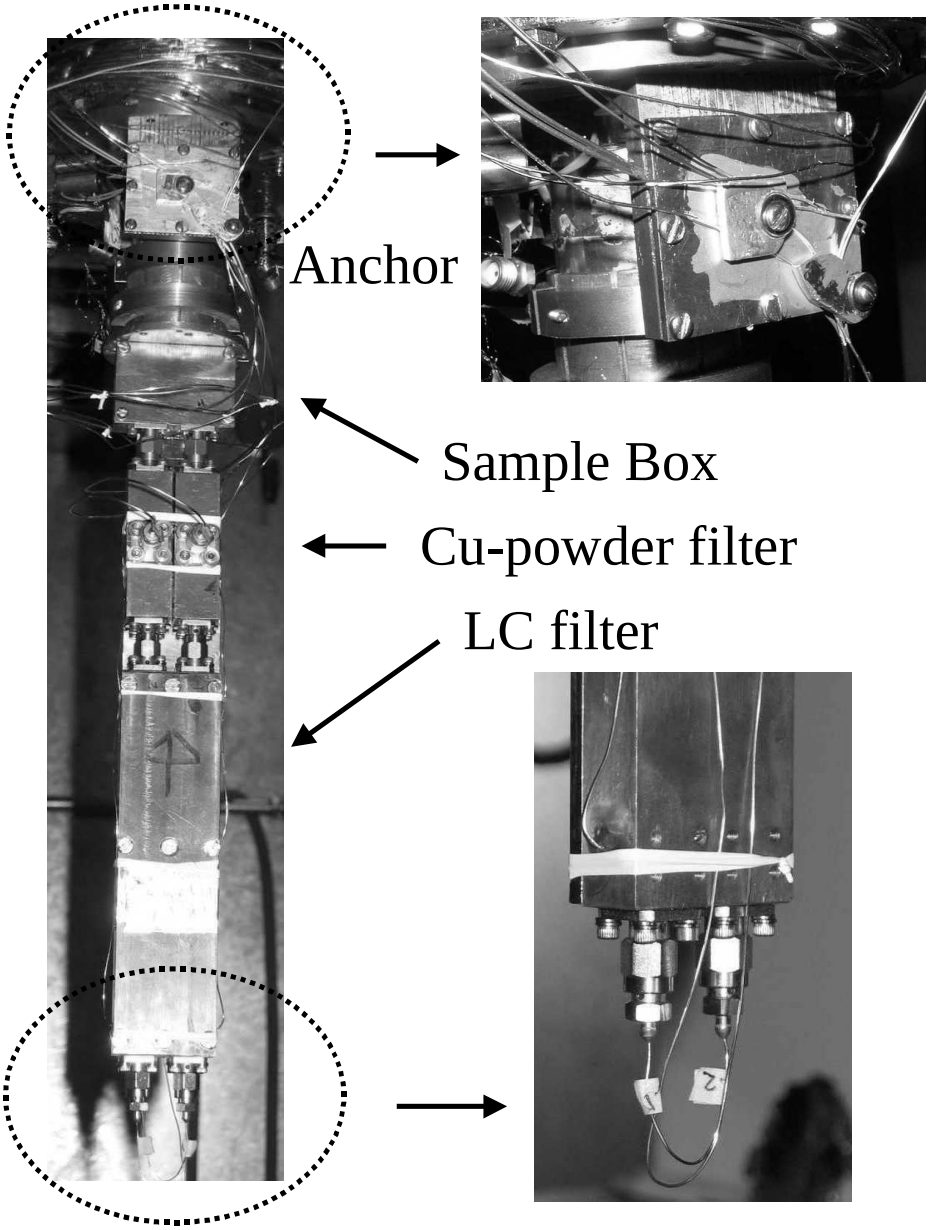

Figure 6.5: The wiring inside the dilution refrigerator vacuum can (bottom part). Current and voltage lines are anchored at mixing chamber and then filtered by LC and Cu-powder microwave filters. Microwaves are capacitively coupled to the current bias lines at the Cu-powder filter.

with very low leakage at low temperatures. The cable has the following electrical properties: The dc resistance per unit length for the inner wire is 50 Ω/m, and 6.9 Ω/m for the jacket, the capacitance per unit length is

$$c = 2\pi\varepsilon\varepsilon_0/\ln(d_2/d_1) \approx 490 \text{ pF/m} \tag{6.1}$$

and the inductance per unit length is

$$l = (\mu\mu_0/2\pi)\ln(d_2/d_1) \approx 0.14 \ \mu\text{H/m} \tag{6.2}$$

Due to the skin effect, the resistance of the cable will increase at high frequencies (> 30MHz). For this cable, one finds the resistance per unit length is $r(\omega) = a\sqrt{\omega}$ for $\omega > 30$ MHz with $a = 2.18 \times 10^{-3}\Omega \text{ s}^{1/2}\text{m}^{-1}$. The characteristic impedance $Z(\omega)$ and the propagation coefficient $\gamma(\omega)$ are [119],

$$Z(\omega) = \sqrt{\frac{r(\omega) + j\omega l}{g(\omega) + j\omega c}} = \sqrt{\frac{r(\omega) + j\omega l}{j\omega c}} \approx Z_0 = \sqrt{l/c} \tag{6.3}$$

$$\gamma(\omega) = \sqrt{(r(\omega) + j\omega l)(g(\omega) + j\omega c)} \approx \frac{r(\omega)}{2Z_0} + j\omega\sqrt{lc} = \alpha + j\beta \tag{6.4}$$

where $g(\omega)$ is the conductance per unit length through the dielectric and is negligibly small. The above approximation holds for frequencies (>100 MHz) where $j\omega l \gg r(\omega)$. From the real part of the propagation constant, we find the attenuation per unit length,

$$A(\omega) = -10\log\frac{P_{out}}{P_{in}} = -10\log\exp^{-2\alpha} = 20\alpha(\omega)/\ln 10 = b\sqrt{\omega} \tag{6.5}$$

where $b = 5.56 \times 10^{-4}\text{s}^{1/2}$ m^{-1}.

The voltage measurement line is similar to the current bias line except for the first section, which is a 40-inch CC-SR-10 semi-rigid cable (probably the same as UT-20-SS-SS from Micro-Coax) from LakeShore Cryotronics, Inc.

The microwave line is a 7-foot UT-34-SS-SS cable from Micro-Coax that is capacitively coupled to the current bias line at the copper-powder filter. Table 6.2 lists the attenuation per unit length for the above three cables in the frequency range of interest.

Table 6.2: Attenuation of Thermocoax cable, LakeShore cable and Micro-Coax cable

Frequency (GHz)	Thermocoax (dB)	LakeShore (dB)	Micro-Coax (dB)
0.001	2.6	-	-
0.01	7.5	-	-
0.02	9.9	-	-
0.05	12.8	-	-
0.1	14.0	-	-
0.2	19.4	2.7	4.7
0.5	31.1	4.2	7.4
1.0	44.2	6.0	10.5
2.0	62.6	8.5	14.9
5.0	99.2	13.4	23.5
10.0	140.3	19.1	33.2
20.0	198.5	27.1	47.2

6.2.1 Microwave frequency filtering

To find the noise seen by the junction, we need to model the transmission of the distributed Johnson noise along the cables. To simplify the calculation, I model the current bias line as two pieces of transmission line at two different temperatures,

although in reality there is a temperature gradient along the cable. I assume the temperature of the first transmission line is T_1, which is somewhere around 100 K and the second piece has a much lower temperature T_2 of around 25 mK. I use the circuit in Fig. 6.6 to model the two transmission lines.

I will assume the second transmission line with a characteristic impedance Z_2 is so lossy that in the frequency of interest $\alpha d \gg 1$, where α is the real part of the propagation constant and d is the length of the cable. In this case, the effect of the Johnson noise due to the real part of the first cable impedance Z_1 on the load formed by the LC filter and the junction, can be described by an effective voltage source V_{N1} with a source impedance of Z_2 [see Fig. 6.6(b)]. The mean-squared value of this effective voltage source in the frequency range of f to $f + df$ is given by

$$dV_{N1}^2 = \frac{4\hbar\omega \mathrm{Re}(Z_1)df}{\exp\left(-\frac{\hbar\omega}{k_B T_1}\right) - 1} \cdot \left|\frac{2Z_2}{Z_1 + Z_2}\right|^2 \exp\left(-2\alpha d\right) \tag{6.6}$$

The noise generated by the transmission line sitting at a temperature of T_2 can be replaced by another voltage source whose source impedance is also Z_2 and its mean-squared value is given by

$$dV_{N2}^2 = \frac{4\hbar\omega \mathrm{Re}(Z_2)df}{\exp\left(-\frac{\hbar\omega}{k_B T_2}\right) - 1} \tag{6.7}$$

Therefore the effect of the two noises is equivalent to a noise V_N with a mean-squared value given by

$$dV_N^2 = dV_{N1}^2 + dV_{N2}^2 \tag{6.8}$$

Note that this noise is not directly seen by the junction due to additional filtering by the LC filter. However, since the LC filter is lossless, the noise given by Eq. 6.8 will set the effective temperature of the junction. It is the noise spectral density at the junction plasma frequency that defines the junction temperature.

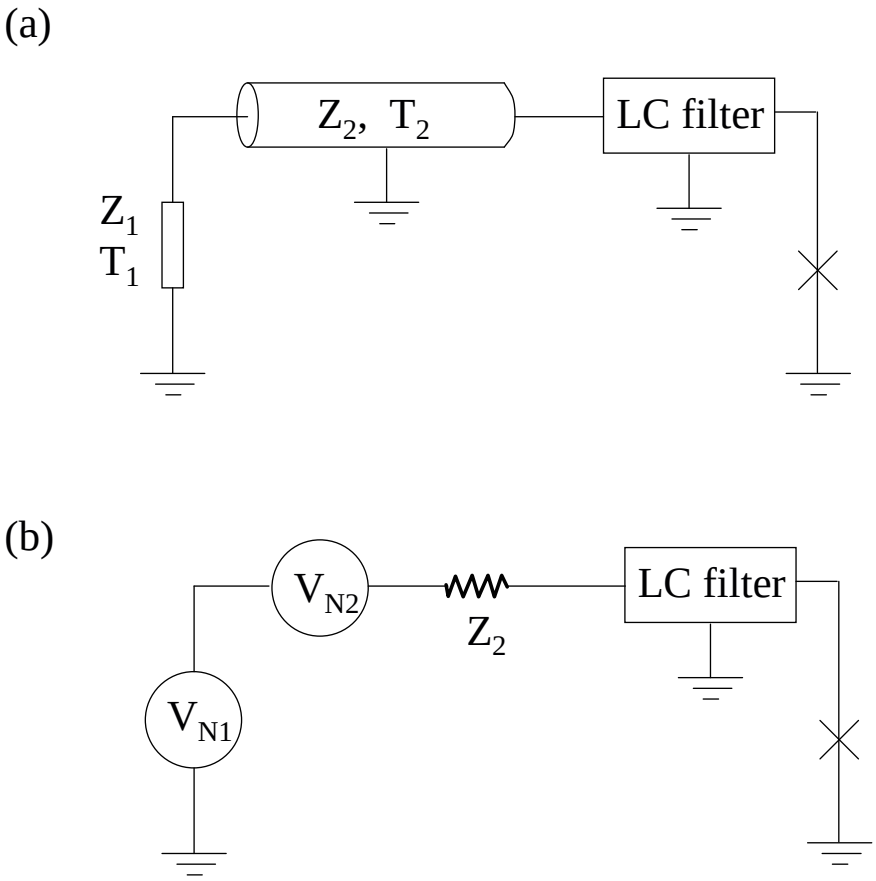

Figure 6.6: Circuit model for noise in the transmission lines. In (a), I model the first transmission line as an impedance of Z_1 sitting at temperature of T_1. I assume the second transmission line has an characteristic impedance of Z_2 at temperature T_2. In (b), I model the effect of the two transmission lines as two effective noise sources V_{n1} and V_{n2} in series with an impedance Z_2. Note the LC filter can be assumed to be non-dissipative.

To see the effect of the hot first transmission line, I introduce an effective temperature T_j that the junction sees such that

$$dV_N^2 = \frac{4\hbar\omega \mathrm{Re}(Z_0)df}{\exp\left(-\frac{\hbar\omega}{k_B T_j}\right) - 1} \mathrm{Re}(Z_0)df \tag{6.9}$$

For the Thermocoax, $Z_2 = 17\ \Omega$. Assuming $Z_1 = 50\ \Omega$, T_1 =100 K and T_2 =25 mK, we can calculate T_j as a function of the attenuation $A = 20\alpha d/\ln 10$. We choose two representative plasma frequencies 5 GHz and 10 GHz to calculate T_j. The results are shown in Table 6.3.

Table 6.3: Junction temperature vs. attenuation of the transmission line

Attenuation (dB)	T_j for 5 GHz (mK)	T_j for 10 GHz (mK)
10	7684	7794
20	871	976
30	168	241
40	69	115
50	42	74
60	31	55
70	26	43
80	25	36
90	25	31
100	25	27

From the above table, we can see that for a junction frequency of 5 GHz, the first 60 dB attenuation reduces T_j to 31 mK. However, in the case of 10 GHz, an attenuation of 90 dB is required to achieve the same temperature. Nevertheless, as we can see from Table 6.2, the attenuation provided by the Thermocoax is enough to provide the required filtering in the 5 to 10 GHz frequency range.

In the experiment with the LJ-isolated Josephson junction, we use niobium cable to replace the Thermocoax to avoid heating in the flux bias line. In this case we need some additional ways to provide attenuation in the microwave frequency range. One way is to use copper-powder filters [120, 121, 122]. In these filters, the inner conductor and the outer wall of the filter are made of copper. The hollow space inside the filter is potted with oxidized copper grains (typically 30 μm in diameter) and Stycast epoxy. The behavior of a dilute Cu-powder filter can be modeled using the conductance $g(\omega)$ of a granular dielectric material,

$$\frac{1}{g(\omega)} = \frac{1}{j\omega C_{gg}} + a_g\sqrt{\omega} \tag{6.10}$$

where C_{gg} is due to inter-grain capacitance, and a_g is a coefficient that describes the skin-depth effect of the resistance across each grain. Substituting Eq. 6.10 into Eqs. 6.4 and 6.5, one can find the real part of the propagation constant and the attenuation. The conductance through the granular dielectric material is zero at dc and increases as inter-grain impedance decreases. However above some frequency where the skin depth in the copper grain is about the grain size, the resistance across each grain will increase, which results in increased attenuation at high frequencies.

Figure 6.7 shows the outside of one of the Cu-powder filters we built. Note the SMA connector in the middle of the filter is for capacitive coupling of microwaves to the current bias line. With this design we achieved good thermalization for the inner connector of the microwave cable and additional filtering for the microwave cable. The measured attenuation from input to output at 4 K is above 80 dB between 1 GHz and 20 GHz.

6.2.2 rf filtering

Microwave filtering is essential to prevent high frequency noise from getting to the junction and to allow the junction to be at the same temperature as the mixing

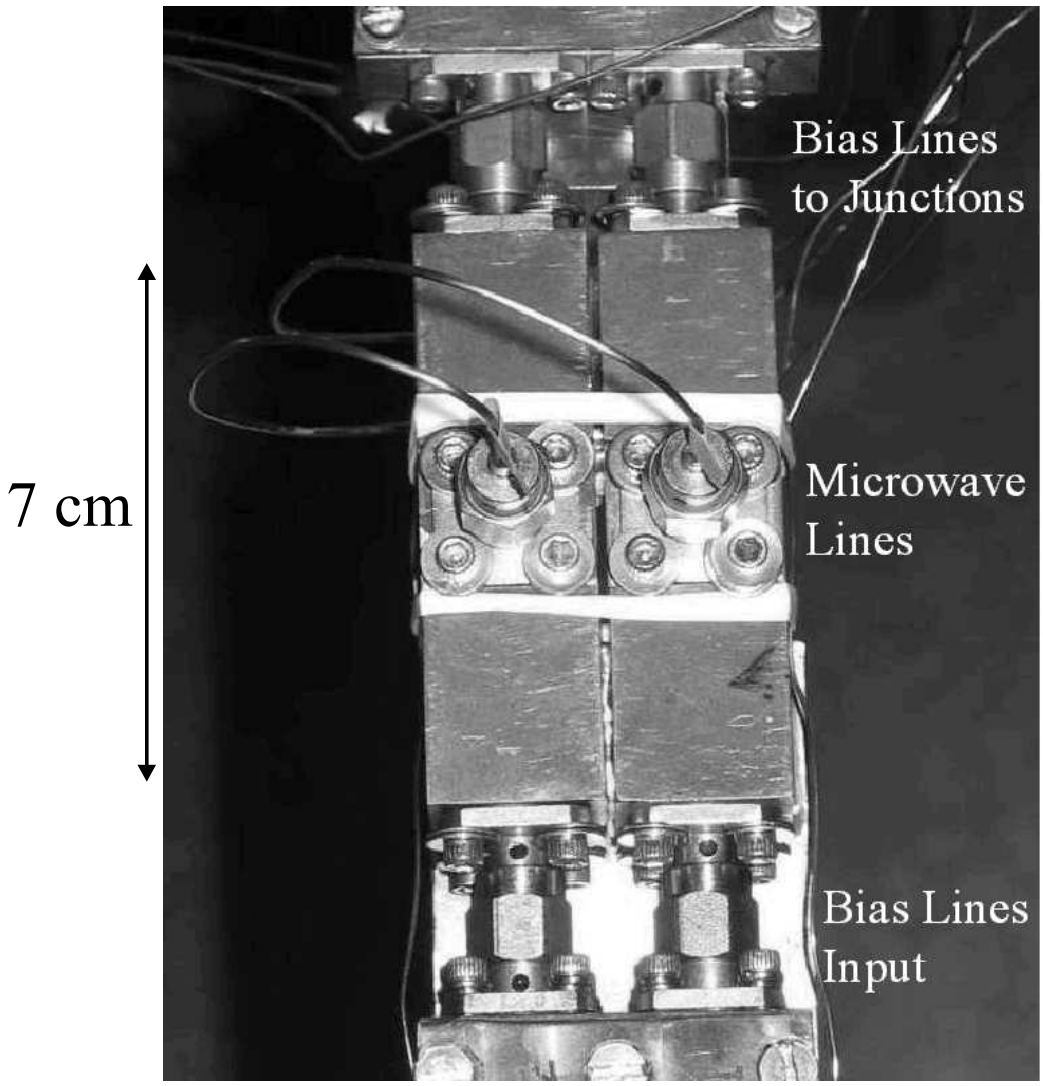

Figure 6.7: The Cu-powder microwave filter. Microwaves are capacitively coupled to the current bias lines at the middle of the filter.

chamber of the fridge. However, according to our discussion in Chapter 4, low frequency noise can induce decoherence. Therefore we need low frequency filtering too. In order to have the low frequency noise reasonably filtered out, we need to have effective filtering from 1 MHz to a few hundred MHz where the microwave filter starts to provide filtering. Below 1 MHz the first transmission line (about 50 Ω at 100 K) still sees the large bias resistor at room temperature which is usually larger than 50 kΩ. Therefore below 1 MHz the noise mainly come from the bias resistor at 300 K. However above 1 MHz, the current noise is essentially dominated by the 50 Ω transmission line at 100 K. Therefore we have to have low-pass filters after the first transmission line. For the cables installed in our fridge, if we have a low-pass filter whose rolloff frequency is 1 MHz, we should have only about 1 nA of current noise from the hot bias resistor and the cables.

In the various experiments we have performed, we tried several kinds of low-pass filters with different rolloff frequencies.

First, we just used a 250 Ω NiCr thin-film resistor mounted on the Mixing chamber to provide filtering. Due to the capacitance of the cable after the resistor, which is about 100 pF, we create a RC filter that has a 3 dB point of 6 MHz. This simple RC filter functioned to some degree and the noise from the hot environment is certainly less than the inherent current noise in the surface-mounted LC resonator (see Chapter 4). The measurement in sample LCJJ-Al was carried out using this filter.

The next filter we tried is a simple commercial LC T-filter [123] manufactured by Mini-Circuits with a nominal 3-dB point of 1.9 MHz at room temperature. The ceramic capacitor has a capacitance of 2 nF, and the inductor is a coil of several turns of copper wires wound on a ferrite core. However as we cooled down the filter, we found its 3-dB point increased to 30 MHz. This is presumably due to the freezing of the permeability of the ferrite core once the temperature is below the Curie temperature. The measurement on sample LCJJ-Nb1 was carried out using this filter.

To avoid this problem we used non-ferrite core inductors and built our own low-pass filter from multi-pole LC stages with 3-dB points ranging from 1 MHz to 100 MHz. Figure 6.8(a) shows a photo of our home-made filter. The capacitors are from American Technical Ceramics [124] and the inductors are from Coil Winding Specialist [125]. The 3-dB point of the filter is around 1 MHz, and attenuation of above 40 dB is achieved from 50 MHz to 10 GHz. The low frequency measurement (see Chapter 8) on sample LCJJ-Nb2 was performed using this rf filter.

Although we had sufficient filtering using the home-made LC filter, we paid a price in reduced bandwidth. In the timing experiment I performed (see Chapter 9), there is a high demand on the rise time of the signal. This means we need to open up the bandwidth perhaps at the price of allowing more noise to reach the junction. Since there is already 10 nA of current noise associated with the on-chip LC filter, we have room to increase the 3-dB point of the LC filter. We thus took out the low frequency stages in the filter and only kept a 1.1 nH-100 pF-1.1 nH T-filter inside. A photo of this filter is shown in Fig. 6.8(b). The high frequency measurement (see Chapter 9) on sample LCJJ-Nb2 was performed using this filter. We also used slightly different inductance values for the measurement on sample LJJJ-Nb; in this case the filter is a 3.3 nH-100 pF-3.3 nH T-filter and the measured 3 dB point of this filter is about 12.5 MHz.

Since LC filters do not cause heating, we mounted them on the mixing chamber to provide rf filtering. On the other hand, the LC filters can cause ringing in the voltage signal (see below) and produce resonant structure in the noise spectral density. A different way to provide rf filtering is to use low-pass RC filters, as we used for sample LCJJ-Al. A resistance of 2 kΩ at the 4 K stage with the capacitance from the transmission line will provide good filtering for frequencies of 2 MHz and above. In this case the thermal noise from the bias line will be dominated by the 2 kΩ resistor.

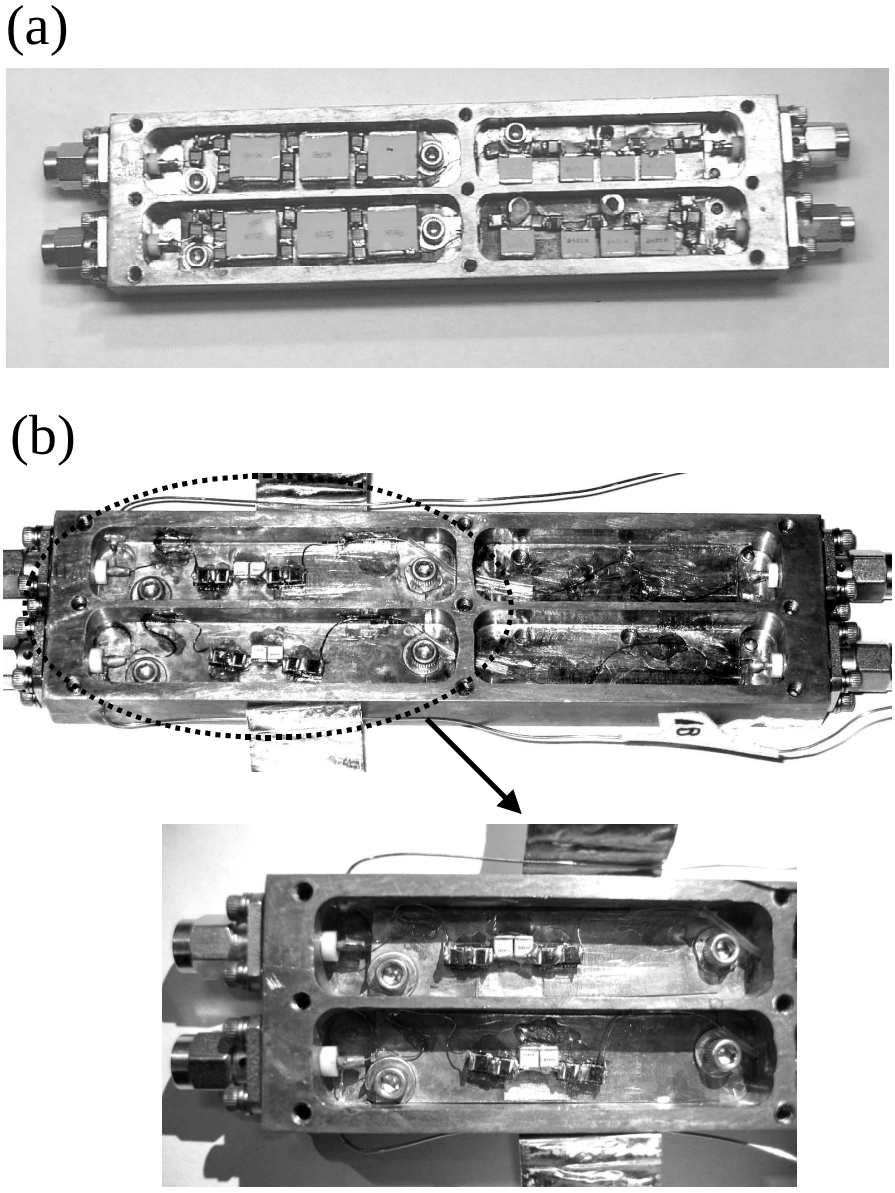

Figure 6.8: LC rf filters. (a) Multi-stage LC filter with a 3 dB point of 1 MHz. (b) Single-stage T filter with a 3 dB point of 16 MHz. (c) Detail of the T-filter.

6.2.3 The voltage signal bandwidth

In our measurements, we monitor the voltage across the junction. But all the electronics are at the top of the cryostat and the junction resistance is not matched to the cable impedance. In this case the voltage signal is limited by the capacitance in the cables. The signal bandwidth is similar to the bandwidth for noise to transmit from the top to the bottom. However, due to the non-linear I-V characteristics of the junction, the two bandwidths are different. Here we use a simple LC model to analyze the relation between the two (see Fig. 6.9).

When we slowly increase the bias current, the current will all go through the junction when it is in the zero-voltage state. Basically the junction behaves like a short. However, at some bias current, the junction quickly switches to a finite voltage state. In order to measure the switching current, we used a peak detection circuit to trigger on the switching voltage. Because the uncertainty in measuring the time when the junction switches is determined by the ratio of voltage noise to the signal slope, a large signal slope is desired.

Let us assume the junction switches to a finite voltage state at a bias current I_s (which is slightly smaller than the critical current of the junction). Since the junction impedance suddenly becomes very large, the voltage cross the junction rapidly increases from zero to the gap voltage V_g (400 μV for Al and 2.8 mV for Nb), we can write down the circuit equation for the current $I(t)$ flowing through the filter inductor L,

$$LC_1\ddot{I}(t) + (\frac{C_1}{C_2} + 1)I(t) = I_s \tag{6.11}$$

Notice that just before the junction switches, all the current goes through the inductor and there is zero voltage across C_1 and C_2. Therefore the initial conditions for Eq. 6.11 are $I(0) = I_s$ and $\dot{I}(0) = 0$. Solving Eq. 6.11, we obtain

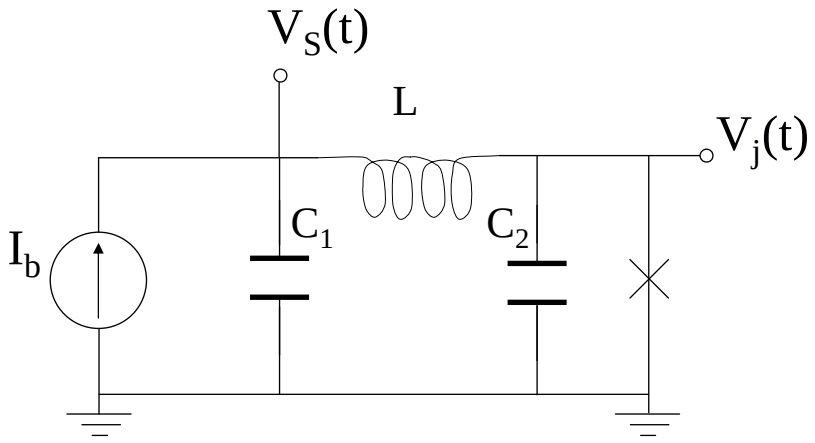

Figure 6.9: A simplified circuit model for analyzing the voltage signal V_S developed when the junction switches. I model the transmission line above the LC_2 filter as a capacitance C_1.

$$I(t) = \frac{C_1}{C_1 + C_2} I_s \cos \omega_0 t + \frac{C_2}{C_1 + C_2} I_s \tag{6.12}$$

where $C = C_1 C_2/(C_1 + C_2)$ and $\omega_0 = 1/\sqrt{LC}$. Then we can find the voltage across C_2 (or the junction) as

$$V_j(t) = \frac{C_1 I_s}{C_2(C_1 + C_2)} t + \frac{I_s}{C_1 + C_2} \frac{\sin(\omega_0 t)}{\omega_0} \tag{6.13}$$

With Eq. 6.13 we now can calculate how long it takes for the voltage across the junction to reach the gap voltage, however what we really measures is the voltage across C_1. We denote this voltage as our signal voltage V_S. Clearly, how this voltage increases depends on the behavior of $V_j(t)$. If the time it takes for $V_j(t)$ to reach the gap voltage is on a time scale much smaller than $1/\omega_0$, then the time scale for V_S to increase will be set by ω_0 and will be independent of the junction critical current. However in our experiments, we observed a time scale that depends on the junction critical current, suggesting we are not in this limit.

In fact under our typical parameters($I_s < 100$ μA, $V_g = 3$ mV, $C_1 \approx 1$ nF, $C_2 \approx 1$ nF, $L \approx 1$ μH), the time it takes for V_j to increase to the gap voltage is larger than $1/\omega_0$. Under this condition, we find $V_S(t)$ is given by

$$V_S(t) = \frac{I_s}{C_1 + C_2} t - \frac{I_s}{C_1 + C_2} \frac{\sin(\omega_0 t)}{\omega_0} \tag{6.14}$$

This kind of oscillation structure in the voltage signal was indeed observed in our experiments (see Fig. **??**), although it was heavily damped due to resistance in the system, which is not included here. The slope of this voltage signal is

$$\frac{dV_S(t)}{dt} = \frac{I_s}{C_1 + C_2} - \frac{I_s}{C_1 + C_2} \cos(\omega_0 t) \tag{6.15}$$

Analysis shows that the maximum slope occurs at $t_m = \pi/\omega_0$, and its value is given by

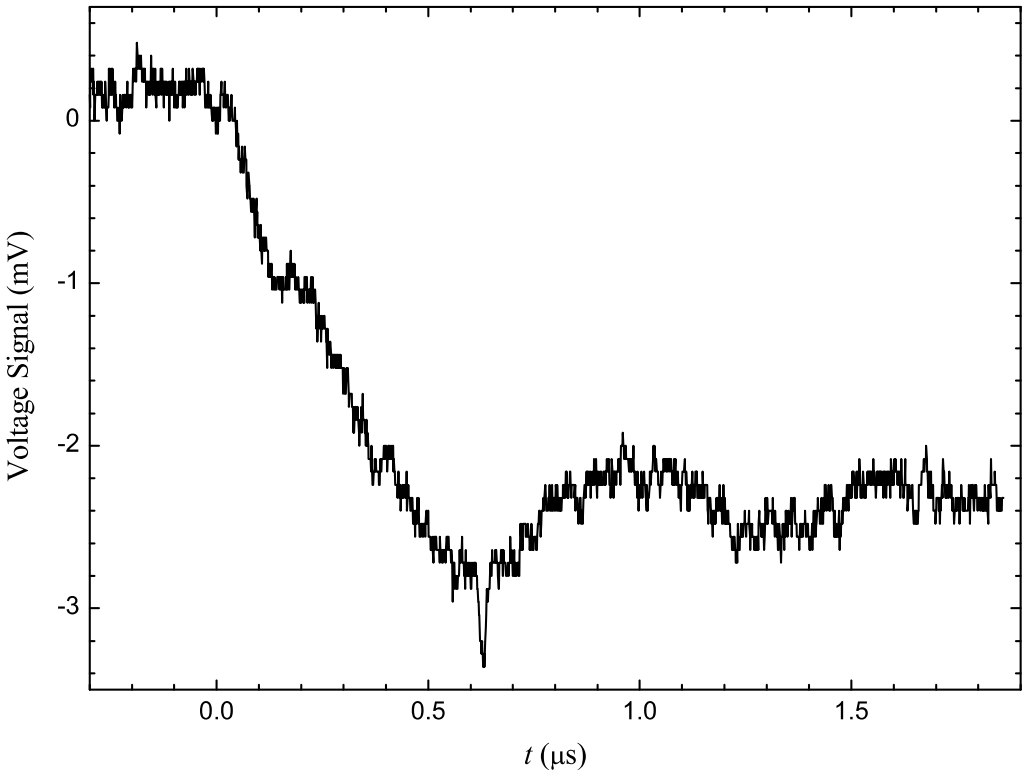

Figure 6.10: Switching voltage signal measured at the top of the cryostat. Shown here is an average waveform of four switching voltage signals taken directly by the Tektronix TDS1002 digital scope (i.e. before the signal is fed into the preamplifier) for a junction with a critical current of 10 μA. Ringing in the signal is clearly visible. The small dip at -3 mV is due to the triggering of the scope.

$$\frac{dV_S(t)}{dt}|_{t=t_m} = \frac{2I_s}{C_1 + C_2} \tag{6.16}$$

In other words, the slope of the voltage signal is equivalent to that from a capacitance of $(C_1 + C_2)/2$ being charged by a current I_s. Of course we need to keep in mind that Eq. 6.16 is valid only if the maximum slope is less than $V_g\omega_0/\pi$. In other words, when the LC filter is there, the maximum signal slope we can achieve is $V_g\omega_0/\pi$. But when the critical current is small, then we will get an even smaller slope than is given by Eq. 6.16. In our case, when the critical current is less than 40 μA, the signal slope will depend on the critical current.

Based on the above analysis, the maximum voltage signal slope is

$$\frac{dV_S}{dt}|_{max} \cong \frac{V_g\omega_0}{\pi} \tag{6.17}$$

For our circuit parameters, it should be around 4×10^4 V/s. In our experiments, we observed a maximum of 2×10^4 V/s. This could be due to the reduction of the bandwidth by the resistance in the bias lines.

If we assume the total equivalent input noise of the amplifier is given by v_n, then we can obtain the time resolution σ_t in detecting when the junction switches,

$$\sigma_t = \frac{v_n}{\frac{dV_S}{dt}|_{max}} \tag{6.18}$$

For the amplifiers used in our experiment, we have $v_n = 500$ nV, leading to a time resolution of 100 ps for junctions with large critical currents where the signal speed is dominated by the line bandwidth (Eq. 6.17) rather than the charging effect (Eq. 6.16).

6.3 Instrumentation

The experimental technique we use involves ramping the bias current through the junction and measuring when the junction switches from the zero-voltage state to the finite-voltage state. With this ramp technique, we measure the escape rate of the junction for a range of bias currents. The basic instruments required in this experiment are an arbitrary waveform generator, low noise amplifiers to amplify the junction switching voltage, detection circuits to detect the amplified signal and precise timing circuits. Figure 6.11 shows a block diagram of the instrumentation setup used in the experiment.

The measurement procedure is as follows. A timer is started when the bias current starts to ramp. At some bias current which is very close to the critical current of the junction, the junction switches to a finite-voltage state. This voltage pulse is amplified and then detected by a Schmitt trigger which converts the signal to a digital pulse. This digital pulse is optically coupled to a receiver outside the screened room and used to generate a second digital signal that triggers the timer to stop counting. The time elapsed is recorded and converted to a current based on the functional form of the ramp. We repeat this measurement about 10^5 times to build up a histogram of the currents at which the junction switched.

Thus we need to measure two quantities, when the junction switches, and the bias current at that time. The former requires good time resolution. The latter requires calibration of the current ramp.

Good time resolution demands high bandwidth and low noise amplifiers. In the above section, we have already discussed filtering of the thermal noise from the bias lines, but extrinsic noise from function generators and external interference from the room can also cause problems.

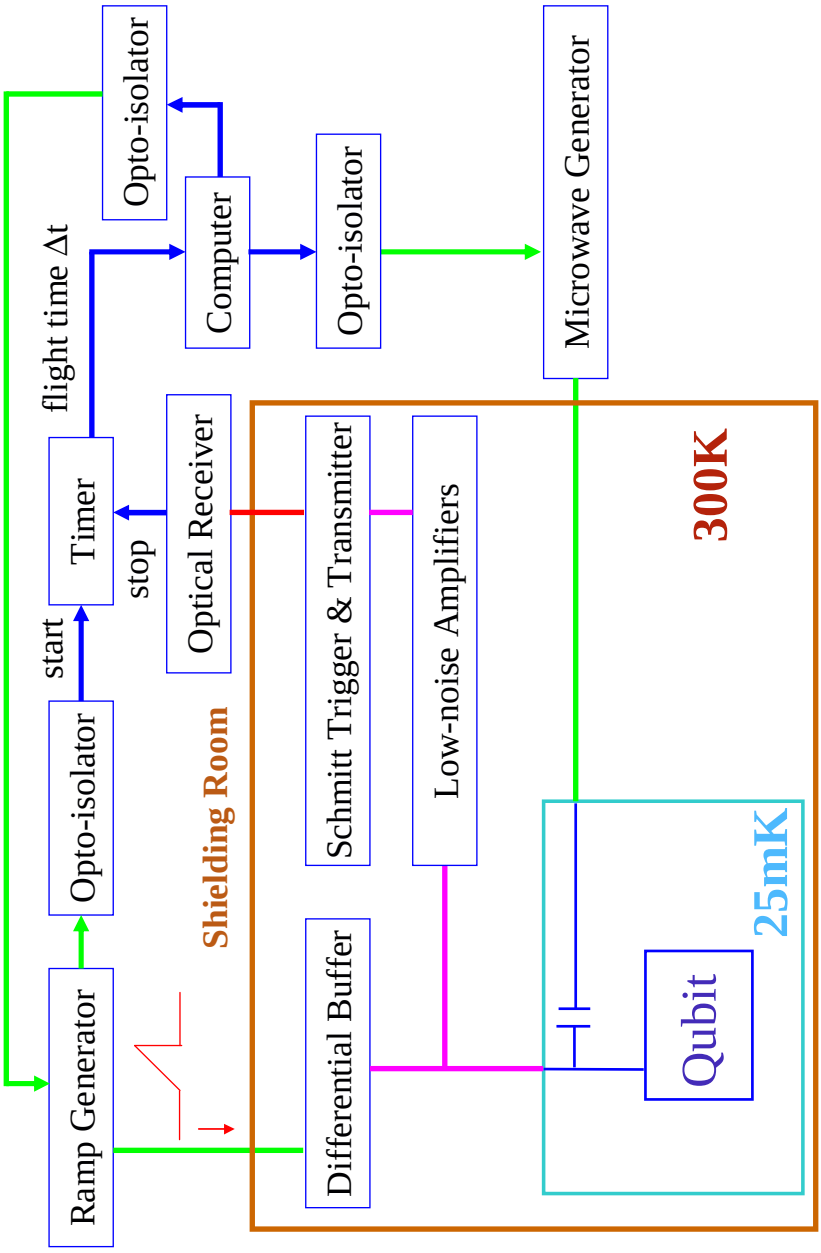

Figure 6.11: Block diagram of the experiment. The differential buffer has the same ground as the cryostat, but the shields of the two inputs are grounded at the screened room wall. The output from the Schmitt trigger is optically coupled to the receiver outside the screened room.

6.3.1 Function generator and buffer

The important characteristics for the function generators, used in our experiments for the current ramp, are low noise and long-time stability. We used an Agilent 33120A 12-bit arbitrary waveform generator in our experiments.

The arbitrary waveform generator, which is built from digital circuits, voltage references and resistors, has its own intrinsic noise. It is generally true that the noise at the output is smaller than the precision set by the bits of the Digital-Analog Converter (DAC). But sometimes the noise can be lower than the precision. The Agilent 33120A has a maximum output of 20 V (p-p), and a total white noise of 200 μV (p-p) when the function generator is outputting a positive ramp with an amplitude of 5 V. This performance is close to that of a 16-bit DAC. However, we have found this model has some peculiar noise at 1 kHz with a level that is equivalent to the white noise background. Since in our experiments we use a ramp with frequencies around 1 kHz, this noise cannot be filtered out.

We also tried a 16-bit arbitrary waveform generator from Tektronix, and found its white noise is close to that of the Agilent 33120A, but it does not have excess low frequency noise. Its cost is one order of magnitude higher than the Agilent 33120A due to its ability to generate various pulse shapes. The white noise level of other 12-bit functions we looked at was much worse than the Agilent 33120A, and some of them also have excess low frequency noise.

I note the actual current noise that goes to the junction will depend on the bias resistor. If we use a bias resistor of 400 kΩ (this is for a junction with a critical current of 13 μA), we will have a current noise of 1 nA (p-p). If 1 nA of current noise goes directly to the junction, it will limit the measured Q to be around 500. Using a broadband isolation scheme (see Chapter 5), we can achieve a significant reduction in the current noise that goes to the junction.

The second requirement on the function generator is its long-time stability. As

mentioned above, we need to repeat the junction switching measurement many times to build a switching histogram. This means we need the electronics to be stable over a time period of hours to tens of hours. Since we do not directly record the bias current at which the junction switches, drift of the ramp function will lead to errors in the switching histogram. Indeed, the Agilent 33120A has this problem: the phase error of this function generator can accumulate to a degree that is beyond the level we can accept. Fortunately, Agilent was able to provide some fixes to correct this problem to a degree that it is no longer noticeable in our measurements.

The digitization of the output due to the DAC is not a problem here since we use a low frequency ramp. A low-pass filter placed after the output of the function generator can smooth the waveform. The maximum frequency waveform that the Agilent 33120A can generate is 15 MHz.

The output from the function generator is fed through the screened room wall without any filtering (for a waveform with high frequency components) or through a 7-kHz T-filter (for a slow ramp). The ramp is then sent to a battery-powered differential buffer. If the differential buffer is not used, the rest of the system (the junction, voltage amplifiers, and Schmitt trigger) are grounded at the screened room wall through the outside jacket of the bias cable. However the rest of the system is also connected to the top of the cryostat, which is always connected through the refrigerator's still pipe to the screened room wall. These two separate grounds produce a ground loop. This means there will be a large common 60 Hz signal on both the core and the shields of the bias cable. Using a differential buffer prevents this problem. There are two kinds of buffers I used in my experiments: one was the Blue amplifier that was designed by Fred Cawthorne [108] and the other type was a simple differential amplifier built from op-amps (AD797 and AMP03).

I used the Blue amplifier with a unity gain and a rolloff frequency of 10 kHz for slow ramps. With this amplifier the voltage noise spectral density from the buffer is about 30 nV/$\sqrt{\text{Hz}}$. However if I use the Blue amplifier for a dc bias, I have to set

the roll-off frequency at 100 kHz. In this setting the noise spectral density goes up to 100 nV/$\sqrt{\text{Hz}}$.

In addition to the Blue amplifier, we built our own buffers using low-noise op-amps. One type of op-amp we used is the AD797 made by Analog Devices with a voltage noise of 1.0 nV/$\sqrt{\text{Hz}}$. We used this op-amp to make a differential amplifier with an input impedance of 1 kΩ and a voltage noise of 6 nV/$\sqrt{\text{Hz}}$. The low input impedance helps to keep the voltage noise low. A balance resistor must be used on the negative input, since the function generator has an output impedance of 50 Ω. Because the AD797 is a very unstable chip, a low-pass RC circuit (typically $R = 10$ kΩ, $C = 168$ pF) is added as a load for the buffer to function properly. We also used AMP03 chips which are differential amplifiers with an input impedance of 25 kΩ. These amplifiers are not sensitive to a lack of balance with the output impedance of the function generator. The differential amplifier built from this chip has a voltage noise of 30 nV/$\sqrt{\text{Hz}}$ and functions with a bandwidth of 1 MHz. Note the power for both the Blue amplifier and the home-made buffer are provided by 12 V lead-acid batteries.

After the buffer, we use a bias resistor to convert the bias voltage to a bias current. We choose a resistance as large as possible to reduce current noise. A switched shorting box follows this bias resistor to protect the junction when it is not being measured.

6.3.2 Ultra-low noise amplifier

When the junction switches to its finite-voltage state, a voltage signal (400 μV for Al junction and 2.8 mV for Nb junction) is developed at the junction and propagates up the wires to the top of cryostat, where it is amplified by a low-noise voltage amplifier. The basic requirements for a good amplifier for detecting pulses are low noise, low drift and wide bandwidth.

One of the amplifiers used in our early experiments is the Stanford Research Model 560 (SR560) preamplifier[1]. The SR560 has a voltage noise of 4 nV/$\sqrt{\text{Hz}}$ for gains above 100 and a bandwidth of 1 MHz. It provides single-ended measurement or can be used in a differential mode. The low-pass and high-pass filters (6dB/decade or 12dB/decade) built inside the amplifier are also very useful[2].

This amplifier is useful in terms of its versatility, but the noise is limited to 4 nV/$\sqrt{\text{Hz}}$ and the bandwidth is limited to 1 MHz. The next generation of amplifiers used in our experiments was built from silicon JFETs. The type of JFET we used is a 2SK117 (Silicon N Channel Junction) from Toshiba. It is generally used for low noise audio amplifiers. It has a voltage noise of 1 nV/$\sqrt{\text{Hz}}$ from 1 kHz and above and has a very low corner frequency for $1/f$ noise ($\sim$100 Hz). The first preamplifier we made was just a single 2SK117 in a common source configuration with a drain resistance of 1 kΩ [see Fig. 6.12(a)]. We measured a gain of 14 and a bandwidth of 3 MHz. The voltage noise of this preamplifier is less than 1 nV/$\sqrt{\text{Hz}}$ and its current noise is about 20 fA/$\sqrt{\text{Hz}}$ at 1 MHz as a result of low gate-to-channel capacitance ($\sim$10 pF). This contributes an additional voltage noise of 2 pV/$\sqrt{\text{Hz}}$ for a lead resistance of 100 Ω in the bias line and can be completely neglected. Note that in this circuit the gate of the JFET is directly connected to our junction without AC coupling. This is because large noise at low frequencies will be present if an AC coupling circuit is used in front of the gate. The gain variation induced by the this DC coupling configuration (the gate voltage now depends on the junction bias current) is negligible.

---

[1]For measurements on our resistively-isolated junction, we used the Blue amplifier. This was not ideal but acceptable since the voltage signal is very slow due to the large isolation resistance. For experiments on other junctions, the Blue amplifier is too slow and also too noisy.

[2]In our early measurements, the voltage line shared the same line with the current bias line, therefore we have a large background signal due to the 100 Ω resistance in the bias line. High-pass filters were used to remove this background.

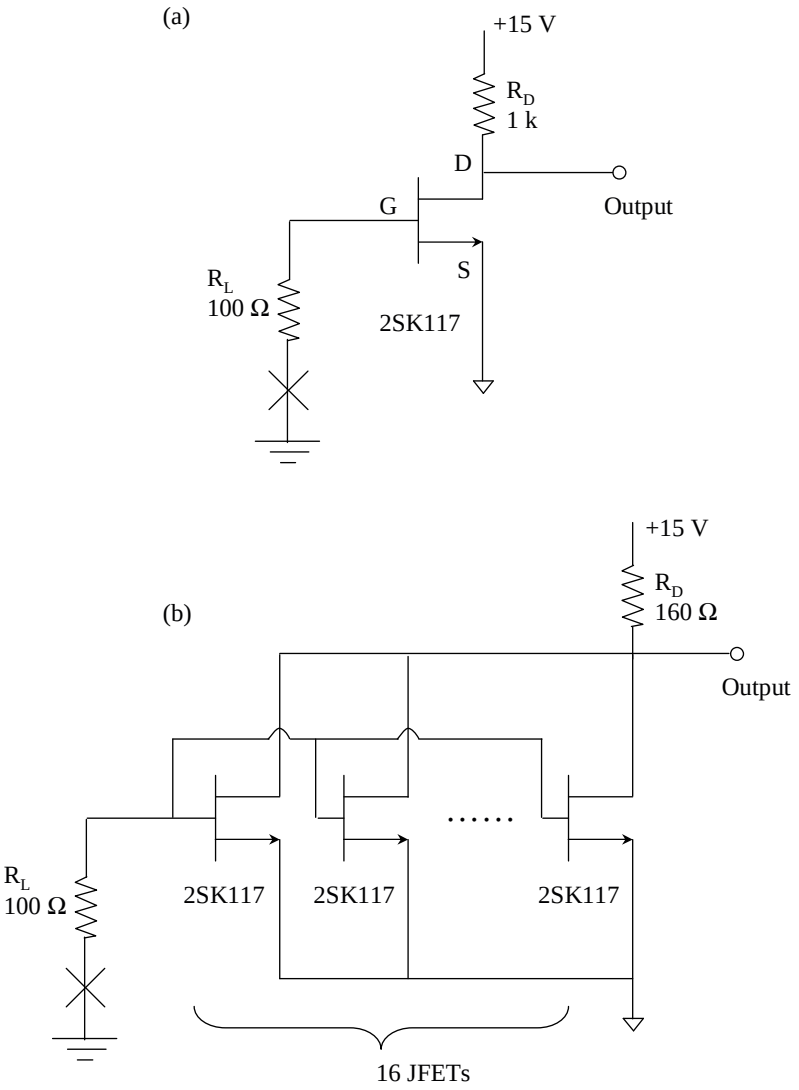

Figure 6.12: An ultra-low noise JFET preamplifier. (a) A single JFET amplifier with a gain of 14, a voltage noise of 1 nV/$\sqrt{\text{Hz}}$ and a current noise of 20 fA/$\sqrt{\text{Hz}}$. (b) A 16-JFET amplifier with a gain of 40, a voltage noise of 0.3 nV/$\sqrt{\text{Hz}}$ and a current noise of less than 1 pA/$\sqrt{\text{Hz}}$.

To further reduce the noise of the preamplifier, we wired sixteen 2SK117 JFETs in parallel to reduce the voltage noise [126]. This 16-JEFT amplifier is shown in Fig. 6.12(b). The voltage noise of a FET is mainly from the Johnson noise in the conducting channel and is given by [127]

$$S_V = \sqrt{8k_BT/3g_m} \tag{6.19}$$

where g_m is the transconductance of the FET. With N parallel JFETs, the total transconductance will be N times a single FET, reducing the voltage noise to $1/\sqrt{N}$ of a single FET. Since the transconductance is already very high, only a small drain resistance is required to get a reasonable gain. A small resistance is also enough to bias the JFETs since the drain currents from all the FETs will flow through this resistor. We used eight 20 Ω resistors for the drain resistance. We measured a gain of 40 and a voltage noise of less than 0.3 nV/$\sqrt{\text{Hz}}$ for this amplifier. The measured bandwidth for this amplifier is above 2 MHz and its current noise is less than 1 pA/$\sqrt{\text{Hz}}$, which contributes a noise of 0.1 nV/$\sqrt{\text{Hz}}$ for a lead resistance of 100 Ω.

We also need to include the Johnson noise generated by the lead resistance, especially by the first section of the cable since it is at 300 K. The hot resistance is about 20 Ω, corresponding to a Johnson noise of 0.6 nV/$\sqrt{\text{Hz}}$. To make full use of our ultra-low noise amplifier, we replaced the first section of the voltage line by a 40-inch LakeShore semi-rigid cable (twisted Manganin wires used previously) that has a resistance of 4 Ω.

When the amplifier is in place for a measurement, the total input noise spectral density S_{tot} is given by

$$S_{tot} = S_V + S_I R_L^2 + 4k_BTR_L \tag{6.20}$$

where S_V and S_I are the 16-JFET amplifier's voltage and current noise, respectively,

R_L is the lead resistance, and T is the temperature of the load resistance. For our amplifier, we find a total root voltage noise spectral density of $\sqrt{S_{tot}} = 0.4$ nV/$\sqrt{\text{Hz}}$. Considering the bandwidth of the amplifier is about 2 MHz, we have a total input rms voltage noise of 0.56 μV.

Although the signal is of the order of 100 mV after the preamplifier, it is inconvenient for trigger circuits to trigger on this level of signal. Moreover, the input of trigger circuits usually has large voltage noise ($\sim$1 mV). Therefore it is useful to amplify the signal further by a low noise second-stage amplifier. The SR560 has a voltage noise of 10 nV/$\sqrt{\text{Hz}}$ for gains below 100, which can still contribute significantly to the total noise, so we built our own second-stage amplifiers. The home-made amplifiers use AD797 or AD829 op-amps have a fixed gain of 50, and a bandwidth of above 1 MHz. The intrinsic noise of AD797 is only 1.0 nV/$\sqrt{\text{Hz}}$. However, due to the resistors used in the amplifier, the input voltage noise is about 4.0 nV/$\sqrt{\text{Hz}}$. The amplifier built from an AD829 has the same amount of noise, but it has a larger slew rate (230 V/μs) than the AD797 amplifier (20 V/μs). A circuit schematic of the AD829 amplifier is shown in Fig. 6.13.

The drain resistor has its own Johnson noise. The current noise from the second stage amplifier introduces additional voltage noise after loading on the drain resistance. Each of these contributions is much smaller than the voltage noise of the second-stage amplifier and can be neglected. For this combined two-stage amplifier, we measured a gain of 2000, and an equivalent input voltage noise of 0.4 nV/$\sqrt{\text{Hz}}$ (referred to the input of the first stage amplifier) with a bandwidth of above 1 MHz.

6.3.3 Ultra-low noise power supply

To achieve the above noise level for the combined amplifier, we also need to be careful with the construction of the power supply. The noise on the power supply for the JFET amplifier is 100% coupled to the output of the JFET amplifier and will be

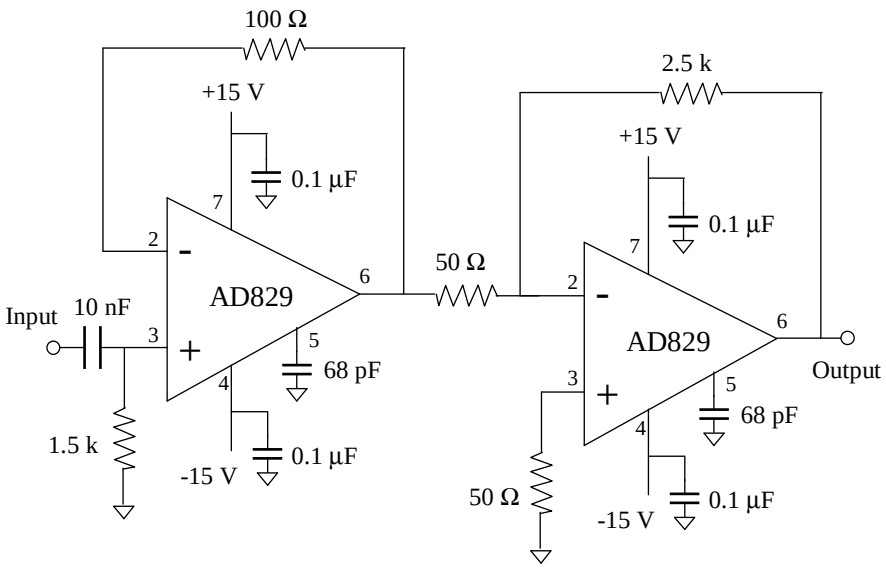

Figure 6.13: The second stage amplifier. The input is AC-coupled with a 3dB point of 10 kHz. The first AD829 chip is a buffer. The second AD829 chip has a gain of 50. Note the 50 Ω resistor on the positive input terminal is for balance so that the effect due to the input bias current can be eliminated.

fed to the second-stage amplifier. Although op-amps have very good power supply noise rejection, it is not sufficient for the kind of noise level we desire. Therefore we built our own ultra-low noise power supplies for the amplifiers.

Figure 6.14 shows the +15 V and -15 V power supplies used in our experiment. Note the power for these power supplies circuits is from two 12 V lead-acid batteries. For the +15 V power supply, when the input voltage changes a little bit, the change will be coupled to the base electrode of the bipolar junction transistor (BJT), therefore the current in the collector electrode will change correspondingly. This causes the voltage across the 15 Ω resistor to change in response. If the gain of the BJT amplifier is right, then the voltage change in the 15 Ω resistor will be exactly the same as the initial change in the input voltage and the output voltage will be kept constant. By tuning the resistance in the emitter to around 7 Ω, we obtained a voltage noise spectral density of 1.0 nV/$\sqrt{\text{Hz}}$ for frequencies 100 kHz and above, and a total rms voltage noise of about 10 μV for frequencies below 100 kHz. The negative power supply works in a similar way, but because the emitter follower always has a gain less than unity, the cancelation is not perfect. We found the -15V power supply has a noise spectral density of 5 nV/$\sqrt{\text{Hz}}$, and the total rms voltage noise for frequencies below 100 kHz is about 50 μV. Since the -15V power supply is only used in the second stage amplifier, this kind of performance is good enough for the applications described here.

6.3.4 Detection circuits

Once we have a large signal (∼5V), we need to detect it and measure when it occurs. Here the zero reference in time is taken to be the start of the ramp. We thus need a trigger circuit to detect the voltage signal, and a timer to count the time elapsed between the start of the ramp and the occurrence of a voltage signal.

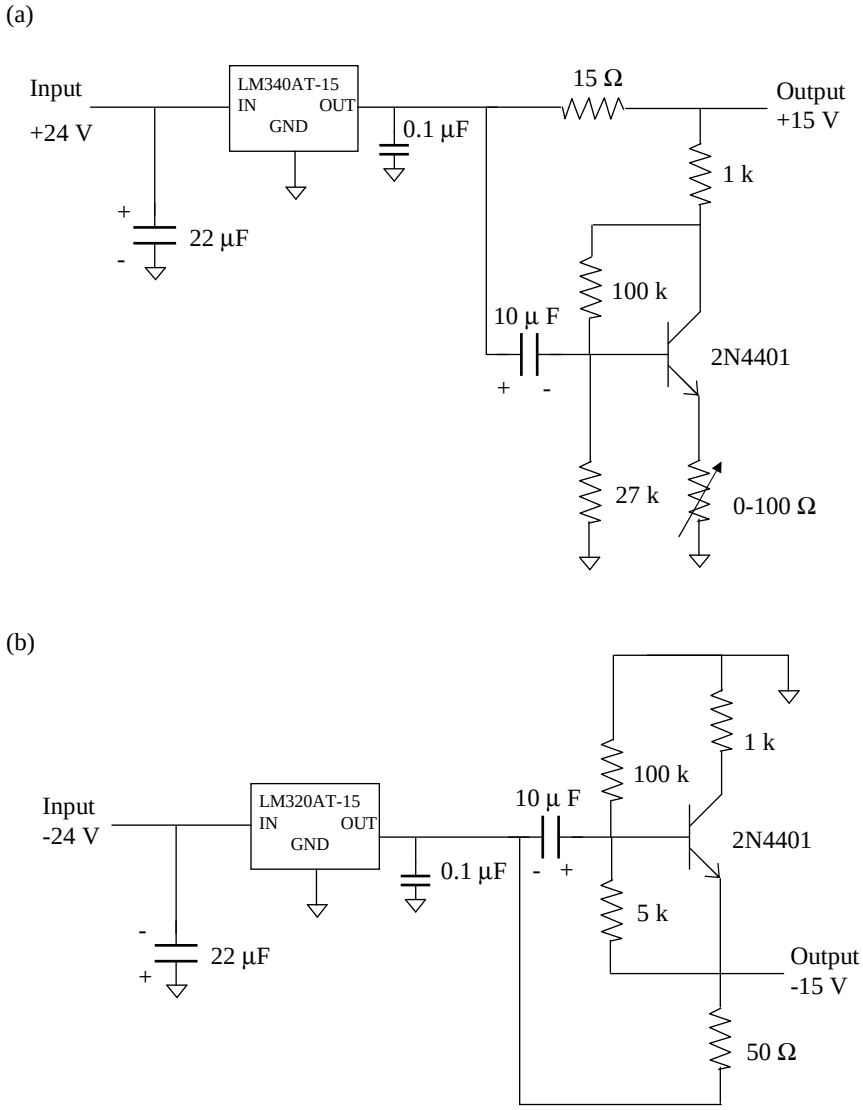

Figure 6.14: The ultra-low noise ±15 V power supplies. Each power supply employs negative feedback with a bipolar junction transistor. A noise spectral density of 1.0 nV/$\sqrt{\text{Hz}}$ is achieved for the +15 V power supply and 5 nV/$\sqrt{\text{Hz}}$ for the -15V power supply. The 24 V input is from two 12 V lead acid batteries in series.

Schmitt trigger and optical transmitter

We could use a timer to directly detect the voltage signal, but then we need to put the timer right next to the output of the second stage amplifier in order to preserve the speed of the waveform. This is not desired because the timer, which must communicate with a computer, can cause grounding and noise problems and affect the performance of the ultra-low-noise voltage amplifiers.

To avoid this problem, we built our own trigger circuit that can run on batteries. Fig. 6.15 shows our trigger circuit, which is basically an adjustable negative level Schmitt trigger with very small hysteresis.

When the voltage decreases below some threshold value, the output of the op-amp will switch from -5 V to 5 V (due to the clamping of the diode, the actual output is -0.7 V or 5 V). The threshold depends on the resistances, and is given by

$$V_{th} = -5\frac{RR_2/(R+R_2)}{R_1 + RR_2/(R+R_2)} - 5\frac{RR_1/(R+R_1)}{R_2 + RR_1/(R+R_1)} \tag{6.21}$$

Thus we can adjust the trigger level by changing R. The hysteresis of the circuit is given by

$$V_{hys} = 10\frac{RR_2/(R+R_2)}{R_1 + RR_2/(R+R_2)} \tag{6.22}$$

and can be made very small by choosing $R << R_1$.

To keep the hysteresis small, we do not want to use a large R to increase the adjustable range of the trigger level. Instead we use two different values of R_2 to provide a large adjustable range for the trigger level. In our case we used 1 kΩ and 4.7 kΩ for R_2 to provide low and high trigger levels.

The power for the Schmitt trigger comes from 12 V lead-acid batteries (5 V and -5 V voltage regulators are also used). Note in Fig. 6.15, the output of the Schmitt trigger is sent to an optical transmitter. By using an optical transmitter, we avoid making electrical connections through the screened room wall and ensure all the

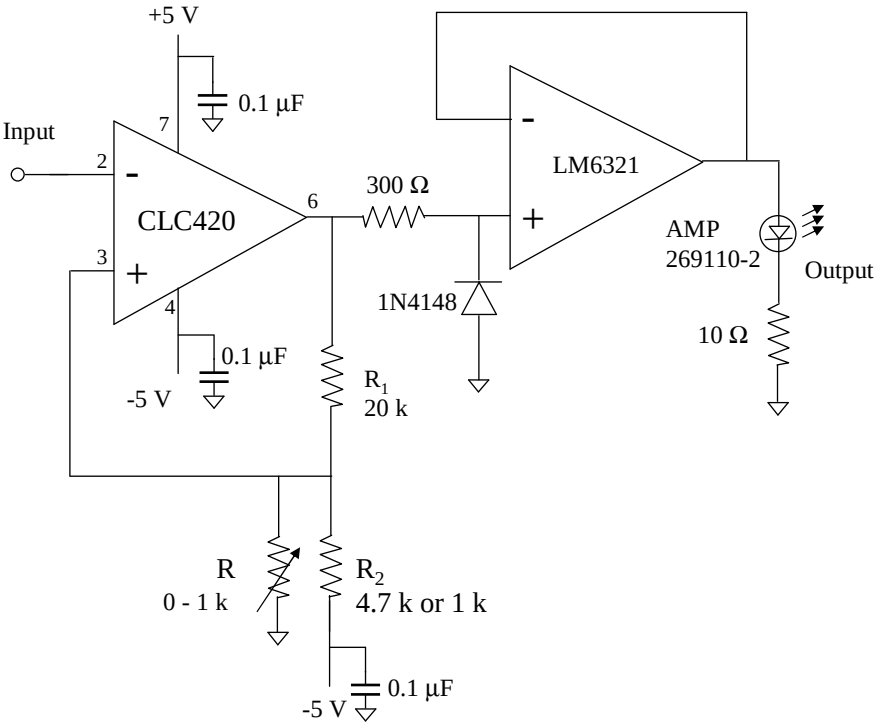

Figure 6.15: The Schmitt trigger. It is built using positive feedback on a fast voltage comparator. The trigger threshold is set by the ratio of R_2 to R_1 with small adjustment by changing the variable resistance R. The output of Schmitt trigger goes to an analog buffer for driving an LED which drains a large current ($\sim$100 mA).

battery-powered electronics inside the screening room are properly grounded.

Optical receiver and timer

The optical output from the transmitter is sent through an optical fiber to a receiver outside the screened room. Another Schmitt trigger is used to convert the small output signal from the receiver to a large digital signal. The circuit is shown in Fig. 6.16. Basically the output of this circuit is high when there is no light at the input and becomes low when light comes in.

The signal from the second Schmitt trigger is fed to the stop terminal of a timer. The timer used in our experiment is a Stanford Research Systems Model 620. The precision of the timer for a single shot is typically 25 ps. [3] We note that the input terminal has a rms noise of 350 μV, which can lead to a large trigger jitter in timing signals with slow transition edges. The start of the timer is triggered by a sync signal from the function generator when the ramp is started.

To prevent forming ground loops and keep the ground of the function generator separated from the grounds of the timer and the computer, we also insert an opto-isolator between the sync output of the function generator and the start input of the timer.

6.3.5 Labview programming

The 'flight' time from the start of the ramp to the arrival of a voltage signal, which is captured by the timer, can be retrieved by a computer through a GPIB interface controlled by a Labview program. This measurement can be repeated as many times as needed, and we typically accumulate 10^5 switching events to generate a histogram.

[3] The absolute accuracy is much worse, typically 500 ps plus that due to an error of about 15 mV in the trigger level.

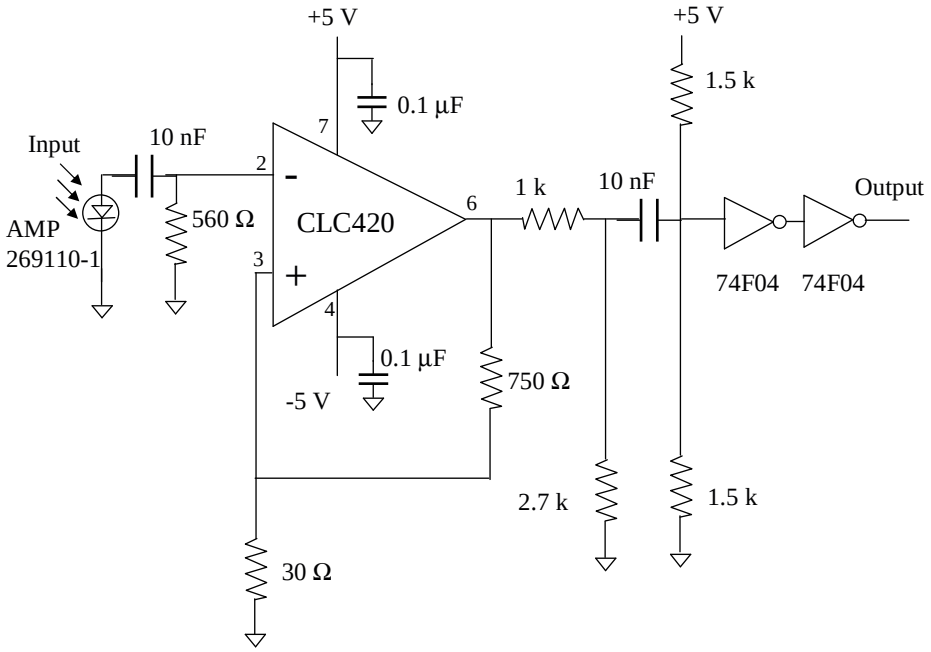

Figure 6.16: The optical receiver and converter. The optical receiver converts the light to a small voltage spike of a few hundred mV and a Schmitt trigger is used to amplify this voltage spike to a negative -5V signal. With AC coupling and adding a 2.5V shift, the signal is converted to a standard TTL signal with high for no light and low for light. A digital buffer is used to drive low input impedance devices if necessary.

Labview programming can also be used to control the parameters of various devices, such as the function generator and the microwave generator. For mapping out the spectra of the system, it is necessary to do a frequency scan. This process can be automated through Labview programming and data can be taken overnight.

Furthermore, we can use the computer to synchronize two devices. In the timing experiment where switching from both junctions is recorded, the synchronization of the two timers can be implemented through Labview programming.

6.4 Summary

In this chapter I discussed the experimental setup involved in this experiment, including the dilution refrigerator, the wiring inside the refrigerator, and the instrumentation. I also discussed the importance of microwave filtering and rf filtering, and how the required filtering was implemented through our wiring inside the fridge. On the apparatus side, I described the demands we have on the signal-to-noise ratio and how these demands were met through our home-made electronics. In short, we need careful wiring of the fridge and high-performance electronics (low noise and large bandwidth) to achieve the kind of sensitive measurements we want.

Chapter 7

Dissipation and Decoherence in Single Qubits

In this chapter, I present measurement results on my samples. In particular I focus on characterization of dissipation and decoherence in Josephson junction qubits. The two important time scales that I want to deduce from my measurements are the dissipation time T_1 and the coherence time T_2. Table 7.1 lists the key parameters for the six different samples on which measurements were made.

7.1 Results on a resistively isolated Josephson junction sample RJJ-Al

Using the time-of-flight technique, junction switching histograms for sample RJJ-Al sample were obtained under different conditions. Figure 7.1 shows a histogram taken at the base temperature of the refrigerator (25 mK).

Using the method described in Chapter 2 and a calibration of the ramp function $I_b(t)$, I convert the histogram to a curve of escape rate versus bias current, which is shown in Fig. 7.2.

I used the master equation discussed in Chapter 3 to calculate the total escape rate for a junction with critical current I_0, capacitance C, shunt resistance R, and

Table 7.1: List of junction qubits that were measured

Samples	I_0^*	C	Isolation	additional filtering
RJJ-Al	464.4 nA	0.3 pF	On-chip resistor, $R = 100$ kΩ	No[a]
LCJJ-Al	13.330 μA	4.25 pF	SMD LC, 10 nH, 10 pF	Yes[b]
LCJJ-Nb1	70.891 μA	4.64 pF	On-chip LC, 10 nH, 80 pF	Yes[c]
LCJJ-Nb2	15.421 μA	4.8 pF	On-Chip LC, 8 nH, 80 pF	Yes[d]
RESJJ-Nb	125.28 μA	1.1 pF	On-Chip $\lambda/2$ resonator	No[e]
LJJJ-Nb	34.055 μA	4.50 pF	On-chip LJ, 3.3 nH,30pH,30pH	Yes[f]

[*] I_0 and C found by fitting measurement results to theory.

[a] Thermocoax directly connected to the junction.

[b] 250 Ω resistor at Mixing Chamber followed a 1-meter-long LakeShore cable.

[c] Commercial rf filter (30 MHz rolloff) at Mixing Chamber followed by home-made Cu-powder filter.

[d] Home-made rf filter (1 MHz rolloff at Mixing Chamber followed by home-made Cu-powder filter.

[e] Thermocoax directly connected to the junction.

[f] Home-made rf filter (13 MHz rolloff) at Mixing Chamber followed by home-made Cu-powder filter.

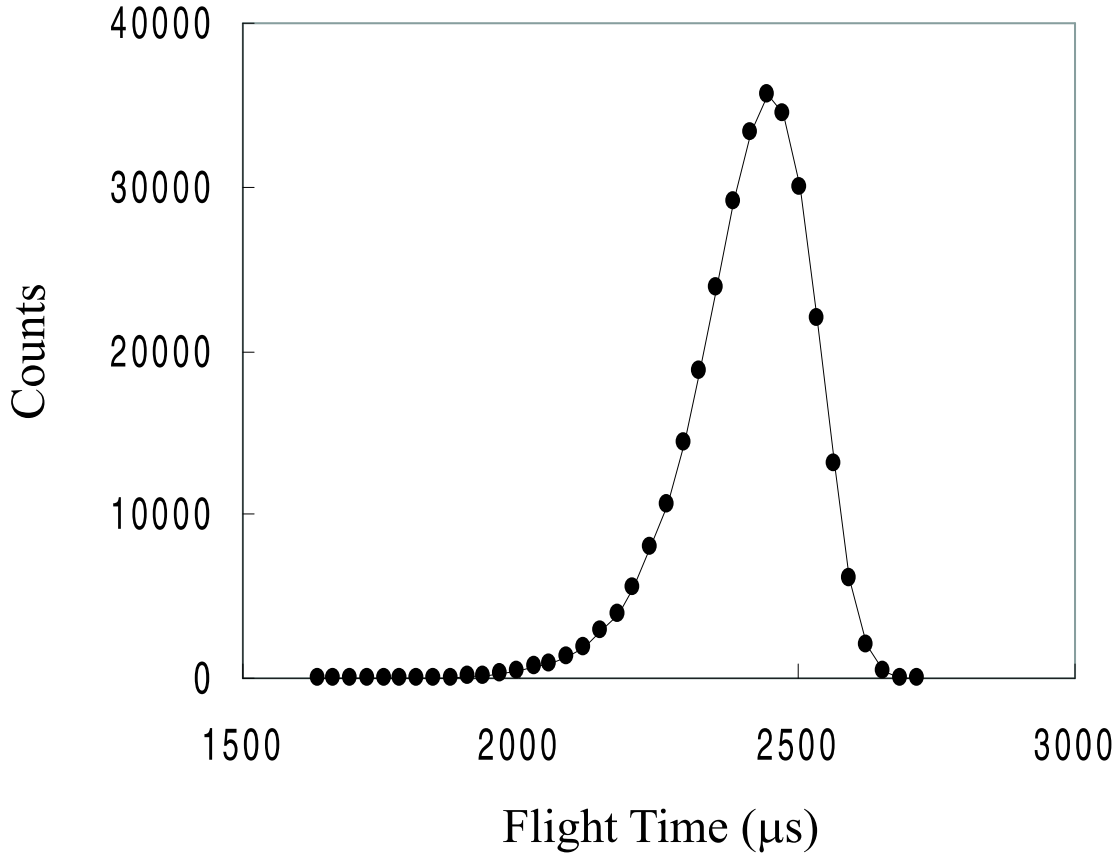

Figure 7.1: A switching histogram for sample RJJ-Al. Data (Data file: 082101b.dat) taken at the base temperature of the fridge (25 mK). The ramp rate was 53 μA/s.

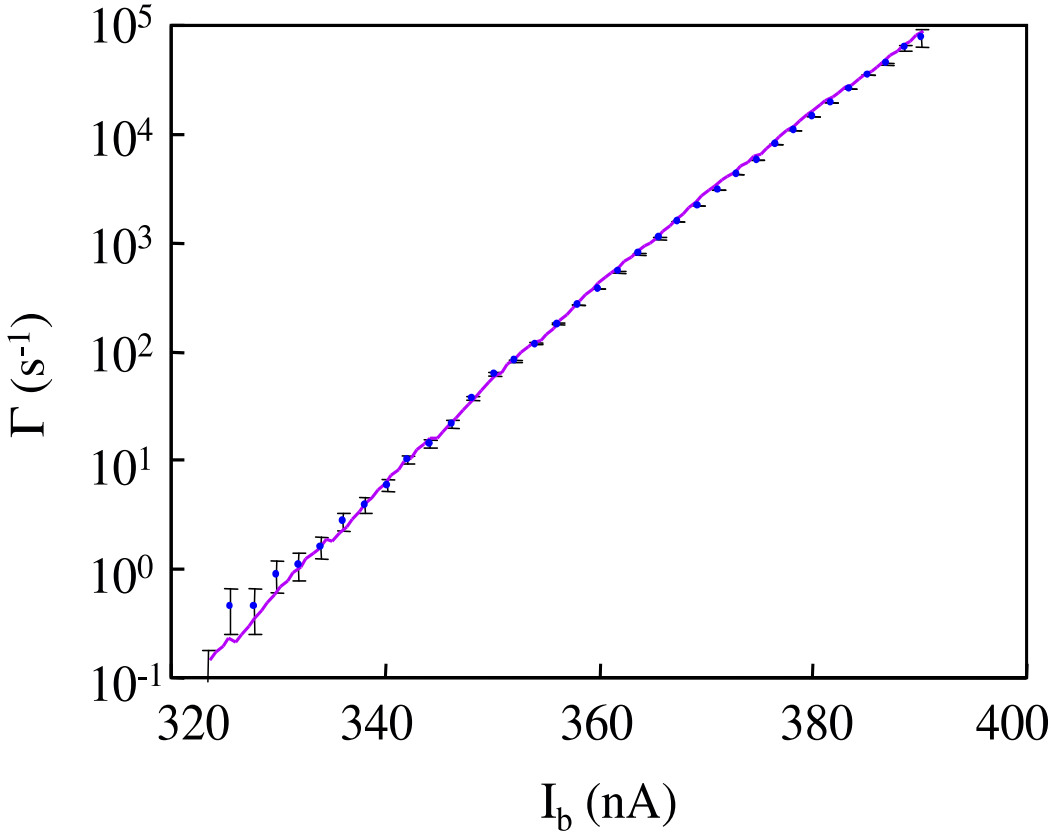

Figure 7.2: Escape rate curve for sample RJJ-Al. Points are data and the solid line is a fit using the master equation 3.2 discussed in Chapter 3 with I_0 =464.6 nA, $RC = 25$ ns, $T = 155$ mK. The ramp rate was 53 μA/s.

temperature T. I obtained a good fit of the data with the parameters I_0=464.6 nA, RC = 25 ns and T = 155 mK. The fit is sensitive to the temperature and the critical current, but not to the RC time constant, since escape is dominated by the thermal activation process because of the high temperature. I can still get a reasonable fit even using RC as small as 1 ns. I also note that the shunt resistance R and the junction capacitance C cannot be independently determined in the thermal regime. If I assume the junction capacitance is about 0.3 pF, estimated from the junction size and the specific capacitance, then the shunt resistance is between 10 kΩ and 80 kΩ.

The high temperature obtained from fitting the data is not surprising since the estimated maximum temperature in the NiCr resistor can be as high as 120 mK. By suppressing the critical current of the junction, I measured the junction temperature as a function of the critical current. The result shows a linear dependence of temperature on the critical current (the temperature is 80 mK at a junction critical current of 160 nA) [79], which is consistent with the model of heat transport via electron diffusion.

At these high temperatures, all the switching happens at low bias currents where the anharmonicity in the potential is weak. Due to thermal smearing of the energy levels and the lack of anharmonicity, we would not be able to observe transitions between individual levels when microwaves are applied. One might expect classical resonant activation phenomena [128] at high temperatures. However in this sample, I also could not observe classical resonance phenomena, suggesting the quality factor of the system is low. From the measurements, I can estimate an upper bound of 10 for the quality factor, leading to a spectroscopic coherence time of less than 0.3 ns.

The short T_1 and T_2^* are not inconsistent with our rough estimate of the shunt resistance, which between 500 Ω and 1 kΩ since the NiCr resistor is shunted by the capacitance formed between the heat sinks and the ground.

7.2 Results on LC isolated Josephson junction samples LCJJ-Al, LCJJ-Nb1 and LCJJ-Nb2

I have tried three LC isolated Josephson junction samples: LCJJ-Al, LCJJ-Nb1 and LCJJ-Nb2. LCJJ-Al and LCJJ-Nb1 are single qubit samples, while LCJJ-Nb2 has two coupled qubits. Here I just concentrate on single qubit characterization.

7.2.1 Spectroscopic coherence time

Figure 7.3 shows a set of histograms taken for sample LCJJ-Al at temperatures of 250 mK, 200 mK, 150 mK, 125 mK, 100 mK, 50 mK and 25 mK. As expected, the histogram moves to the right as the temperature decreases, and the width of the histogram shrinks, signifying thermal activation is being suppressed. Between 50 mK and 25 mK, the histogram does not change much. This is probably due to self-heating since analysis of the 25 mK data suggests a junction temperature of 45 mK (see below). Nevertheless the temperature is low enough compared to the level spacing ($\sim$300 mK) that escape is dominated by quantum tunneling.

I next used microwave spectroscopy to probe the energy levels at the base temperature of the refrigerator. An example of this measurement is shown in Fig. 7.4. One can clearly see two resonance peaks corresponding to $|0> \rightarrow |1>$ and $|1> \rightarrow |2>$ transitions.

Due to the anharmonicity of the well, the $|1> \rightarrow |2>$ level spacing is smaller than the $|0> \rightarrow |1>$ level spacing. Therefore when microwaves with a fixed frequency are applied to the system, the higher order transition occurs at lower bias current[1]. Figure 7.5 shows a plot of the relative difference, or enhancement.

From the enhancement plot, we can find the peak position and the peak width. The peak position can provide us information on the critical current and the junc-

[1]The well gets shallower and the level spacings decrease as the bias current increases.

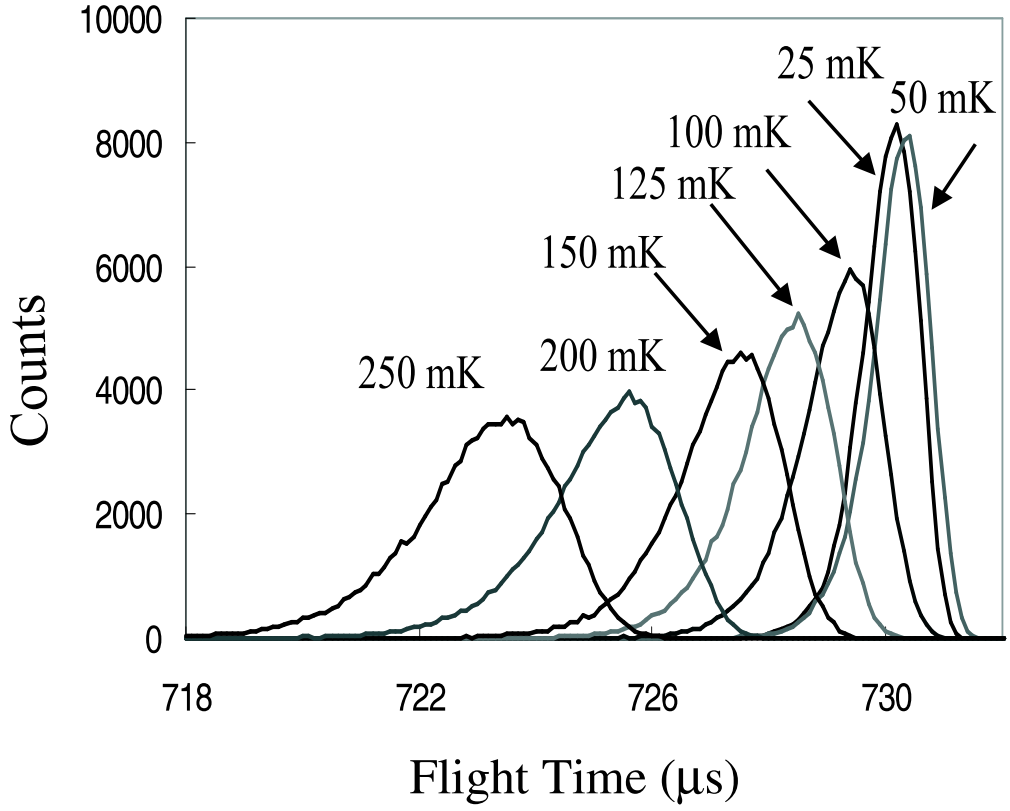

Figure 7.3: Macroscopic quantum tunneling results on sample LCJJ-Al. Switching histogram moves to higher bias currents as the temperature decreases. The width of the peak also shrinks.

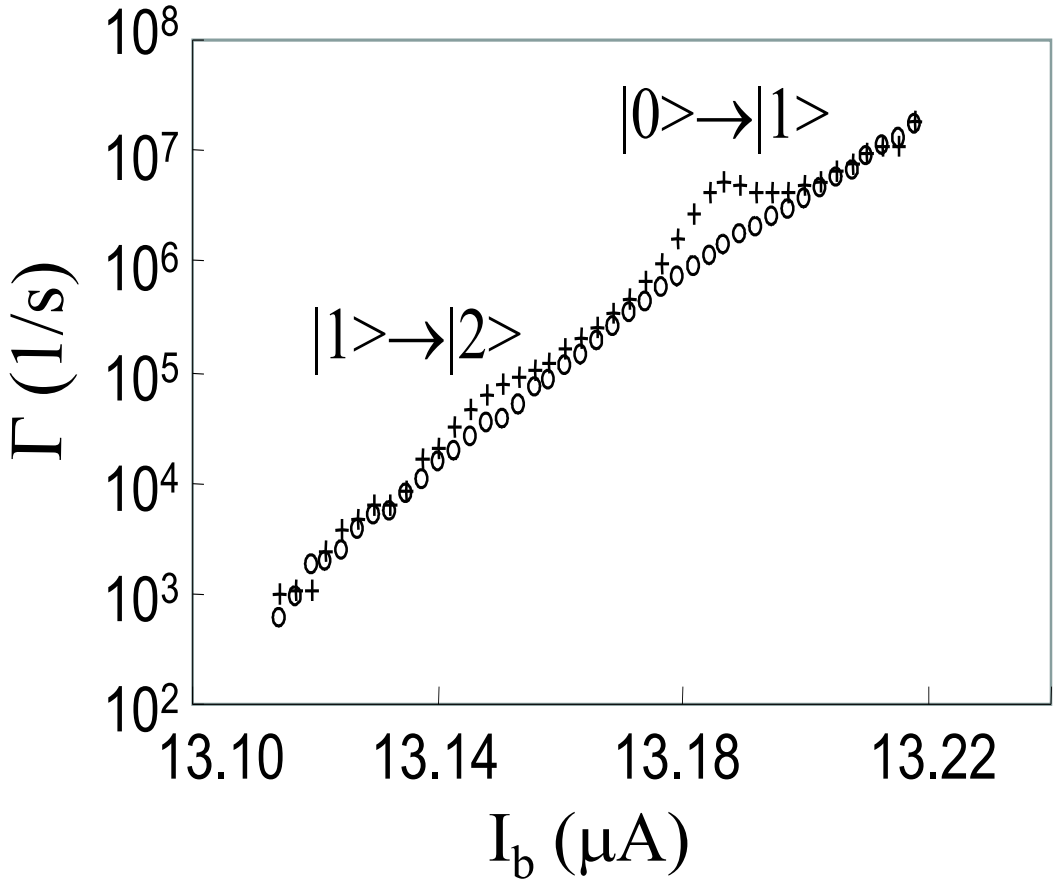

Figure 7.4: Resonant activation on sample LCJJ-Al. Circles are measured escape rates without microwaves. Crosses are escape rates when 5.5 GHz microwaves were applied. Date were taken at the base temperature of the fridge (25 mK).

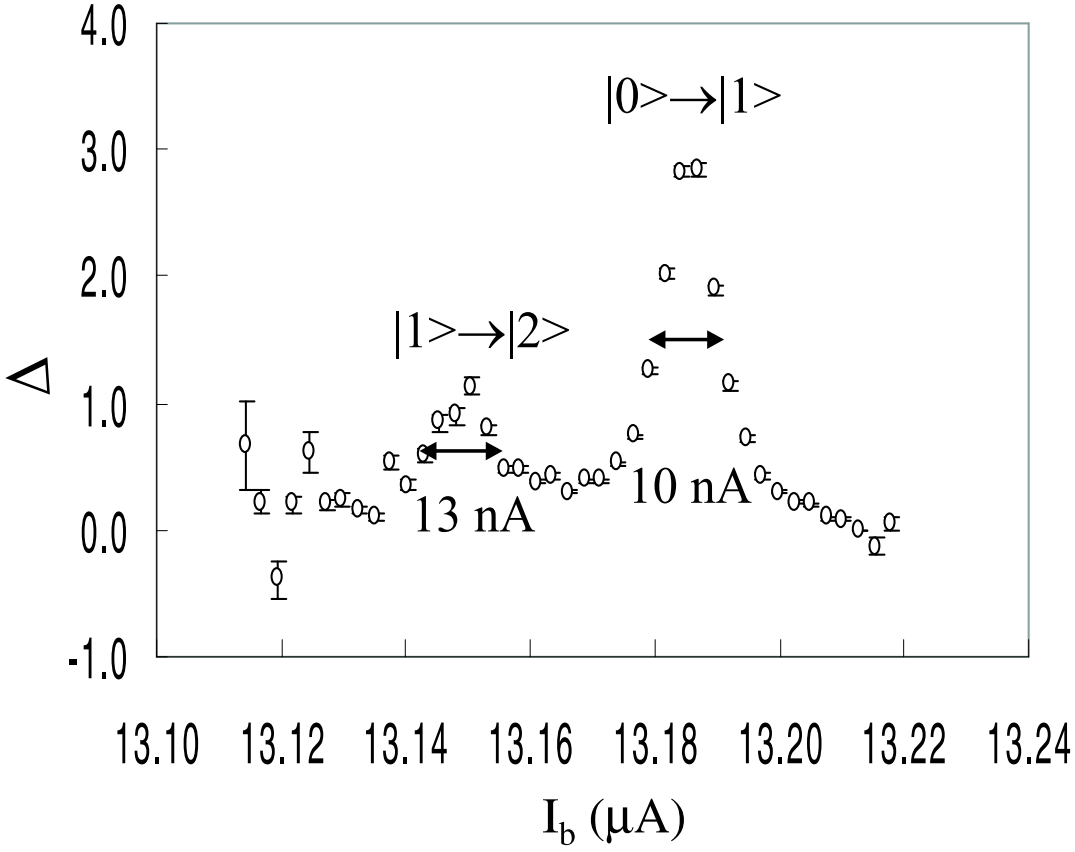

Figure 7.5: Escape rate enhancement in sample LCJJ-Al when 5.5 GHz microwave current is applied at 25 mK. Two resonances corresponding to $|1> \rightarrow |2>$ and $|0> \rightarrow |1>$ transitions were observed. The full width at half maximum (FWHM) of the $|0> \rightarrow |1>$ is about 10 nA.

tion capacitance, while the peak width, according to discussions in Chapter 4, is a measure of coherence in the system.

Similar results to the one shown in Fig. 7.5 were obtained when we apply microwaves of various frequencies to the system. After identifying the peak positions, I can plot the dependence of the level spacings on bias currents. The result is shown in Fig. 7.6. By fitting the spectrum using the energy level spacing formulae of a current-biased Josephson junction, I can then deduce the critical current and the junction capacitance. For sample LCJJ-Al, I obtained $I_0 = 13.316 \pm 0.008$ μA and $C = 3.84 \pm 0.2$ pF.

With Fig. 7.6, I can also convert the resonance width in current to a frequency width. This width can be interpreted as the sum of the widths of the levels involved in the transition. For the $|0> \rightarrow |1>$ transition shown in Fig. 7.5, I find the half width at half maximum is 85 MHz, corresponding to a spectroscopic coherence time of 1.9 ns. Using the same procedure, I can then find the spectroscopic coherence times for different microwave frequencies. The result is shown in Fig. 7.7.

I note that Fig. 7.7 shows that the spectroscopic coherence time increases with microwave frequency. One might think this is due to the frequency dependence of the shunt resistance. However when we performed the measurement at a reduced junction critical current, we found a larger coherence time at the same frequency. Therefore this effect of smaller T_2^* at low frequencies cannot be due to frequency dependence of the isolation scheme. Further analysis revealed that this effect is due to current noise and tunneling rate broadening [102]. The resonance width measures the uncertainty in the energy levels, which includes life-time-related uncertainties such as the relaxation rate and tunneling rate. Since the tunneling rates from the quantized energy levels increase exponentially with bias currents, at high bias currents where the $|0> \rightarrow |1>$ level spacing is small, the tunneling rate can cause severe resonance broadening. Current noise also tends to broaden resonances at low frequencies [99]. This is because the $|0> \rightarrow |1>$ level spacing decreases more

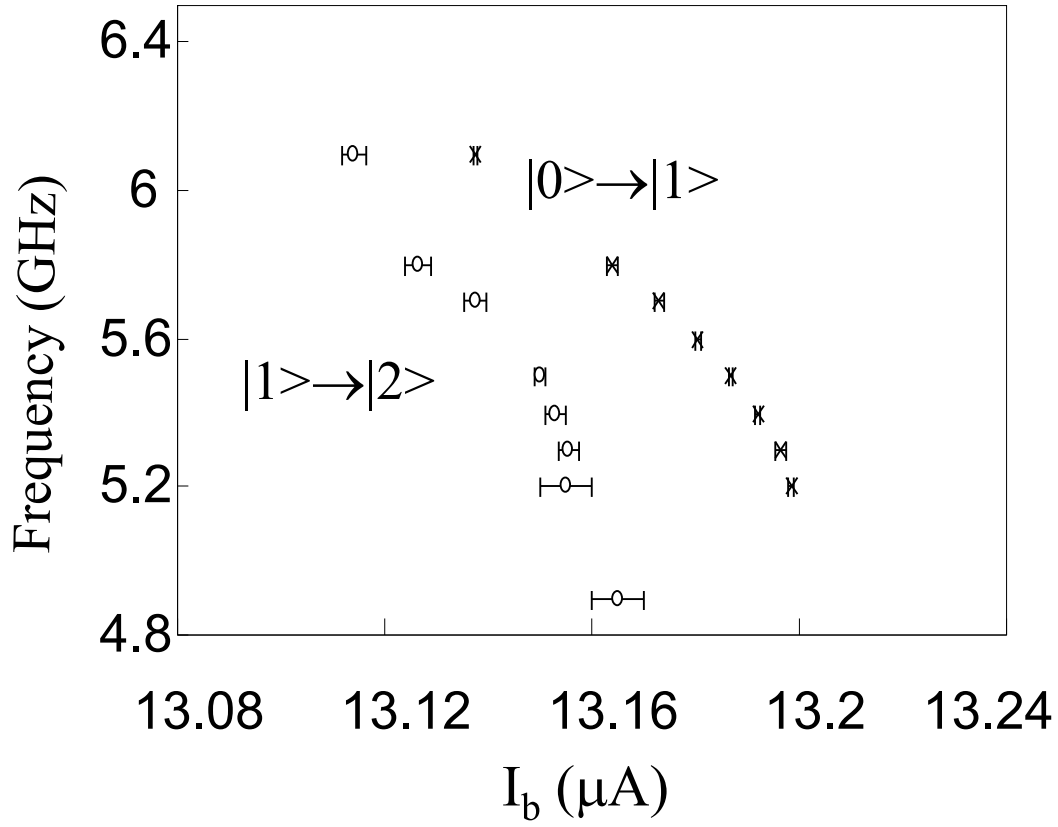

Figure 7.6: Energy spectrum of sample LCJJ-Al. Resonances positions were measured for different microwave frequencies. Data were taken at the base temperature of the refrigerator (25 mK).

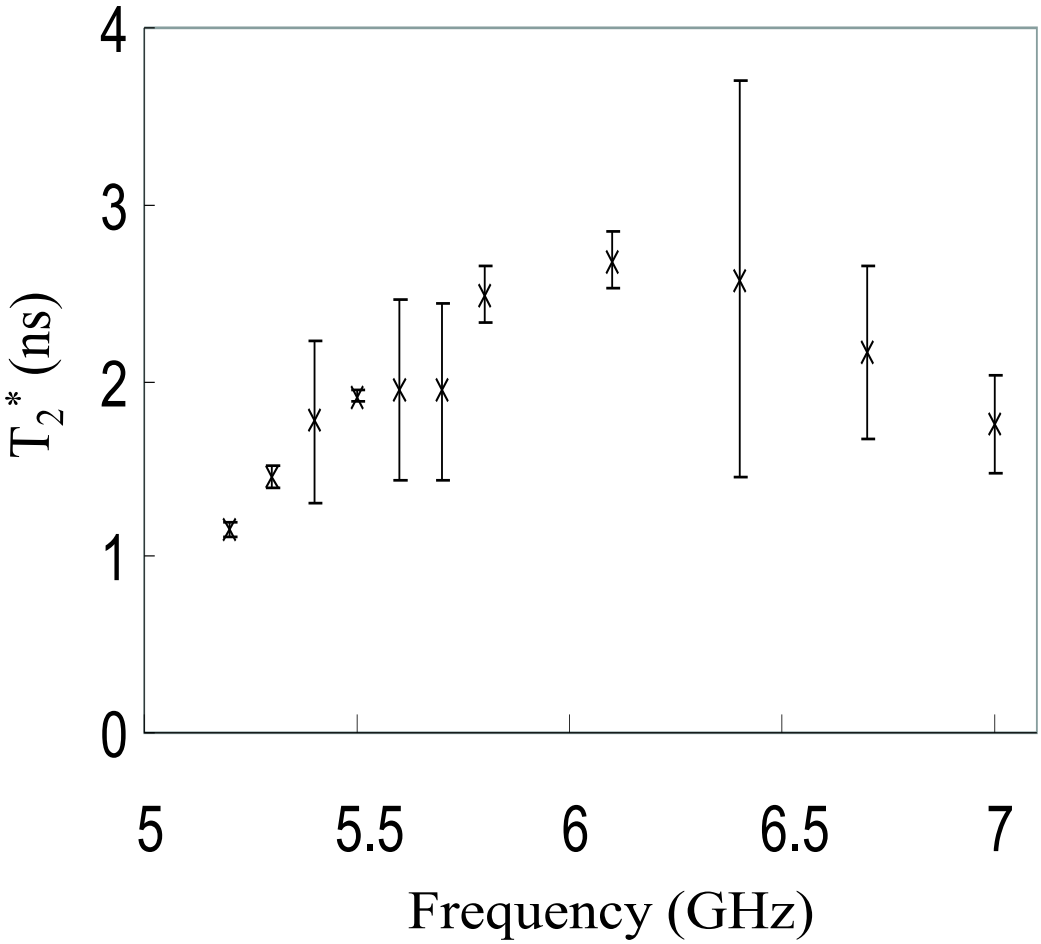

Figure 7.7: Spectroscopic coherence time T_2^* for sample LCJJ-Al. The T_2^* is about 2 - 3 ns. It gets shorter at low frequencies due to current noise and the increased tunneling rate.

rapidly at high bias currents (see Fig. 7.6), therefore for the same amount of current noise, the level spacing fluctuation is larger at high bias currents.

I also performed spectroscopy measurements on LCJJ-Nb1 and LCJJ-Nb2 at the base temperature of the refrigerator[2]. One example of microwave-induced escape rate enhancement is shown in Fig. 7.8 for sample LCJJ-Nb1.

For sample LCJJ-Nb1, the measurement was done for a large junction critical current so that the plasma frequency is around 10 GHz. I could not observe clear resonances at lower frequencies. This is not surprising since the junction was hot (150 mK, see below) and this sample suffers from a large amount of low frequency noise. We suspect this is due to poor thermal-anchoring of the commercial rf filter[3] (from Mini-Circuits). The large thermal noise from the filter thus heats the junction. From the width of the $|0> \rightarrow |1>$ resonance, I found a spectroscopic coherence time T_2^* of 0.9 ns.

For sample LCJJ-Nb2, a home-made rf filter (3dB point around 1 MHz) was used to replace the commercial rf filter. We observed clear resonances at 5 GHz, and the junction temperature (35 mK) deduced from the measurement was close to the base temperature of the refrigerator. This junction has a critical current of 15.421 μA and a capacitance of 4.8 pF. From the peak width, we found a spectroscopic coherence time $T_2^* \approx$3 ns. I note that for this sample some changes outside the screened room were also made, including isolating the sync output of the function generator from the input of the timer using an opto-isolator[4].

---

[2]For LCJJ-Nb2, one junction is ramped, and the other junction is biased at zero current. Therefore the two junctions are effectively decoupled and the measurement can be considered to probe single junction properties.

[3]The commercial rf filter is sealed in a stainless steel barrel with SMA connectors at the two ends. Inside the barrel the body of the filter is mounted on a plastic circuit board that is a poor thermal conductor.

[4]The peak width with the opto-isolator was 30% smaller than that without the isolator.

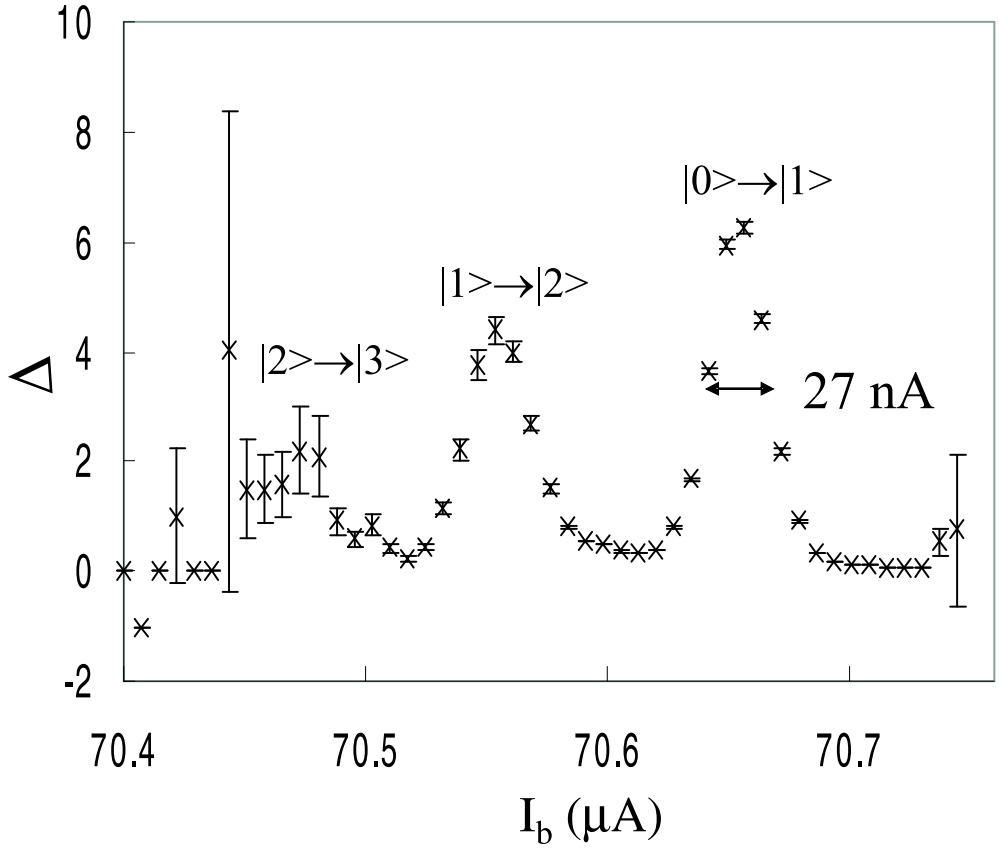

Figure 7.8: Escape rate enhancement when 9.8 GHz microwaves applied to sample LCJJ-Nb1. Three resonances corresponding to $|2> \rightarrow |3>$, $|1> \rightarrow |2>$ and $|0> \rightarrow |1>$ were observed. The full width at half maximum(FWHM) of the $|0> \rightarrow |1>$ transition is about 27 nA.

7.2.2 Analysis of the relaxation time in LCJJ-Al and LCJJ-Nb1

In the absence of current noise, the spectroscopic coherence time T_2^* should be equal to the coherence time T_2 and twice the relaxation time T_1. We expected T_1 for these LC isolated qubits to be at least 200 ns. There are two questions that need to be answered: first, what is T_1 in these qubits? Second, what is causing the short T_2^*?

To answer the first question, a reliable measurement of T_1 would be helpful. We can get a rough estimate for T_1 by answering the second question. Note that the resonance widths for the $|0> \rightarrow |1>$ and $|1> \rightarrow |2>$ transitions were in the ratio of 1 to 1.3 instead of 1 to 3, which would have been the case if the broadening were due to dissipation alone. Therefore there must exist another source of decoherence in addition to dissipation. The fact that the peaks have nearly the same width in current suggests that the broadening is caused by low frequency current noise, which would produce just such a simple 'smearing' along the current axis.

I can use the stochastic Bloch equation (see Chapter 4) to analyze the resonance shapes. Shown in Fig. 7.9 are the measured spectrum (circles) for sample LCJJ-Al where 5.5 GHz microwaves were applied to the system and a best fit (dashed curve) from simulating Eq. 4.18 with $R = 2.75$ kΩ , $T = 44.7$mK, $\sigma_I = 6.7$ nA, $f_c = 600$ MHz, $I_1 = 0.1744$ nA, $I_0 = 13.330$ μA and $C = 4.25$pF. Here I_1 denotes the microwave current amplitude. Notice I have assumed a noise with a constant spectral density from 0 to f_c and a total rms value of σ_I.

I note that the measured spectrum and simulations are in very good agreement, and the cutoff frequency (600 MHz) and the level of rms current noise (6.7 nA) are reasonable for our LC isolation circuit. In fact, we expect the noise is centered around $1/2\pi\sqrt{L_i C_i} \approx 500$ MHz, and the total rms value is $\sqrt{k_B T/L} = 7.9$ nA. Although there are seven fitting parameters, close examination shows that the two peaks are neither Lorentzian nor Gaussian, so the good fit I have obtained is non-

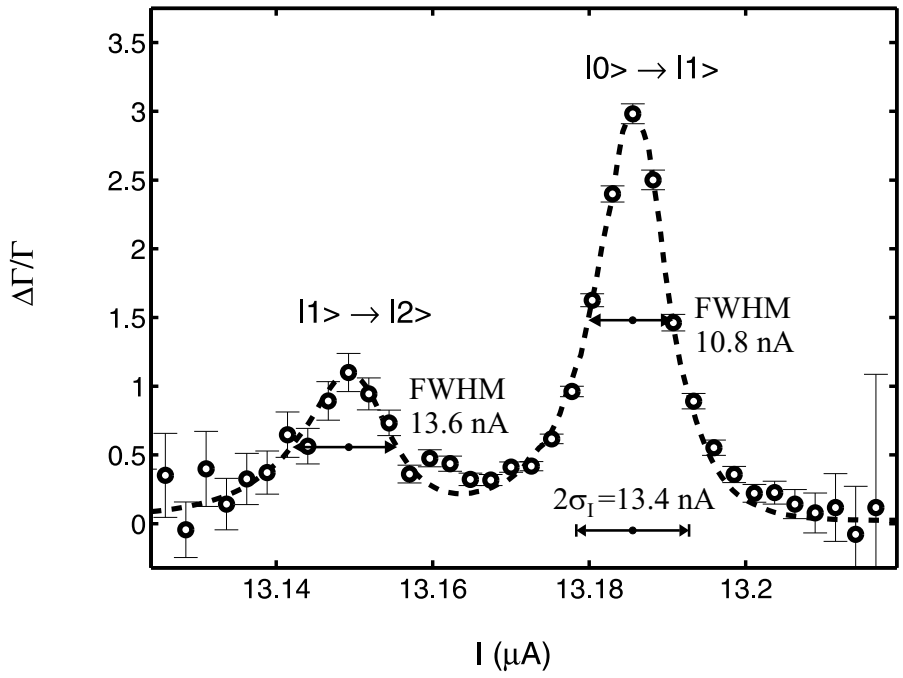

Figure 7.9: Noise-induced resonance broadening for sample LCJJ-Al. The fitting parameters are $R = 2.75$ kΩ , $T = 44.7$mK, $\sigma_I = 6.7$ nA, $f_c = 600$ MHz, $I_1 = 0.1744$ nA, $I_0 = 13.330$ μA and $C = 4.25$ pF.

trivial.

From these parameters I find $T_1 = RC = 12$ ns. I also note that the observed half width ($\sim$5 nA) of the $|0> \rightarrow |1>$ transition is considerably smaller than the $1.65\sigma_I$ ($\sim$11 nA) width that one would expect from Eq. 4.46. This suggests the high frequency part of the spectrum is averaged out and does not contribute to broadening, which agrees with our prediction for $f_c >> 1/2\pi T_1$.

To fit the measured spectrum for sample LCJJ-Nb1, simulations using the stochastic Bloch equation were also performed. The result is shown in Fig. 7.10 with circles being data and the dashed curve being a best fit to the data with the parameters: $R = 1.5$ kΩ , $T = 150$ mK, $\sigma_I = 10.3$ nA, $f_c = 30$ MHz, $I_1 = 3.1$ nA, $I_0 = 70.891$ μA and $C = 4.64$ pF. For this junction the cutoff frequency (30 MHz) is much lower than the resonance frequency of the on-chip LC network (180 MHz), perhaps due to the fact that the commercial rf low-pass filter is dominating the noise contribution and it has a resonance frequency at 30 MHz. [5] The level of rms current noise is also larger than that for LCJJ-Al due to the elevated temperature of the rf filter.

From the above parameters I find $T_1 = RC = 7$ ns. I note that the observed half width ($\sim$14 nA) of the $|0> \rightarrow |1>$ transition is close to $1.65\sigma_I$ ($\sim$17 nA). Since in this case $f_c \approx 1/2\pi T_1$, the noise is not high frequency and we do not expect the effect of the noise to be averaged out. The result of this is the resonance width is determined by the total rms current noise.

Note that for both samples T_2^* (2 ns for LCJJ-Al and 1 ns for LCJJ-Nb1) is much less than the relaxation times T_1 (12 ns for LCJJ-Al and 7 ns for LCJJ-Nb1). This suggests that in our system decoherence is dominated by current noise rather than dissipation.

[5]The 3-dB point of the rf filter is 1.9 MHz at room temperature, but the inductance is built from a ferrite core whose magnetic moments are completely saturated at millikelvin temperatures leading to an increase in the 3-dB point to 30 MHz.

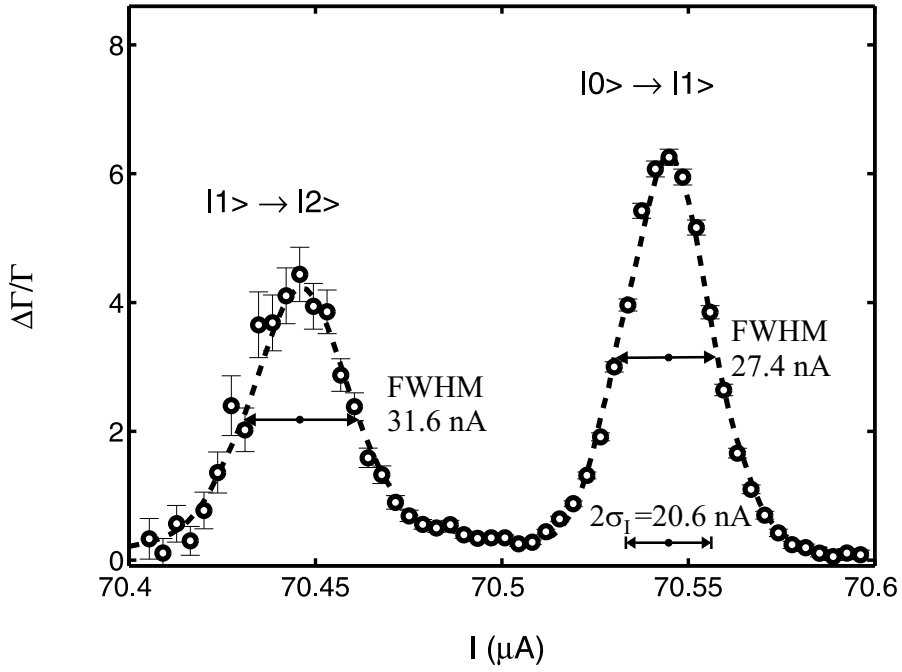

Figure 7.10: Noise-induced resonance broadening for sample LCJJ-Nb1. The fitting parameters are $R = 1.5$ kΩ , $T = 150$mK, $\sigma_I = 10.3$ nA, $f_c = 30$ MHz, $I_1 = 3.1$ nA, $I_0 = 70.891$ μA and $C = 4.64$ pF.

I also note that the relaxation times deduced from this stochastic Bloch equation analysis are much smaller than our expected values of at least 200 ns. The cause of this inconsistency has not been determined so far. One possible explanation is that there is extra dissipation due to quasiparticles generated after the junction switches to the voltage state. Since quasiparticles act as a parallel channel for dissipation and cannot be filtered by isolation circuits placed next to the junction, our isolation schemes does not filter them. This quasiparticle poisoning problem may be diagnosed by varying the duty cycle of the switching measurement. Some preliminary measurements suggest that the temperature of the junction decreases by a few millikelvin when the experiment repetition rate goes from 300 Hz to 10 Hz [79]. However 100 ms of waiting time seems not to help much, which might imply the quasiparticles have a very low recombination rate when fewer quasiparticles are present. Work by Lang *et al.* [129] found that it can take more than 100 ms of waiting time in order not to see noticeable changes in resonance widths. Despite this, we have not seen conclusive evidence that quasiparticle poisoning is the cause for shortening of the relaxation time.

On the other hand, I note that the shunt resistance R we measure is much higher than the 50 Ω we would find if the junction were directly connected to the bias leads. This suggests that the LC isolation scheme is working at some level by stepping up the lead impedance around the transition frequency, but it is not doing a good job of blocking low frequency current noise.

7.2.3 Relaxation time in LCJJ-Nb2

The level-depletion technique discussed in Chapter 3 can be used to measure the relaxation time T_1.

This technique relies on measurement of the escape rates and the collapse feature corresponding to population depletion in high levels. The measurement must be

carefully performed to avoid junction critical current drift, electronics drift and other features such as bistable switching[6]. Since the collapse feature occurs at the bias current where the tunneling rate from the $|1>$ state is equal to the relaxation rate, one needs to be able to measure escape rates that are as high as the relaxation rate. This typically requires a moderate ramp rate for the bias current in order to avoid excessive escape at lower escape rates.

For sample LCJJ-Nb2, we were able to measure a collapse feature [130]. Figure 7.11 shows the measured escape rates at 25 mK and 90 mK. One can clearly see the 90 mK escape rate curve collapses to the 25 mK escape rate curve at 33.45 μA, signifying population depletion in the first excited state. By using Eq. 3.2 in Chapter 3, good fits to the data were obtained with $I_0 = 33.65$ μA and $C = 4.2$ pF for the 25 mK curve and two additional parameters $R = 1$ kΩ and $T = 98$ mK for the 90 mK curve.

From these parameters, we thus deduce a relaxation time of $T_1 = 4$ ns for the junction. We note the spectroscopic coherence time deduced for the same junction but at a different critical current (15.421 μA) is $T_2^* = 3$ ns. This indicates resonance broadening due to current noise in this sample since if only dissipation were responsible for the resonance width we should have found $T_2^* = 2T_1 = 8$ ns.

7.3 Results on a resonantly isolated Josephson junction sample RESJJ-Nb

We tried spectroscopy measurement on sample RESJJ-Nb, but no clear resonances were observed in the frequency range of 9 GHz-11 GHz, where the resonator is supposed to provide isolation. One possible explanation is the frequency at which

[6]Sometimes junction switching displays two distinct voltage signals, this may create a bump feature that resembles the real collapse feature corresponding to population depletion.

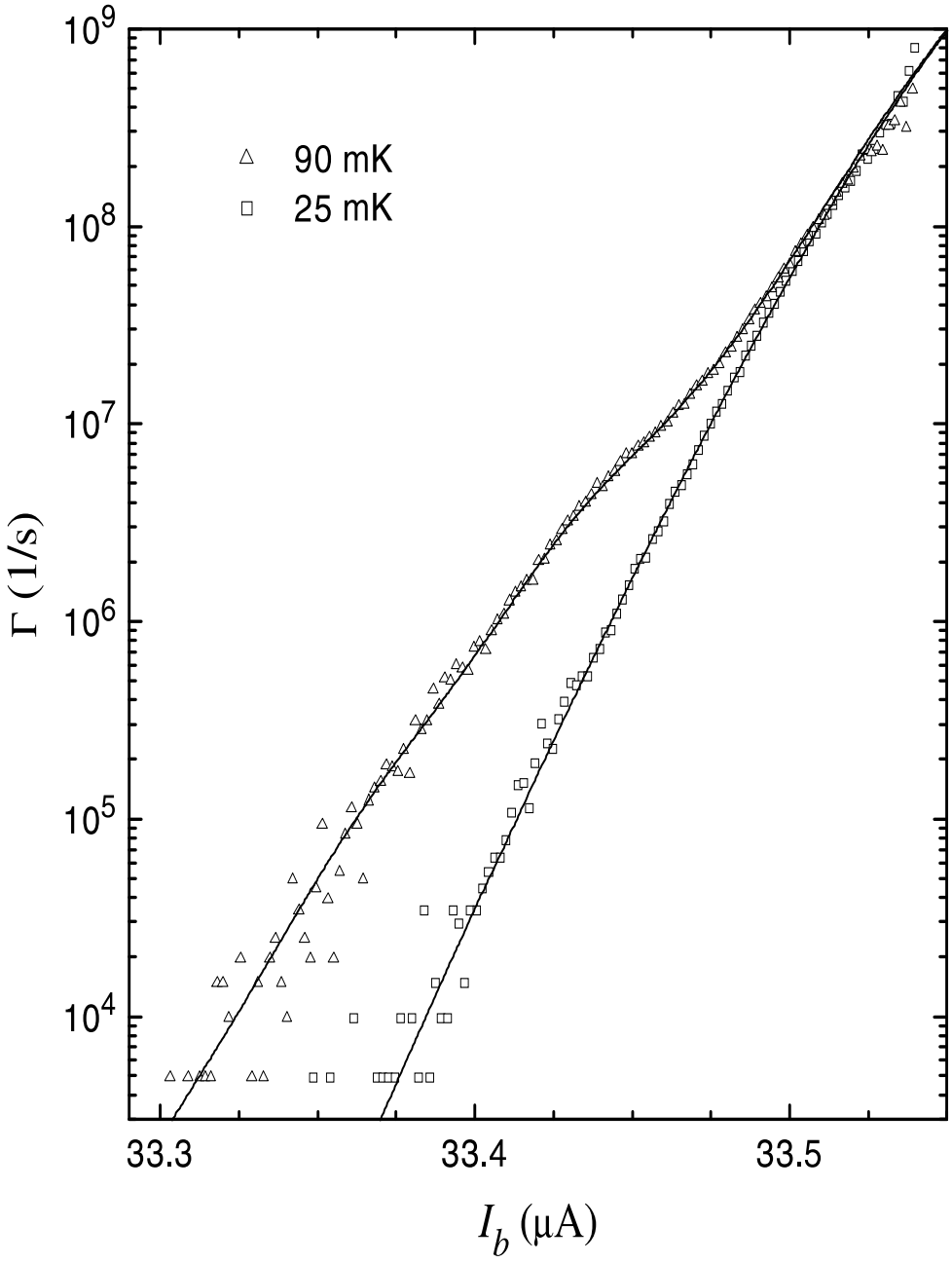

Figure 7.11: Population depletion in sample LCJJ-Nb2. Squares and triangles are data, lines are fits using the master equation. Notice the collapse feature occurs at 33.45 μA. The 25 mK data were fitted with $I_0 = 33.65$ μA and $C = 4.2$ pF and the 90 mK data was fitted with two additional parameters $R = 1$ kΩ and $T = 98$ mK. The current ramp was 0.7 A/s.

the resonant circuit works is outside the frequency range that has been probed.

The population depletion technique was also used to measure the relaxation time in this system (see Fig. 7.12).

From the collapse feature at 124.3 μA, I estimate the background escape rate is 5×10^4/s. Therefore a rough estimate of the relaxation time will be 40 ns[7].

7.4 Results on an LJ isolated Josephson junction sample LJJJ-Nb

Switching histograms of ramping the bias current at many fixed flux currents were taken to find out L_i and M (see Fig. 7.13). When the bias current I_b and the flux current $I_f = L_i I_b / M$ were applied simultaneously, one guarantees the qubit junction switches first assuming no flux trapped in the loop (see Chapter 5). A typical histogram under this biasing scheme is shown in Fig. 7.14. The multiple switching states are a result of different flux trapped in the closed loop formed by the junctions and the inductor. The two adjacent bias currents at which escape happens are separated by Φ_0/L_i, indicating the fluxes trapped in the junction loop for the two initial states differ by one flux quantum.

Since each sub-histogram corresponds to a different initial state, escape rates should be calculated for each sub-histogram. For better statistics, the sub-histogram with the largest weight was picked for data analysis.

7.4.1 Spectroscopic coherence time

When microwaves were applied to sample LJJJ-Nb, sharp resonance peaks were observed as shown in Fig. 7.15. From the peak width and measurements of ΔE vs.

[7]By pumping the system with microwaves and then turning off the microwaves, I find the escape rate curve has a decay time of 10 ns.

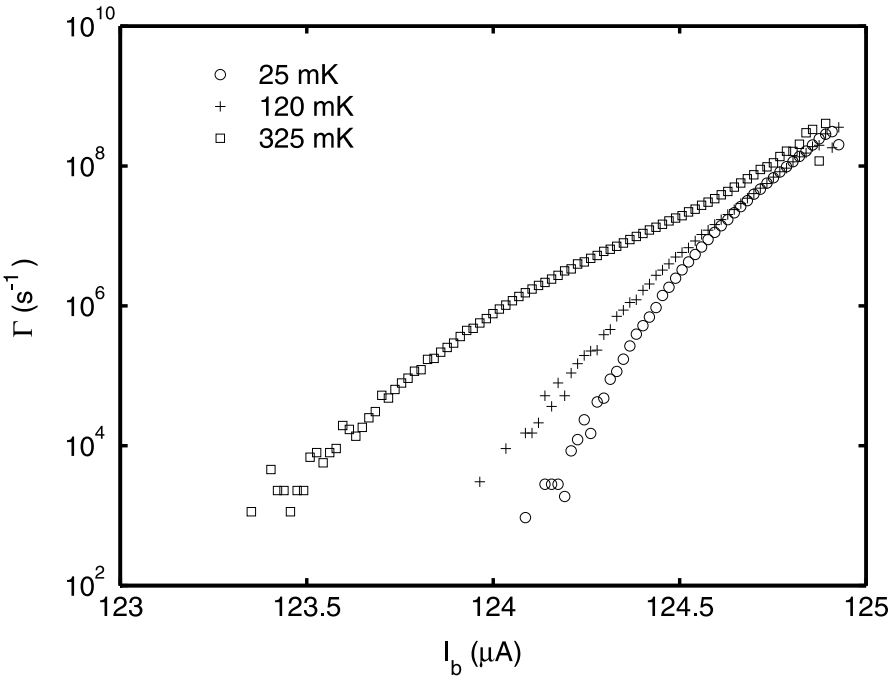

Figure 7.12: Population depletion in sample RESJJ-Nb. Notice the collapse feature occurs at 124.3 μA. From that, I estimate the background escape rate is 5×10^4/s. Therefore a rough estimate of the relaxation time will be $T_1 = 40$ ns.

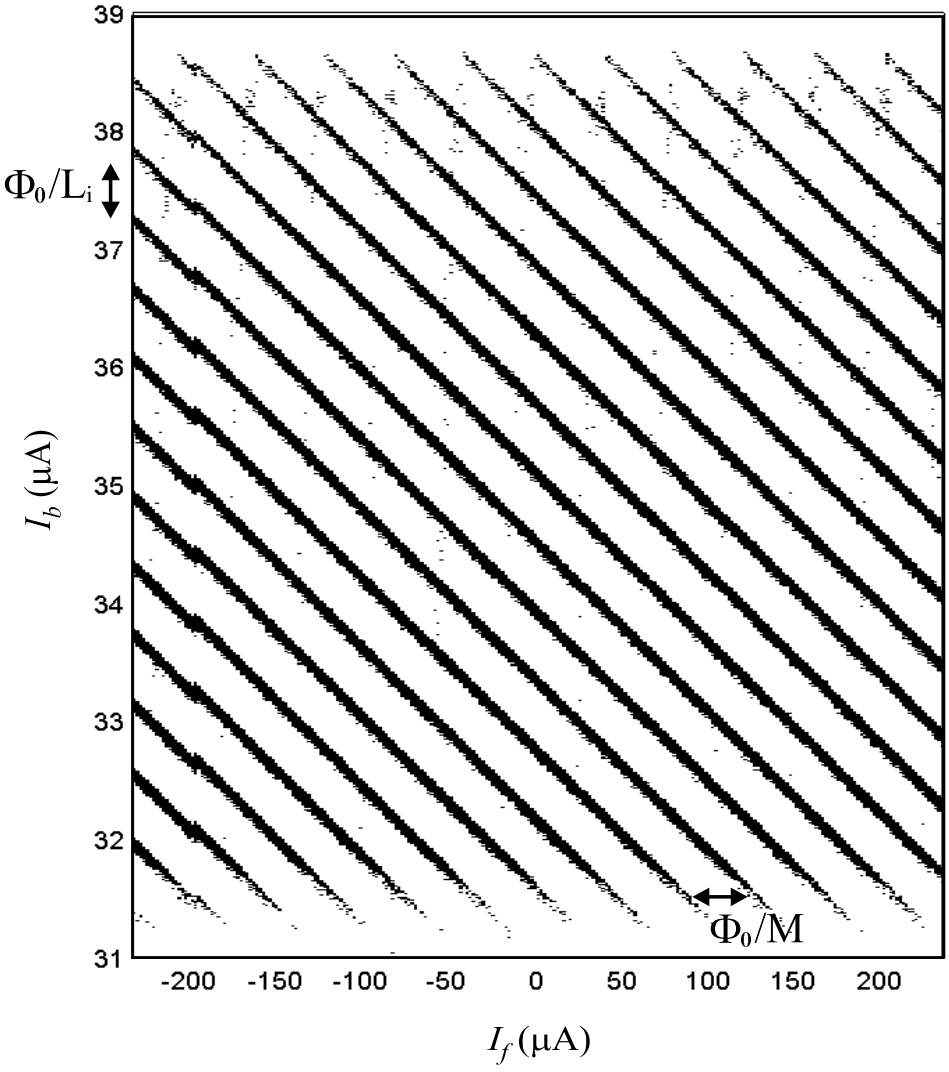

Figure 7.13: A switching histogram for sample LJJJ-Nb while bias current ramped and flux current fixed. The measurement is then repeated for many different fluxes. Multiple switching histograms are due to different flux states of the system.

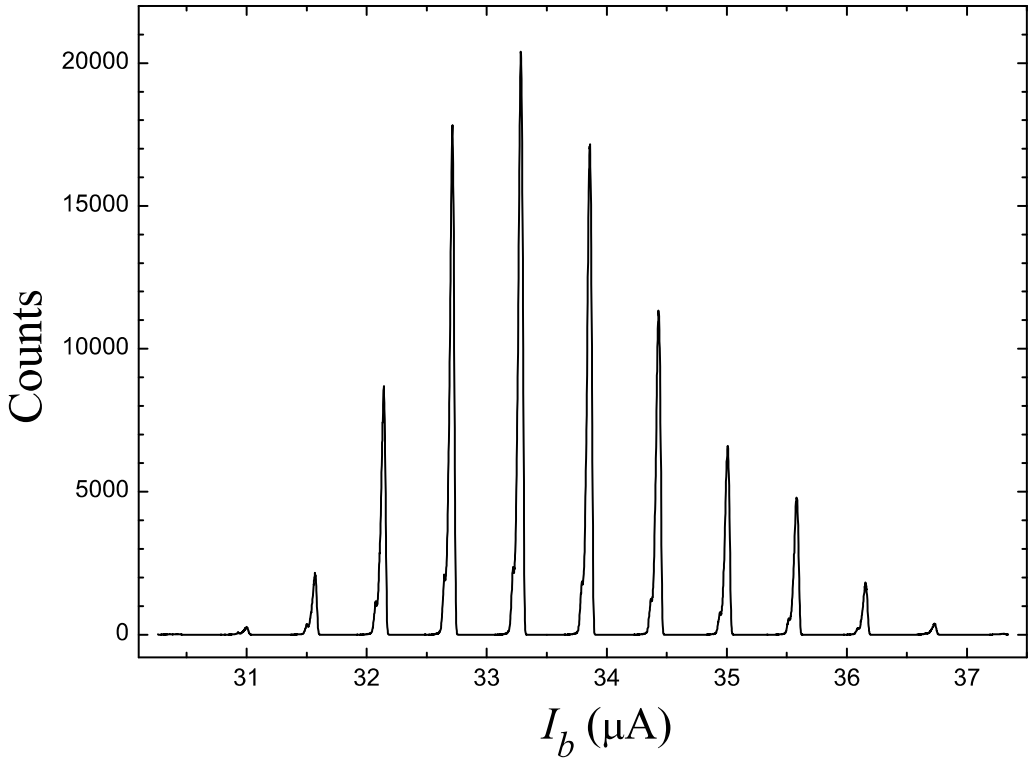

Figure 7.14: A switching histogram for sample LJJJ-Nb while bias current and flux current are ramped simultaneously such that $I_f \approx L_i I_b / M$. Multiple switching histograms are due to different flux states of the system.

I, we deduce the spectroscopic coherence time $T_2^* \approx 4.4$ ns.

At elevated temperatures, in addition to the $|0> \rightarrow |1>$ transition, $|1> \rightarrow |2>$ and $|2> \rightarrow |3>$ transitions were also observed. The widths of these transitions are 1:1.5:2, not quite in the ratio of 1:3:5, but broadening of higher order transitions are clearly visible. This suggests the resonance width is dominated by decoherence from dissipation. However, it could also be due to escape rate broadening. I note that the resonance widths also broaden was observed at higher temperatures. This is expected as the resonance width accounts for all the uncertainties in the energy level, including relaxation rate, tunneling rate and thermal-noise-induced inter-level transition rates that increase with temperature.

7.4.2 Rabi oscillations

We attempted Rabi oscillations experiments in several samples, but only LJJJ-Nb sample yield oscillations. We chose the start of the microwave pulse to be the center of the resonance peak measured under continuous microwaves. The ramp was also slow enough such that the system was in resonance with the applied microwave for a time interval that was much longer than the expected coherence time. The microwave pulse is turned off at the end of the bias current ramp. A histogram obtained for 7.6 GHz microwaves is shown in Fig. 7.16.

Oscillations in the counts were clearly visible corresponding to coherent pumping between the ground state and excited states. The histogram can be converted to escape rate $\Gamma_m(t)$ (see Fig. 7.17).

Assuming just two levels are involved, we can write the probability of finding the system in the first excited state $|1>$ at time t,

$$P_1(t) = \frac{\Gamma_m(t) - \Gamma_0(t)}{\Gamma_1(t) + \Gamma_0(t)} \approx \frac{\Gamma_m(t)}{\Gamma_1(t)} \tag{7.1}$$

where Γ_0 and Γ_1 are the tunneling rates from the ground state and the first excited

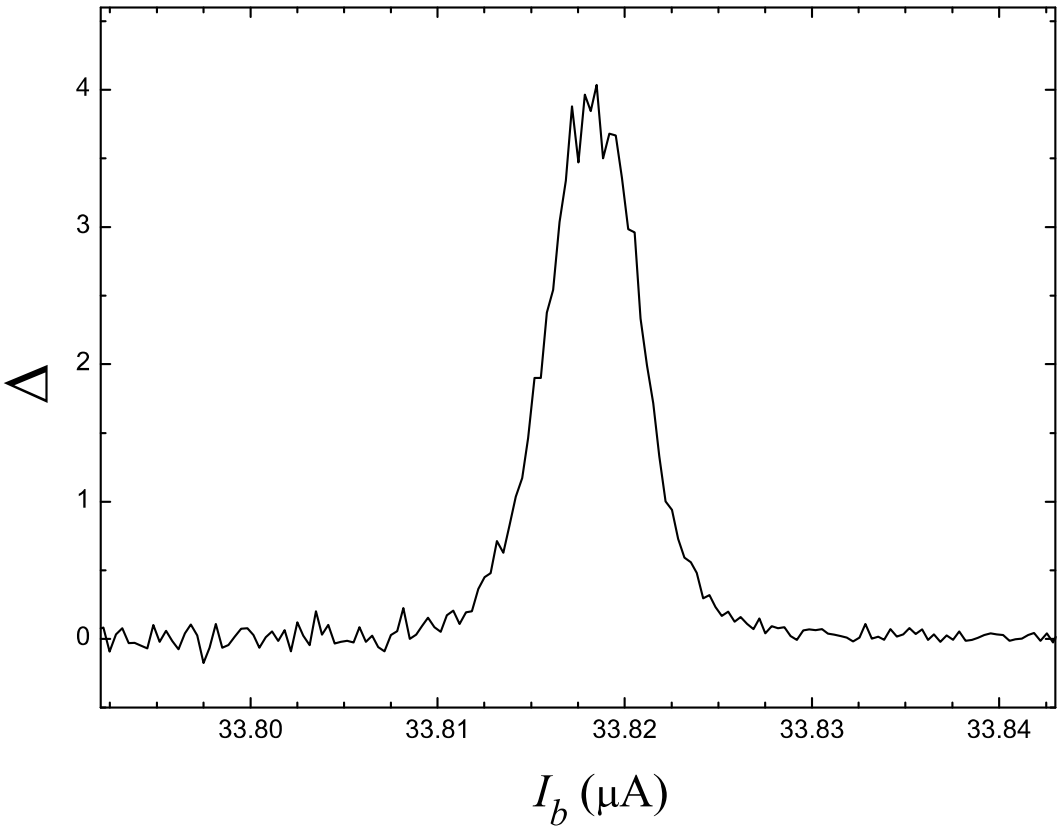

Figure 7.15: Escape rate enhancement on sample LJJJ-Nb (7.6 GHz). Data taken at 25 mK, but weak $|1> \rightarrow |2>$ transition is still visible (not shown here). The full width at half maximum for the $|0> \rightarrow |1>$ transition is about 5.5 nA corresponding to T_2^* of 4.4 ns.

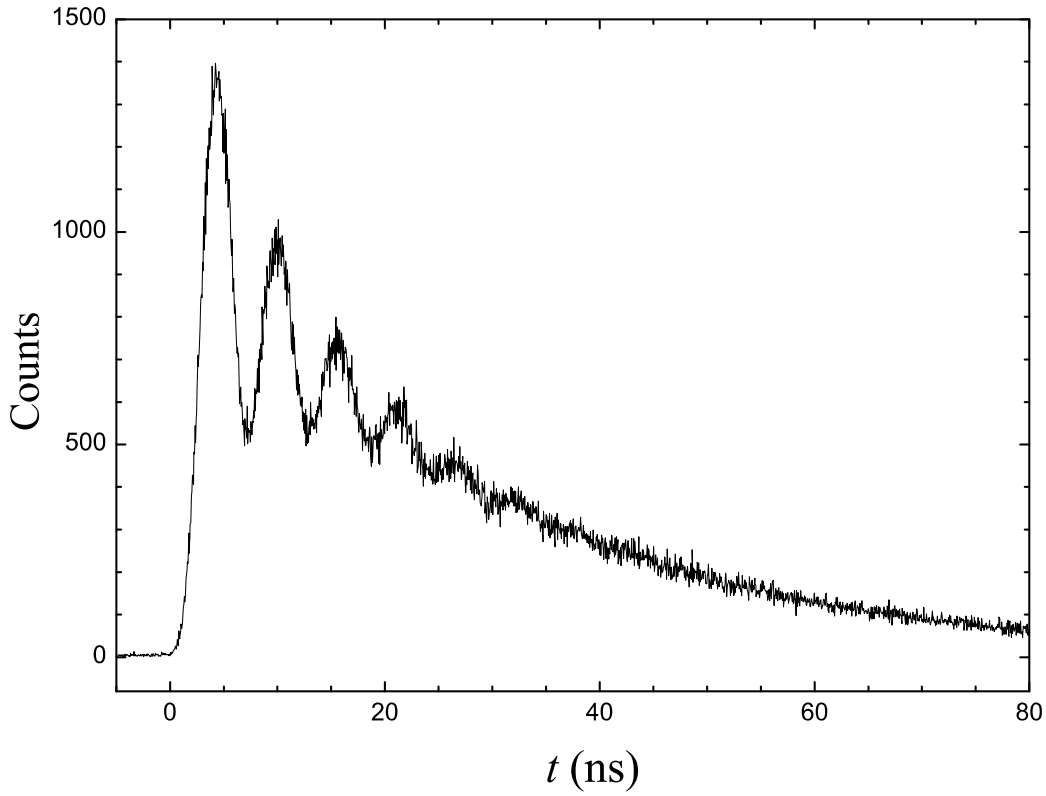

Figure 7.16: Switching counts oscillation on sample LJJJ-Nb (7.6 GHz). The data were taken with the sweep method introduced in Chapter 4 with microwaves turned on at $t = 0$.

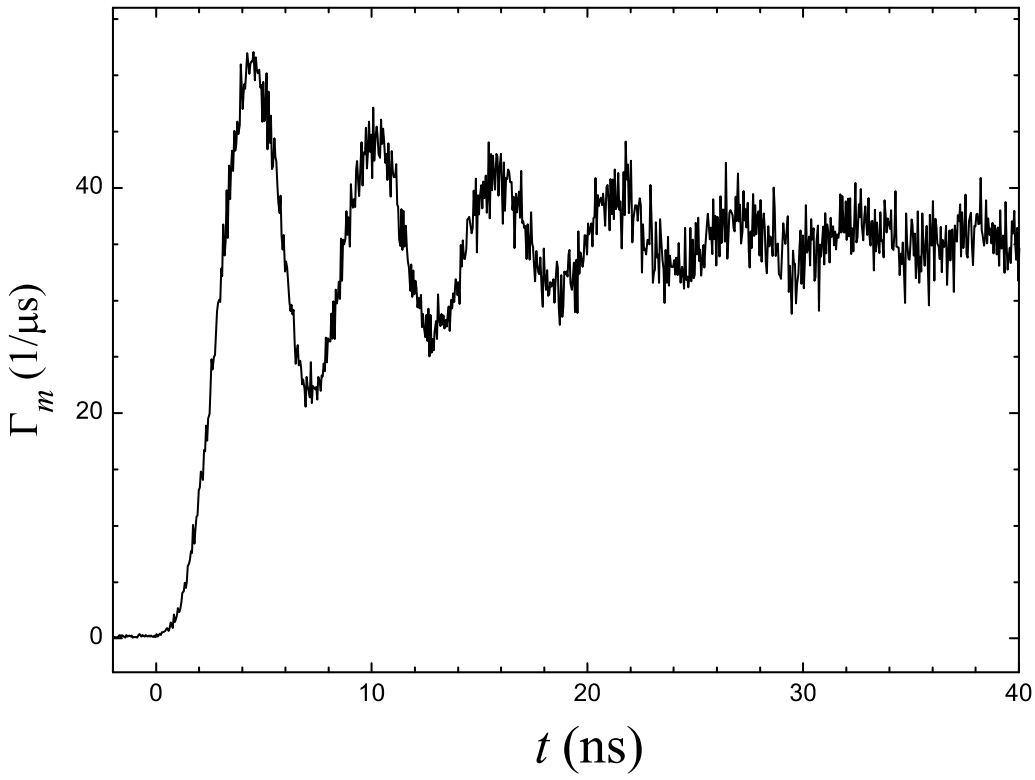

Figure 7.17: Escape rate oscillation on sample LJJJ-Nb (7.6 GHz). Escape rates converted from the histogram shown in Fig. 7.16.

state respectively, and can be calculated using the junction parameters. In fact if one finds Γ_m no longer increases with microwave power, then the system is in saturation and the equilibrium value (after coherence is lost) of $P_1(t)$ should be 1/2. From that, one can get Γ_1 without doing any complicated calculations. The measured P_1 as a function of t is plotted in Fig. 7.18.

Oscillation of the population in the first excited state is clearly visible, indicating the system is oscillating between the ground state and the first excited state. This behavior is commonly referred as Rabi oscillations between two levels in atomic physics when excitations with the right frequency are applied to the system.

By fitting this oscillation curve using Eq. 4.64, we find $T' = 10$ ns. I note the decay time of the coherent oscillations is neither T_1 nor T_2, but T' which is given by (see Chapter 4)

$$\frac{1}{T'} = \frac{1}{2T_1} + \frac{1}{2T_2} \tag{7.2}$$

Using $T_1 = 50$ ns and $T' = 10$ ns, I find $T_2 \approx 5.6$ ns from Eq. 7.2. I note that I have already assumed decoherence can be completely described by a phase coherence time in order to obtain Eq. 7.2. In other words, I expect $T_2^* = T_2$. Here I see that the spectroscopic coherence time (4.4 ns) is slightly smaller than the spectroscopic coherence time of 4.4 ns.

7.5 Summary

In this Chapter, I have presented results on six different qubits: RJJ-Al, LCJJ-Al, LCJJ-Nb1, LCJJ-Nb2, RESJJ-Nb and LJJJ-Nb. Key time scales (T_1, T_2^* and T' were deduced from the measurements. Table 7.2 summarizes the results.

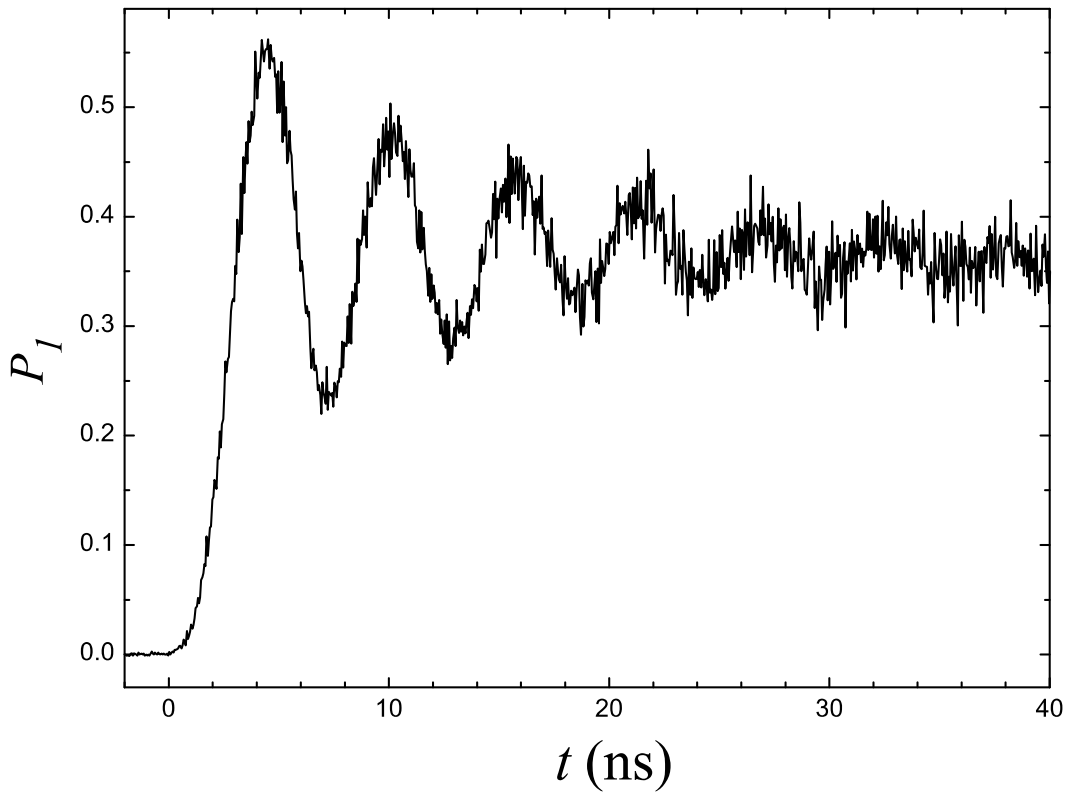

Figure 7.18: Rabi oscillations on sample LJJJ-Nb (7.6 GHz) microwaves applied after $t = 0$. The microwave power is high, therefore the equilibrium value of P_1 is almost 1/2. The decay time of the oscillation is about 10 ns.

Table 7.2: Times obtained for various qubits implemented

Samples	Expected T_1	T_1	T_2^*	T'
RJJ-Al	< 1 ns	1-25 ns	< 0.3 ns	-
LCJJ-Al	230 ns	12 ns	1.9 ns	-
LCJJ-Nb1	120 μs	7 ns	0.9 ns	-
LCJJ-Nb2	80 μs	4 ns	3 ns	-
RESJJ-Nb	200 ns	40 ns	-	-
LJJJ-Nb	1 μs	50 ns*	4.4 ns	10 ns

*Here the relaxation time is obtained by measuring the decay of the escape rate when microwaves were turned off [131].

Chapter 8

Spectroscopy of Multiparticle Entanglement

So far this thesis has only described results on single qubits. However, a real quantum computer will require coupling together many qubits. In this chapter, I present our spectroscopy measurements on sample LCJJ-Nb2, which acts as a coupled three-particle system (resonator and two junctions). Our results demonstrate the qubit properties of a resonator when it is coupled to a Josephson junction, provide evidence for resonant coupling between two junction qubits, and indicate the existence of entangled states between the three macroscopic degrees of freedom.

8.1 A coupled macroscopic three body system

Figure 8.1 shows a circuit schematic of our three-particle system, which consists of two Josephson junctions (J1 and J2) connected together by a series inductor-capacitor (LC) resonator. This system can be viewed in three distinct ways. First, it can be viewed as an LC resonator that is isolated by and detected using two junctions. Second, the system can be viewed as two junction qubits coupled by a tuned element, the resonator. Third, it can be viewed as a three-qubit system where the quantum states of the junction qubits and the resonator are all used for infor-

mation storage and manipulation. All three viewpoints are useful in understanding the system behavior, and will be discussed below.

The three degrees of freedom of this system are the macroscopic [71] quantum variables γ_1 and γ_2 (the gauge-invariant phase differences across junctions J1 and J2), and $\gamma_3 = 2\pi LI/\Phi_0$ corresponding to the current flowing through the total inductance $L = L_1 + L_2$. The classical equations of motion for the system are

$$m_1\ddot{\gamma}_1 + m_3\omega_{30}^2\gamma_3 = -\frac{\partial U_1(\gamma_1)}{\partial\gamma_1} \tag{8.1}$$

$$m_2\ddot{\gamma}_2 - m_3\omega_{30}^2\gamma_3 = -\frac{\partial U_2(\gamma_2)}{\partial\gamma_2} \tag{8.2}$$

$$\ddot{\gamma}_1 - \ddot{\gamma}_2 - \ddot{\gamma}_3 = \omega_{30}^2\gamma_3 \tag{8.3}$$

where $m_i = C_i(\Phi_0/2\pi)^2$, $i = 1, 2, 3$ are the effective masses for γ_1, γ_2 and γ_3 with C_1 and C_2 the junction capacitances and C_3 the capacitance of the resonator. $\omega_{30} = 1/\sqrt{LC_3}$ is the angular frequency of the resonator, and $U_1(\gamma_1)$ and $U_2(\gamma_2)$ are the washboard potentials for Junctions J1 and J2 respectively, given by

$$U_1(\gamma_1) = -\frac{\Phi_0}{2\pi}\left(I_{c1}\cos\gamma_1 + I_{b1}\gamma_1\right) \tag{8.4}$$

$$U_2(\gamma_2) = -\frac{\Phi_0}{2\pi}\left(I_{c2}\cos\gamma_2 + I_{b1}\gamma_2\right) \tag{8.5}$$

where I_{c1} and I_{c2} are the junctions' critical currents, and I_{b1} and I_{b2} are the junction bias currents.

One can construct the following Lagrangian

$$L = \frac{1}{2}m_1\dot{\gamma}_1^2 + \frac{1}{2}m_2\dot{\gamma}_2^2 + \frac{1}{2}m_3(\dot{\gamma}_1 - \dot{\gamma}_2 - \dot{\gamma}_3)^2 - U_1(\gamma_1) - U_1(\gamma_1) - \frac{1}{2}m_3\omega_{30}^2 \tag{8.6}$$

to generate the above equations of motions.

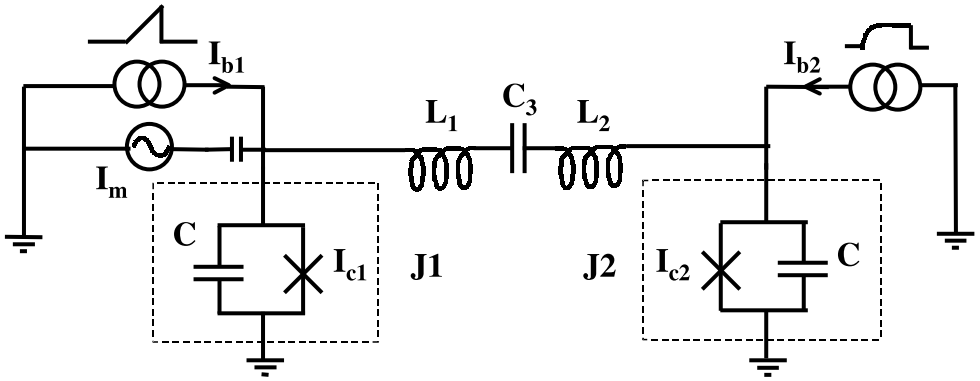

Figure 8.1: A coupled macroscopic three-body system comprised of two Josephson junctions and an LC resonator. Bias currents through the two junctions are I_{b1} and I_{b2} respectively. I_m is a microwave current that can be used to probe the energy levels of the system. I have assumed the same capacitance C for the two junctions.

Given the Lagrangian, one can find the canonical momenta p_i , $i = 1, 2, 3$ for the three degrees of freedom

$$p_1 = m_1\dot{\gamma}_1 + m_3(\dot{\gamma}_1 - \dot{\gamma}_2 - \dot{\gamma}_3) \tag{8.7}$$

$$p_2 = m_2\dot{\gamma}_1 - m_3(\dot{\gamma}_1 - \dot{\gamma}_2 - \dot{\gamma}_3) \tag{8.8}$$

$$p_3 = -m_3(\dot{\gamma}_1 - \dot{\gamma}_2 - \dot{\gamma}_3) \tag{8.9}$$

and obtain the following Hamiltonian

$$H = \frac{(p_1 + p_3)^2}{2m_1} + \frac{(p_2 - p_3)^2}{2m_2} + \frac{p_3^2}{2m_3} + U_1(\gamma_1) + U_1(\gamma_1) + \frac{1}{2}m_3\omega_{30}^2 \tag{8.10}$$

In this experiment, the junctions have the same area, so we can assume $C_1 = C_2 = C$ and thus $m_1 = m_2 \equiv m = C(\Phi_0/2\pi)^2$.

To see the coupling between the three degrees of freedom, we rewrite Eq. 8.10 by introducing a renormalized mass $m_3' = (\Phi_0/2\pi)^2 C_3 C/(C + 2C_3)$ and a renormalized frequency $\omega_3 = 1/\sqrt{L_3 C_3 C/(C + 2C_3)}$ for the LC resonator. We then have

$$H = \frac{p_1^2}{2m} + U_1(\gamma_1) + \frac{p_2^2}{2m} + U_2(\gamma_2) + \frac{p_3^2}{2m_3'} + \frac{1}{2}m_3'\omega_3^2\gamma_3^2 + \xi\frac{p_1 p_3}{\sqrt{mm_3'}} - \xi\frac{p_2 p_3}{\sqrt{mm_3'}} \tag{8.11}$$

where $\xi = \sqrt{C_3/(C + 2C_3)}$ is a dimensionless coupling coefficient.

The first two terms in Eq. 8.11 are the Hamiltonian for J1 alone. It has dynamics analogous to that of a particle moving in a tilted washboard potential as discussed in Chapter 2. The second pair of terms describes J2, which has the same dynamics as J1, while the third pair describes the harmonic oscillator dynamics of the LC resonator. Finally, the last two terms represent capacitive coupling between each junction and the resonator. The momenta in the Hamiltonian are proportional

to the charge stored on each capacitor in the circuit [132], and thus the coupling between the LC oscillator and each qubit is simply electrostatic.

Sample LCJJ-Nb2 was made by Hypres, Inc. A photo of the sample is shown in Fig. 5.12 in Chapter 5. The Josephson junctions are thin-film 10 μm $\times$ 10 μm, Nb/AlOx/Nb junctions on a 5 mm $\times$ 5 mm silicon chip. The coupling inductor is a 780 μm $\times$ 90 μm thin-film niobium loop connecting the two junctions, and the coupling capacitance consists of two capacitors in series, each of them formed by 60 μm $\times$ 60 μm parallel niobium plates separated by a 200 nm layer of SiO_2. With this geometry we estimate the inductance $L = 1.5$ nH and the capacitance $C_3 = 0.37$ pF. The chip is mounted inside the Cu sample box, and all the measurements presented in this Chapter were preformed at the base temperature of the refrigerator (25 mK).

As discussed in Chapter 3, microwaves can be applied to the system to drive transitions from the ground state to the excited states. Since the excited states have much higher tunneling rates, by measuring the enhancement in escape rate, we can probe the quantized energy levels in the system.

8.2 An LC resonator qubit

Figure 8.2 shows the spectrum of the system when the bias current for junction J1 is ramped and junction J2 is held at $I_{b2} = 0$. The circles denote measured resonance peak positions when microwaves are continuously applied to induce transitions from the ground state to excited states. The dashed lines are from quantum mechanical calculations using the Hamiltonian in Eq. 8.11 with the following parameters: $I_{c1} =$ 21.388 μA, $I_{c2} = 22.536$ μA and $C = 4.8$pF, $L = L_1 + L_2 = 1.71$ nH and $I_{b2} = 0$. The zero-biased junction J2 is effectively decoupled from the rest of the system since it has a much larger energy scale ($\sim$19 GHz) than both junction J1 and the LC resonator ($\sim$7 GHz). Therefore, we observe a spectrum essentially due to junction J1 and the LC resonator only.

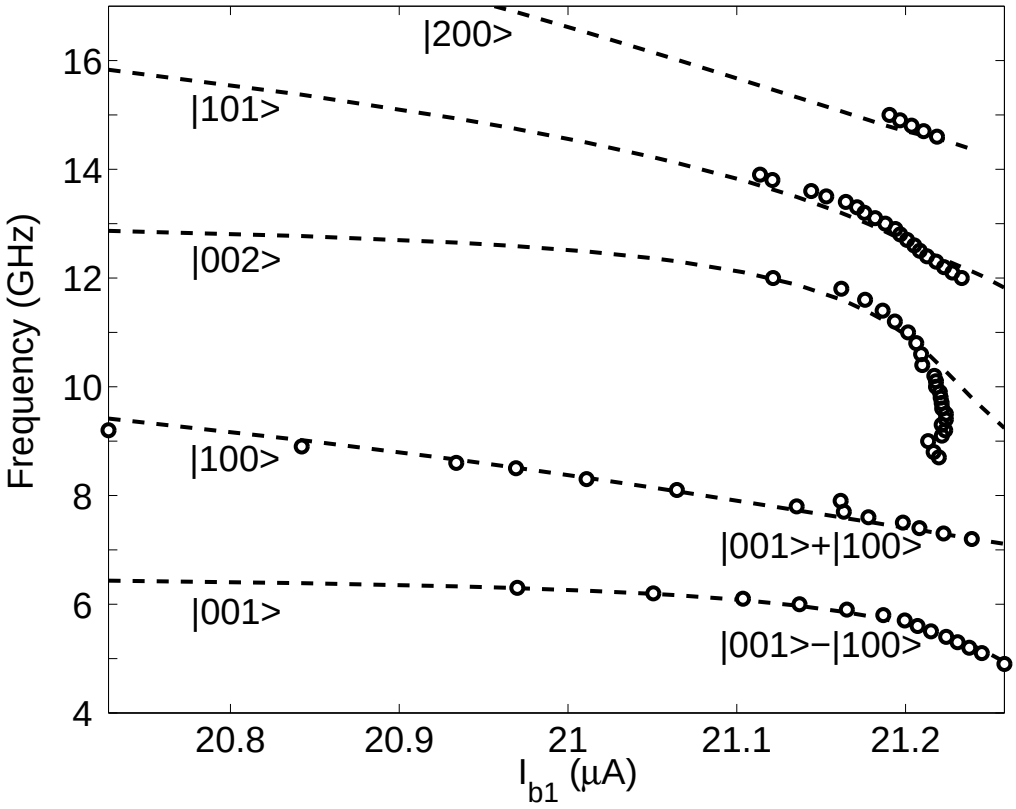

Figure 8.2: Spectrum of junction J1 coupled to an LC resonator. J2 is zero-biased and thus essentially decoupled from the rest of the system. Circles are data, dashed lines are fits from Eq. 8.11 with the parameters: $I_{c1} = 21.388\ \mu$A, $C = 4.8$ pF, $L = L_1 + L_2 = 1.71$ nH and $I_{b2} = 0$.

The minimum avoided crossing between the first excited state and the second excited state occurs at $I_{b1} = 21.18\ \mu$A. Entangled states of the form $(|001> \pm |100>)/\sqrt{2}$ are predicted here, where the first, second, and third positions in the ket denote the states of J1, J2, and the resonator, respectively. The next three excited states at the degeneracy point are $(|002> + |200> - \sqrt{2}|101>)/2$, $(|002> - |200>)/\sqrt{2}$, and $(|002> + |200> + \sqrt{2}|101>)/2$.

Figure 8.3 shows the measured spectrum for the case $I_{b1} = 0$ while ramping the bias current for J2. We find good agreement between data and theoretical calculations using the same parameters as that for Fig. 8.3 and $I_{b1} = 0$, i.e. we used a single set of five parameters to fit the ten curves in Figs. 8.2 and 8.3.

Since a classical oscillator would only possess a single absorption frequency, the observation of discrete higher order transitions in Figs. 8.2 and 8.3 such as transitions from $|000>$ to states involving $|002>$, provides evidence for the quantum nature of the LC resonator. For a harmonic oscillator, this type of higher order transition would be forbidden. But here, the resonator is coupled to the anharmonic junctions and this leads to entangled states that can be excited. These states also allow us to detect the state of the resonator through tunneling of the junctions. This entanglement between a superconducting qubit (the Josephson junction) and an LC resonator can be thought of as a macroscopic cavity QED experiment, analogous to the entanglement between a two-level atom and a single mode of an electromagnetic cavity [44].

8.3 Entanglement between three qubits

We can also use spectroscopy to probe entangled states between all three degrees of freedom. We proceed by biasing J2 at a constant current while ramping the bias current for J1. Figure 8.4 shows a measured spectrum, where red indicates enhancement in escape rate when microwaves are continuously applied (this measurement

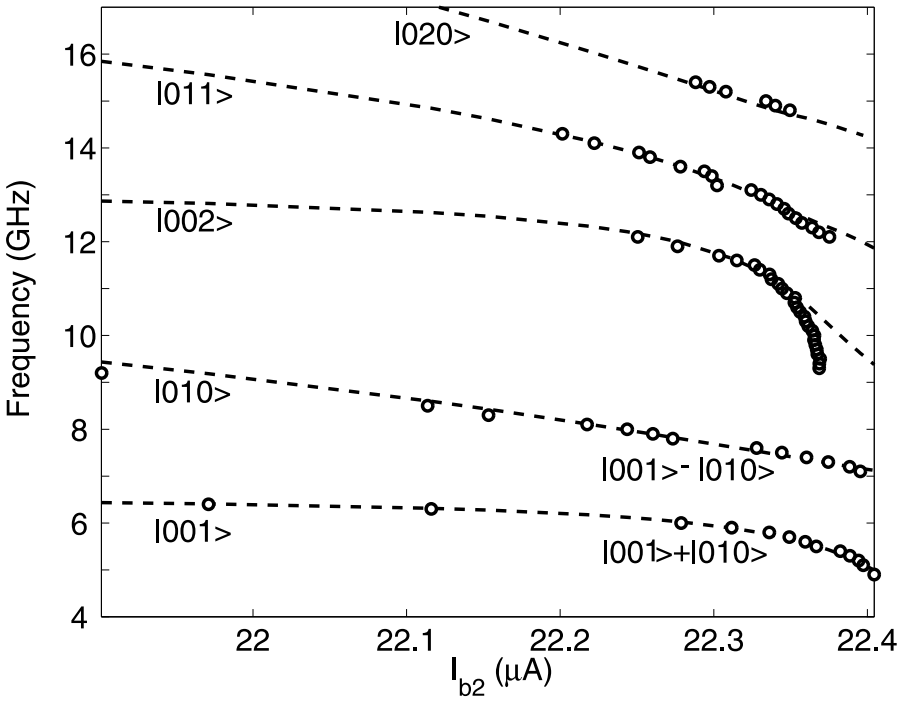

Figure 8.3: Spectrum of junction J2 coupled to an LC resonator. J1 is zero-biased. Circles are data, dashed lines are fits from Eq. 8.11 with the parameters: $I_{c2} = 22.536$ μA and $C = 4.8$ pF, $L = L_1 + L_2 = 1.71$ nH and $I_{b1} = 0$.

is referred to as the "3-qubit experiment" later on.). The dashed curves are the calculated transitions using the Hamiltonian in Eq. 8.11 with the previously determined parameters and one additional adjustable parameter $I_{b2} = 22.330\ \mu$A (the measured I_{b2} is 22.110 μA; the discrepancy appears to come from the calibration of the current ramp which has overestimated the critical current of junction J2 by 1%).

Comparison with simulations indicate that the lowest three excited states are formed from the subspace spanned by $|100>$, $|010>$ and $|001>$. In our case $\omega_3 \approx \omega_2$, where ω_2 is the $|0>$ to $|1>$ level spacing for J2. Therefore, for J1 at low bias we expect the first two excited states to be $(|001> \pm |010>)/\sqrt{2}$ with a splitting of $\xi\hbar\omega_3$ (see Fig. 8.4 for $I_{b1} < 21\ \mu$A).

Note the presence of a triple degeneracy point at $I_{b1} = 21.18\ \mu$A, where the first three excited states make their closest approach. At this bias, the predicted lowest three excited states are $(|100> - |010> - \sqrt{2}|001>)/2$, $(|100> + |010>)/\sqrt{2}$, and $(|100> - |010> + \sqrt{2}|001>)/2$ with corresponding energies of $\hbar\omega_3(1 - \xi/\sqrt{2})$, $\hbar\omega_3$ and $\hbar\omega_3(1 + \xi/\sqrt{2})$. The first and third excited states are entangled states involving the two junctions and the LC resonator, while the second excited state corresponds to an in-phase oscillation of the two junctions that does not couple to the resonator. The higher levels shown in Fig. 8.4 also agree well with our calculations. The theoretical description of these quantum states, however, is significantly more complicated than the lower levels, as they correspond to entangled states with multiple excitations in all three degrees of freedom [133].

8.4 Resonant coupling between two junction qubits

We note that the observed avoided crossings between the in-phase state and the two out-of-phase states at the triple degeneracy point are in good agreement with our model, which predicts strong coupling with a dimensionless coupling coefficient of

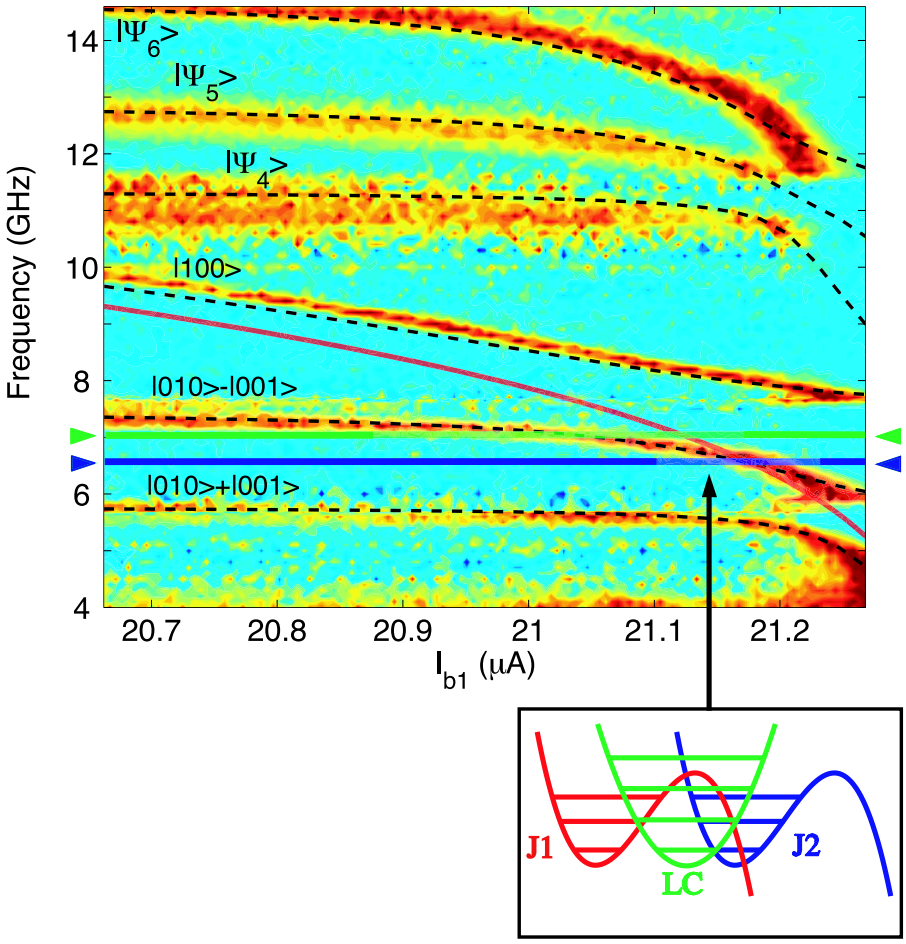

Figure 8.4: Spectrum of the macroscopic three-body system (sample LCJJ-Nb2) at 25 mK. Color denotes measured enhancement in escape rate due to microwaves when the bias current for J1 is ramped and J2 is biased at $I_{b2} = 22.330\ \mu$A. Red for maximum enhancement and light blue for zero. The red line represents the uncoupled level spacing for J1, and the horizontal blue and green lines are for J2 and the LC resonator respectively. The dashed curves are fits using Eq. 8.11 with the parameters shown in Figs. 8.2 and 8.3 and $I_{b2} = 22.330\ \mu$A. At the triple degeneracy point ($I_{b1} = 21.15\mu$A) where the frequencies of the three particles are close to each other (shown in the black box), entangled states between all three particles are predicted.

$\xi/\sqrt{2} = \sqrt{C_3/(C+2C_3)/2} \approx 0.18$.

When ω_3 is much greater than either junction frequency and the junction frequencies are detuned from each other, we expect the coupling strength is proportional to ξ^4. Quantum logic gates that are similar to the two-qubit gates [134] designed for the purely capacitive coupling can also be built for this circuit.

This resonant coupling scheme, which offers the potential for a large ratio of coupling to decoupling, opens up the possibility of using an LC resonator as a data bus [135, 136, 48] for interacting multi-qubit systems in a superconducting quantum computer.

8.5 Capacitive coupling between two junction qubits

When both junction frequencies are equal to the resonator frequency ω_3, a resonant coupling strength that is proportional to ξ is achieved between the two junction qubits. However there is still coupling between the two junctions when ω_3 is much greater than either junction frequency but the two junctions are tuned to the same frequency ω.

In the limit $\omega \ll \omega_3$, one should be able to ignore the energy stored in the inductor. Therefore the coupling between the two junction qubits reduces to capacitive coupling[1]. Quantum mechanically we can think of the LC resonator as being in its ground state since its excited states have very high energies. Figure 8.5 shows a schematic of the circuit in this limit.

For this regime of pure capacitive coupling, we only have two degrees of freedom, γ_1 and γ_2, and the Hamiltonian for the system is

$$H = \frac{p_1^2}{2M} + U_1(\gamma_1) + \frac{p_2^2}{2M} + U_2(\gamma_2) + +\zeta\frac{p_1 p_2}{M} \tag{8.12}$$

[1] At frequencies much below the resonance frequency of the series LC resonator, the resonator behaves capacitively.

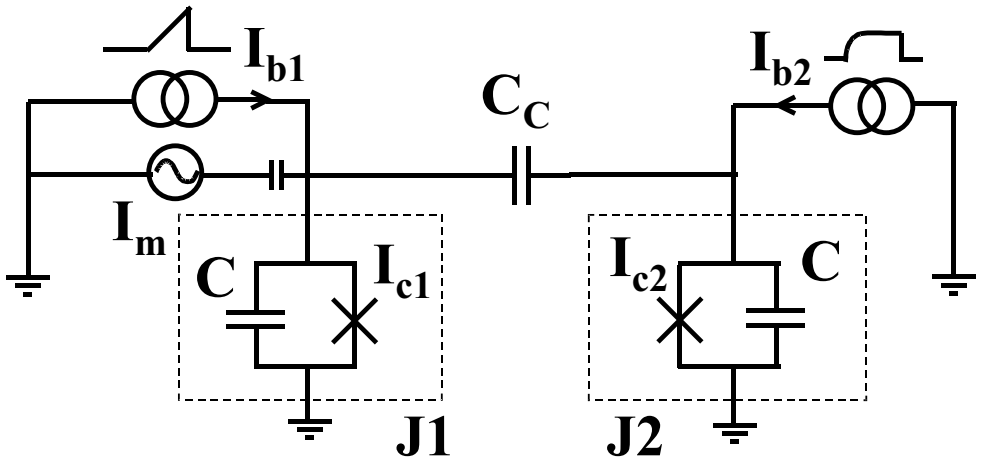

Figure 8.5: Two capacitively coupled Josephson junctions. Bias currents through the two junctions can be controlled by I_{b1} and I_{b2}. I_m is a microwave current and is used to probe the energy levels of the system. I have assumed the same capacitance C for the two junctions.

where $\zeta = C_c/(C_c+C)$ is a dimensionless coupling coefficient and $M = \left(\frac{\Phi_0}{2\pi}\right)^2 C(1+\zeta)$ is the renormalized mass for each junction.

This capacitive coupling regime was what we examined in our early experiments [137]. To do this, we applied a magnetic field that is in the plane of the junction overlap area to suppress the junction currents so that the junction frequencies were around 5 GHz, reasonably lower than the resonator frequency 7 GHz. Figure 8.6 shows the measured spectrum when the bias current J2 is ramped and that for J1 is held at a constant bias of $I_{b1} = 14.630$ μA (this measurement is referred to as the "2-qubit experiment" later on). Note that the minimum avoided crossing occurs at $I_{b2} = 15.275$ μA, where theory predicts the first two excited states are of the form $(|01> \pm |10>)/\sqrt{2}$. Here the first and second position in the ket denote J1 and J2 respectively.

Also shown in Fig. 8.6 are resonance peak positions (black squares) measured when the bias current J2 is ramped and J1 is held at $I_{b1} = 0$. In this case, the two junctions are effectively decoupled; thus one is measuring the spectrum of junction J2 only. The dashed diagonal black curve is a fit to the data using the single junction $|0> \rightarrow |1>$ level spacing formula with $I_{c2} = 15.421 \pm 0.002$ μA and $C(1+\zeta) = 5.63 \pm 0.07$ pF.

The critical current for junction J1 can also be found by measuring the spectrum of junction J1 when J2 is zero-biased. Fitting the data leads to $I_{c1} = 14.779 \pm 0.004$ μA.

We then fit the spectrum shown in Fig. 8.6 using the Hamiltonian in Eq. 8.12 and varying I_{c1}, C and C_c. The fits obtained using $I_{c1} = 14.778$ μA, $C = 4.8$ pF and $C_c = 0.7$ pF are shown as white lines in Fig. 8.6. Note the parameters obtained are in good agreement with those obtained by fitting the single junction spectra.

One surprise was that the coupling capacitance C_c is almost twice C_3 (0.37 pF) found before in the 3-qubit experiment, the physical capacitance in the circuit. This discrepancy is not accidental, although it puzzled us for some time. The key thing

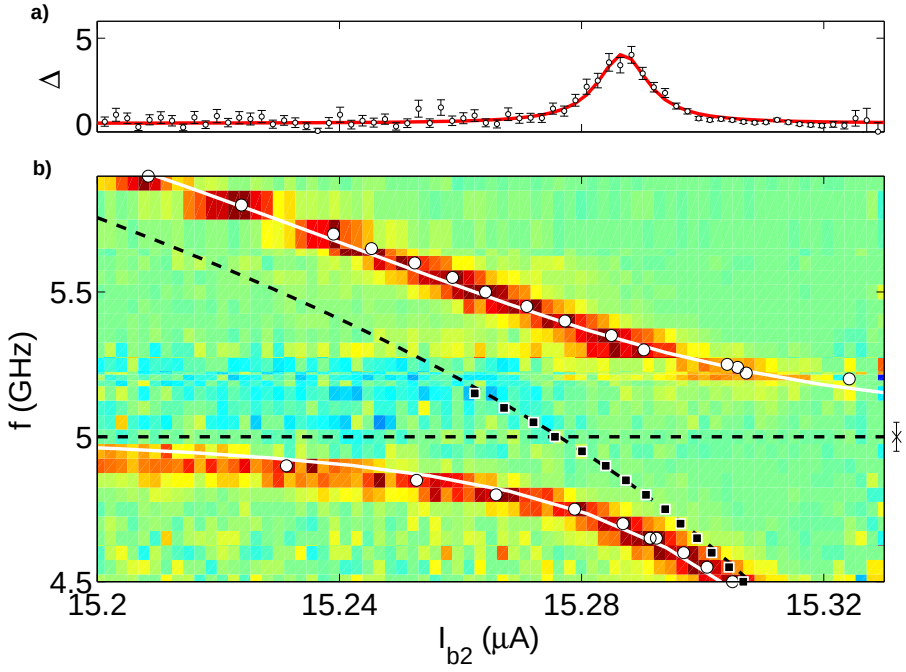

Figure 8.6: Spectrum of two capacitively coupled junctions. (a) Measured resonance enhancement peak for $|00>\rightarrow(|01>-|10>)/\sqrt{2}$ transition for microwave power applied at f=4.7 GHz. (b) Color plot of normalized Δ as a function of microwave drive frequency (y-axis) and bias current I_{b2} through J2 (x-axis). Each data set (horizontal stripe, as in (a) above) is normalized so the highest peak is unity (red), with green signifying zero, and blue negative enhancement. For each frequency, we adjust the microwave power so the maximum $\Delta < 5$. Open circles mark centers of resonance peaks. Solid white lines are from theoretical calculation using the following parameters: $I_{c2} = 15.421\ \mu$A , $I_{c1} = 14.778\ \mu$A, $I_{b1} = 14.630\ \mu$A, $C = 4.8$ pF and $C_c = 0.7$ pF . For comparison, decoupled $|0>\rightarrow|1>$ energy spacing for J1 is shown by the dashed horizontal black line and cross while J2 is the dashed diagonal black line and squares.

to realize is that we can neglect the inductor only when ω_3 is much larger than the junction frequency. But here, the junction frequency (5 GHz) is not small compared to ω_3 (7 GHz), therefore one still has to include the effect of the LC resonator.

Analysis of this regime using Eq. 8.11 shows that the LC mediated interaction between the two tuned junctions can be modeled by a frequency dependent coupling [133]

$$\zeta(\omega) = \xi^2/(1 - \xi^2 - \omega^2/\omega_3^2) \tag{8.13}$$

where ω is the junction frequency. For ω= 5 GHz, and ω_3= 7 GHz, we have $\zeta(\omega) = 0.14$, in good agreement with the measured number $\zeta = C_c/(C_c + C) = 0.13$.

However for $\omega \ll \omega_3$ and small coupling, Eq. 8.13 reduces to $\zeta(\omega) \approx \xi^2 = C_3/C$, which is just the frequency-independent coupling coefficient discussed in the pure capacitive coupling model with $C_c = C_3$.

In comparison with the resonant coupling regime, the coupling between the two junctions decreases from ξ to ξ^2 with this low-frequency capacitive coupling scheme. The coupling strengths in both schemes are proportional to ξ^4, when the two junctions are detuned from each other and the resonator.

8.6 Coherence times

While the resonance peak positions reveal the spectrum of the system, the peak widths contain information about the decoherence in the system.

The half width at half maximum of the peak can be converted to a width in frequency, from which the spectroscopic coherence time T_2^* can be obtained (see Chapter 4). For the spectrum shown in Fig. 8.6, we found T_2^* is about 2-4 ns for both the single junction resonances and coupled junction resonances [79]. Similar to the data shown in Fig. **??** for sample LCJJ-Al, the coherence times also get shorter for lower frequencies probably due to higher tunneling rates and current noise.

The spectroscopic coherence times for the resonances shown in Fig. 8.4 are around 2 ns, which is shorter than that for the resonances shown in Fig. 8.6. In the 3-qubit experiment, I used a different rf filter that has a much higher rolloff frequency (∼16 MHz) than that for the 2-qubit experiment (∼2 MHz). This increase in bandwidth may lead to a significant amount of current noise in the junctions as discussed in Chapter 6. Thus I suspect this broadening is due to current noise.

I note that the resonances in Fig. 8.4 broaden severely for high bias currents. Also, in Figs. 8.2 and 8.3, the level spacing for the third excited state drops vertically on the right side, which deviates considerably from the fit. A similar phenomenon also occurs in Fig. 8.4 but is not that pronounced as in Figs. 8.2 and 8.3. The cause of this deviation is unknown. Further analysis is needed to understand this peak shifting phenomenon, which seems to occur only for very broad transitions.

The higher states shown in Fig. 8.4 seem to be broader than the lower states. This is probably because the upper states have much higher tunneling rates. In particular, state decomposition shows $|\Psi_4>$ has a large weight in $|020>$, i.e. the dc-biased junction (J2) is in its second excited state, which explains why the transitions from $|000>$ to this state are so broad.

8.7 Summary

In this chapter, I presented microwave spectroscopy results on a coupled macroscopic three-body system comprised of an LC resonator and two Josephson junctions. The quantum nature of the resonator was revealed through coupling to Josephson junction qubits. Entangled states between the two junctions were probed when the junctions are out of resonance with the LC resonator. Finally our results support the existence of entangled states between all three degrees of freedom when both junctions are in resonance with the LC resonator. This spectroscopy technique can also be extended to study multi-qubit systems.

Chapter 9

Correlated Escape Measurement

In the previous chapters I described how I used spectroscopy to probe the quantized energy levels in single qubits, two capacitively coupled junction qubits and a macroscopic three-qubit system. Comparison with quantum mechanical calculations implies that the states probed in the two-qubit and three-qubit experiments are entangled states. For example, in the two-qubit experiment, theory predicts the states are of the form $(|01> \pm |10>)/\sqrt{2}$ at the minimum avoided crossing point. However we have not directly measured these states. In addition, state measurement is also required for quantum logic gates. In this Chapter I discuss a method to do state measurement in the coupled qubit system (LCJJ-Nb2) and present some preliminary results on measuring entangled states.

9.1 Measuring entangled states

The Hamiltonian of two capacitively coupled qubits in Eq. 8.12, when diagonalized, will produce a set of energies and states. The energies form the spectrum of the system that can be probed spectroscopically. Agreement between theoretically predicted spectrum and the measured spectrum will imply that the states, which have not been measured directly, are probably like those predicted by theory. But can we verify these states?

9.1.1 Entangled states

The lowest excited state for the two coupled junction system is predicted to be of the form

$$|\Psi>= \alpha|01> +\beta|10> \tag{9.1}$$

where $|\alpha|^2$ and $|\beta|^2$ are the probability of finding the system in $|01>$ and $|10>$ respectively, and $|\alpha|^2 + |\beta|^2 = 1$.

Note $|\Psi>$ in Eq. 9.1 cannot in general be written as a product of individual qubit states. This leads to the following special property: the result of a measurement on one particle depends on the state of the other particle, i.e., the result of a measurement on one particle is correlated with that of a simultaneous measurement on the other particle. This correlation does not depend on the distance between the two particles, or whether there is physical interaction between the two. This kind of states are said to be "entangled".

Therefore, to measure this state, we need two detectors that are simultaneously measuring the states of each qubit. If the results are always $|01>$ or $|10>$ with probabilities of $|\alpha|^2$ and $|\beta|^2$ respectively, and $|\alpha|^2+|\beta|^2 = 1$, then we have confirmed the state[1].

Therefore the problem becomes to measure both individual qubit states simultaneously and distinguish whether the outcome is $|00>$, $|01>$, $|10>$ or $|11>$.

9.1.2 The measurement scheme

As discussed in Chapter 2, the tunneling rate Γ_1 from the first excited state is much higher than that from the ground state Γ_0. Therefore, measuring the escape rate of each junction seems to be a good way to distinguish the above four states, $|00>$, $|01>$, $|10>$ or $|11>$.

[1]There is a relative phase that remains undetermined.

If $|1>$ has a tunneling rate of infinity and $|0>$ has zero tunneling rate, then one might expect the four states could be identified by four different escape phenomena:

(i) If no escapes are measured for both junctions, then it implies the system is in $|00>$;

(ii) If escape for J1 is measured but no escape for J2, then it implies the system is in $|10>$;

(iii) If escape for J2 is measured but no escape for J1, then it implies the system is in $|01>$;

(iv) If escapes are measured for both junctions, then it implies the system is in $|11>$.

However in reality Γ_0 is not zero, and Γ_1 is only 500-1000 times larger than Γ_0. This will complicate the simple state assignment given above. For example, events where both junctions escape could mean the system is in $|00>$. This uncertainty in state assignment is called the measurement fidelity. By choosing appropriate biasing conditions, the fidelity can be made reasonably high.

Another problem is the effect produced by escape of one junction on the other junction. When the first junction escapes, the phase particle rolls down the wash-board potential and radiates power in a frequency range from GHz to THz. Due to the capacitive coupling between the two junctions (see Fig. 9.1(a)), this emitted radiation is coupled[2] to the other junction. Under this microwave radiation, the second junction is forced to switch even if it was initially in the ground state. Due to this effect, the states ($|01>$, $|10>$ and $|11>$) all correspond to events in which both junctions switch. However, there is still some differences between the switching events from the states:

(i) $|01>$ corresponds to J2 escaping first followed by J1 escaping.

(ii) $|10>$ corresponds to J1 escaping first followed by J2 escaping.

[2]The radiation can be expressed in terms of a microwave current with an amplitude of ζI_{c1}, where ζ is the coupling coefficient.

(iii) $|11>$ corresponds to J1 escaping first followed by J2 escaping, or J2 escaping first followed by J1 escaping.

The idea is that after one junction escapes, there is a short delay before the other junction escapes. Therefore, in principle we can still distinguish $|10>$ from $|01>$. However for our sample LCJJ-Nb2, this delay is very small, typically 200 ps, probably set by the inverse of the junction frequency (5 GHz). Figure 9.1(b) shows a schematic of the timing of the escapes from the two junctions. In order to detect this small delay, our detection circuit must be able to achieve a time resolution of less than 200 ps; otherwise we will not be able to tell which junction escapes first. Ultimately I was able to get a timing resolution of 100 ps by using ultra-low noise amplifiers and a large bandwidth voltage line (see Chapter 6).

In our spectroscopy experiments, the polarities of the current ramps used to bias the junctions are arbitrary. Usually the same polarities are used for the two ramps that bias the two junctions. However, since the junction impedance becomes large after it escapes, the bias current will flow through the coupling capacitance. This extra current (ζI_{c1}) will force the other junction to switch almost instantaneously. To lessen this effect, we used opposite polarities for the two current ramps. In this case, the first junction switching will tend to lower the bias current for the other junction.

9.2 Correlated escapes from the ground state $|00>$

It is possible to bias the junctions at such a low current that no escape can occur from the ground states. However, since the escape rate from the first excited state is only 500-1000 times larger than that from the ground state, it will take a very long time to accumulate enough switching events. Therefore the experiment is run with some escapes from the ground state.

Before studying correlated escapes from the excited states of the system, I first

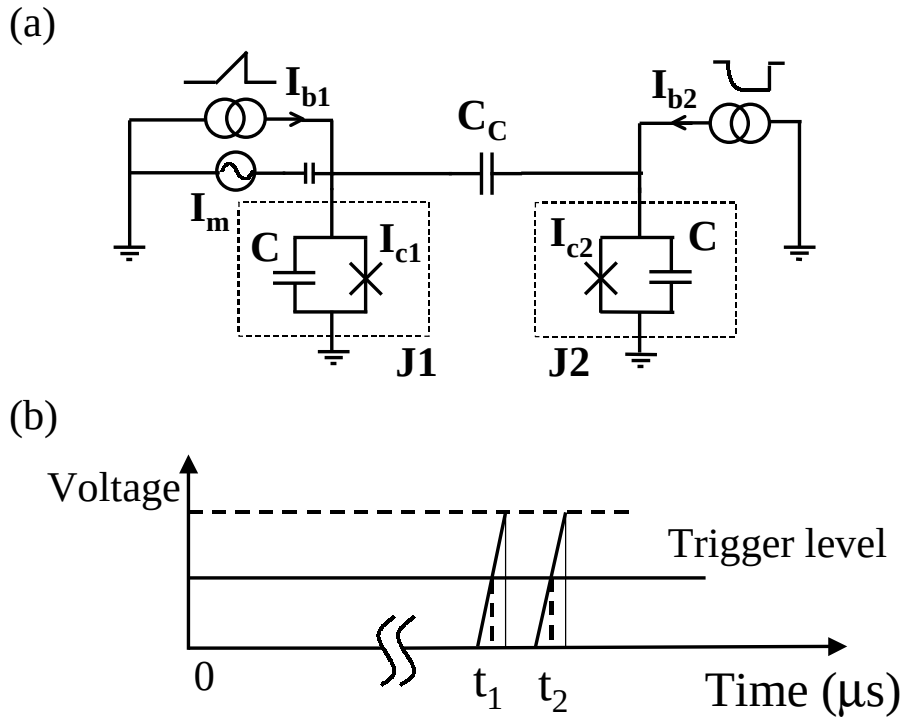

Figure 9.1: Correlated escape measurement on two capacitively coupled Josephson junctions. (a) Two capacitively coupled Josephson junctions. Notice opposite bias polarities were used for the two bias currents. (b) A schematic of the timing experiment. If $t_1 < t_2$, then J1 escapes first, and vice versa.

take a look at the correlation in escapes from the ground state, which already yields some interesting results.

As in the 2-qubit spectroscopy experiment, I ramp the bias current I_{b2} for J2 and fix the bias current I_{b1} for J1. Since the bias current for J1 is fixed, it has a roughly time-independent washboard potential and tunneling rates. However, the level spacing and tunneling rates for J2 are changing as a result of the bias current ramp. Figure 9.2 shows the tunneling rates from the ground states of the two junctions. As the bias current for J2 increases, the tunneling rate ($\Gamma_{0,J2}$) from the ground state of J2 increases from much smaller than $\Gamma_{0,J1}$ to much larger than $\Gamma_{0,J1}$, where $\Gamma_{0,J1}$ is the tunneling rate from the ground state of J1.

Therefore at the point where $\Gamma_{0,J2} = \Gamma_{0,J1}$ one should find 50% probability that J1 escapes first and 50% probability that J2 escapes first. In general for the $|00>$ state, the probability that J1 escapes first is determined by the ratio of the tunneling rates

$$P_{J1} = \frac{\Gamma_{0,J1}}{\Gamma_{0,J1} + \Gamma_{0,J2}} \tag{9.2}$$

Therefore, for small I_{b2}, since $\Gamma_{0,J2} \ll \Gamma_{0,J1}$, we expect P_{J1} to be equal to 1, and for large I_{b2} such that $\Gamma_{0,J2} \gg \Gamma_{0,J1}$, we expect P_{J1} to be essentially zero.

Figure 9.3 shows the measured switching histogram from the ground state of the two coupled junction system. The x-axis is the bias current for J2 and the y-axis is the delay ($\Delta t = t_2 - t_1$) between the two switching times for J2 and J1. The color denotes the number of counts in each grid. Since $\Delta t = t_2 - t_1$, $\Delta t > 0$ implies J1 escapes first and $\Delta t < 0$ implies J2 escapes first[3]. Therefore we expect to see J1 escapes first for small I_{b2} and J2 escapes first for large I_{b2}. This is indeed observed. Most escape events occur around 119.4 μA due to the large tunneling rate from the

[3]Note though that the $\Delta t = 0$ line was chosen to make this happen. In the raw data, the $\Delta t = 0$ line can be at some arbitrary number since the voltage signals from the two junctions have different shapes, speeds, and trigger levels.

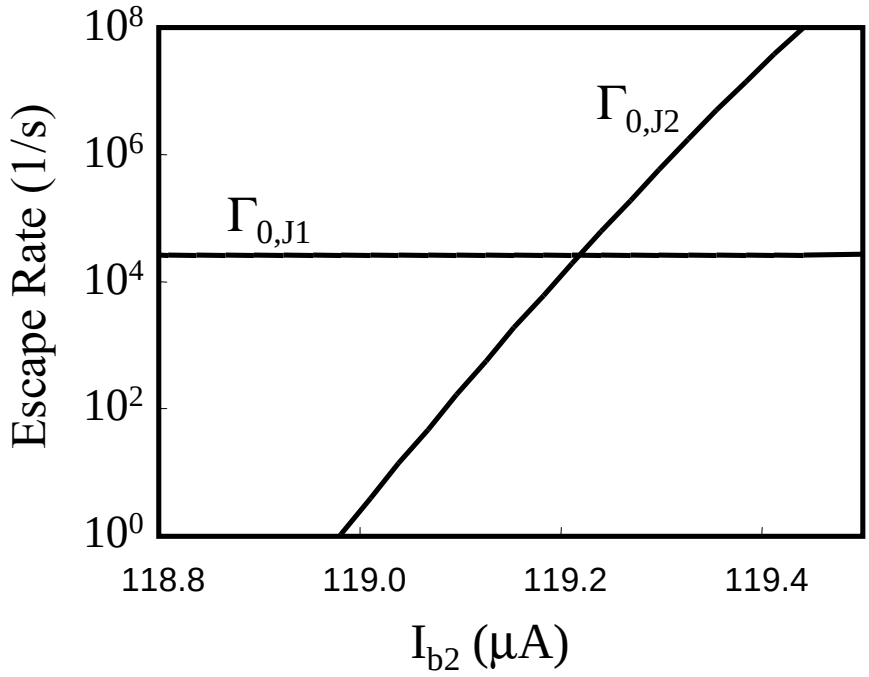

Figure 9.2: Tunneling rates from the ground states of the two junctions. The bias current for J1 is held constant, which leads to a constant $\Gamma_{0,J1}$; however the bias current for J2 is changing, resulting in a changing tunneling rate $\Gamma_{0,J2}$. At $I_{b1} \sim 119.2\ \mu A$, the two rates cross each other.

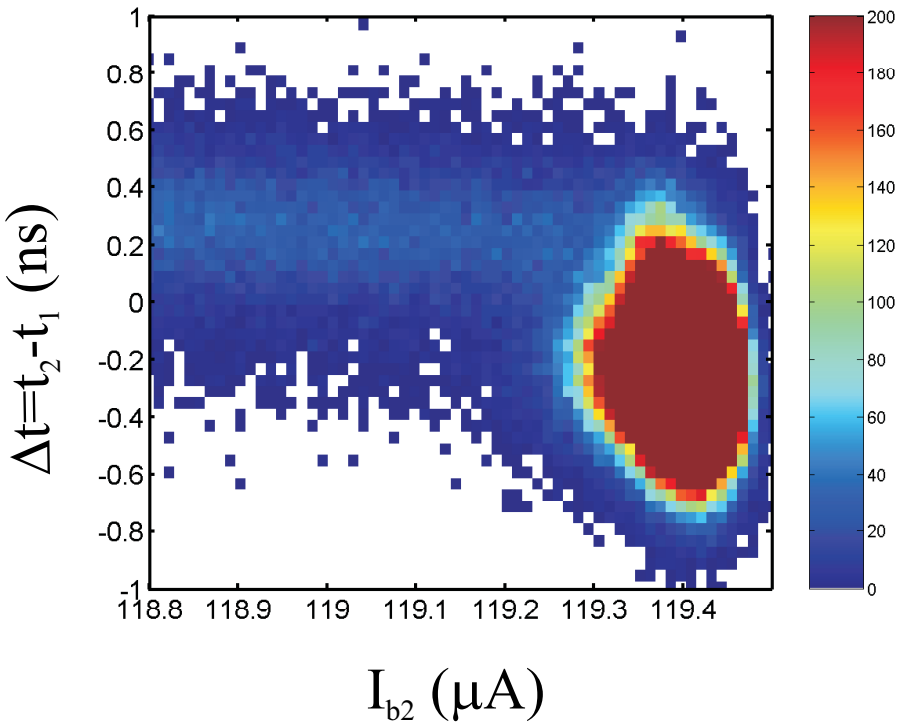

Figure 9.3: A 2-D switching histogram from the ground state. Note $\Delta t = t_2 - t_1 > 0$ implies J1 escapes first. Therefore J1 escapes first on the left side, and J2 escapes first on the right side.

ground state of J2 that has caused all not-yet-switched junctions to switch.

We can then calculate the probability that J1 escapes first by taking the ratio of the counts that are above the $\Delta t = 0$ line to the total counts for each bias current. The result is shown in Fig. 9.4. The solid curve is a theoretical prediction, in rough agreement with the data. The probability does not quite go to unity for low I_{b1} and the measured transition region around 119.25 μA is broader than the calculation, probably because the time resolution ($\sim$100 ps) is not small compared to the delay (200 ps).

As shown in Fig. 9.2, if we increase the fixed bias current for $J1$, then $\Gamma_{0,J1}$ will increase and cross the $\Gamma_{0,J2}$ curve at a higher I_{b2}. The result of this is the transition point in the delay plot (see Fig. 9.4) will shift to a higher bias current. Indeed this

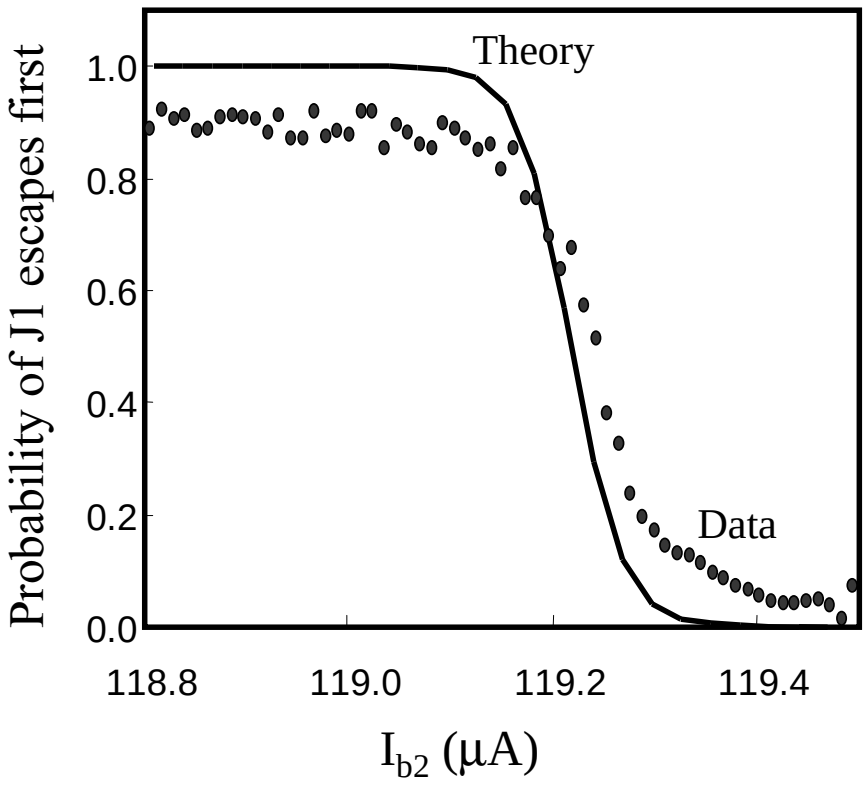

Figure 9.4: Probability that J1 escapes first from the state $|00>$ for sample LCJJ-Nb2 at 25 mK. The solid curve is a prediction using Eq. 9.2 with the rates obtained from the measurement.

effect was also observed in our experiment.

9.3 Correlated escapes from excited states $\alpha|01> + \beta|10>$

The rough agreement between theory and data for the state $|00>$ provided some plausibility to the idea of measuring states via escape event timing. Next I applied continuous microwaves to drive transitions from the ground state to the excited states and measured correlated escapes from the coupled junction system.

9.3.1 The spectrum

Figure 9.5 shows the measured spectrum of the system between 12 GHz and 15 GHz. One sees two branches, one above 14 GHz and the other below 14 GHz. There is a minimum avoided crossing at 119.15 μA. Since the frequency of the LC resonator is around 7 GHz, these states are very likely to be coupled to the second excitation of the resonator[4]. Therefore a full analysis using Eq. 8.11 in Chapter 8 is necessary to figure out the state decomposition[5]. However if we approximate the LC resonator as an inductor at these frequencies, then one would expect a position-position coupling between the two junctions instead of a momentum-momentum coupling for junction frequencies much lower than the LC resonance frequency. The result of this position-position coupling is similar to that of capacitive coupling, which leads to entangled states between the two junctions.

[4]Although we can run the experiment in a frequency range below 7 GHz, for small critical current junctions the time resolution is not good enough to distinguish which junction escapes first.

[5]At that time I did these measurements, we did not understand that we had an LC resonator or its possible effects.

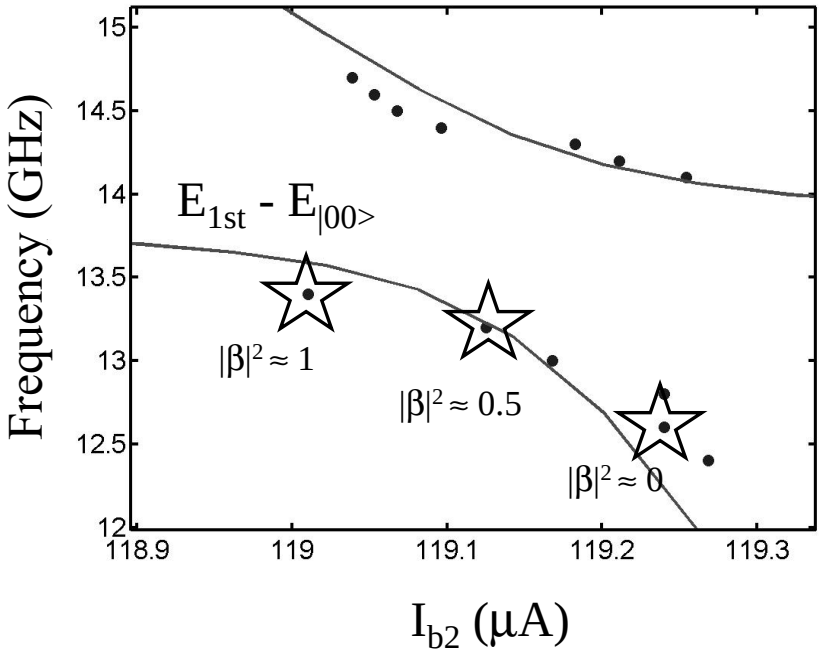

Figure 9.5: Spectrum of the three-body system at high frequencies. Solid circles are data. The line is a theoretical fit using the 2-qubit model with an effective capacitive coupling. Note the three highlighted frequencies correspond to states where $|\beta|^2$ is believed to be approximately 1, 1/2 and 0, respectively.

Therefore for the lower branch, I expect the states might be $|10>$, $(|10>+|01>)/\sqrt{2}$ and $|01>$ from left to right (see Fig. 9.5).

9.3.2 Theoretical prediction

Since these states probably involve the first excited state of the junction, we have to consider the tunneling rates both from $|0>$ and $|1>$. Figure 9.6 shows the tunneling rates $\Gamma_{0,J1}$, $\Gamma_{1,J1}$, $\Gamma_{0,J2}$, $\Gamma_{1,J2}$ as a function of the bias current for J2. Since I_{b1} is held constant, $\Gamma_{0,J1}$ and $\Gamma_{1,J1}$ are time-independent, while $\Gamma_{0,J2}$ and $\Gamma_{1,J2}$ increase with I_{b2}.

Similar to the correlated escape from the ground state, for an excited state with a general form $\alpha|01>+\beta|10>$, we expect the probability that J1 escapes first is

$$P_{J1} = |\alpha|^2 \frac{\Gamma_{0,J1}}{\Gamma_{0,J1}+\Gamma_{1,J2}} + |\beta|^2 \frac{\Gamma_{1,J1}}{\Gamma_{1,J1}+\Gamma_{0,J2}} \tag{9.3}$$

Under the conditions $\Gamma_{0,J1} \ll \Gamma_{1,J2}$ and $\Gamma_{1,J1} \gg \Gamma_{0,J2}$, i.e. the tunneling rate from $|1>$ is larger than that from $|0>$, then $P_{J1} = |\beta|^2$. Thus the probability that J1 escapes first is a measure of $|\beta|^2$. Notice the tunneling rate from $|1>$ is not always larger than that from $|0>$, because the bias current for junction J2 is changing. In Fig. 9.6, this condition is satisfied only in a narrow region from 118.9 μA to 119.3 μA. Based on this discussion, we expect:

(i) For $|10>$, the probability that J1 escapes first is $\sim$1;

(ii) For $(|10>+|01>)/\sqrt{2}$, the probability that J1 escapes first is $\sim$1/2;

(iii) For $|01>$, the probability that J1 escapes first is $\sim$0.

9.3.3 Measurement results

Figure 9.7 shows the switching histogram when microwaves of 13.4 GHz were applied to the system. Compared to the histogram for the ground state, there are some additional counts at low bias currents and $\Delta t > 0$. These are switching counts from

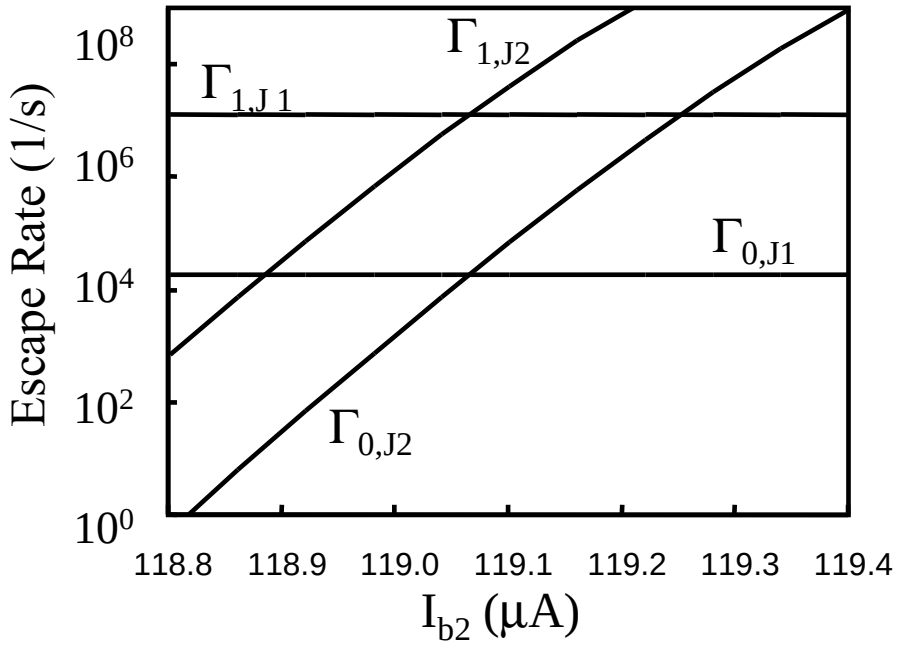

Figure 9.6: Tunneling rates from the ground and excited states of the two junctions. The bias current for J1 is held constant, which leads to constant $\Gamma_{0,J1}$ and $\Gamma_{1,J1}$. However the bias current for J2 is changing, which results in changing tunneling rates $\Gamma_{0,J2}$ and $\Gamma_{1,J2}$.

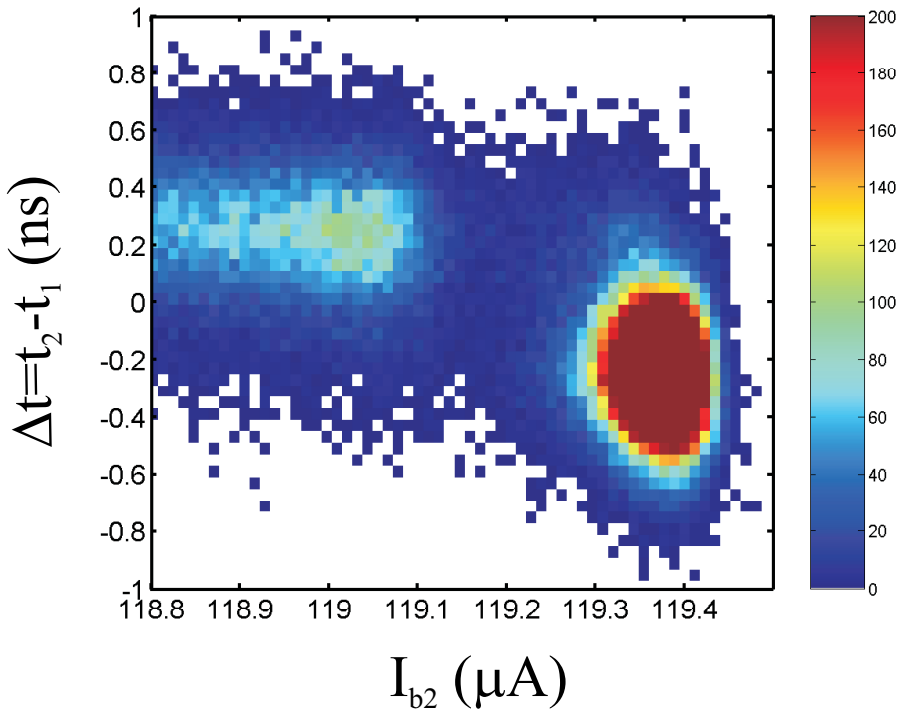

Figure 9.7: The timing switching histogram when 13.4 GHz microwaves were applied to sample LCJJ-Nb2. The expected state at this frequency is $|10>$; this implies J1 escapes first, which is consistent with our measurement.

the excited state to which the system is pumped. All the counts due to microwaves are in the region of $\Delta t > 0$ signifying J1 escapes first, which implies the state should be $|10>$. This is consistent with our expectation of the state with a energy of 13.4 GHz according to the spectrum shown in Fig. 9.5.

Figure 9.8 shows the switching histogram when microwaves of 13.2 GHz were applied to the system. Note the additional counts due to microwaves at 119.15 μA. It seems most of the additional counts are in the upper plane where $\Delta t > 0$, but there are also some counts in the lower plane, suggesting $|\beta|^2$ is neither unity nor zero. Because of the large background escape from the ground state, for the counts in the upper plane, we need to subtract the background to figure out the exact portion of the counts that is due to escape from the excited state. We did not try this subtraction so we could not perform a quantitative analysis of $|\beta|^2$. On the

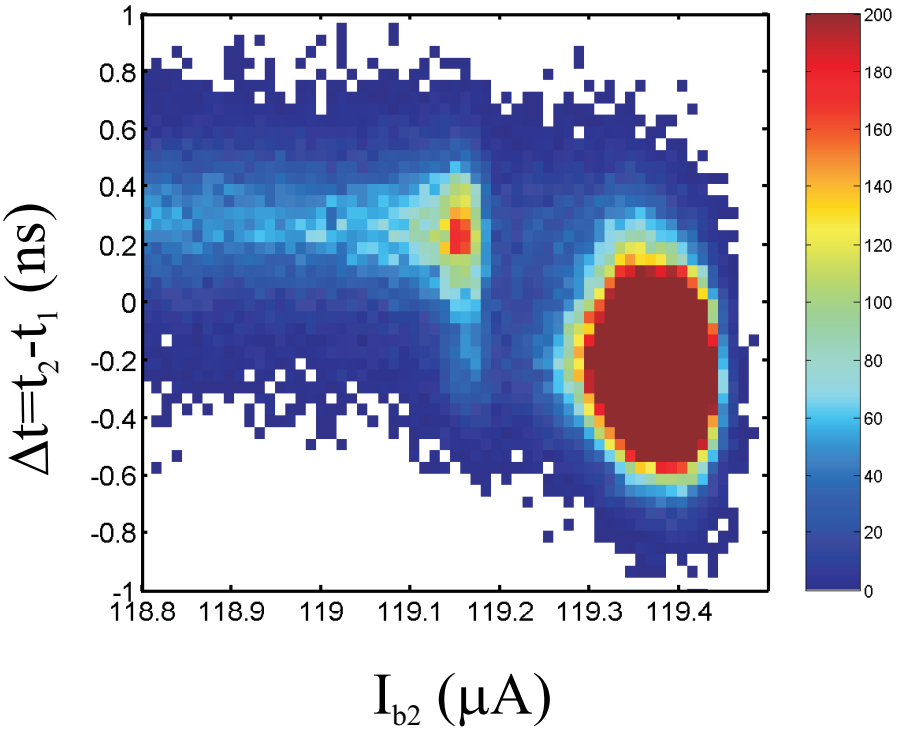

Figure 9.8: The timing switching histogram when 13.2 GHz microwaves were applied to sample LCJJ-Nb2. The expected state at this frequency is $(|10> - |01>)/\sqrt{2}$, which implies J1 has a 50% probability to escape first.

other hand, based on the spectrum shown in Fig. 9.5, one expects the state has the form of $(|10> - |01>)/\sqrt{2}$, i.e. $|\beta|^2 = 1/2$. Therefore the data and theory are at least in qualitative agreement.

Figure 9.9 shows the switching histogram when microwaves of 12.6 GHz were applied to the system. In contrast to the above two cases, all the counts due to microwaves now occur in the lower half plane where $\Delta t < 0$. This means J2 now escapes first, which implies the state should be $|01>$. This is consistent with our expectation of the state with an energy of 12.6 GHz according to the spectrum shown in Fig. 9.5.

Due to the large background counts and the marginal time resolution, it is difficult to deduce a number for $|\beta|^2$. However the measured states are qualitatively

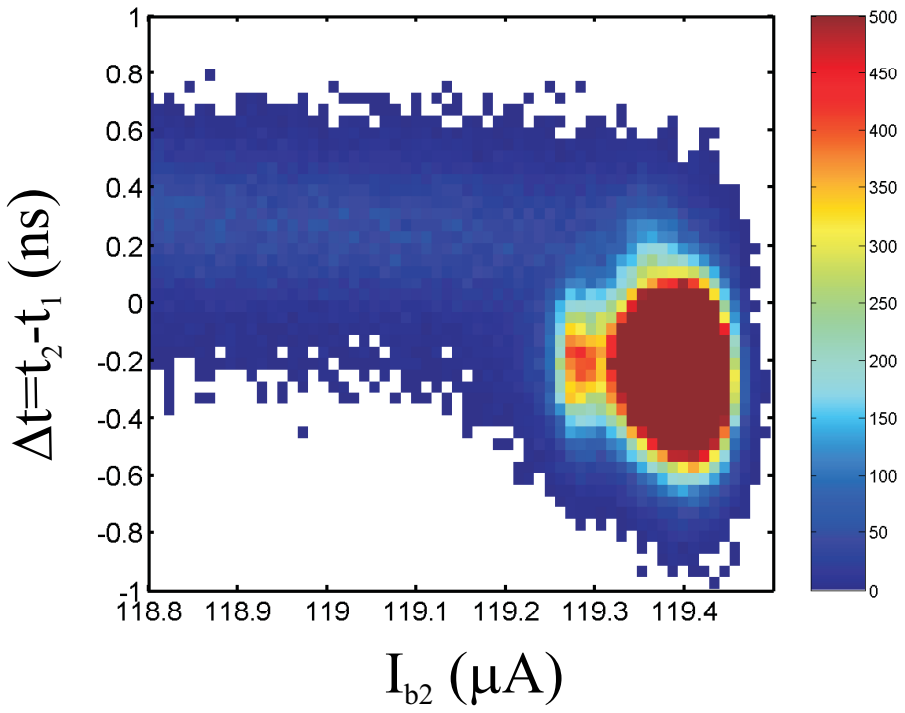

Figure 9.9: The switching histogram when 12.6 GHz microwaves were applied to sample LCJJ-Nb2. The expected state at this frequency is $|01>$; this implies J2 escapes first, which is consistent with our measurement.

consistent with theoretical expectations. Thus after modification and improvement, such as reducing the background escape from the ground state (or finding ways to subtract it) and improving the time resolution, it may be possible to use this correlated escape measurement technique to do quantitative state measurement.

9.4 Summary

In this chapter, I have described a technique to do state measurement, particularly to measure the states of the form $\alpha|01> + \beta|10>$. Measurement of correlation between escapes of two junctions can be used to distinguish the four states: $|00>$, $|01>$, $|10>$ and $|11>$. Due to the coupling of the first junction to the second junction, we cannot just track whether each junction escapes or not, but have to measure which junction escapes first. With a time resolution of 100 ps, we demonstrated that it is possible to tell which junction escapes first. The preliminary results on measuring the excited states of a two-coupled-junction system indicate this correlated escape measurement technique can be used to do quantitative state measurement.

One remaining issue is that when we observe an event in which J1 escapes and then J2 escapes after a short delay, we cannot tell whether this corresponds to $|10>$ or $|11>$. However, in the above experiment since we are concerned only with the first and second excited states, which do not contain $|11>$ according to theory, we can just put $|11>$ aside. However, for gates in a real quantum computer, one does not know which state is being measured, and all possible state decompositions need to be considered. One possible solution to this problem is to decrease the coupling between the two junctions to prevent forced switching of the junction that is in $|0>$. In general one expects the $|11>$ state to have a delay that is different from that for the $|10>$ state. Further work on this aspect is needed.

Chapter 10

Conclusion

In this thesis I have reported research on quantum computing using superconducting circuits. My work involved two main components: characterization of a current-biased Josephson junction qubit and investigation of coupling between multiple qubits.

10.1 Characterization of a phase qubit

In characterizing a phase qubit, I attacked the problem theoretically and experimentally.

The relaxation process was modeled using the master equation and effects of the shunt resistance and temperature on the energy relaxation time (T_1) of the qubit were examined. A simple method of testing the quality factor of a qubit with a long relaxation time, the population depletion technique, was suggested.

A stochastic Bloch equation was used to study decoherence in a phase qubit theoretically. I found that the effect of high frequency noise can be simply described by a dephasing rate ($1/T_2$) due to averaging of the noise with frequencies above the relaxation rate. However for low frequency noise, decoherence cannot be simply described by a dephasing rate. In this case a spectroscopic coherence time (T_2^*) is appropriate and includes decoherence due to both dissipation and noise. This

stochastic Bloch equation method can be readily generalized to analyze decoherence in other types of superconducting qubits.

On the experimental side, a variety of qubit isolation circuits were designed and T_1 and T_2^* of the phase qubit with these isolation circuits were characterized by several different methods. The resistively isolated junction qubit (RJJ-Al) had a severe heating problem which prevented us from seeing quantum effects. All three LC isolated junction qubits (LCJJ-Al, LCJJ-Nb1 and LCJJ-Nb2) showed clear quantum phenomena (macroscopic quantum tunneling, energy level quantization). The measured spectroscopic coherence times (T_2^*) for all three samples are in the range of 1-3 ns, consistent with decoherence due to current noise. The relaxation times (T_1) deduced from fits to the resonance peaks for LCJJ-Al and LCJJ-Nb1 are 12 ns and 7 ns respectively, and the measured T_1 for LCJJ-Nb2 is 4 ns. T_1 values for all three samples are considerably smaller than designed for reasons that are not clear at the present time.

No quantized levels were observed for the resonantly isolated junction qubit (RESJJ-Nb). The relaxation time measured using the population depletion technique is about 40 ns.

The inductor-junction isolated qubit (LJJJ-Nb) demonstrates a better T_2^* than all our previous samples. Coherent quantum oscillations (Rabi oscillations) were observed in this sample with a decay time of about 14 ns. The spectroscopic coherence time T_2^* is about 8 ns. The width of the $|1> \rightarrow |2>$ is broader than the $|0> \rightarrow |1>$, implying that decoherence is dominated by dissipation. In other words, a rough estimate of T_1 is $T_1 \approx T_2^* = 8$ ns. This number is much shorter than what we would expect for this design (1 μs).

Although the coherence time measured here is not as long as we wanted, it is probably long enough for demonstration of simple logic operations.

10.2 Coupling between multiple qubits

The coupled three-body system I examined is comprised of two Josephson junction qubits and an LC resonator. Our measurements support the idea that this macroscopic three-body system is indeed governed by quantum mechanics.

The LC resonator has a size of almost 1 mm with a natural frequency of 7 GHz and was probed through coupling to Josephson junctions, which are anharmonic.

In the low frequency range, this circuit can be described as two junction qubits coupled by a capacitor. A dimensionless coupling coefficient of $C_c/(C_c + C)$ results when the level spacings of the two junctions are tuned together. The coupling can be essentially turned off by detuning the junction frequencies. Our measured spectrum agrees well with theory, consistent with the existence of entangled states between the two junction qubits.

When the junction frequencies are tuned to the LC mode, our spectroscopy results indicate the existence of entangled states between all three degrees of freedom. In this regime, the system can be viewed as two remote qubits (junctions) being coupled by a flying qubit (a single photon in the resonator). This is analogous to a QED experiment of two atoms interacting with a resonant cavity. Our results demonstrate the possibility of coupling two remote qubits and can perhaps be viewed as a first step in realizing a distributed superconducting quantum computer.

10.3 Future work

There are many open questions in the field of superconducting quantum computing. Answering these questions will move us closer to realizing the construction of a quantum computer, and further our understanding of how quantum mechanics works in the macroscopic world.

The major question that begs for a clear answer is, why the measured T_1 is

much shorter than the expected value? What other relaxation channels have been overlooked in our analysis? Is it due to quasiparticle poisoning, the quality of the junction and the material, or other factors? Is the longest T_1 obtained on NbN/AlN/NbN junctions [70] a result of the material? Answers to these questions will help us figure out the large discrepancy between the measured and expected T_1.

Our preliminary results on state measurement shows that we can roughly distinguish $|01>$ from $|10>$. But this method cannot tell the difference between $|11>$ and $|01>$ (or $|10>$) . This is acceptable if one is told the state to be measured is a superposition of $|01>$ and $|10>$. But for real quantum computing, the state is unknown, and any state in Hilbert space is possible. Therefore the ability to distinguish between all possible states is required. This still needs to be demonstrated for a multi-qubit system.

The coherence times measured in the LJJJ-Nb sample are probably long enough to pursue coherent control experiment between two qubits. Any demonstration of coherence in a 3-qubit system will be a great step towards error correction and building a quantum computer.

Finally, I note that as the system gets more and more complicated, it will be very interesting to see how quantum mechanical phenomena survive in a complicated macroscopic world. Systems built from Josephson junctions appear to be superb test objects for such studies.

Appendix A:

Tunneling Rate from Cubic Potential

The quantum tunneling rate from the i-th state can be calculated using the WKB method, i.e.

$$\Gamma_i = \frac{\omega_i}{2\pi} \exp\left(-\frac{2}{\hbar}\int_{q_1}^{q_2} \sqrt{2m(U_c(q) - E_i)}\, dq\right) \tag{A-1}$$

where ω_i and E_i are the attempt frequency and energy of the particle in the i-th state, and q_1 and q_2 are the boundaries where $E_i = U_c(q_1) = U_c(q_2)$.

Therefore the problem reduces to an evaluation of the definite integral. For the cubic potential

$$U_c(q) = \frac{27}{4}\Delta U \left(\frac{q}{q_0}\right)^2 \left(1 - \frac{q}{q_0}\right) \tag{A-2}$$

we can rewrite Eq. A-1 as

$$\Gamma_i = \frac{\omega_i}{2\pi} \exp\left(-\frac{27\Delta U}{\hbar\omega_p} I\right) \tag{A-3}$$

where I is an definite integral and given by

$$I = \int_{y_1}^{y_2} \sqrt{y^2 - y^3 - \alpha^2}\, dy \tag{A-4}$$

here $\alpha^2 = 4E_i/27\Delta U$, and y_1 and y_2 are the two positive roots that satisfy $y^2 - y^3 - \alpha^2 = 0$.

For Levels deep inside the well, we have $\alpha^2 \ll 1$; therefore to forth order in α, we have $y_1 = \alpha + \alpha^2/2$, and $y_2 = 1 - \alpha^2$, and we can also expand the integral I to fourth order in α and obtain

$$I = \int_{y_1}^{y_2} \sqrt{y^2 - y^3}\, dy - \frac{\alpha^2}{2} \int_{y_1}^{y_2} \frac{1}{\sqrt{y^2 - y^3}}\, dy \tag{A-5}$$

After some algebra, we evaluate the above integral to be

$$I = \frac{4}{15} + \frac{1}{2} \ln \alpha\alpha^2 - \left(\frac{23}{30} + \frac{\ln 2}{2} \right) \alpha^2 + O(\alpha^3) \tag{A-6}$$

Therefore, for the ground state, $E_0 \approx \hbar\omega_p/2$, and the first excited state, $E_1 \approx 3\hbar\omega_p/2$, we have

$$\Gamma_0 = 12.7 \left(\frac{7.2\Delta U}{\hbar\omega_p} \right)^{1/2} \frac{\omega_0}{2\pi} \exp\left(-\frac{7.2\Delta U}{\hbar\omega_p} \right) \tag{A-7}$$

and

$$\Gamma_1 = 393.2 \left(\frac{7.2\Delta U}{\hbar\omega_p} \right)^{3/2} \frac{\omega_1}{2\pi} \exp\left(-\frac{7.2\Delta U}{\hbar\omega_p} \right) \tag{A-8}$$

Appendix B:

Transition Rate Due to Thermal Noise

The inter-level transition rates due to thermal noise for a lightly damped junction can be calculated using first-order perturbation theory.

Let $|i>$ be the initial state of the qubit, and $C_{ij}(t)$ be the amplitude of the qubit in the final state $|j>$ as a result of the perturbation due to the noise, $H_n = -\Phi_0 I_n(t)\gamma/2\pi$.

Using the time-dependent perturbation theory (to first order), we have

$$C_{ij}(t) = \frac{i}{2e}\int_0^t e^{i\omega_{ji}t} I_n(t) < j|\gamma|i > \, dt \tag{B-1}$$

where $\omega_{ji} = (E_j - E_i)/\hbar$ is the level spacing and we assume $\omega_{ji} > 0$. Then the transition probability will be

$$|C_{ij}(t)|^2 = \frac{|<j|\gamma|i>|^2}{4e^2}\int_0^t e^{-i\omega_{ji}t_1} I_n(t_1)\, dt_1 \int_0^t e^{i\omega_{ji}t_2} I_n(t_2)\, dt_2 \tag{B-2}$$

Taking an ensemble average of Eq. B-2 and using the relation between the noise correlation function and its power spectral density, we can simplify Eq. B-2 to

$$|C_{ij}(t)|^2 = \frac{|<j|\gamma|i>|^2}{4e^2}\int_0^\infty S(f)\, df \int_0^t \int_0^t e^{i\omega_{ji}(t_2-t_1)} \cos(i\omega(t_1 - t_2)\, dt_1 dt_2 \tag{B-3}$$

where $S(f)$ is the power spectral density of the noise current. Simplifying the above equation, we get

$$|C_{ij}(t)|^2 = \frac{|<j|\gamma|i>|^2}{2e^2}\int_0^\infty S(f)\left[\frac{\sin^2\frac{(\omega-\omega_{ji})t}{2}}{(\omega-\omega_{ji})^2}+\frac{\sin^2\frac{(\omega+\omega_{ji})t}{2}}{(\omega+\omega_{ji})^2}\right]df \tag{B-4}$$

Next we take the limit of $t\to\infty$, and notice

$$\lim_{t\to\infty}\frac{\sin^2\frac{(\omega-\omega_{ji})t}{2}}{(\omega-\omega_{ji})^2} = \frac{\pi t}{2}\delta(\omega_{ji}-\omega) \tag{B-5}$$

We obtain

$$\lim_{t\to\infty}|C_{ij}(t)|^2 = \frac{\pi t|<j|\gamma|i>|^2}{4e^2}\int_0^\infty S(f)\delta(\omega_{ji}-\omega)\,df \tag{B-6}$$

Note for a simple shunt resistance of R, the thermal noise has a spectral density

$$S(f) = \frac{4\hbar\omega}{R}\frac{1}{\exp(\hbar\omega/k_BT)-1} \tag{B-7}$$

Substitute Eq. B-7 into Eq. B-6, we obtain

$$\lim_{t\to\infty}|C_{ij}(t)|^2 = \frac{t\hbar\omega_{ji}|<j|\gamma|i>|^2}{2Re^2}\frac{1}{\exp(\hbar\omega_{ji}/k_BT)-1} \tag{B-8}$$

And finally the transition rate W_{ij}^t, the transition probability in unit time, is

$$W_{ij}^t = \lim_{t\to\infty}\frac{|C_{ij}(t)|^2}{t} = \frac{\Delta E}{2Re^2}\frac{|<i|\gamma|j>|^2}{\exp\left(\Delta E/k_BT\right)-1} \tag{B-9}$$

where $\Delta E = |E_j - E_i|$ is the level spacing between the i-th and j-th level, and $<i|\gamma|j>$ is the matrix element between the i-th and j-th levels.

Appendix C:

A Stochastic Bloch Equation

The density operator $\hat{\rho}$ of the total system obeys:

$$i\hbar\dot{\hat{\rho}} = [\hat{H}_{tot}, \hat{\rho}] \tag{C-1}$$

where $\hat{H}_{tot}$ is the Hamiltonian of the qubit and the environment,

$$\hat{H}_{tot} = \hat{H}_0 + \hat{H}_B + \hat{H}_C \tag{C-2}$$

where $\hat{H}_0$ is the Hamiltonian of the isolated junction given by Eq. 4.5, and $\hat{H}_B$ and $\hat{H}_C$ are the bath and coupling Hamiltonian respectively.

Assuming a harmonic oscillator bath and bilinear coupling [81, 93] as first proposed by Caldeira and Leggett, then $\hat{H}_B$ and $\hat{H}_C$ can be written as [81]

$$\hat{H}_B = \sum_{i=1}^{N} \left(\frac{\hat{p}_i^2}{2m_i} + \frac{1}{2} m_i \omega_i^2 \hat{x}_i^2 \right) \tag{C-3}$$

$$\hat{H}_C = -\hat{\gamma} \sum_{i=1}^{N} c_i \hat{x}_i + \sum_{i=1}^{N} c_i \frac{c_i^2 \hat{\gamma}^2}{2m_i \omega_i^2} \tag{C-4}$$

where $\hat{x}_i$ and $\hat{p}_i$ are the generalized coordinate and momentum operators of the i-th oscillator in the bath with mass of m_i, frequency of ω_i, and coupling coefficient c_i .

Tracing both sides of Eq. C-1 over the bath coordinates, I obtain

$$i\hbar\dot{\hat{\rho}}_S = [\hat{H}_0, \hat{\rho}_S] + Tr_B[\hat{H}_B, \hat{\rho}] + Tr_B[\hat{H}_C, \hat{\rho}] \tag{C-5}$$

One can show $Tr_B[\hat{H}_B, \hat{\rho}] = 0$. To evaluate $Tr_B[\hat{H}_C, \hat{\rho}]$, I use Eq. C-4 and expand to find

$$Tr_B[\hat{H}_C, \hat{\rho}] = \int (-\hat{\gamma}) < \vec{x}|\hat{C}\hat{\rho}|\vec{x} > \, d\vec{x} - \int < \vec{x}|\hat{\rho}\hat{C}|\vec{x} > (-\hat{\gamma})\, d\vec{x} \tag{C-6}$$

where $|\vec{x} >= |x_1 x_2 \cdots x_N >$ and $d\vec{x} = dx_1 dx_2 \cdots dx_N$, and

$$\vec{C} = \Sigma_i c_i \hat{x}_i - \Sigma_i \frac{c_i^2 \hat{\gamma}}{2m_i\omega_i^2} \tag{C-7}$$

Next introduce the Heisenberg operator,

$$\vec{C}(t) = \hat{U}^\dagger(t)\hat{C}\hat{U}(t) = \Sigma_i c_i \hat{x}_i(t) - \Sigma_i \frac{c_i^2 \hat{\gamma}(t)}{2m_i\omega_i^2} \tag{C-8}$$

where $\hat{U}(t) = \exp(-i\hat{H}_{tot}t/\hbar)$, $\hat{x}_i(t)$ is the coordinate operator of the i-th oscillator in Heisenberg picture, and $\hat{\gamma}(t)$ is the Heisenberg coordinate operator of the qubit. We can rewrite Eq. C-6 as

$$\begin{aligned} Tr_B[\hat{H}_C, \hat{\rho}] = &\int (-\hat{\gamma}) < \vec{x}|\hat{U}(t)\hat{C}(t)\hat{U}^\dagger(t)\hat{\rho}|\vec{x} > \, d\vec{x} \\ &- \int < \vec{x}|\hat{\rho}\hat{U}(t)\hat{C}(t)\hat{U}^\dagger(t)|\vec{x} > (-\hat{\gamma})\, d\vec{x} \end{aligned} \tag{C-9}$$

In the Heisenberg picture, one can show

$$\hat{x}_i(t) = \hat{x}_i(0)\cos(\omega_i t) + \frac{\hat{p}_i(0)}{m_i\omega_i}\sin(\omega_i t) + \frac{c_i}{m_i\omega_i}\int_0^t \hat{\gamma}(t')\sin(\omega_i(t-t'))\, dt' \tag{C-10}$$

Then we can rewrite $\hat{C}(t)$ as

$$\hat{C}(t) = \hat{\xi}(t) + \hat{\eta}(t) + \Sigma_i \frac{c_i^2}{2m_i\omega_i^2}\hat{\gamma}(t) \tag{C-11}$$

where

$$\hat{\xi}(t) = \Sigma_i c_i \left[\hat{x}_i(0) \cos(\omega_i t) + \frac{\hat{p}_i(0)}{m_i \omega_i} \sin(\omega_i t) \right] \tag{C-12}$$

$$\hat{\eta}(t) = -\int_0^t \kappa(t-t') \dot{\hat{\gamma}}(t')\, dt' - \kappa(t)\hat{\gamma}(0) \tag{C-13}$$

and $\hat{x}_i(0)$ and $\hat{p}_i(0)$ are the coordinate and momentum operator of the i-th oscillator in Heisenberg picture at $t = 0$. The coefficient $\kappa(t)$ is defined as

$$\kappa(t) = \frac{2}{\pi} \int_0^\infty \frac{J(\omega)}{\omega} \cos(\omega t)\, d\omega \tag{C-14}$$

where

$$J(\omega) = \frac{\pi}{2} \Sigma_i \frac{c_i^2}{m_i \omega_i} \delta(\omega - \omega_i) \tag{C-15}$$

The last term on the right hand side of Eq. C-11 will renormalize the qubit characteristic frequency, but under our experimental conditions, its effect is negligible and can be ignored. From Eqs. C-12 and C-13, we can see $\hat{\xi}(t)$ acts as a random force and $\hat{\eta}(t)$ acts as a memory damping force.

Next I substitute Eq. C-11 into Eq. C-9, obtaining

$$\begin{aligned} Tr_B[\hat{H}_C, \hat{\rho}] = & \int (-\hat{\gamma}) < \vec{x}|\hat{U}(t)\hat{\xi}(t)\hat{U}^\dagger(t)\hat{\rho}|\vec{x} > \, d\vec{x} \\ & - \int < \vec{x}|\hat{\rho}\hat{U}(t)\hat{\xi}(t)\hat{U}^\dagger(t)|\vec{x} > \, d\vec{x}(-\hat{\gamma}) + i\hbar D(\hat{\rho}_S) \end{aligned} \tag{C-16}$$

where $D(\hat{\rho}_S)$ denotes the contribution of the memory damping and is given by

$$\begin{aligned} D(\hat{\rho}_S) = & \frac{1}{i\hbar} \int (-\hat{\gamma}) < \vec{x}|\hat{U}(t)\hat{\eta}(t)\hat{U}^\dagger(t)\hat{\rho}|\vec{x} > \, d\vec{x} \\ & - \frac{1}{i\hbar} \int < \vec{x}|\hat{\rho}\hat{U}(t)\hat{\eta}(t)\hat{U}^\dagger(t)|\vec{x} > \, d\vec{x}(-\hat{\gamma}) \end{aligned} \tag{C-17}$$

Since $\hat{\xi}(t)$ is of the order of the coupling coefficient c_i, it follows that to first order in c_i we can evaluate the integral in Eq. C-17 using the approximations

$$\hat{U}(t) \approx \exp(-i\hat{H}_S t/\hbar)\exp(-i\hat{H}_B t/\hbar) \tag{C-18}$$

$$\hat{\rho} \approx \hat{\rho}_S \bigotimes \hat{\rho}_S \tag{C-19}$$

I obtain

$$Tr_B[\hat{H}_C, \hat{\rho}] = [-\hat{\gamma}\xi(t), \hat{\rho}_S] + i\hbar D(\hat{\rho}_S) \tag{C-20}$$

where

$$\begin{aligned}\xi(t) &= \int < \vec{x}|\hat{\xi}(t)\hat{\rho}_B(0)|\vec{x} > \, d\vec{x} \\ &= \Sigma_i c_i \left[Tr_B(\hat{x}_i(0)\hat{\rho}_B(0))\cos(\omega_i t) + \frac{Tr_B(\hat{p}_i(0)\hat{\rho}_B(0))}{m_i\omega_i}\sin(\omega_i t)\right]\end{aligned}$$

Next evaluating the correlation function for $\xi(t)$, I obtain

$$< \xi(t)\xi(0) >_{ensemble} = 4\hbar \int_0^\infty J(\omega)\cos(\omega\tau)\left(\frac{1}{2} + \frac{1}{e^{\hbar\omega/k_B T} - 1}\right)\frac{d\omega}{2\pi} \tag{C-21}$$

Equation C-21 gives the power spectral density of the random function $\xi(t)$. In fact, one can see that there are two parts, the $\frac{1}{2}$ term from zero-point noise, and the Boltzman which can be interpreted as John-Nyquist noise.

For the junction, I identify the random noise $\xi(t)$ as the current noise $I_n(t)$ flowing through the junction, i.e.

$$\xi(t) = \frac{\Phi_0}{2\pi} I_n(t) \tag{C-22}$$

Substituting Eq. C-20 into Eq. C-5, I find the equation of motion for the reduced density matrix

$$\frac{\partial \hat{\rho}_S}{\partial t} = \frac{1}{i\hbar}[\hat{H}_0 + \hat{H}_n, \hat{\rho}_S] + D(\hat{\rho}_S) \tag{C-23}$$

where $\hat{H}_n = -\Phi_0 I_n(t)\hat{\gamma}/2\pi$, $I_n(t)$ is the current noise flowing through the junction and $D(\hat{\rho}_S)$ is a memory damping term.

Comparing Eq. C-21 with Eqs. 4.1 and 4.2, I can make a connection between $J(\omega)$, which is defined through the microscopic quantities c_i, m_i and ω_i, and the circuit parameters $Y(\omega)$, namely

$$J(\omega) = \omega \left(\frac{\Phi_0}{2\pi}\right)^2 \mathrm{Re}[Y(\omega)] \tag{C-24}$$

Or

$$Y(\omega) = \frac{2\pi^3}{\Phi_0^2} \sum_{i=1}^{N} \frac{c_i^2}{m_i \omega_i} \delta(\omega - \omega_i) \tag{C-25}$$

i.e. $Y(\omega)$ can be linked to the microscopic quantities m_i, ω_i, and c_i.

Appendix D:

Transitions due to Noise

Setting $\delta\omega(t) = 0$ and $\Omega = 0$ in Eqs. 4.22-4.25 and neglecting $\Gamma_0\rho'_{00}$ and $\Gamma_1\rho'_{11}$, we Fourier transform Eqs. 4.22-4.25 to the frequency domain to find

$$\frac{1}{2\pi}\int_{-\infty}^{\infty}\alpha\dot{I}_n x'_+ e^{-i\omega t}\,dt = -2\alpha^2\int_{-\infty}^{\infty}\frac{(\omega-\omega')(\Gamma_{10}/2+i\omega')g(\omega-\omega')}{i\omega'+\Gamma_{10}/2)^2+\omega_0^2} \times\int_{-\infty}^{\infty}(\omega'-\omega'')\tilde{x}'_z(\omega'')g(\omega'-\omega'')\,d\omega'' \tag{D-1}$$

where

$$\tilde{x}'_z(\omega) = \frac{1}{2\pi}\int_{-\infty}^{\infty}x'_z(t)e^{-i\omega t}\,dt \tag{D-2}$$

$$g(\omega) = \frac{1}{2\pi}\int_{-\infty}^{\infty}I_n(t)e^{-i\omega t}\,dt \tag{D-3}$$

The Fourier transform of a stationary noise obeys [138]:

$$< g(\omega_1)g(\omega_2) >_{ensemble} = \frac{1}{4\pi}S_I(\omega_1/2\pi)\delta(\omega_1+\omega_2) \tag{D-4}$$

where $S_I(\omega/2\pi)$ is the power spectral density of the random noise and $<>_{ensemble}$ denotes an ensemble average. Taking the ensemble average of Eq. D-1, substitute Eq. D-4 into Eq. D-1, I find

$$\frac{1}{2\pi}\int_{-\infty}^{\infty}\alpha\dot{I}_n x'_+ e^{-i\omega t}\,dt = \frac{\alpha^2}{2\pi}\tilde{x}'_z(\omega)\int_{-\infty}^{\infty}\frac{(\omega-\omega')^2(\Gamma_{10}/2+i\omega')S_I(\frac{\omega-\omega'}{2\pi})}{(\Gamma_{10}/2+i\omega')^2+\omega_0^2}\,d\omega' \quad \text{(D-5)}$$

The integral on the right side depends on ω, however, if we make an approximation that in the long time limit $x'_z(t)$ is mainly a dc component, then we can set $\omega = 0$ in the integral. If we define

$$\Gamma_+ = \alpha^2\int_0^{\infty} S_I(\omega/2\pi)\omega^2\frac{\Gamma_{10}(\omega_0^2+\omega^2+\Gamma_{10}^2/4)}{(\omega_0^2-\omega^2+\Gamma_{10}^2/4)^2+\omega^2\Gamma_{10}^2}\,\frac{d\omega}{2\pi} \quad \text{(D-6)}$$

Eq. D-5 becomes

$$\frac{1}{2\pi}\int_{-\infty}^{\infty}\alpha\dot{I}_n x'_+ e^{-i\omega t}\,dt = \Gamma_+\tilde{x}'_z(\omega) \quad \text{(D-7)}$$

or

$$\alpha\dot{I}_n x'_+(t) = \Gamma_+ x'_z(t) \quad \text{(D-8)}$$

Similarly, one can show that $\alpha\dot{I}_n x'_z$ is equivalent to $\Gamma_+ x'_+$.

Appendix E:

Decoherence due to Noise

After neglecting $\Gamma_0\rho'_{00}$ and $\Gamma_1\rho'_{11}$ and applying the rotating wave approximation [100] to Eqs. 4.22-4.25, I obtain the following equation for the Fourier transform of $(e^{-i\omega t}\rho'_{01} - e^{i\omega t}\rho'_{10})/2i$:

$$B(\omega)V(\omega) = -\frac{\Omega}{2}\delta(\omega) + \varepsilon\int_{-\infty}^{\infty} h(\omega-\omega')V(\omega')\left(\frac{1}{i\omega+\Gamma_{10}/2} + \frac{1}{i\omega'+\Gamma_{10}/2}\right)d\omega' - \int_{-\infty}^{\infty}\frac{h(\omega-\omega')\,d\omega'}{i\omega'+\Gamma_{10}/2}\int_{-\infty}^{\infty} h(\omega'-\omega'')V(\omega'')\,d\omega'' \quad \text{(E-1)}$$

where $B(\omega) = i\omega + \Gamma_{10}/2 + \frac{\Omega^2}{i\omega+\Gamma_{10}} + \frac{\varepsilon^2}{i\omega+\Gamma_{10}/2}$, $V(\omega)$ and $h(\omega)$ are Fourier transforms of $(e^{-i\omega t}\rho'_{01} - e^{i\omega t}\rho'_{10})/2i$ and the level spacing fluctuation $\delta\omega(t)$ respectively.

Next, we try the following ansatz solution for Eq. E-1:

$$V(\omega) = \nu\delta(\omega) + D(\omega)h(\omega) \quad \text{(E-2)}$$

where $D(\omega)h(\omega)$ is everywhere finite, and $D(\omega)$ has no direct dependence on $h(\omega)$. Substituting Eq. E-2 into Eq. E-1, I find

$$B(\omega)V(\omega) = -\frac{\Omega}{2}\delta(\omega) + \varepsilon\nu h(\omega)\left(\frac{1}{i\omega+\Gamma_{10}/2}+\frac{1}{\Gamma_{10}/2}\right) + \varepsilon\int_{-\infty}^{\infty} h(\omega-\omega')h(\omega')D(\omega')\left(\frac{1}{i\omega+\Gamma_{10}/2}+\frac{1}{i\omega'+\Gamma_{10}/2}\right)d\omega' - \nu\int_{-\infty}^{\infty}\frac{h(\omega-\omega')h(\omega')}{i\omega'+\Gamma_{10}/2}\,d\omega' - \int_{-\infty}^{\infty}\frac{h(\omega-\omega')\,d\omega'}{i\omega'+\Gamma_{10}/2}\int_{-\infty}^{\infty}h(\omega'-\omega'')h(\omega'')D(\omega'')\,d\omega'' \quad \text{(E-3)}$$

Using Eq. D-4, I can simplify Eq. E-3 as [1]

$$B(\omega)\nu\delta(\omega) + B(\omega)h(\omega)D(\omega) = -\frac{\Omega}{2}\delta(\omega) + \varepsilon\nu h(\omega)\left(\frac{1}{i\omega+\Gamma_{10}/2}+\frac{1}{\Gamma_{10}/2}\right) + \frac{\varepsilon\delta(\omega)}{4\pi}\int_{-\infty}^{\infty}S_d(\omega'/2\pi)D(\omega')\left(\frac{1}{\Gamma_{10}/2}+\frac{1}{i\omega'+\Gamma_{10}/2}\right)d\omega' - \frac{\nu\delta(\omega)}{4\pi}\int_{-\infty}^{\infty}\frac{S_d(\omega'/2\pi)d\omega'}{i\omega'+\Gamma_{10}/2} - \frac{h(\omega)}{4\pi\Gamma_{10}}\int_{-\infty}^{\infty}S_d(\omega''/2\pi))D(\omega'')\,d\omega'' \quad \text{(E-4)}$$

Separating $\omega = 0$ terms from $\omega \neq 0$ terms, I have:

$$B(0)\nu = -\frac{\Omega}{2}\delta(\omega) + \frac{\varepsilon}{4\pi}\int_{-\infty}^{\infty}S_d(\omega'/2\pi)D(\omega')\left(\frac{1}{\Gamma_{10}/2}+\frac{1}{i\omega'+\Gamma_{10}/2}\right)d\omega' - \frac{\nu}{4\pi}\int_{-\infty}^{\infty}\frac{S_d(\omega'/2\pi)}{i\omega'+\Gamma_{10}/2}\,d\omega' \quad \text{(E-5)}$$

$$B(\omega)D(\omega) = \varepsilon\nu\left(\frac{1}{i\omega+\Gamma_{10}/2}+\frac{1}{\Gamma_{10}/2}\right) - \frac{1}{4\pi\Gamma_{10}}\int_{-\infty}^{\infty}S_d(\omega'/2\pi))D(\omega')\,d\omega' \quad \text{(E-6)}$$

Solving Eqs. E-6 for $D(\omega)$, I find

[1] The simplification of the last term on the right hand side is based on the assumption that the noise is low frequency compared to Γ_{10} . However even for high frequency noise this simplification does not affect the final result for $< \rho'_{11} >$ since the contribution from this term is small for high frequency noise.

$$D(\omega) = \frac{\varepsilon\nu}{B(\omega)} \left(\frac{1}{i\omega + \Gamma_{10}/2} + \frac{1}{\Gamma_{10}/2} - \frac{\int_{-\infty}^{\infty} \left(\frac{1}{i\omega' + \Gamma_{10}/2} + \frac{1}{\Gamma_{10}/2} \right) \frac{S_d(\omega'/2\pi)}{B(\omega')}\, d\omega'}{2\pi\Gamma_{10} + \int_{-\infty}^{\infty} S_d(\omega'/2\pi) B(\omega')\, d\omega'} \right) \tag{E-7}$$

Indeed $D(\omega)$ has no direct dependence on $h(\omega)$ since the integrals involving $S_d(\omega/2\pi)$ yield constants. This justifies the form of the ansatz solution Eq. E-3. Substituting Eq. E-7 into Eq. E-5, I find:

$$\nu = \frac{-\Omega\Gamma_{10}/2}{\Omega^2 + (1+A)\Gamma_{10}^2/2 + (2-B)\varepsilon^2} \tag{E-8}$$

where A and B are given by Eqs. 4.35 and 4.36 respectively. Finally I have the time average of ρ'_{11}:

$$< \rho'_{11} >= \frac{\Omega^2/2}{\Omega^2 + (1+A)\Gamma_{10}^2/2 + (2-B)\varepsilon^2} \tag{E-9}$$

which is Eq. 4.34.

BIBLIOGRAPHY

[1] R. P. Feynman, Int. J. Theor. Phys. **21**, 467 (1982).

[2] D. Deutsch, Proceedings of the Royal Society of London: Series A - Mathematical and Physical Sciences **A400**, 97 (1985).

[3] D. Deutsch and R. Jozsa, Proceedings of the Royal Society of London: Series A - Mathematical and Physical Sciences **A439**, 553 (1985).

[4] P. W. Shor, Probing the limits of superconductivity, in *35th Annu. Symp. Foundations of Computer Science*, edited by S. Goldwasser, Los Alamitos, California, 1994, IEEE Computer Society Press.

[5] S. Lloyd, Science **273**, 1073 (1996).

[6] L. K. Grover, Phys. Rev. Lett. **79**, 325 (1997).

[7] A. Ekert and R. Jozsa, Phil. Trans. R. Soc. Lond. A **356**, 1769 (1998).

[8] C. H. Bennett and S. J. Wiesner, Phys. Rev. Lett. **69**, 2881 (1992).

[9] C. H. Bennett, G. Brassard, C. Crepeau, R. Jozsa, A. Peres, and W. K. Wootters, Phys. Rev. Lett. **70**, 1895 (1993).

[10] M. A. Nielsen and I. L. Chuang, *Quantum Computation and Quantum Information*, 2001 ed. (Cambridge Univ. Press, Cambridge, 2001).

[11] R. Hughes *et al.*, *A quantum information science and technology roadmap*,version 2.0, (April 2004, http://qist.lanl.gov).

[12] D. P. DiVincenzo, Phys. Rev. A **51**, 1015 (1995).

[13] S. Lloyd, Phys. Rev. Lett. **75**, 346 (1995).

[14] A. Einstein, B. Podolsky, and N. Rosen, Phys. Rev. **47**, 777 (1935).

[15] E. Schrödinger, Naturw **23**, 807,823,844 (1935).

[16] C. H. Bennett, D. P. DiVincenzo, J. A. Smolin, and W. K. Wootters, Phys. Rev. A **54**, 3824 (1996).

[17] J. S. Bell, Physics **1**, 195 (1964).

[18] R. Jozsa and N. Linden, Proceedings of the Royal Society of London: Series A - Mathematical and Physical Sciences **A459**, 2011 (2003).

[19] L. K. Grover, Phys. Rev. A **52**, R2493 (1995).

[20] A. M. Steane, Phys. Rev. Lett. **77**, 793 (1996).

[21] A. M. Steane and B. Ibinson, Fault-tolerant logical gate networks for css codes, (4-Nov-03) preprint *quant-ph*/0311014.

[22] D. A. Lidar and K. B. Whaley, Decoherence-free subspaces and subsystems in irreversible quantum dynamics, in *Springer Lecture Notes in Physics*, edited by F. Benatti and R. Floreanini, Berlin, 2003, Springer-Verlag.

[23] A. Abragam, *The Principles of Nuclear Magnetism* (Oxford University Press, London, 1961).

[24] P. Slitcher, *Principles of Magnetic Resonance*, 3rd ed. (Springer-Verlag, Berlin, 1990).

[25] D. G. Cory, A. F. Fahmy, and T. F. Havel, Proceedings of the National Academy of Science(USA) **94**, 1634 (1997).

[26] W. S. Warren, Science **277**, 1688 (1997).

[27] L. M. K. Vandersypen, M. Steffen, G. Breyta, C. S. Yannoni, M. H. Sherwood, and I. L. Chuang, Nature **414**, 883 (2001).

[28] J. I. Cirac and P. Zoller, Phys. Rev. Lett. **74**, 4091 (1995).

[29] F. Schmidt-Kaler, H. Häffner, M. Riebe, S. Gulde, G. P. T. Lancaster, T. Deuschle, C. Becher, C. F. Roos, J. Eschner, and R. Blatt, Nature **422**, 408 (2003).

[30] D. Leibfried, B. DeMarco, V. Meyer, D. Lucas, M. Barrett, J. Britton, W. M. Itano, B. Jelenkovic, C. Langer, T. Rosenband, and D. J. Wineland, Nature **422**, 412 (2003).

[31] C. F. Roos, M. Riebe, H. Häffner, W. Hänsel, J. Benhelm, G. P. T. Lancaster, C. Becher, F. Schmidt-Kaler, and R. Blatt, Science **304**, 1478 (2004).

[32] D. Leibfried, M. D. Barrett, T. Schaetz, J. Britton, J. Chiaverini, W. M. Itano, J. D. Jost, and D. J. Wineland, Science **304**, 1476 (2004).

[33] D. Kielpinski, C. Monroe, and D. J. Wineland, Nature **417**, 709 (2002).

[34] J. I. Cirac and P. Zoller, Nature **404**, 579 (2000).

[35] T. Pellizzari, Phys. Rev. Lett. **79**, 5242 (1997).

[36] R. G. Devoe, Phys. Rev. A **58**, 910 (1998).

[37] I. H. Deutsch, G. K. Brennen, and P. S. Jessen, Fortschritte der Physik **48**, 925 (2000).

[38] H. J. Briegel, T. Calarco, D. Jaksch, J. Cirac, and P. Zoller, Journal of Modern Optics **47**, 941 (2000).

[39] G. K. Brennen, C. M. Caves, P. S. Jessen, and I. H. Deutshc, Phys. Rev. Lett. **82**, 1060 (1999).

[40] S. Peil, J. V. Porto, B. Laburthe-Tolra, J. M. Obrecht, B. E. King, M. Subbotin, S. I. Rolston, and W. D. Phillips, Phys. Rev. A **67**, 051603(R) (2003).

[41] N. J. Cerf, C. Adami, and P. G. Kwiat, Phys. Rev. A **57**, R1477 (1998).

[42] S. D. Bartlett, B. C. Sanders, S. L. Braunstein, and K. Nemoto, Phys. Rev. Lett. **88**, 097904 (2002).

[43] E. Knill, R. Laflamme, and G. J. Milburn, Nature **409**, 46 (2001).

[44] J. M. Raimond, M. Brune, and S. Haroche, Rev. Mod. Phys. **73**, 565 (2001).

[45] J. Ye, D. W. Vernooy, and H. J. Kimble, Phys. Rev. Lett. **83**, 4987 (1999).

[46] G. R. Guthohrlein, M. Keller, K. Hayaska, W. Lange, and H. Walther, Nature **414**, 49 (2001).

[47] A. B. Mundt, A. Kreuter, C. Becher, D. Leibfried, J. Eschner, F. Schmidt-Kaler, and R. Blatt, Phys. Rev. Lett. **89**, 103001 (2002).

[48] A. Blais, R.-S. Huang, A. Wallraff, S. M. Girvin, and R. J. Schoelkopf, Phys. Rev. A **69**, 062320 (2004).

[49] A. Wallraff, D. Schuster, A. Blais, L. Frunzio, R.-S. Huang, J. Majer, S. Kumar, S. M. Girvin, and R. J. Schoelkopf, Circuit quantum electrodynamics: coherent coupling of a single photo to a cooper pair box, cond-mat/0407325.

[50] H. Xu, F. W. Strauch, S. K. Dutta, P. R. Johnson, R. C. Ramos, A. J. Berkley, H. Paik, J. R. Anderson, A. J. Dragt, C. J. Lobb, and F. C. Wellstood,

Spectroscopy of multiparticle entanglement in a macroscopic superconducting circuit, Submitted for publication.

[51] D. Loss and D. P. DiVincenzo, Phys. Rev. A **57**, 120 (1998).

[52] B. E. Kane, Nature **393**, 133 (1998).

[53] P. Recher, E. V. Sukhorukov, and D. Loss, Phys. Rev. Lettt. **85**, 1962 (2000).

[54] G. P. Berman, G. D. Doolen, P. C. Hammel, and V. I. Tsifrinovich, Phys. Rev. B **61**, 14694=14699 (2000).

[55] Y. Makhlin, G. Schön, and A. Shnirman, Rev. Mod. Phys. **73**, 357 (2001).

[56] M. F. Bocko, A. M. Herr, and M. J. Feldman, IEEE Trans. Appl. Supercon. **7**, 3638 (1997).

[57] J. E. Mooij, T. P. Orlando, L. Levitov, L. Tian, C. H. van der Wal, and S. Lloyd, Science **285**, 1036 (1999).

[58] T. P. Orlando, J. E. Mooij, L. Tian, C. H. van der Wal, L. S. Levitov, S. Lloyd, and J. J. Mazo, Phys. Rev. B **60**, 15398 (1999).

[59] C. H. van der Wal, A. C. J. ter Haar, F. K. Wilhelm, R. N. Schouten, C. J. P. M. Harmans, T. P. Orlando, S. Lloyd, and J. E. Mooij, Science **290**, 773 (2000).

[60] J. R. Friedman, V. Patel, W. Chen, S. K. Tolpygo, and J. E. Lukens, Nature **406**, 43 (2000).

[61] V. Averin, Solid State Commu. **105**, 659 (1998).

[62] Y. Nakamura, Y. A. Pashkin, and J. S. Tsai, Nature **398**, 786 (1999).

[63] D. Vion, A. Aassime, A. Cottet, P. Joyez, H. Pothier, C. Urbina, D. Esteve, and M. H. Devoret, Science **296**, 886 (2002).

[64] R. C. Ramos, M. A. Gubrud, A. J. Berkley, J. R. Anderson, C. J. Lobb, and F. C. Wellstood, IEEE Trans. on Appl. Supercond. **11**, 998 (2001).

[65] I. Chiorescu, Y. Nakamura, C. J. P. M. Harmans, and J. E. Mooij, Science **299**, 1869 (2003).

[66] Y. A. Pashkin, T. Yamamoto, O. Astafiev, Y. Nakamura, D. V. Averin, and J. S. Tsai, Nature **421**, 823 (2003).

[67] T. Yamamoto, Y. A. Pashkin, O. Astafiev, Y. Nakamura, and J. S. Tsai, Nature **425**, 941 (2003).

[68] J. M. Martinis, S. Nam, J. Aumentado, and C. Urbina, Phys. Rev. Lett. **89**, 117901 (2002).

[69] S. Han, Y. Yu, X. Chu, S. Chu, and Z. Wang, Science **293**, 1457 (2001).

[70] Y. Yu, S. Han, X. Chu, S. Chu, and Z. Wang, Science **296**, 889 (2002).

[71] A. J. Leggett, Prog. Theor. Phys. (Suppl.) **69**, 80 (1980).

[72] M. Tinkham, *Introduction to Superconductivity*, 2nd ed. (McGraw-Hill, New York, 1996).

[73] B. D. Josephson, Phys. Lett. **1**, 251 (1962).

[74] M. Gubrud, R. C. Ramos, A. J. Berkley, R. J. Anderson, C. J. Lobb, and F. C. Wellstood, IEEE Trans. on Appl. Supercond. **64**, 189 (2001).

[75] H. A. Kramers, Physica (Utrecht) **7**, 284 (1940).

[76] M. Büttiker, E. P. Harris, and R. Landauer, Phys. Rev. B **28**, 1268 (1983).

[77] R. F. Voss and R. A. Webb, Phys. Rev. Lett. **47**, 265 (1981).

[78] M. H. Devoret, J. M. Martinis, and J. Clarke, Phys. Rev. Lett. **55**, 1908 (1985).

[79] A. J. Berkley, *A Josephson Junction Qubit*, PhD thesis, University of Maryland, 2003.

[80] J. M. Martinis, M. H. Devoret, and J. Clarke, Phys. Rev. Lett. **55**, 1543 (1985).

[81] A. O. Caldeira and A. J. Leggett, Ann. Phys. (N.Y.) **149**, 374 (1983).

[82] T. A. Fulton and L. N. Dunkleberger, Phys. Rev. B **9**, 4760 (1974).

[83] A. I. Larkin and Y. N. Ovchinnikov, Sov. Phys. JETP **64**, 185 (1986).

[84] K. S. Chow, D. A. Browne, and V. Ambegaokar, Phys. Rev. B **37**, 1624 (1988).

[85] P. Kopietz and S. Chakravarty, Phys. Rev. B **38**, 97 (1988).

[86] T. Shibata, Phys. Rev. B **43**, 6760 (1991).

[87] F. W. Strauch, private communication.

[88] P. Silvestrini, Y. N. Ovchinnikov, and R. Criso, Phys. Rev. B **41**, 7341 (1990).

[89] P. Silvestrini, V. G. Palmieri, B. Ruggiero, and M. Russo, Phys. Rev. Lett. **79**, 3046 (1997).

[90] B. Ruggiero, M. G. Castellano, G. Torrioli, C. Cosmelli, F. Chiarello, V. G. Palmieri, C. Granata, and P. Silvestrini, Phys. Rev. B **59**, 177 (1999).

[91] H. Xu, A. J. Berkley, M. A. Gubrud, R. C. Ramos, J. R. Anderson, C. J. Lobb, and F. C. Wellstood, IEEE Trans. on Appl. Supercond. **13**, 956 (2003).

[92] A. J. Leggett, S. Chakravarty, A. T. Dorsey, M. P. A. Fisher, A. Garg, and W. Zwerger, Rev. Mod. Phys. **59**, 1 (1987).

[93] U. Weiss, *Quantum Dissipative Systems*, 2nd ed. (World Scientific, Singapore, 1999).

[94] M. H. Devoret, Quantum fluctuation in electrical circuits, in *Quantum Fluctuation*, edited by E. G. S. Reynaud and J. Zinn-Justin, Amsterdam, 1997, Elsevier Science.

[95] J. B. Johnson, Phys. Rev. **32**, 97 (1928).

[96] H. Nyquist, Phys. Rev. **32**, 110 (1928).

[97] L. Tian, S. Lloyd, and T. P. Orlando, Phys. Rev. B **65**, 144516 (2002).

[98] A. Shnirman, Y. Makhlin, and G. Shön, Physica Scripta **T102**, 147 (2002).

[99] H. Xu, A. J. Berkley, M. A. Gubrud, R. C. Ramos, J. R. Anderson, C. J. Lobb, and F. C. Wellstood, Spectroscopic resonance broadening in a josephson junction qubit due to current noise, to appear in Phys. Rev. B.

[100] C. Cohen-Tannoudji, J. Dupont-Roc, and G. Grynberg, *Atom-Photon Interactions : Basic Processes and Applications*, 3rd ed. (John Wiley & Sons, New York, 1992).

[101] J. M. Martinis, S. Nam, J. Aumentado, and K. M. Lang, Phys. Rev. B **67**, 094510 (2003).

[102] A. J. Berkley, H. Xu, M. A. Gubrud, R. C. Ramos, J. R. Anderson, C. J. Lobb, and F. C. Wellstood, IEEE Trans. on Appl. Supercond. **68**, 060502(R) (2003).

[103] A. C. Anderson and R. E. Peterson, Phys. Lett. **55**, 518 (1972).

[104] M. L. Roukes, M. R. Freeman, R. S. Germain, R. C. Richardson, and M. B. Ketchen, Phys. Rev. Lett. **55**, 422 (1985).

[105] F. C. Wellstood, C. Urbina, and J. Clarke, IEEE Trans. on Appl. Magn. **25**, 1001 (1989).

[106] F. C. Wellstood, *Excess noise in the dc SQUID*, PhD thesis, University of California, Berkeley, 1988.

[107] I. Jin, *Low Noise dc Superconducting Quantum Interference Devices for Gravity Wave Detection*, PhD thesis, University of Maryland, 1997.

[108] F. Cawthorne, *Dynamics of Josephson Junctions and Josephson junction arrays*, PhD thesis, University of Maryland, 1998.

[109] Murata-erie p/n LQW1608A10NG00T1, www.murata.com.

[110] American Technical Ceramics ATC100A series, www.atceramics.com.

[111] Epotek H20E Two component silver filled epoxy, www.epotek.com.

[112] Hypres Inc. Nb/AlOx/Nb foundary, www.hypres.com.

[113] S. S. Mohan, M. del Mar Hershenson, S. P. Boyd, and T. H. Lee, IEEE Journal of Solid State Circuits **34**, 1419 (1999).

[114] G. J. Dolan, Appl. Phys. Lett. **31**, 337 (1977).

[115] J. Aumentado, private communication.

[116] V. Ambegaokar and A. Baratoff, Phys. Rev. Lett. **10**, 486 (1963).

[117] Thermocoax Philips cable type 1 NcAc, www.thermocoax.com.

[118] P. Zorin, Appl. Phys. Lett. **64**, 189 (1995).

[119] S. Y. Liao, *Microwave Devices and Circuits*, 3rd ed. (Prentice Hall, Englewood Cliffs, NJ, 1990).

[120] J. M. Martinis, M. H. Devoret, and J. Clarke, Phys. Rev. B. **35**, 4682 (1987).

[121] A. Fukushima, A. Sato, A. Iwasa, Y. Nakamura, T. Komatsuzaki, and Y. Sakamoto, IEEE Trans. on Instrum. and Meas. **46**, 289 (1997).

[122] K. Bladh, D. Gunnarsson, E. Hürfeld, S. Devi, C. Kristoffersson, B. Smalander, S. Pehrson, T.Claeson, P. Delsing, and M. Taslakov, Rev. Sci. Instrum. **74**, 1323 (2003).

[123] low-pass filter, model SLP-1.9, 2.5 MHz 3dB point, www.mini-circuits.com.

[124] American Technical Ceramics ATC KIT 12-700B 10 to 100 pF, www.atceramics.com.

[125] Coil Winding Specialist 1210 series SMI - Wound Ceramic Chip Inductor, CCI-1210-10N, R10, 2R2, www.coilws.com.

[126] C. Gonzalez and F. Pedersen, An ultra low noise ac beam transformer for deceleration and diagnostics of low intensity beams, in *the 1999 Particle Accelerator Conference* Vol. 1, pp. 474–476, IEEE, 1999.

[127] A. van der Ziel, *Noise: Sources, Characteristics, Measurements* (Prentice Hall, Englewood Cliffs, NJ, 1970).

[128] J. M. Martinis, *Macroscopic quantum tunneling and energy level quantization in the zero-voltage state of a current-biased Josephson junction*, PhD thesis, University of California, Berkeley, 1985.

[129] K. M. Lang, S. Nam, J. Aumentado, C. Urbina, and J. M. Martinis, IEEE Trans. on Appl. Supercond. **13**, 989 (2003).

[130] S. K. Dutta, H. Xu, A. J. Berkley, M. A. Gubrud, R. C. Ramos, J. R. Anderson, C. J. Lobb, and F. C. Wellstood, to appear in Phys. Rev. B Rapid Commu. .

[131] S. K. Dutta, H. Xu, H. Paik, R. C. Ramos, J. R. Anderson, C. J. Lobb, and F. C. Wellstood, In progress.

[132] P. R. Johnson, F. W. Strauch, A. J. Dragt, R. C. Ramos, J. R. Anderson, C. J. Lobb, and F. C. Wellstood, Phys. Rev. B **67**, 020509(R) (2003).

[133] F. W. Strauch, P. R. Johnson, A. J. Dragt, C. J. Lobb, J. R. Anderson, and F. C. Wellstood, In progress.

[134] F. W. Strauch, P. R. Johnson, A. J. Dragt, C. J. Lobb, J. R. Anderson, and F. C. Wellstood, Phys. Rev. Lett. **91**, 167005 (2003).

[135] A. Blais, A. M. van den Brink, and A. M. Zagoski, Phys. Rev. Lett. **90**, 127901 (2003).

[136] F. Plastina and G. Falci, Phys. Rev. B **67**, 224514 (2003).

[137] A. J. Berkley, H. Xu, R. C. Ramos, M. A. Gubrud, F. W. Strauch, P. R. Johnson, J. R. Anderson, A. J. Dragt, C. J. Lobb, and F. C. Wellstood, Science **300**, 1548 (2003).

[138] J. S. Bendat, *Principles and Applications of Random Noise Theory* (John Wiley & Sons, Inc., New York, 1958).